East European Journal of Physics. 1. 428–446 (2026)
DOI: 10.26565/2312-4334-2026-1-51 ISSN 2312-4334

NUMERICAL INVESTIGATION OF HEAT TRANSFER ANALYSIS USING ELECTROMAGNETOHYDRODYNAMICS WITH AGGREGATED NANOPARTICLES

A. Lokeshwari, **Peri K. Kameswaran***
Department of Mathematics, School of Advanced Sciences, Vellore Institute of Technology, Vellore 632014, India
Corresponding Author e-mail: perikamesh@gmail.com,
Received October 22, 2025; revised January 8, 2026; accepted January 11, 2026

Optimizing heat transmission remains a significant contemporary challenge in modern technological applications. Nanofluids exhibit strong potential thermal conductivity for enhancing heat transfer and improving energy system efficiency. In comparison to dispersed nanoparticles, aggregated nanoparticles are noteworthy for evaluating the thermal behavior of nanoparticles at the nanoscale. In spite of that aggregation effect, the fractal dimension of the aggregated nanoparticles will have a transformative effect on heat transfer. The objective of the present study is to investigate the influence of electromagnetohydrodynamic effects on heat transfer in a nanofluid containing aggregated nanoparticles over an exponentially stretching sheet. The governing equations for momentum and energy are transformed into a system of nonlinear ordinary differential equations with specified boundary conditions. An analytical solution is presented for a specific instance where the electric field parameter is absent. Numerical solutions are achieved for various ranges of physical parameters, and computed results are validated with existing literature. The findings indicate that nanoparticle aggregation leads to thickening the thermal boundary layer and improving heat transfer. In addition to this synergistic effect of aggregation and electric field, it leads to the decrease in velocity profiles. At 5% volume fraction, aggregated nanoparticles provide a heat transfer enhancement of approximately 34% over dispersed nanoparticles. The temperature profiles exhibit a rising trend with an increasing volume fraction. In the presence of aggregated nanoparticles, both the skin friction coefficient and the Nusselt number increase with rising magnetic field strength.

Keywords: *Aggregated nanoparticles; Electric field; Magnetic field; Radiation; Viscous dissipation; Exponential stretching sheet*

PACS: 04.50.Kd, 04.20.Jb

1. INTRODUCTION

Over the past several decades, research has been designed for various experimental setups and methodologies to analyze how aggregation influences nanofluid behavior and to develop methods for controlling aggregation to optimize its thermal performance. Nanoparticles aggregation occurs in which individual particles stick together and form a cluster. Numerous factors have been involved in this phenomenon like, interaction between nanoparticles, Van der Waals forces, surface charges (Lee et al. [1]), etc. Aggregated nanoparticles (especially metals like platinum, gold, silver, or iron oxides) are widely used as catalysts, inks for printing electrical circuits, and removal of contaminants from water due to their high surface area-to-volume ratio.

Gaganpreet and Srivastava [2] examined the influence of viscosity and thermal conductivity of aggregated nanoparticles in a nanofluid. They found that as the size of the aggregated spherical nanoparticles increases, exactly for radii $r_a = 3r, 4r, 5r$ the viscosity also increases. Liao et al. [3] studied nanoparticles aggregation on the thermal conductivity of nanofluid by molecular dynamic solutions. They observed a particle size is a key factor to determine the potential mechanisms that affect the thermal conductivity of nanofluid. Feng et al. [4] investigated the effective thermal conductivity of nanofluid based on the structure of nanolayer and nanoparticles aggregation. Their study reveals that nanoparticles aggregation has an effective thermal conductivity even at lower volume fractions. Mahanthesh [5] investigated the study of the flow and heat transport of aggregation kinematics of nanoparticles with quadratic radiative heat flux using a modified Buongiorno model. They figured out that the magnitude of velocity is higher in the case of strong convective heating.

Experimental studies have shown that aggregated nanoparticles can increase the efficiency of heat conductivity in comparison to the dispersed particle. Aggregated nanoparticles can enhance heat transfer in nanofluid through their unique structure, which forms conductive networks or pathways. This can significantly improve the thermal conductivity and convective heat transfer properties. Chen et al. [6] studied the experimental and theoretical study of aggregated nanoparticles and their thermal radiation properties. They have experimentally validated their results, showing that aggregated nanoparticles exhibit more effective heat transfer compared to individual nanoparticles. Motevasel et al. [7] studied the heat conductivity of four types of nanofluids containing aggregated nanoparticles and also compared their results with experimental validation. They analyzed that the nanoparticle's aggregation has a better attribution of heat conductivity even at low volume concentration. Muhammad et al. [8] have reported that the aggregative and non-aggregative effects of nanofluid flow in the application of cooling systems in liquid rocket engines. They found the aggregative and non-aggregative nanoparticle flows are similar for both velocity and temperature profiles for particular cases; however, noticeable differences emerged at higher values of radiation and volume fraction. Pang et al. [9] analyzed the nanoparticles

Cite as: A. Lokeshwari, P.K. Kameswaran, East Eur. J. Phys. 1, 428 (2026), https://doi.org/10.26565/2312-4334-2026-1-51

aggregation model for heat conduction mechanism in nanofluid. They concluded that the interfacial thermal resistance and nanolayer have minimal impact on the thermal conductivity, even if nanoparticles concentration is very minimal. Numerous researchers Ellahi et al. [10], Sathya and Naveen [11] studied the role of aggregation and non-aggregation effects of nanoparticles in determining the thermal behavior of nanofluids. They found that the aggregation effects of nanoparticles have a better efficiency of heat transfer compared to individual nanoparticles.

Electromagnetohydrodynamics is the study of fluid flow influenced by both electric and magnetic fields. EMHD flows are especially relevant in microfluidics, cooling systems, spacecraft thermal control, and biomedical devices, where external electric and magnetic fields are used to control fluid movement at small scales. Duraihem [12] targeted the EMHD Darcy–Forchheimer flow of Sutterby nanofluid over a stretching sheet using the finite difference approach. Ramesh et al. [13] explored the EMHD flow of hybrid nanofluid flow over an exponential stretching sheet. They resulted that the velocity distribution is strengthened with increasing Helmholtz–Smoluchowski velocity, whereas the temperature distribution exhibits a diminishing trend. Loganayagi and Kameswaran. [14] investigated the effects of an electromagnetic field and heat source/sink on two-dimensional nanofluid flow over a stretching cylinder. Their findings indicate that Gadolinium is particularly suitable for thermomagnetic generators due to its optimal operating temperature range. Madhu et al. [15] scrutinized the impacts of nanoparticles aggregation across a stretching sheet with an analytical solution. Their study explores how the aggregation state of nanoparticles influences heat transfer efficiency and highlights its significant role in thermal conductivity with the influence of porous medium. Swain et al. [16] conducted a study to investigate the influence of aggregated nanoparticles on radiative 3D flow of Maxwell fluid over a permeable stretching surface.

In addition to the above considered effects, it is interesting to study the effects of thermal radiation due to its applications. When nanofluids are employed, the presence of nanoparticles can alter the radiative heat transfer characteristics by modifying the absorption, scattering, and emission properties of the base fluid. Kameswaran et al. [17] examined the radiation effects on MHD flow over an exponential stretching sheet and also found analytical solutions using hyper-geometric functions, highlighting the significant role of radiation in modifying the thermal boundary layer behavior. It is evident that thermal radiation enhances the temperature within the boundary layer region. Wang et al. [18] studied the effects of thermal radiation and nanoparticles aggregation on the gap between cone and disk. Consequently, the phenomenon of nanoparticle aggregation has been extensively examined by various researchers such as Rajput et al. [19], Ali et al. [20], and Rafique et al. [21] across diverse scientific and engineering domains.

Only a limited study has generalized the effects of nanoparticle aggregation in the existing literature. Madhu et al. [15] investigated the influence of nanoparticle aggregation and porous media on flow over an exponential stretching sheet, without considering the effects of magnetic and electric fields. Kameswaran et al. [17] examined the role of thermal radiation on hydromagnetic newtonian fluid flow over an exponential stretching sheet, neglecting both nanoparticle aggregation and electric field effects. Motivated by these limitations, the present study investigates the impact of aggregated and non-aggregated nanoparticles on heat transfer in electromagnetohydrodynamic (EMHD) flow over an exponential stretching sheet, incorporating the combined effects of electric and magnetic fields, thermal radiation, and viscous dissipation. The results are presented graphically to illustrate and compare the heat transfer characteristics of nanofluids with and without nanoparticle aggregation. The research questions are formulated based on the discussion of how nanoparticle aggregation influences the flow and heat transfer characteristics of EMHD nanofluids.

- How does the aggregation of nanoparticles affect the thermal fields?
- How does induction of nanoparticle aggregation by an electric field impact both the flow dynamics and thermal behavior of nanofluids?
- How do aggregated and non-aggregated nanoparticles affect EMHD flow over an exponential stretching sheet?
- How do electric and magnetic fields, thermal radiation, and viscous dissipation influence the behavior of nanofluid flow and heat transfer?

2. MATHEMATICAL MODEL

We consider the steady, incompressible, laminar, two-dimensional electromagnetohydrodynamic flow of a viscous liquid over an exponentially stretching sheet. The geometric representation of the flow model is illustrated in Fig. 1.

- Assume the origin is positioned at the slit, with the plate extending along the x-axis.
- The sheet's velocity is modeled as an exponential function of the distance x, where $U_w = U_0 e^{\frac{x}{L}}$, with U being the velocity at the slit and L a characteristic length.
- The fluid temperature is denoted by T, while T_w represents the wall temperature and T_∞ denotes the ambient temperature of the sheet, which is assumed constant, where $T_w = T_\infty + T_0 e^{\frac{2x}{L}}$.
- A uniform electric field $E(x)$ and magnetic field of intensity $B(x)$ are simultaneously applied, both oriented perpendicular to the flow direction.

- Moreover, a modified Krieger-Dougherty model and a Maxwell-Bruggeman [5] model were used for aggregated nanoparticle viscosity and thermal conductivity, respectively.

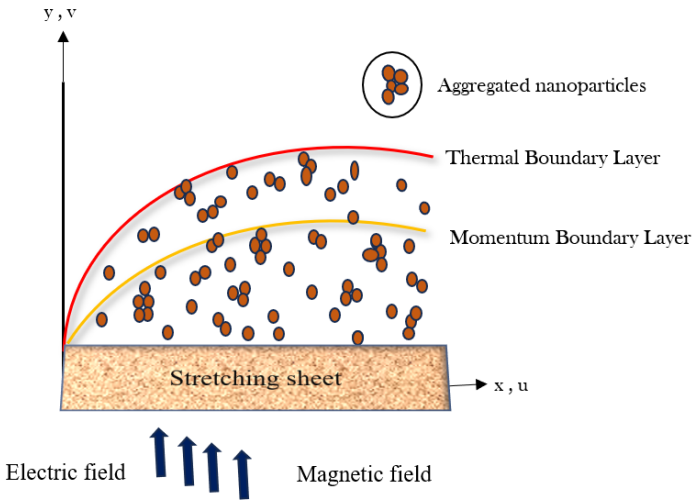

Figure 1. Structural diagram of the model

2.1. Mathematical formulation

Based on the following assumptions, the corresponding system of mathematical equations is formulated as follows: (Kameswaran et al. [17])

$$\frac{\partial u}{\partial x}+\frac{\partial v}{\partial y}=0, \tag{1}$$

$$u\frac{\partial u}{\partial x}+v\frac{\partial v}{\partial y}=\frac{\mu_{nf}}{\rho_{nf}}\left(\frac{\partial^2 u}{\partial y^2}\right)+\frac{\sigma_{nf}}{\rho_{nf}}\left(EB-B^2u\right), \tag{2}$$

$$u\frac{\partial T}{\partial x}+v\frac{\partial T}{\partial y}=\frac{K_{nf}}{(\rho C_p)_{nf}}\left(\frac{\partial^2 T}{\partial y^2}\right)-\frac{1}{(\rho C_p)_{nf}}\left(\frac{\partial q_r}{\partial y}\right)+\frac{\sigma_{nf}}{(\rho C_P)_{nf}}(uB-E)^2 + \frac{\nu_f}{(C_p)_f}\left(\frac{\partial u}{\partial y}\right)^2. \tag{3}$$

The boundary conditions for the Eqs. (1)-(3) are as follows:

$$u=U_w=U_0e^{\frac{x}{L}}, \quad v=0, \quad T=T_w=T_\infty+T_0e^{\frac{2x}{L}}, \quad \text{at} \quad y=0. \tag{4}$$

$$u\to 0, \qquad T\to T_\infty, \qquad as \quad y\to\infty. \tag{5}$$

Here, the velocity component u along the x direction and the velocity component v along the y direction respectively.

Following Rosseland's approximation, q_r is the heat-radiation flux,

$$q_r=-\frac{4\sigma^*}{3k^*}\frac{\partial T^4}{\partial y}, \tag{6}$$

Here σ^* represents the Stefan-Boltzman constant and k^* denotes a mean absorption coefficient. The term is T^4 linearized by expanding about the ambient temperature T_∞. Using Taylor series expansion and neglecting higher-order terms, we approximate $T^4\cong 4T_\infty^3T-3T_\infty^4$.

Introducing a stream function $\psi(x,y)$ such that,

$$u=\frac{\partial\psi}{\partial y} \quad \text{and} \quad v=-\frac{\partial\psi}{\partial x},$$

The stream function is identically satisfying Eq. (1).

The following similarity variables are taken into account for the exponential stretching sheet problem and are defined as follows: (Mabood et al. [22]).

$$u = U_0 e^{\frac{x}{L}} f_\eta(\eta), \quad v = -\left(\frac{\nu_f U_0}{2L}\right)^{\frac{1}{2}} e^{\frac{x}{2L}} [f(\eta) + \eta f_\eta(\eta)],$$
$$T = T_\infty + T_0 e^{\frac{2x}{L}} \theta(\eta), \quad \eta = \left(\frac{U_0}{2\nu_f L}\right)^{\frac{1}{2}} y e^{\frac{x}{2L}}, \tag{7}$$

Here, the dimensionless stream function is referred to as $f(\eta)$ and the dimensionless temperature is referred to as $\theta(\eta)$ and η is referred to as a similarity variable. Using Eq. (7), the Eq. (1) gets satisfied and Eq. (2)-(3) is transformed into an ordinary differential equations as described below:

$$\left(\frac{Z_1}{Z_2}\right) f_{\eta\eta\eta} - 2f_\eta^2 + f f_{\eta\eta} + \left(\frac{Z_3}{Z_2}\right)[M(E - f_\eta)] = 0, \tag{8}$$
$$\left(\frac{Z_4}{Z_5}\right)\frac{\theta_{\eta\eta}}{Pr} + \frac{4}{3}R\frac{\theta_{\eta\eta}}{Pr}\left(\frac{1}{Z_5}\right) + \theta_\eta f - 4f_\eta\theta + \left(\frac{Z_3}{Z_5}\right) MGb\left(f_\eta - E\right)^2 + Gbf_{\eta\eta}^2 = 0, \tag{9}$$

along with the boundary conditions,

$$f(0) = 0, \quad f_\eta(0) = 1, \quad \lim_{\eta\to\infty} f_\eta(\eta) = 0$$
$$\theta(0) = 1, \quad \lim_{\eta\to\infty} \theta(\eta) = 0. \tag{10}$$

The dimensionless parameters emerging in Eqs. (8)-(9) are stated below,

$$M = \frac{2\sigma_f B_0^2 L}{\rho_f U_0}, \quad R = \frac{4\sigma^* T_\infty^3}{k^* k_f}, \quad E = \frac{E_o}{U_0 B_0}, \quad Pr = \frac{\nu_f(\rho C_p)_f}{k_f},$$
$$Gb = \frac{U_0^2}{(C_p)_f T_0}, \quad Z_1 = \frac{\mu_{nf}}{\mu_f}, \quad Z_2 = \frac{\rho_{nf}}{\rho_f}, \quad Z_3 = \frac{\sigma_{nf}}{\sigma_f}, \quad Z_4 = \frac{K_{nf}}{K_f},$$
$$Z_5 = \frac{(\rho C_P)_{nf}}{(\rho C_P)_f}.$$

The viscosity of the base fluid is defined as μ_f, the density of the base fluid is indicated as ρ_f and the density of the nanofluid is denoted as ρ_{nf}. K_{nf} indicates a thermal conductivity of the nanofluid while k_f is referred to as the thermal conductivity of the base fluid. The specific heat capacity of the nanofluid is represented as $(\rho C_P)_{nf}$ and the specific heat capacity of the base fluid is denoted as $(\rho C_P)_f$, the solid volume portion of the nanofluid is indicated as ϕ, the dynamic viscosity is referred as μ_{nf}. The density of nanofluid is assumed to be ρ_{nf}. The symbol for thermal conductivity and heat capacity of nanofluid are represented as K_{nf} and $(\rho C_p)_{nf}$.

2.2. Effective Thermophysical properties of Nanofluid

Viscosity and thermal conductivity are two thermophysical properties of nanofluid that are influenced by the cluster of nanoparticles in the fluid. In the case where the impact of nanoparticles aggregation is insignificant, the effective dynamic viscosity and thermal conductivity were calculated using the modified Brinkman and Maxwell models (Makhdoum et al. [23]).

2.3. Aggregated nanoparticles parameters

Thermophysical properties are designated in accordance with the aggregation behavior of nanoparticles. The nanoparticle measurement results coincided precisely after taking into account the aggregation component of the nanoparticle. The

Table 1. Thermophysical properties of Copper and Water (Swain et al. [16])

Nanoparticle	$\rho(kg/m^3)$	$C_p(J/kgK)$	$\sigma(s/m)$	$k(W/mK)$	Prandtl number
Copper (Cu)	8933	385	$5.8 * 10^7$	401	-
Water H_2O	997.1	4179	0.05	0.613	5.83

symbol ϕ_{agg} is signed as an aggregated nanoparticle volume fraction and it is defined as $\phi_{agg} = \phi\left(\frac{R_{agg}}{R_p}\right)^{3-D_f}$. Here R_{agg} indicates the radius of the aggregated nanoparticle and R_p refers to the radius of the individual dispersed nanoparticle. D_f is termed as a fractal index, where D_f=1.8, $\frac{R_{agg}}{R_p} = 3.34$, $\phi_m = 0.605$, $\eta = 2.5$. The constants used in the present study are referred from: [Mahanthesh [5], Swain et al. [16]].

The Modified Krieger-Dougherty model and the modified Maxwell model are utilized to account for nanoparticle aggregation in thermal conductivity and effective viscosity as seen in Table 3. The thermal conductivity of the aggregated term is coined as (k_a), where,

$$\frac{k_a}{k_f} = \frac{1}{4}[(3\phi_{int}-1)\frac{k_s}{k_f} + (3(1-\phi_{int})-1) + [((3\phi_{int}-1)\frac{k_s}{k_f} + (3(1-\phi_{int})-1))^2 + 8\frac{k_s}{k_f}]^{\frac{1}{2}}] \text{ where, } \phi_{int} = \left(\frac{R_{agg}}{R_p}\right)^{D_f-3}$$

Here, the subscripts s and f are figured as nanofluid and fluid, respectively.

2.4. Effect of Electromagnetic Field on Nanoparticle Aggregation

The electromagnetic field influences nanoparticle aggregation by altering interparticle forces and particle motion. Specifically, the magnetic field produces Lorentz forces that suppress fluid velocity and Brownian motion, increasing the likelihood of particle–particle collisions and aggregation. In addition, the electric field induces electrophoretic motion and particle polarisation, leading to dipole–dipole attractions that further influence on aggregate formation. The role of the electromagnetic field is manifested indirectly through its influence on the flow dynamics via the Lorentz force. The modified velocity field directly impacts the transport of momentum and thermal energy. Simultaneously, the presence of nanoparticle aggregation alters the effective thermophysical properties, such as viscosity, thermal conductivity, and electrical conductivity. These effective properties determine the strength of the electromagnetic body force, which subsequently governs the overall flow and heat transfer performance.

2.5. Skin friction and Heat transfer Coefficients

The skin friction coefficient quantifies frictional losses and energy dissipation in fluid flow, and it is governed by fluid viscosity, flow velocity, surface roughness, and boundary layer behavior.

Table 2. Thermophysical properties of nanofluid without aggregation (Mackolil et al. [24])

Properties	Without Aggregation
Dynamic Viscosity	$\frac{\mu_{nf}}{\mu_f} = \frac{1}{(1-\phi)^{2.5}}$
Density	$\frac{\rho_{nf}}{\rho_f} = (1-\phi) + \phi\frac{\rho_s}{\rho_f}$
Electrical Conductivity	$\frac{\sigma_{nf}}{\sigma_f} = 1 + \frac{3\left(\frac{\sigma_s}{\sigma_f}-1\right)\phi}{\left(\frac{\sigma_s}{\sigma_f}+2\right)-\left(\frac{\sigma_s}{\sigma_f}-1\right)\phi}$
Thermal Conductivity	$\frac{k_{nf}}{k_f} = \frac{(k_s+2k_f)-2\phi(k_f-k_s)}{(k_s+2k_f)+\phi(k_f-k_s)}$
Specific heat capacity	$\frac{(\rho C_P)_{nf}}{(\rho C_P)_f} = (1-\phi) + \phi\frac{(\rho C_P)_s}{(\rho C_P)_f}$

Table 3. Thermophysical properties of nanofluid with aggregation (Rawat et al. [25] and Rana et al. [26])

Properties	With Aggregation
Dynamic Viscosity	$\frac{\mu_{nf}}{\mu_f} = \left(1-\frac{\phi_{agg}}{\phi_m}\right)^{(-\eta)\phi_m}$
Density	$\frac{\rho_{nf}}{\rho_f} = \left(1-\phi_{agg}\right) + \phi_{agg}\left(\frac{\rho_s}{\rho_f}\right)$
Electrical Conductivity	$\frac{\sigma_{nf}}{\sigma_f} = 1 + \frac{3\left(\frac{\sigma_s}{\sigma_f}-1\right)\phi_{agg}}{\left(\frac{\sigma_s}{\sigma_f}+2\right)-\left(\frac{\sigma_s}{\sigma_f}-1\right)\phi_{agg}}$
Thermal Conductivity	$\frac{k_{nf}}{k_f} = \frac{(k_a+2k_f)-2\phi_{agg}(k_f-k_a)}{(k_a+2k_f)+\phi_{agg}(k_f-k_a)}$
Specific heat capacity	$\frac{(\rho C_P)_{nf}}{(\rho C_P)_f} = \left(1-\phi_{agg}\right) + \phi_{agg}\frac{(\rho C_P)_s}{(\rho C_P)_f}$

The Skin friction coefficient is expressed as follows:

$$C_f = \frac{2\tau_w}{\rho_f U_w^2}, \tag{11}$$

where τ_w represents the shearing stress at the wall surface due to fluid motion, and it is defined as:

$$\tau_w = -\mu_{nf}\left[\frac{\partial u}{\partial y}\right]_{y=0} = -\mu_{nf}\left[\frac{U_0}{L}\sqrt{\frac{Re}{2}}\right] e^{\frac{3x}{2L}} f_{\eta\eta}(0) \tag{12}$$

Here, μ_{nf} denotes the dynamic viscosity coefficient, and the Reynolds number is represented as $Re = \frac{LU_0}{\nu}$

By using Eq. (12) in Eq. (11) we obtain,

$$(Re)^{0.5} C_f = -\left(\frac{Z_1}{Z_2}\right)\sqrt{2} f_{\eta\eta}(0) \tag{13}$$

The Nusselt number is a key dimensionless parameter used in heat exchanger design, offering insights into optimizing system performance by quantifying the enhancement in heat transfer due to fluid motion. The Nusselt number is expressed as follows:

$$Nu_L = \frac{L}{K_f}\left(\frac{q_w}{T_w - T_\infty}\right) \tag{14}$$

The rate of heat transfer in terms of thermal flux at the wall is expressed as:

$$q_w = -K_{nf}\left[\frac{\partial T}{\partial y}\right]_{y=0} = -K_{nf}\left[\frac{T_w - T_\infty}{L}\sqrt{\frac{Re}{2}}\right] e^{\frac{x}{2L}} \theta_\eta(0) \tag{15}$$

here K_{nf} is referred as the coefficient of Thermal conductivity of the fluid. By using Eq. (15) in Eq. (14) we obtain,

$$(Re)^{-0.5} Nu_L = -(Z_4/\sqrt{2})\theta_\eta(0) \tag{16}$$

3. EXACT SOLUTION

For particular case in which the absence of an electric field, the governing momentum and energy equations reduce to simplified forms.
i.e., $E \to 0$, Eq. (8) and Eq. (9) along with boundary conditions are compressed by

$$\frac{Z_1}{Z_2} f_{\eta\eta\eta} + f f_{\eta\eta} - 2f_\eta^2 - \frac{Z_3}{Z_2} M f_\eta = 0, \tag{17}$$

$$\left(\frac{Z_4}{Z_5}\right)\frac{\theta_{\eta\eta}}{Pr} + \frac{4}{3}R\frac{\theta_{\eta\eta}}{Pr}\left(\frac{1}{Z_5}\right) + \theta_\eta f - 4f_\eta\theta + \left(\frac{Z_3}{Z_5}\right) M G_b f_\eta^2 + G_b f_{\eta\eta}^2 = 0, \tag{18}$$

along with the boundary conditions,

$$\begin{aligned} &f(0) = 0, \quad f_\eta(0) = 1, \quad f_\eta(\infty) \to 0, \\ &\theta(0) = 1, \quad \theta(\infty) \to 0. \end{aligned} \tag{19}$$

3.1. Momentum equation

Integrating Eq. (17) with η once over to the interval $[0, \eta]$, we obtain

$$\frac{Z_1}{Z_2} f_{\eta\eta} + f f_\eta - \int_0^\eta \left[3f_\eta^2 + \frac{Z_3}{Z_2} M f_\eta\right] d\eta + S = 0, \tag{20}$$

Using boundary conditions, where $\eta \to [0, \infty)$ we obtain and

$$\begin{aligned} S &= -\frac{Z_1}{Z_2} f_{\eta\eta}(0), \\ S &= \int_0^\infty \left[3f_\eta^2 + \frac{Z_3}{Z_2} M f_\eta\right] d\eta, \end{aligned} \tag{21}$$

Once again Integrating Eq. (20), we attain,

$$\frac{Z_1}{Z_2} f_\eta + \frac{1}{2} f^2 = \int_0^\eta \left[\int_0^\eta \left[3 f_\eta^2 + \frac{Z_3}{Z_2} M f_\eta \right] d\eta \right] d\eta - S\eta + \frac{Z_1}{Z_2}, \tag{22}$$

Now, the solution procedure of Eq. (22) may be reduced to the sequential solutions.

$$\frac{Z_1}{Z_2} f_\eta^{(n)} + \frac{1}{2} f^{(n)2} = RHS[f_\eta^{(n-1)}], \tag{23}$$

The Eq. (21) can be solved by introducing an appropriate zero-order approximation as $f_\eta^{(0)}(\eta)$ for $f_\eta(\eta)$. This substitution simplifies the problem, effectively transforming it into a sequence of Riccati-type differential equations. As a result, the overall solution procedure becomes an iterative process, where each step involves solving a Riccati equation with updated approximations based on the previous iteration.

We assume a zero-order approximation as,

$$f(\eta) = \frac{1 - e^{-S\eta}}{S} \tag{24}$$

where S is a parameter associated with nanoparticle volume fraction. Integrating Eq. (24) with respect to η we get,

$$\begin{aligned} f_\eta(\eta) &= e^{-S\eta} \\ f_{\eta\eta} &= -S e^{-S\eta} \end{aligned} \tag{25}$$

After finding the derivatives of Eq. (24) substituting in the Eq. (21), the estimated value of S can be obtained as

$$S = \sqrt{\frac{3}{2} + \frac{Z_3}{Z_2} M}, \qquad S = -\frac{Z_1}{Z_2} f_{\eta\eta}^{(0)}(0) \tag{26}$$

Replacing all the derivatives from the zero-order approximation on the right-hand side of the Eq. (22), the equation for the first-order iteration is formulated as follows:

$$\frac{Z_1}{Z_2} f_\eta^{(n)} + \frac{1}{2} f^{(n)2} = \frac{Z_1}{Z_2} + \frac{3}{4S^2}[e^{-2S\eta} - 1] + \frac{Z_3}{Z_2}\frac{M}{S^2}[e^{-S\eta} - 1] \tag{27}$$

Additionally, we assume that the first-order approximation of f satisfies to the boundary conditions. Consequently,the nonlinear Riccati-type equation can be expressed using the confluent hypergeometric Whittaker function.

3.2. Energy Equation

By introducing this new variable, [See Kameswaran et al. [17]]

$$\xi = \frac{-Pr}{S^2} e^{-S\eta} \tag{28}$$

After finding derivatives of Eq. (28) and substituting into Eq. (18) and takes the form of

$$\xi\theta_{\xi\xi}\left[Z_4 + \frac{4}{3}R\right] + \theta_\xi\left[Z_4 + \frac{4}{3}R - \frac{Pr}{S^2}Z_5 - \xi Z_5\right] + 4\theta Z_5 = \frac{-G_b}{Pr}\left[Z_3 M + Z_5 S^2\right]\xi S^2 \tag{29}$$

the temperature boundary condition are modified into,

$$\theta\left(-\frac{Pr}{S^2}\right) = 1, \qquad \theta(0) = 0. \tag{30}$$

The solution for Eq. (29) is assumed in the form of $\theta(\xi) = \theta_c(\xi) + \theta_p(\xi)$,
where $\theta_c(\xi)$ and $\theta_p(\xi)$ represent complementary and particular solutions. The complementary solution of Eq. (29) indicates a confluent hypergeometric equation(Kummer's function).

$$\theta_c(\xi) = a_0 \xi^\alpha M\left[\alpha - 4, \alpha + 1, \frac{-\xi}{\lambda_2}\right] \tag{31}$$

here $\lambda_2 = Z_4 + \left(\frac{4}{3}\right) R$, $\lambda_3 = Z_5$, $\alpha = Pr^* \left(\frac{\lambda_3}{\lambda_2}\right)$,
where $Pr^* = \frac{Pr}{S^2}$ is the modified Prandtl number.
The particular solution is obtained in the form of

$$\theta_p(\xi) = A\xi^2 + B\xi^3 + C\xi^4, \tag{32}$$

where,

$$A = -\left(\frac{Gb}{Pr^*}\right) \frac{Z_3 M + Z_5 S^2}{4\lambda_2 - 2Pr^* Z_5},$$

$$B = \frac{-2A}{9\lambda_2 - 3Pr^* Z_5},$$

$$C = \frac{-B}{16\lambda_2 - 4Pr^* Z_5},$$

By applying the boundary conditions, the solution is obtained and expressed in terms of the relevant variable, we get,

$$\theta(\eta) = a_0 \frac{e^{S\eta\alpha} M\left[\alpha - 4, \alpha + 1, -\alpha e^{-S\eta}\right]}{M\left[\alpha - 4, \alpha + 1, -\alpha\right]} + APr^{*2} e^{-2S\eta} - BPr^{*3} e^{-3S\eta} + CPr^{*4} e^{4S\eta}, \tag{33}$$

where, $a_0 = 1 - APr^{*2} + BPr^{*3} - CPr^{*4}$.

4. MATHEMATICAL DEMONSTRATION

The governing equations Eqs. (8)-(9) along with the boundary conditions (10) are solved numerically using MATLAB-bvp4c. The MATLAB function bvp4c is used to numerically solve highly nonlinear boundary-value problems. The following parameters are defined as follows:

$$f = y_1, \quad f' = y_2, \quad f'' = y_3, \quad \theta = y_4, \quad \theta' = y_5. \tag{34}$$

Hence by using Eq. (34), the above system of ordinary differential equations from Eqs. (8)-(9) is determined as follows,

$$y_3' = \frac{Z_2}{Z_1}\left[2y_2^2 - y_1 y_3 - \frac{Z_3}{Z_2} M\left(E - y_1\right)\right] \tag{35}$$

$$y_5' = \frac{Z_5}{Z_4 + \frac{4}{3}R}\left[Pr\left(4y_2 y_4 - y_1 y_5 - \left(\frac{Z_3}{Z_5}\right) Gb\left(M(y_2 - E)^2\right) + Gby_3^2\right)\right] \tag{36}$$

The boundary conditions now to be transformed into,

$$y_1(0) = 0, \quad y_2(0) = 1, \quad y_3(0) = A_3, \quad y_4(0) = 1, \quad y_5(0) = A_5 \tag{37}$$

where A_3 and A_5 are considered as intial guess values for the transformations.

5. VALIDATION OF TABULAR RESULTS

From Table 4 and Table 5, it is observed that the present results show good agreement with existing results of (Kameswaran et al. [17]). Table 6 shows that skin friction values for with aggregation and without aggregation of nanoparticles.

6. DISCUSSION OF GRAPHICAL RESULTS

In this problem, we have concentrated on the effects of various pertinent physical parameters on velocity profile ($f(\eta)$), temperature profile ($\theta(\eta)$), skin friction (C_f), and heat transfer rate (Nu_L) with and without Aggregation effect from Figs. (3)-(15). The impact of the magnetic parameter on the velocity distribution is found in Fig. 3 for Cu/H_2O nanofluid. The range of magnetic field is chosen between the values of $0 \leq M \leq 3$. The impact of the magnetic parameters is intensified in the EMHD flow, resulting in a decrease in velocity for both cases of presence and absence of aggregation effects of nanoparticles. This occurs due to the resistive force known as the Lorentz force, where the magnetic field lines are inclined with respect to the electromagnetic force that disturbs the nanofluid flow over an exponentially stretching sheet. The results concluded that in the presence of the aggregation effect, the velocity reduces for increasing the range of magnetic parameters. This happens because aggregated nanoparticles stick together to form clustered structures through hydrodynamic force and appear larger in size compared to dispersed nanoparticles, and this will lead to reducing the speed of flow, and larger aggregated nanoparticles also have more drag, and this force slows down the fluid movement, which

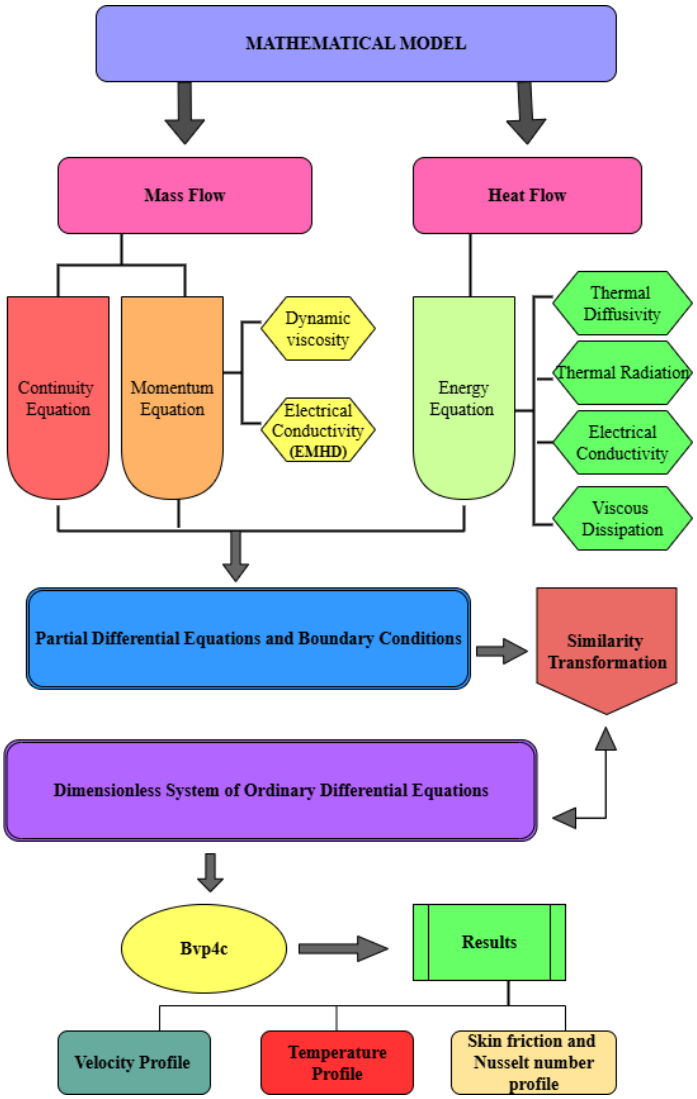

Figure 2. Demonstration of Mathematical model

Table 4. Values of $-f_{\eta\eta}(0)$ are confirmed with Kameswaran et al. [17] for distinct values of M and for fixed values of $E = Pr = R = Gb = 0$

M	Kameswaran et al. [17]	Current results
0	1.28181	1.28181
1	1.62918	1.62918
2	1.91262	1.91262
3	2.15874	2.15874
4	2.37937	2.37937
5	2.58113	2.58113

leads to decreasing the velocity. As a result, aggregated nanoparticles slow down the fluid behavior in the boundary layer region.

Fig. 4 reveals the influence of magnetic parameters on the temperature profile. The temperature rises for both cases while increasing the range of magnetic field parameters. This is because of when magnetic fields are applied to nanoparticles, which results in greater heat buildup especially near heated surfaces in stretching sheets. Generally aggregated nanoparticles can have stronger magnetic interactions; therefore, they can trap more heat. In this case, aggregated nanoparticles can form thermal bridges between the particles, which facilitate better heat transfer compared to non-aggregated nanoparticles.

Table 5. Values of $-\theta_\eta(0)$ are confirmed with Kameswaran et al. [17] for fixed values $M = 1, E = 0, Pr = 7, Gb = 0.2$ of varying values of R

R	Kameswaran et al. [17]	Current results
0	4.55621	4.55621
0.5	3.48315	3.48315
1	2.90580	2.90580
2	2.26050	2.26050
3	1.88981	1.88981

Table 6. Skin friction values $-f_{\eta\eta}(0)$ for with and without aggregation for different parameters

M	E	R	ϕ	Gb	Without Aggregation	With Aggregation
0					1.31521	1.40339
1					1.65638	1.73038
2					1.9366	2.00296
3					2.18066	2.24216
	10^{-3}				1.65638	1.73038
	10^{-4}				1.65704	1.73038
	10^{-5}				1.65711	1.7311
		1			1.65638	1.73038
		1.5			1.65638	1.73038
		2			1.65638	1.73038
		2.5			1.65638	1.73038
			0.01		1.65638	1.73038
			0.02		1.68197	1.79393
			0.03		1.70538	1.82495
			0.05		1.72672	1.82703
				0.1	1.65638	1.73038
				0.5	1.65638	1.73038
				1	1.65638	1.73038
				1.5	1.65638	1.73038

The results of the electric parameter on the velocity distribution are clearly demonstrated in Fig. 5. The Electric parameters are selected within the interval of 10^{-3} to 10^{-5}. From the graph, it is noticed that the flow decelerates for both aggregated and non-aggregated nanoparticles. As we applied the electric field to fluid, the nanoparticles have some interaction between the electric and magnetic fields that can create complex forces between them, and these complex forces generally affect the speed of the fluid flow. If the range of electric parameters increases, the aggregated nanoparticles have different electrophoretic mobility compared to the individual nanoparticles in electric field distribution within the fluid. Hence, aggregated nanoparticles have greater resistance to flow, which can slow the velocity of the fluid.

The outcomes of the electric parameter on the temperature profile are illustrated in Fig. 6. It is observed that the temperature profile increases for both cases of presence and absence of aggregation. When an electric field is applied to the nanofluid, it generates heat, and it is observed that the temperature increases more. From the graph, we conclude that heat transfer is enhanced by the aggregation effect. When aggregated nanoparticles form interparticle contacts and create a region of higher energy density and significant thermal resistance. The region of high thermal resistance can cause the temperature to increase more rapidly with aggregated nanoparticles compared with dispersed nanoparticles.

The temperature patterns for varying the values of the radiation parameter are examined through Fig. 7 with the presence and absence of aggregated nanoparticles. The range of radiation parameters is taken between $1 \leq R \leq 2.5$. The radiation parameter characterizes the relative contribution of the convective heat transfer coefficient to the thermal radiation transfer coefficient. As the radiation value increases, the temperature profile increases more in the presence of aggregated nanoparticles. This means that nanoparticles with aggregation form a structure with cavities or highly irregular geometries that may concentrate radiation on certain things because of localized resonant effects. This results in localized heating to strengthen the temperature gradients and leads to thickening of the thermal boundary layer. When the nanoparticles

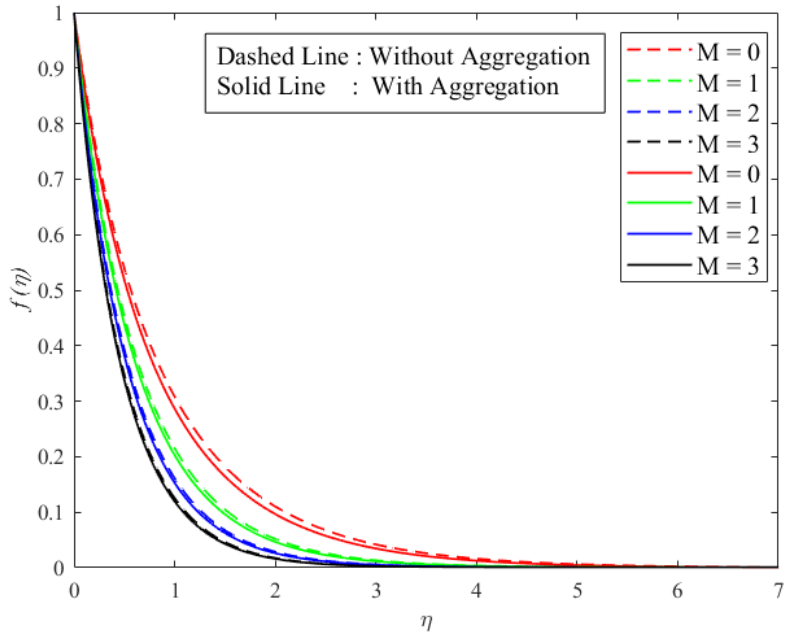

Figure 3. Variation of magnetic parameter on velocity profile for fixing other parameters are $E = 10^{-3}, R = 1, Pr = 5.83, \phi = 0.01, Gb = 0.2$.

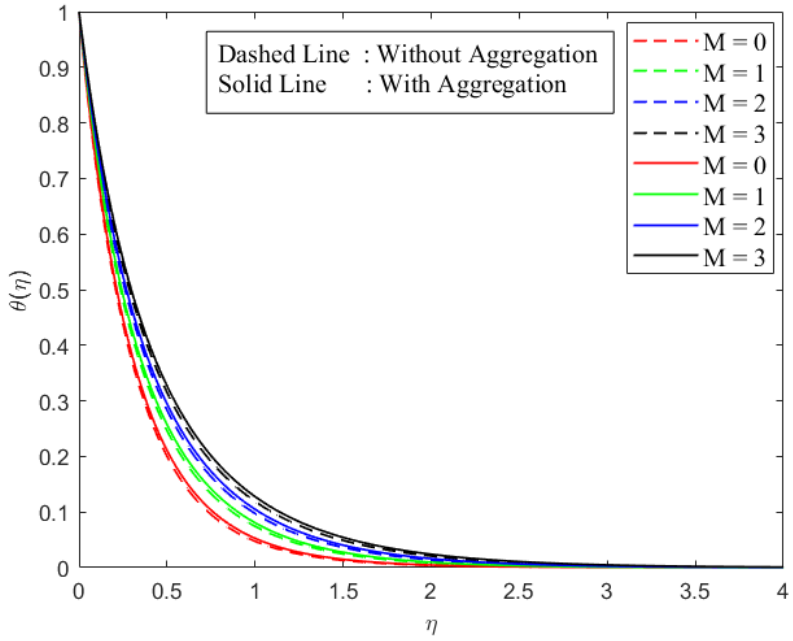

Figure 4. Variation of magnetic parameter on temperature profile for $E = 10^{-3}, R = 1, Pr = 5.83, \phi = 0.01, Gb = 0.2$.

aggregate into clusters, the multiple scattering plays a significant influence in absorbing and scattering radiation due to the small gaps between the aggregated nanoparticles, and both absorption and scattering are enhanced greatly in the near infrared.

Fig. 8 expresses the relationship between the volume fraction of the solids of velocity profile. The range volume fraction is considered between 1% to 4%. The graph represents that aggregated nanoparticles have a greater velocity profile than that of dispersed nanoparticles. The boundary layer can be affected differently by aggregated nanoparticles than by dispersed nanoparticles. In certain instances, aggregation can cause a more prominent velocity gradient close to the wall, as they can act like larger particles, causing more friction and resistance to flow near the boundary. The Krieger-Dougherty model can be utilized to describe the viscosity of the suspension, resulting in an increase in effective viscosity with volume

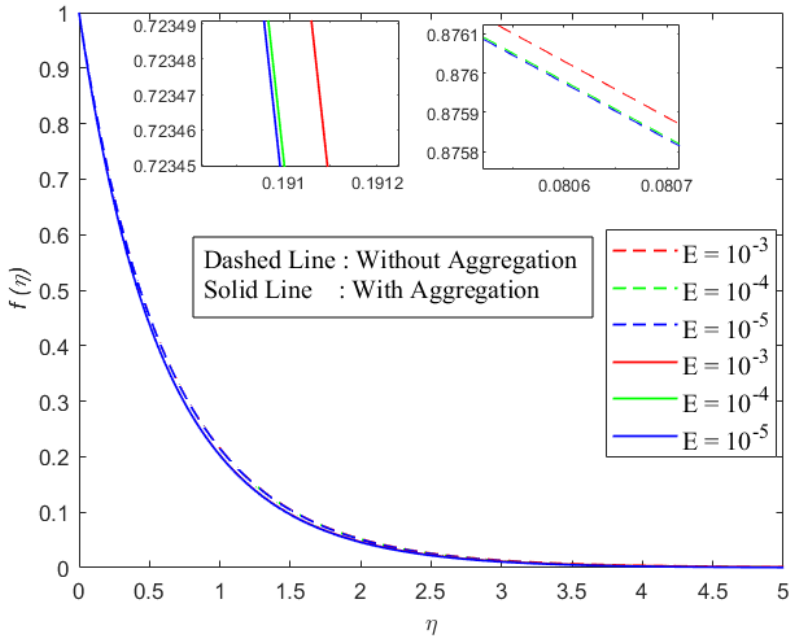

Figure 5. Variation on electric parameter on velocity profile for $M = 1, R = 1, Pr = 5.83, \phi = 0.01, Gb = 0.2$.

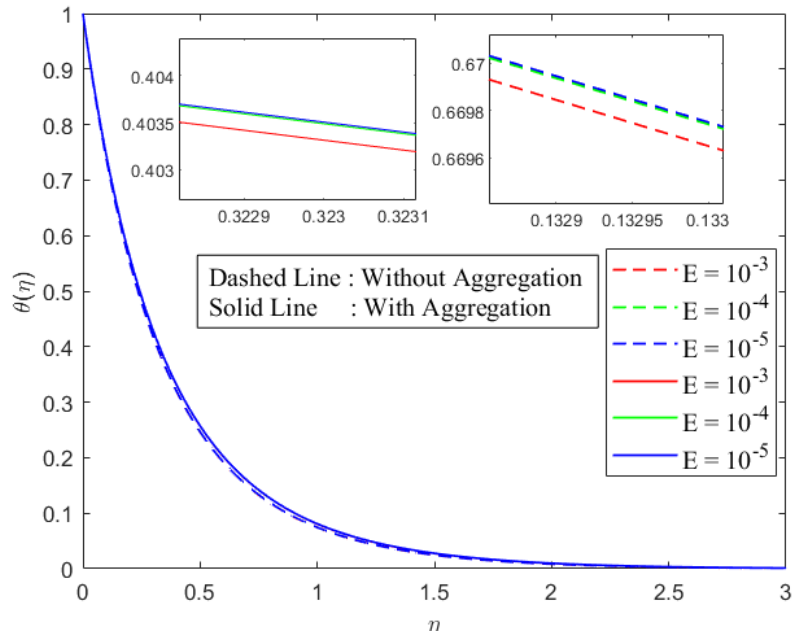

Figure 6. Variation on electric parameter on temperature profile for $M = 1, R = 1, Pr = 5.83, \phi = 0.01, Gb = 0.2$.

fraction. As a result, the velocity profile has a more decreasing sequence in the presence of aggregated nanoparticles.

The effects of the volume fraction on the temperature profile are exemplified in Fig. 9 in both cases of with and without aggregation. The efficiency of heat transfer is directly correlated with the volume fraction of nanoparticles. It is recognized that higher volume fractions of nanoparticles facilitate more heat transfer efficiently in the presence of aggregated nanoparticles than dispersed nanoparticles. This is due to aggregated nanoparticles leading to a higher surface area for heat exchange between the fluid and the nanoparticles; the total surface area of these aggregated particle could be larger than the individual nanoparticles. By increasing its surface area, the aggregated nanoparticles can absorb more heat from the surrounding fluid and enhance their thermal absorption capacity.

Fig. 10 illustrates the influence of accelerated rates of the Gebhart number on the temperature distribution. The range of viscous dissipation considered here is 0.1 to 1.5. The viscous dissipation parameter relates to the process by which the

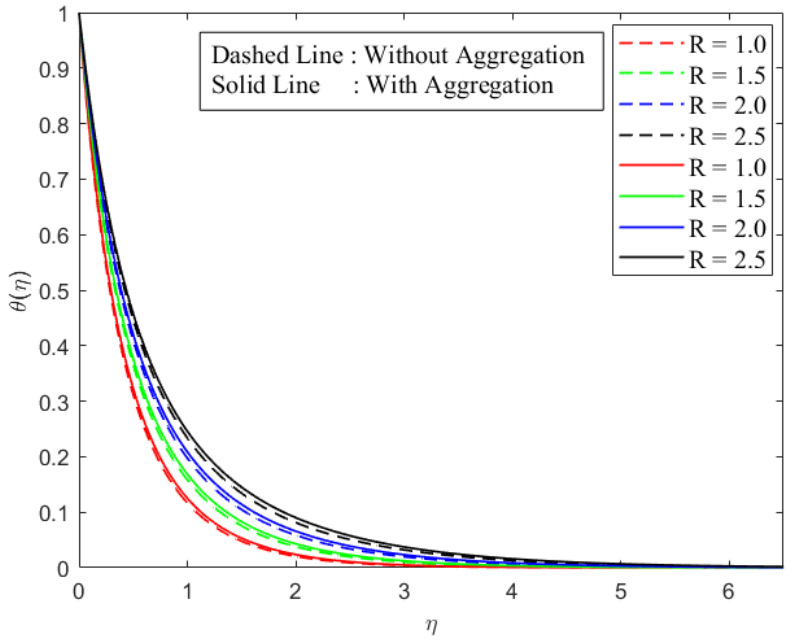

Figure 7. Variation of radiation parameter on temperature profile for $M = 1, E = 10^{-3}, Pr = 5.83, \phi = 0.01, Gb = 0.2$.

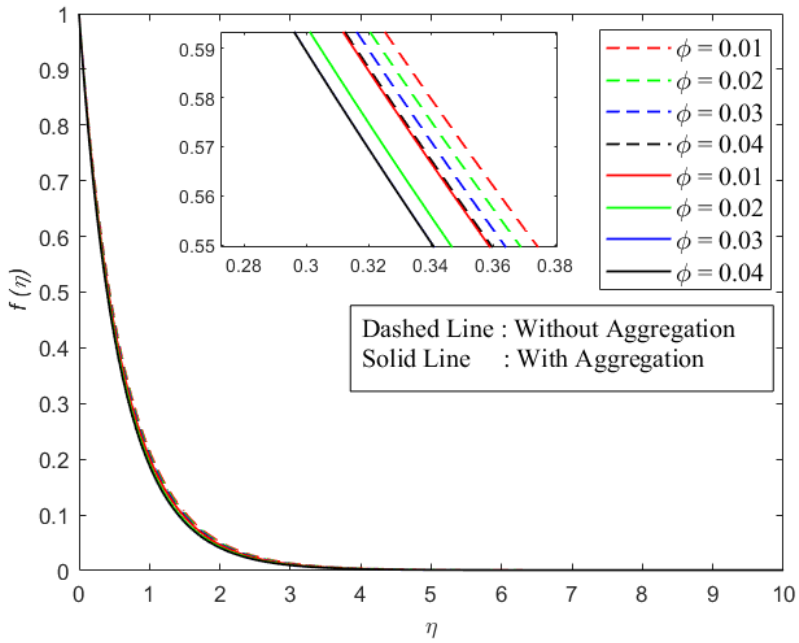

Figure 8. Variation of volume fraction on velocity profile for $M = 1, E = 10^{-3}, R = 1.5, Pr = 5.82, Gb = 0.2$.

fluid friction (mechanical energy) is transformed into heat (thermal energy) due to the internal friction (fluid viscosity) between the fluid layers. From this graph, it is clearly seen that the temperature increase strengthens the values for viscous dissipation parameter with aggregated nanoparticles. The aggregation of nanoparticles increases the effective viscosity of the nanofluid, thereby intensifying internal friction, leading to localized internal heat generation near boundaries. As a result, the combined effect of nanoparticles aggregation and viscous heating can be considered in the design and optimization of high-performance thermal systems.

The behavior of the skin friction coefficient with varying volume fraction and magnetic parameters is illustrated in Fig. 11 for both aggregated and non-aggregated nanoparticles. It is observed that the skin friction coefficient decreases monotonically with an increase in the magnetic parameter in both cases. This happens because the clustered nanoparticles make the fluid more viscous, which enhances the effective viscosity and momentum diffusion within the boundary layer. The

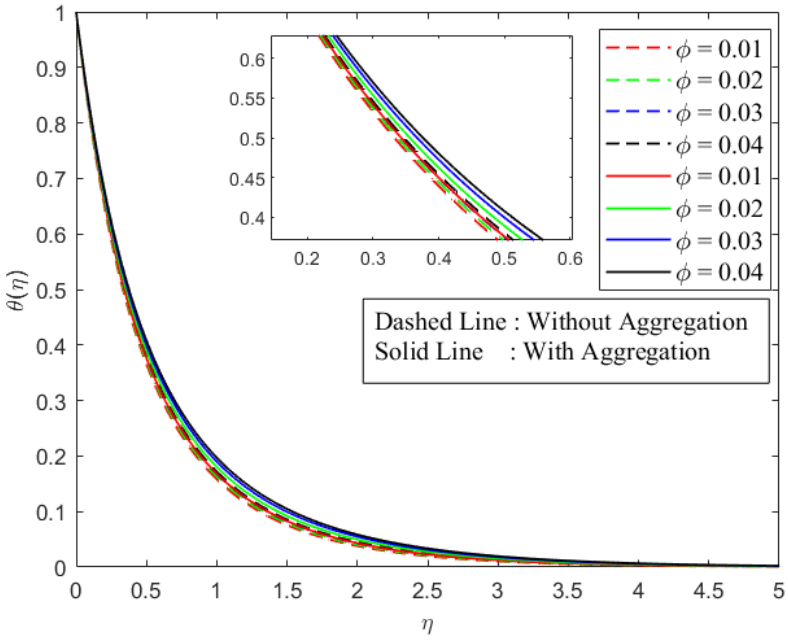

Figure 9. Variation of volume fraction parameter on temperature profile for $M = 1,\ E = 10^{-3},\ R = 1.5,\ Pr = 5.83,$ $Gb = 0.2$.

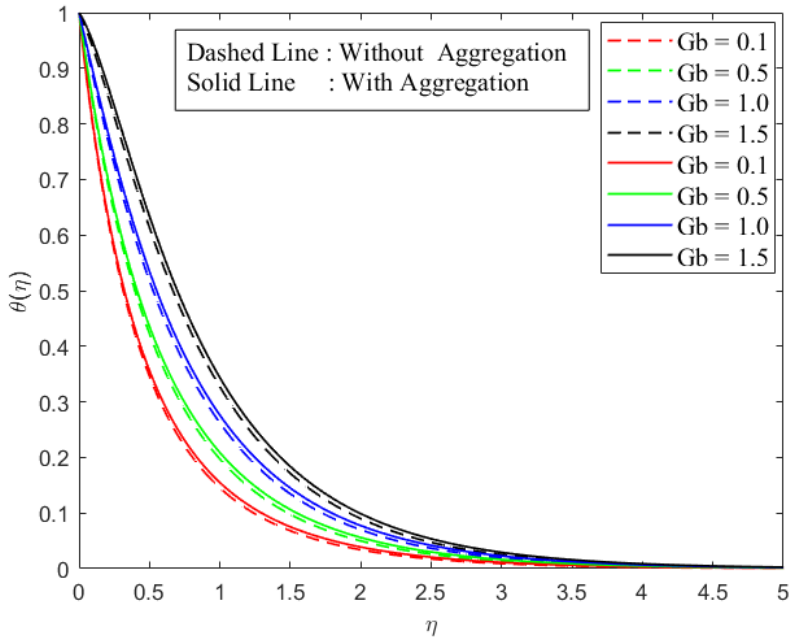

Figure 10. Variation of viscous dissipation parameter on temperature profile for $M = 1, E = 10^{-3}, R = 1, Pr = 5.83,$ $\phi = 0.1$

aggregated structures introduce additional resistance to the magnetic damping mechanism, thereby diminishing the overall influence of the Lorentz force on the flow. Consequently, the skin friction coefficient decreases with increasing magnetic parameters; the rate of reduction is lower in the presence of aggregation.

Fig. 12 illustrates the variation of the skin friction coefficient concerning the electric parameter E for both aggregated and non-aggregated nanoparticles. The analysis is conducted for three different values of the electric parameters that rise from 10^{-4} to 10^{-2}. It is evident from the graph that the skin friction coefficient decreases slightly with increasing electric parameters for both aggregation and non-aggregation cases. Notably, the presence of nanoparticles in aggregation leads

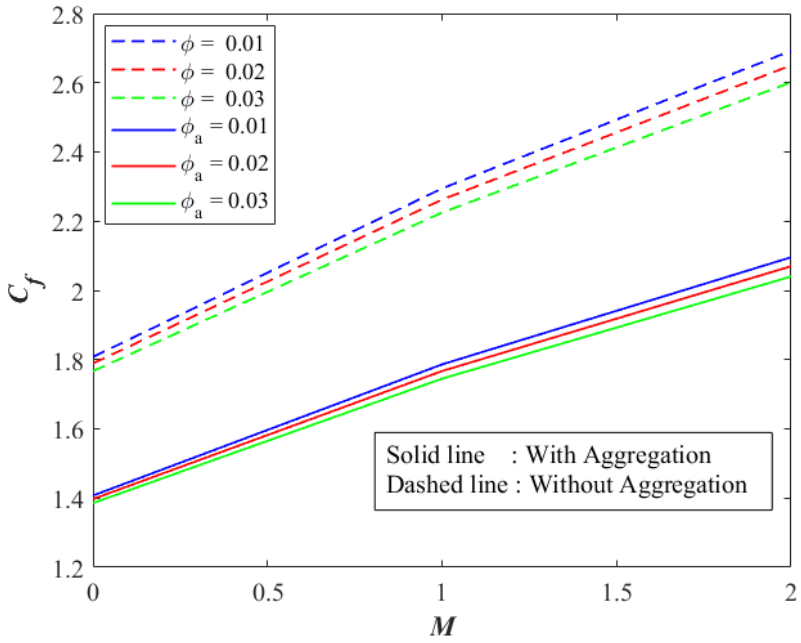

Figure 11. Variation of skin friction coefficient for increasing values of magnetic parameter for $E = 10^{-3}, R = 1, Pr = 5.83, Gb = 0.5$.

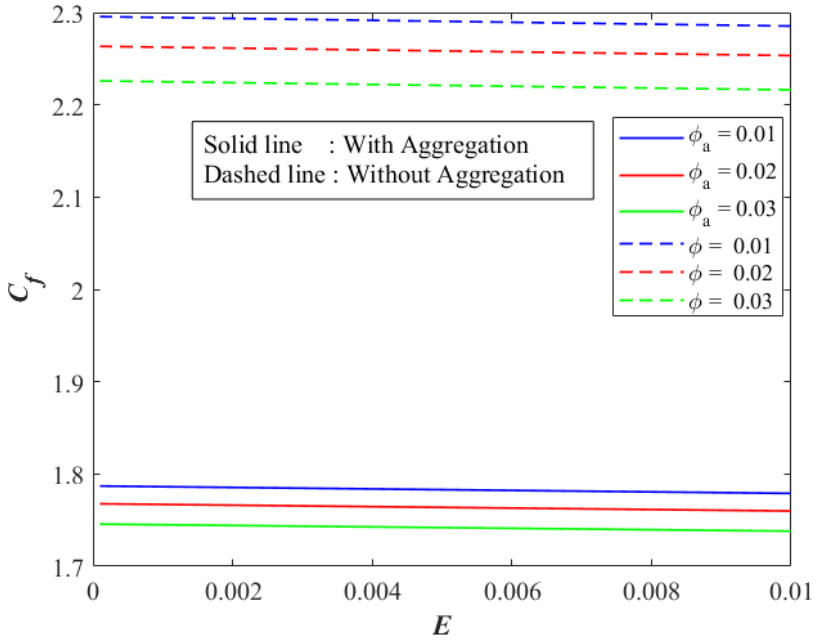

Figure 12. Variation of skin friction coefficient for increasing values of electric parameters for $M = 1, R = 1, Pr = 5.83, Gb = 0.5$.

to a consistently higher skin friction coefficient compared to the non-aggregated case. This indicates that aggregation increases the effective viscosity or momentum transfer near the wall, thereby increasing the resistance to flow.

The variation in the skin friction coefficient as a function of the radiation parameter R with volume fraction is evaluated for aggregated and non-aggregated nanoparticles shown in Fig. 13. It is observed that the skin friction coefficient remains almost constant across the entire range of the radiation parameters for both aggregated and non-aggregated. This behavior suggests that the radiation parameter has a negligible influence on the surface shear stress under the given flow conditions. This behavior indicates that nanoparticle aggregation enhances wall shear stress. Physically, this implies that the radiation-related energy transport does not significantly alter the momentum boundary layer thickness.

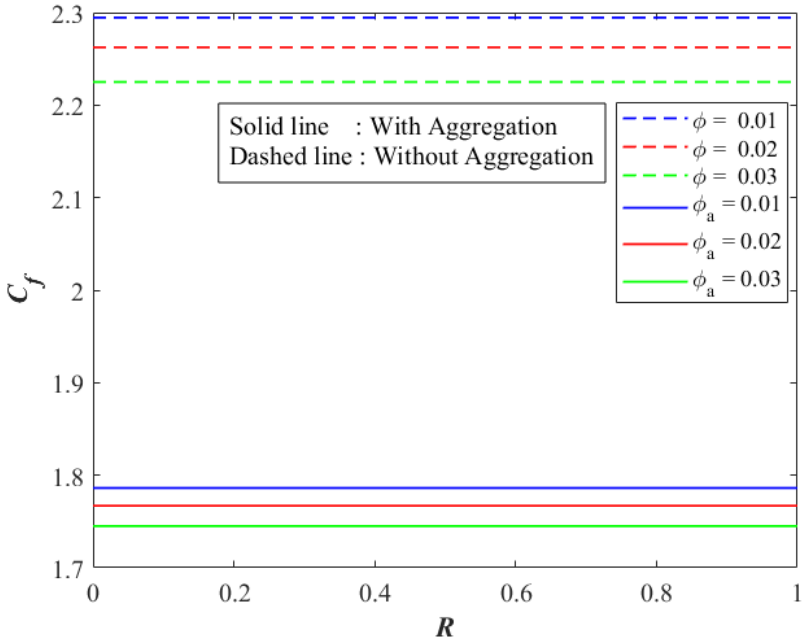

Figure 13. Variation of skin friction coefficient for increasing values of radiation parameter for $M = 1, E = 10^{-3}, Pr = 5.83, Gb = 0.5$.

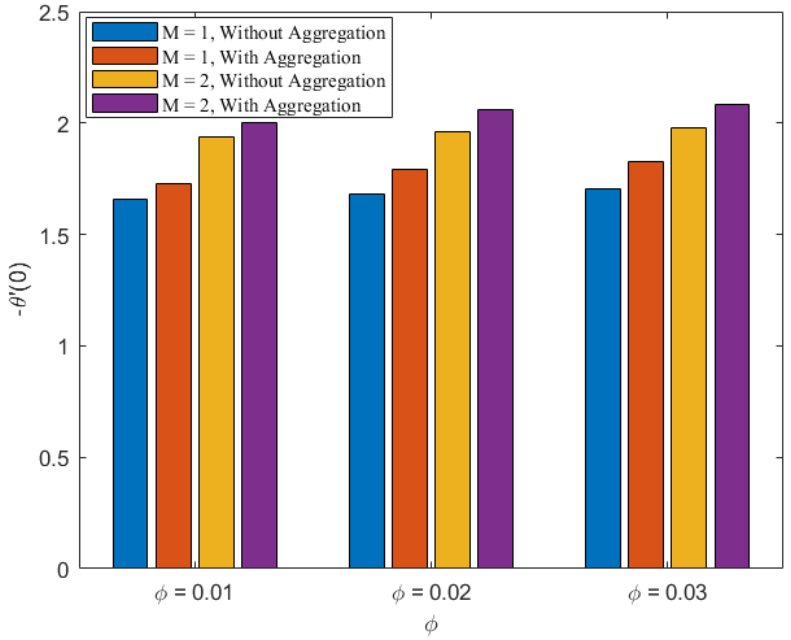

Figure 14. Behavior of heat transfer coefficient with increase in nanoparticle volume fraction for $E = 10^{-3}, R = 1.5, Pr = 5.83$ and $Gb = 1$.

The variation of the Nusselt number with respect to the magnetic parameter M for nanoparticle models with and without aggregation is shown in Fig. 14. An increase in the magnetic parameter results in a higher Nusselt number in both cases. In both magnetic field scenarios, the heat transfer coefficient with aggregation is consistently higher than the corresponding non-aggregated case. This can be attributed to the formation of nanoparticle clusters that facilitate superior thermal pathways and minimize interfacial resistance. The results emphasize that nanoparticle aggregation, along with higher volume fractions and stronger magnetic parameters, significantly augments the heat transfer performance of the nanofluid.

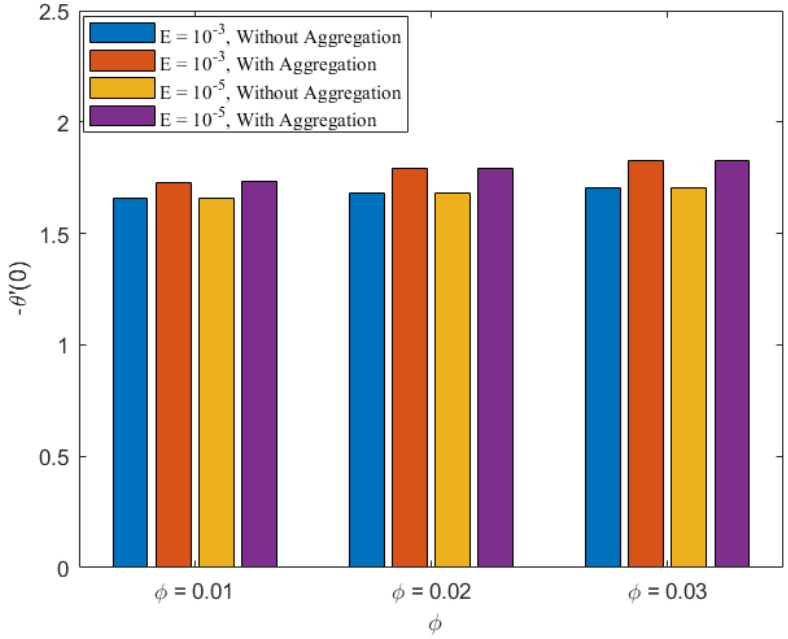

Figure 15. Behavior of heat transfer coefficient with increase in nanoparticle volume fraction for $M = 1, R = 1.5, Pr = 5.83$ and $Gb = 1$.

Fig. 15 demonstrates the Nusselt number increases with an increase in the values of the nanoparticle volume fraction for both aggregated and non-aggregated nanopartiles. The analysis reveals that as the electric parameter increases, the Nusselt number exhibits higher values in the presence of aggregated nanoparticles. Because the aggregated nanoparticle exhibits superior heat transfer performance compared to the non-aggregated case. The influence of the electric parameter is relatively mild, but at lower values of the electric parameter, the improvement due to aggregation remains consistent, indicating that aggregation effects dominate over changes in the electric parameter. Overall, the results confirm that nanoparticle aggregation amplifies the thermal transport, particularly at larger nanoparticle values.

7. CONCLUSION

The key contributions of the present study are summarized as follows:

- With an increasing magnetic parameter, the flow velocity of aggregated nanoparticles decreases by approximately 59% due to higher drag from larger clusters.
- Temperature profile increases in the presence of electric field for both aggregated and non-aggregated nanoparticles.
- The temperature rise is 15% higher for aggregated nanoparticles, indicating enhanced heat transfer due to aggregation effects.
- Increasing the radiation parameter raises the temperature profile with aggregated nanoparticles showing higher heat transfer due to enhanced radiation trapping and scattering within the aggregates.
- Electromagnetic effects improve heat transfer in the nanofluid, with aggregated nanoparticles exhibiting higher Nusselt numbers due to cluster formation that enhances thermal pathways.
- The nanoparticles aggregation model will be noticeable and more predominant than the homogeneous model due to its significant influence on the effective viscosity of the fluid.

8. PRACTICAL IMPLICATIONS

Aggregated nanoparticles in Cu/H_2O nanofluids significantly enhance heat transfer, with Nusselt numbers increasing under magnetic and electric fields, and higher radiation further improving thermal performance. Due to the nanoparticles aggregation, researchers and engineers can enhance heat transfer in nanofluid systems. Nanoparticles aggregation combined with enhanced thermal conductivity can significantly improve the efficiency of industrial thermal management systems, heat exchangers, and cooling devices.

9. RECOMMENDATIONS FOR FUTURE STUDIES

This study can be extended to future research based on nanofluid cooling systems for electric vehicles (EVs) by incorporating suction and injection at the boundaries to actively control flow and enhance heat transfer. The focus can be on how nanoparticle aggregation, shape, and size affect thermal performance under these conditions. By optimizing nanoparticle concentration, flow rates, and suction/injection strategies, the study can provide practical guidelines for designing efficient, high-performance EV thermal management systems that improve cooling efficiency while minimizing energy consumption.

ORCID

A. Lokeshwari, https://orcid.org/0009-0008-7591-9536; **Peri K. Kameswaran**, https://orcid.org/0000-0002-6357-7048

REFERENCES

[1] D. Lee, J.W. Kim, and B.G. Kim, "A new parameter to control heat transport in nanofluids: surface charge state of the particle in suspension," The Journal of Physical Chemistry B, **110**(9), 4323-4328 (2006). https://doi.org/10.1021/jp057225m.

[2] Gaganpreet, and S. Srivastava, "Effect of aggregation on thermal conductivity and viscosity of nanofluids," Applied Nanoscience, **2**(3), 325-331 (2012). https://doi.org/10.1007/s13204-012-0082-z.

[3] J. Liao, A. Zhang, S. Qing, X. Zhang, and Z. Luo, Z, "Investigation on the aggregation structure of nanoparticle on the thermal conductivity of nanofluids by molecular dynamic simulations," Powder Technology, **395**, 584-591 (2022). https://doi.org/10.1016/j.powtec.2021.10.007

[4] Y. Feng, B. Yu, P. Xu, and M. Zou, "The effective thermal conductivity of nanofluids based on the nanolayer and the aggregation of nanoparticles," Journal of Physics D: Applied Physics, **40**(10), 3164 (2007). https://doi.org/10.1088/0022-3727/40/10/020

[5] B. Mahanthesh, "Flow and heat transport of nanomaterial with quadratic radiative heat flux and aggregation kinematics of nanoparticles," International Communications in Heat and Mass Transfer, **127**, 105521 (2021). https://doi.org/10.1016/j.icheatmasstransfer.2021.105521

[6] J. Chen, C.Y. Zhao, and B.X. Wang, "Effect of nanoparticle aggregation on the thermal radiation properties of nanofluids: an experimental and theoretical study," International Journal of heat and mass transfer, **154**, 119690 (2020). https://doi.org/10.1016/j.ijheatmasstransfer.2020.119690

[7] M. Motevasel, A.R.S. Nazar, and M. Jamialahmadi, "The effect of nanoparticles aggregation on the thermal conductivity of nanofluids at very low concentrations: experimental and theoretical evaluations," Heat and Mass Transfer, **54**(1), 125-133 (2018). https://doi.org/10.1007/s00231-017-2116-2

[8] N. Muhammad, N. Ahmed, M. Rani, and B.B. Mohsin, "Application of deep learning to study aggregative and non-aggregative nanofluid flow within the nozzle of a liquid rocket engine," International Communications in Heat and Mass Transfer, **155**, 107449 (2024). https://doi.org/10.1016/j.icheatmasstransfer.2024.107449

[9] C. Pang, J.Y. Jung, and Y.T. Kang, "Aggregation based model for heat conduction mechanism in nanofluids," International Journal of Heat and Mass Transfer, **72**, 392-399 (2014). https://doi.org/10.1016/j.ijheatmasstransfer.2013.12.055

[10] R. Ellahi, M. Hassan, and A. Zeeshan, "Aggregation effects on water base Al2O3—nanofluid over permeable wedge in mixed convection," Asia-Pacific Journal of Chemical Engineering, **11**(2), 179-186 (2016). https://doi.org/10.1002/apj.1954

[11] P. Sathya, and P. Naveen, "Crucial role of nanoparticle aggregation effect on non-Darcian flow of micropolar nanofluid over Riga plate with Navier's slip: a regression analysis," The European Physical Journal Plus, **139**(5), 458, (2024). https://doi.org/10.1140/epjp/s13360-024-05230-y

[12] F.Z. Duraihem, "Electro-magnetohydrodynamic (EMHD) Darcy–Forchheimer flow of Sutterby nanofluid with variable thermal conductivity over a stretching sheet: Finite difference approach," Modern Physics Letters B, **39**(17), 2550019 (2025). https://doi.org/10.1142/S0217984925500198.

[13] K. Ramesh, K.K. Asogwa, T. Oreyeni, M.G. Reddy, and A. Verma, A, "EMHD radiative titanium oxide-iron oxide/ethylene glycol hybrid nanofluid flow over an exponentially stretching sheet," Biomass Conversion and Biorefinery, **14**(16), 18887-18896 (2024). https://doi.org/10.1007/s13399-023-04033-y

[14] V. Loganayagi, and P.K. Kameswaran, "Impacts of Heat Source/Sink and Electromagnetic Field on Heat Transfer in Ferrofluid Flow," Advances in Mathematics: Scientific Journal, **10**(4), 2095-2104 (2021). https://doi.org/10.37418/amsj.10.4.24

[15] J. Madhu, J.K. Madhukesh, K.V. Prasad, and A. Kulshreshta, "Exact solutions for nanoparticle aggregation and porous medium effects over a stretching surface," Multiscale and Multidisciplinary Modeling, Experiments and Design, **8**(2), 134 (2025). https://doi.org/10.1007/s41939-024-00724-9

[16] K. Swain, S.M. Ibrahim, G. Dharmaiah, G, and S. Noeiaghdam, "Numerical study of nanoparticles aggregation on radiative 3D flow of maxwell fluid over a permeable stretching surface with thermal radiation and heat source/sink," Results in Engineering, **19**, 101208 (2023). https://doi.org/10.1016/j.rineng.2023.101208

[17] P.K. Kameswaran, M. Narayana, P. Sibanda, and G. Makanda, "On radiation effects on hydromagnetic Newtonian liquid flow due to an exponential stretching sheet," Boundary Value Problems, **2012**(1), (2012). https://doi.org/10.1186/1687-2770-2012-105

[18] F. Wang, S.P. Rani, K. Sarada, R.P. Gowda, H.Y. Zahran, and E.E. Mahmoud, "The effects of nanoparticle aggregation and radiation on the flow of nanofluid between the gap of a disk and cone," Case Studies in Thermal Engineering, **33**, 101930 (2022). https://doi.org/10.1016/j.csite.2022.101930

[19] G.R. Rajput, B.P. Jadhav, and S.N. Salunkhe, "Magnetohydrodynamics boundary layer flow and heat transfer in porous medium past an exponentially stretching sheet under the influence of radiation," Heat Transfer, **49**(5), 2906-2920 (2020). https://doi.org/10.1002/htj.21752

[20] A. Ali, H.S. Khan, S. Saleem, S, and M. Hussan, M, "EMHD nanofluid flow with radiation and variable heat flux effects along a slandering stretching sheet," Nanomaterials, **12**(21), 3872 (2022). https://doi.org/10.3390/nano12213872

[21] K. Rafique, Z. Mahmood, A.M. Alqahtani, A.M. Elsiddieg, U. Khan, W. Deebani, and M. Shutaywi, "Impacts of thermal radiation with nanoparticle aggregation and variable viscosity on unsteady bidirectional rotating stagnation point flow of nanofluid," Materials Today Communications, 36, 106735 (2023). https://doi.org/10.1016/j.mtcomm.2023.106735

[22] F. Mabood, W.A. Khan, andA.M. Ismail, A, "MHD flow over exponential radiating stretching sheet using homotopy analysis method," Journal of King Saud University-Engineering Sciences, **29**(1), 68-74 (2017). https://doi.org/10.1016/j.jksues.2014.06.001

[23] B.M. Makhdoum, Z. Mahmood, B.M. Fadhl, M.S. Aldhabani, U. Khan, and S.M. Eldin, "Significance of entropy generation and nanoparticle aggregation on stagnation point flow of nanofluid over stretching sheet with inclined Lorentz force," Arabian Journal of Chemistry, **16**(6), 104787 (2023). https://doi.org/10.1016/j.arabjc.2023.104787

[24] J. Mackolil, and B. Mahanthesh, B, "Sensitivity analysis of Marangoni convection in TiO2–EG nanoliquid with nanoparticle aggregation and temperature-dependent surface tension," Journal of Thermal Analysis & Calorimetry, **143**(3), (2021). https://doi.org/10.1007/s10973-020-09642-7

[25] S.K. Rawat, M. Yaseen, A. Shafiq, M. Kumar, and Q.M. Al-Mdallal, "Nanoparticle aggregation effect on nonlinear convective nanofluid flow over a stretched surface with linear and exponential heat source/sink," International Journal of Thermofluids, **19**, 100355 (2023). https://doi.org/10.1016/j.ijft.2023.100355

[26] P. Rana, B. Mahanthesh, J. Mackolil, and W. Al-Kouz, "Nanofluid flow past a vertical plate with nanoparticle aggregation kinematics, thermal slip and significant buoyancy force effects using modified Buongiorno model," Waves in Random and Complex Media, **34**(4), 3425-3449 (2024). https://doi.org/10.1080/17455030.2021.1977416

ЧИСЛОВЕ ДОСЛІДЖЕННЯ АНАЛІЗУ ТЕПЛОПЕРЕНОСУ З ВИКОРИСТАННЯМ ЕЛЕКТРОМАГНІТОГІДРОДИНАМІКИ З АГРЕГОВАНИМИ НАНОЧАСТИНКАМИ

А. Локешварі, **Пері К. Камесваран**

Кафедра математики, Школа передових наук, Технологічний інститут Веллор, Веллор 632014, Індія

Оптимізація теплопередачі залишається суттєвою сучасною проблемою в сучасних технологічних застосуваннях. Нанорідини демонструють сильну потенційну теплопровідність для покращення теплопередачі та підвищення ефективності енергетичної системи. Порівняно з диспергованими наночастинками, агреговані наночастинки є важливими для оцінки теплової поведінки наночастинок у нанорівні. Незважаючи на цей ефект агрегації, фрактальна розмірність агрегованих наночастинок матиме трансформаційний вплив на теплопередачу. Метою цього дослідження є дослідження впливу електромагнітогідродинамічних ефектів на теплопередачу в нанорідині, що містить агреговані наночастинки над експоненціально розтягуваним шаром. Визначальні рівняння для імпульсу та енергії перетворюються на систему нелінійних звичайних диференціальних рівнянь із заданою межею умови. Представлено аналітичне рішення для конкретного випадку, коли параметр електричного поля відсутній. Чисельні рішення отримані для різних діапазонів фізичних параметрів, а обчислені результати перевірені на основі існуючої літератури. Результати показують, що агрегація наночастинок призводить до потовщення теплового граничного шару та покращення теплопередачі. На додаток до цього синергетичного ефекту агрегації та електричного поля, це призводить до зменшення профілів швидкості. При об'ємній частці 5% агреговані наночастинки забезпечують покращення теплопередачі приблизно на 34% порівняно з диспергованими наночастинками. Температурні профілі демонструють тенденцію до зростання зі збільшенням об'ємної частки. У присутності агрегованих наночастинок як коефіцієнт тертя поверхні, так і число Нуссельта збільшуються зі зростанням напруженості магнітного поля.

Ключові слова: *агреговані наночастинки; електричне поле; магнітне поле; випромінювання; в'язка дисипація; експоненціальне розтягування листа*

East European Journal of Physics. 1. 447-459 (2026)
DOI:10.26565/2312-4334-2026-1-52 ISSN 2312-4334

FINITE DIFFERENCE ANALYSIS OF PRANDTL NUMBER AND PARTICLE VOLUME FRACTION EFFECTS ON SKIN FRICTION AND HEAT TRANSFER IN BUOYANCY DRIVEN TWO-PHASE FLOW WITH SUSPENDED PARTICULATE MATTER (SPM)

Sasanka Sekhar Bishoyi[1], Sakambari Mishra[2], Aditya Kumar Pati[3]*, Prasanta Kumar Rath[3]
[1]*NIST University, Berhampur, Ganjam, Odisha, India*
[2]*College of Basic Science and Humanities, Odisha University of Agriculture and Technology, Bhubaneswar, Odisha, India*
[3]*Centurion University of Technology and Management, Paralakhemundi, Odisha, India*
**Corresponding author e-mail: apati@cutm.ac.in*
Received December 2, 2025; revised January 15, 2026; accepted January 20, 2026

A numerical investigation has been conducted on incompressible, laminar two-phase buoyancy driven flow containing suspended particles around a vertical plate. Despite the relevance of such systems, prior studies have largely overlooked natural convection two-phase flows with particulate matter, particularly concerning the roles of parameters like the Prandtl number and volume fraction. Addressing this research gap is crucial, as these parameters significantly influence flow behavior and heat transfer, which are vital in environmental, industrial, and thermal applications. This study focuses on exploring the effects of volume fraction and Prandtl number on two-phase flow characteristics using an implicit finite difference method applied on a non-uniform grid. The analysis evaluates boundary layer behavior, heat transfer rates, and skin friction coefficients. Streamline patterns are illustrated for different Prandtl number values, while contour topologies are presented to demonstrate the combined influence of the Prandtl number and volume fraction on skin friction and the heat transfer rate. Results show that increasing the volume fraction reduces both the Nusselt number and the skin friction coefficient, while a higher Prandtl number enhances both. The enhanced thermal response observed with higher Prandtl numbers is particularly beneficial in manufacturing processes involving flat wall-like structures that are susceptible to thermal stress. These findings hold practical significance for the design and optimization of heat exchangers, lubrication systems, and thermal management solutions in electronic devices.

Keywords: *Heat Transfer; Buoyancy driven flow; Prandtl Number; Particle Volume Fraction; Suspended Particulate Matter; Implicit Finite Difference Method*

PACS: 44.05.+e, 44.20.+b, 44.25.+f, 47.10.ad, 47.11.Bc, 47.15.Cb

1. INTRODUCTION

Natural convection is an essential heat transfer process occurring in fluids, primarily driven by buoyancy forces that arise due to differences in temperature. This phenomenon significantly influences a broad spectrum of uses, from environmental processes such as ocean currents and atmospheric circulation to various industrial systems like cooling mechanisms in power plants and electronic devices. The ability of natural convection to efficiently transfer heat without requiring external mechanical forces makes it a key factor in maintaining thermal equilibrium and enhancing the performance of both natural and engineered systems. Many natural convection processes take place in environments characterized by temperature stratification. For example, a room warmed by electric wires installed in the ceiling can develop thermal stratification. Similarly, in the case of a fire in a room with an open door or window, fresh air flows in near the floor, resulting in a layered thermal effect. Accurately predicting heat transfer in natural convective flows is crucial for various engineering applications, including building climate control, electronics cooling, heat exchange processes, and safety considerations such as managing heat from fires. The analysis of natural convective flow past a vertical plate has been extensively researched because of its wide-ranging applications in engineering, such as building climate management, cooling electronic devices, and the growth of crystals. It remains a significant topic of interest both theoretically and experimentally because of the numerous potential variations in boundary conditions. Several studies [1-7] have focused on investigating natural convection past a vertical plate within a stratified medium, recognizing its significant importance. Recently, several researchers have focused on two-phase flow in the context of heat transfer applications. For instance, Obalalu et al. [8] investigated the influence of a heat source/sink and solar radiation on two-phase flow over a vertically deformable sheet. Hameed et al. [9] examined natural convection and heat transfer in dome-shaped enclosures filled with nanofluids under two-phase flow conditions. Shi et al. [10] conducted an experimental study on two-phase flow instability triggered by direct contact condensation in an open natural circulation system. Akter et al. [11] carried out a finite difference simulation to analyze natural convection in two-phase flow along a vertically heated wavy surface. More recently, Zamri et al. [12] studied the impact of fluid-particle interaction and mass concentration on velocity, temperature, and skin friction in two-phase flow. Earlier research focused on finding similarity solutions, as these variables provide substantial physical insights with minimal effort. The diversity in approaches highlights the complex nature of these thermal processes and the ongoing need to understand them better.

Cite as: S.S. Bishoyi, S. Mishra, A.K. Pati, P.K. Rath, East Eur. J. Phys. 1, 447 (2026), https://doi.org/10.26565/2312-4334-2026-1-52

Dust particles in the boundary layer can originate from various sources, such as combustion processes, flow dynamics in rocket tubes, dust entrainment in clouds during nuclear explosions, soil erosion due to natural winds, blood flow in capillaries and paint spraying. A comprehensive understanding of particle interactions with fluid flows is crucial in each of these situations. Understanding this knowledge is essential for efficiently applying computational fluid dynamics (CFD) models to improve and optimize the effectiveness of current machinery and procedures, identify and resolve operational issues, explore retrofit possibilities, and design new systems and plants, including scaling up processes. To address these needs, numerous researchers have developed and thoroughly examined multiphase flow equations to better predict and control such complex interactions. Soo [13] has created a mathematical framework for exploring multiphase flows. In recent years, a number of studies [14-30] have focused on examining two-phase flow or boundary layer flow, highlighting the increasing interest in these phenomena due to their significant implications for practical heat transfer applications. Researchers have been exploring how these flow dynamics impact various thermal processes, demonstrating their relevance in improving the efficiency and effectiveness of heat transfer systems.

Earlier investigations on natural convection have largely focused on single-phase fluids, with relatively limited emphasis on flows involving suspended particulate matter (SPM). In particular, the existing literature highlights a clear deficiency in studies addressing the coupled influence of particle volume fraction and Prandtl number in two-phase natural convection flows involving suspended particulate matter. Although natural convective boundary layer flow over a vertical plate plays a vital role in many engineering and environmental applications including industrial cooling, heat exchanger design, and pollutant dispersion, the effects of suspended particulates on such flows have not been adequately quantified. Most reported studies either neglect particulate effects or treat them in a simplified manner, thereby overlooking their significant impact on momentum and thermal transport mechanisms.

This research gap is critical because the presence of suspended particles can substantially modify both the momentum boundary layer and the thermal boundary layer through complex particle–fluid interactions, leading to notable variations in skin friction and heat transfer rates. Furthermore, changes in particle concentration (volume fraction) directly influence the effective thermophysical properties of the fluid, while variations in the Prandtl number govern the relative dominance of momentum diffusivity and thermal diffusivity. Despite their practical importance, the combined and interactive effects of these parameters on skin friction and heat transfer characteristics in two-phase natural convection flows involving suspended particulate matter remain insufficiently explored.

Motivated by this unresolved gap, the present investigation offers a novel and systematic analysis of the simultaneous effects of Prandtl number and volume fraction on boundary layer characteristics, heat transfer, and skin friction in steady, laminar, incompressible two-phase natural convective flow along a vertical plate containing suspended particulates. By employing a reliable finite difference numerical technique, this study provides new physical insights into particulate-laden natural convection and contributes to the advancement of accurate modeling and efficient thermal system design involving two-phase convective flows.

2. MATHEMATICAL ANALYSIS

To demonstrate the effects of Prandtl number and volume fraction, we examined a plate that is extensive in both length and width, positioned in a plane that is vertical to the floor, and has the capacity to be either heated or cooled. The x-coordinate is oriented along the plate, while the y-coordinate is oriented perpendicular to it. The temperature of the plate surface is denoted as T_w, and it asymptotically reduces to the ambient fluid temperature T_∞ as one move away from the plate. The fluid velocity at the plate surface starts from zero, increases to a maximum near the surface, and then asymptotically decreases to zero at greater distances. The temperature and velocity of the particle phase differ from those of the fluid on the plate. Figure 1 illustrates the geometry of the flow.

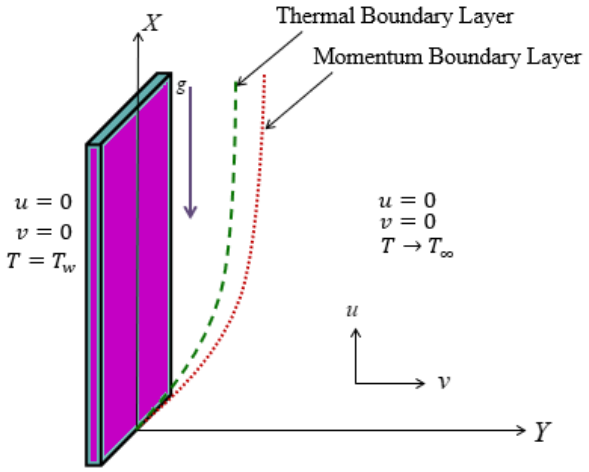

Figure 1. Geometry of the flow

Otterman [31] showed that traditional boundary layer approximations can be applied to the fluid phase when the particulate phase density is similar to that of the fluid. Additionally, it has been established that the boundary layer approximation is not needed for the momentum equations governing the particle phase, and it is essential to account for the transverse component of particle momentum. Consequently, in this context, the y-component of the momentum equation for the fluid phase is omitted, while the particle phase y-component is maintained.

Based on the assumptions outlined earlier, the governing equations describing the two-phase flow, as formulated by Tripathy et al. [14], Mishra et al. [15] and Misra et al. [32], are given below:

$$\frac{\partial u}{\partial x}+\frac{\partial v}{\partial y}=0 \tag{1}$$

$$u_p\frac{\partial \rho_p}{\partial x}+v_p\frac{\partial \rho_p}{\partial y}=D_p\frac{\partial^2 \rho_p}{\partial y^2} \tag{2}$$

$$(1-\varphi)\rho\left(u\frac{\partial u}{\partial x}+v\frac{\partial u}{\partial y}\right)=(1-\varphi)\mu\frac{\partial^2 u}{\partial y^2}-\frac{1}{\tau_p}\varphi\rho_s(u-u_p)+(1-\varphi)\rho g\beta(T-T_\infty) \tag{3}$$

$$\varphi\rho_s\left(u_p\frac{\partial u_p}{\partial x}+v_p\frac{\partial u_p}{\partial y}\right)=\frac{\partial}{\partial y}\left(\varphi\mu_s\frac{\partial u_p}{\partial y}\right)+\frac{1}{\tau_p}\varphi\rho_s(u-u_p)+\varphi(\rho_s-\rho)g \tag{4}$$

$$\varphi\rho_s\left(u_p\frac{\partial v_p}{\partial x}+v_p\frac{\partial v_p}{\partial y}\right)=\frac{\partial}{\partial y}\left(\varphi\mu_s\frac{\partial v_p}{\partial y}\right)+\frac{1}{\tau_p}\varphi\rho_s(v-v_p) \tag{5}$$

$$(1-\varphi)\rho c_p\left(u\frac{\partial T}{\partial x}+v\frac{\partial T}{\partial y}\right)=(1-\varphi)\,k\frac{\partial^2 T}{\partial y^2}+\frac{1}{\tau_T}\varphi\rho_s c_s(T_p-T)+(1-\varphi)\mu\left(\frac{\partial u}{\partial y}\right)^2 \tag{6}$$

$$\varphi\,\rho_s c_s\left(u_p\frac{\partial T_p}{\partial x}+v_p\frac{\partial T_p}{\partial y}\right)=\frac{\partial}{\partial y}\left(\varphi k_s\frac{\partial T_p}{\partial y}\right)-\frac{1}{\tau_T}\varphi\rho_s c_s(T_p-T)+\varphi\mu_s\left[u_p\frac{\partial^2 u_p}{\partial y^2}+\left(\frac{\partial u_p}{\partial y}\right)^2\right] \tag{7}$$

Here D_p is the binary diffusion coefficient. If the variation of temperature is minimal; D_p, μ_s and k_s can be assumed to be constant. In this case, the term $\frac{\partial}{\partial y}\left(\varphi\mu_s\frac{\partial u_p}{\partial y}\right)$ can be replaced by $\varphi\mu_s\frac{\partial^2 u_p}{\partial y^2}$, in the particle phase x-momentum equation, reflecting the random motion of particles, analogous to similar terms in the fluid phase. Additionally, the term $\frac{\partial}{\partial y}\left(\varphi k_s\frac{\partial T_p}{\partial y}\right)$ in the energy equation for particle phase may be substituted with $\varphi k_s\frac{\partial^2 T_p}{\partial y^2}$. Generally, $D_p\approx\upsilon_p$ and D_p is often significantly smaller than υ. Nevertheless, we choose to retain the terms involving D_p and υ_p to examine their respective impacts on the solutions of these equations, regardless of how minimal these influences may be in many flow scenarios.

Given the above considerations, equations (1) through (7) simplify to

$$\frac{\partial u}{\partial x}+\frac{\partial v}{\partial y}=0 \tag{8}$$

$$v_p\frac{\partial \rho_p}{\partial y}+u_p\frac{\partial \rho_p}{\partial x}=\upsilon_p\frac{\partial^2 \rho_p}{\partial y^2} \tag{9}$$

$$v\frac{\partial u}{\partial y}+u\frac{\partial u}{\partial x}=\nu\frac{\partial^2 u}{\partial y^2}+g\beta(T-T_\infty)-(u-u_p)\frac{1}{1-\varphi}\,\frac{1}{\tau_p}\frac{\rho_p}{\rho} \tag{10}$$

$$v_p\frac{\partial u_p}{\partial y}+u_p\frac{\partial u_p}{\partial x}=\nu_s\frac{\partial^2 u_p}{\partial y^2}+\left(1-\frac{\rho}{\rho_s}\right)g+\frac{1}{\tau_p}(u-u_p) \tag{11}$$

$$v_p\frac{\partial v_p}{\partial y}+u_p\frac{\partial v_p}{\partial x}=-\frac{1}{\tau_p}(v_p-v)+\nu_s\frac{\partial^2 v_p}{\partial y^2} \tag{12}$$

$$v\frac{\partial T}{\partial y}+u\frac{\partial T}{\partial x}=\frac{1}{1-\varphi}\frac{1}{\tau_T}(T_p-T)\frac{\rho_p}{\rho}\frac{C_s}{C_p}+\frac{\mu}{\rho C_p}\left(\frac{\partial u}{\partial y}\right)^2+\frac{\kappa}{\rho C_p}\frac{\partial^2 T}{\partial y^2} \tag{13}$$

$$v_p\frac{\partial T_p}{\partial y}+u_p\frac{\partial T_p}{\partial x}=\frac{\mu_s}{\rho_s C_s}\left[u_p\frac{\partial^2 u_p}{\partial y^2}+\left(\frac{\partial u_p}{\partial y}\right)^2\right]-\frac{1}{\tau_T}(T_p-T)+\frac{\kappa_s}{\rho_s C_s}\frac{\partial^2 T_p}{\partial y^2} \tag{14}$$

Introducing the dimensionless variables such as

$y^*=\frac{y}{L}\sqrt{Re}$, $x^*=\frac{x}{L}$, $v^*=\frac{v}{U}\sqrt{Re}$, $u^*=\frac{u}{U}$, $v_p^*=\frac{v_p}{U}\sqrt{Re}$, $u_p^*=\frac{u_p}{U}$, $T_p{}^*=\frac{T_p-T_\infty}{T_w-T_\infty}$, $T^*=\frac{T-T_\infty}{T_w-T_\infty}$, $\rho_p^*=\frac{\rho_p}{\rho_{p_0}}$, $\rho_s^*=\frac{\rho_s}{\rho_{p_0}}$,

in the equations numbered (8) through (14), and after omitting the asterisks, the fundamental boundary layer equations describing the flow field, as outlined by Tripathy et al. [14], are given by

$$\frac{\partial u}{\partial x}=-\frac{\partial v}{\partial y} \tag{15}$$

$$v_p\frac{\partial \rho_p}{\partial y}+u_p\frac{\partial \rho_p}{\partial x}=\epsilon\frac{\partial^2 \rho_p}{\partial y^2} \tag{16}$$

$$v\,\frac{\partial u}{\partial y}+u\,\frac{\partial u}{\partial x}=\frac{Gr\,T}{Re^2}-\alpha\rho_p(u-u_p)\frac{1}{1-\varphi}\,\frac{F\,L}{U}+\frac{\partial^2 u}{\partial y^2} \tag{17}$$

$$u_p\,\frac{\partial u_p}{\partial x}+v_p\,\frac{\partial u_p}{\partial y}=\frac{1}{Fr}\left(1-\frac{1}{\gamma}\right)+\frac{F\,L}{U}(u-u_p)+\epsilon\,\frac{\partial^2 u_p}{\partial y^2} \tag{18}$$

$$v_p\,\frac{\partial v_p}{\partial y}+u_p\,\frac{\partial v_p}{\partial x}=\frac{F\,L}{U}(v-v_p)+\epsilon\,\frac{\partial^2 v_p}{\partial y^2} \tag{19}$$

$$v\,\frac{\partial T}{\partial y}+u\,\frac{\partial T}{\partial x}=\frac{1}{Pr}\,\frac{\partial^2 T}{\partial y^2}+\frac{2\,\alpha}{3\,Pr}\,\frac{F\,L}{U}\rho_p(T_p-T)\,\frac{1}{1-\varphi}+Ec\left(\frac{\partial u}{\partial y}\right)^2 \tag{20}$$

$$v_p\,\frac{\partial T_p}{\partial \eta}+u_p\,\frac{\partial T_p}{\partial x}=\frac{F\,L}{U}\,(T-T_p)+\frac{3}{2}Pr\,\epsilon Ec\left[\left(\frac{\partial u_p}{\partial y}\right)^2+u_p\,\frac{\partial^2 u_p}{\partial y^2}\right]+\frac{\epsilon}{Pr}\,\frac{\partial^2 T_p}{\partial y^2}, \tag{21}$$

with the boundary conditions (Misra et al. [32])

$$y=0:\rho_p=\rho_{pw}(x),T_p=T_{pw}(x),T=T_w=1,v=0,u=0\,,v_p=0,u_p=u_{pw}(x), \tag{22}$$

$$y\to\infty:,\ \rho_p=1,T_p=0,T=T_\infty=0,v_p=0,u=u_p=0. \tag{23}$$

Computational algorithm of the present study is depicted in Fig. 2.

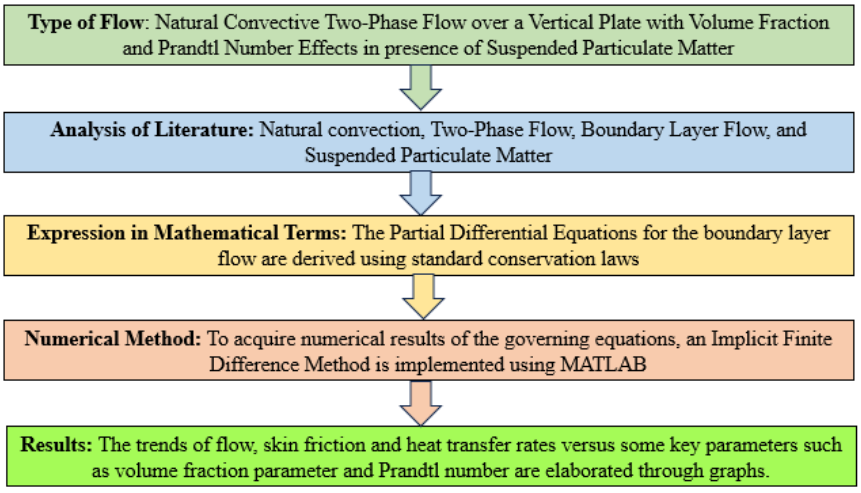

Figure 2. Computational algorithm

3. METHOD OF SOLUTION:

Finite difference expressions are utilized for the different terms in equations (15) to (21) as follows in order to create a computational procedure that makes use of a non-uniform grid:

$$\frac{\partial W}{\partial x}=\frac{0.5\,W_j^{n-1}-2W_j^n+1.5\,W_j^{n+1}}{\Delta x}+o(\Delta x^2) \tag{24}$$

$$\frac{\partial W}{\partial y}=\frac{W_{j+1}^{n+1}-r_y^2\,W_{j-1}^{n+1}-(1-r_y^2)W_j^{n+1}}{r_y\,(r_y+1)\,\Delta y}+o(\Delta y^2) \tag{25}$$

$$\frac{\partial^2 W}{\partial y^2}=2\,\frac{r_y\,W_{j-1}^{n+1}-(1+r_y)W_j^{n+1}+W_{j+1}^{n+1}}{(r_y+1)r_y\,\Delta y^2}+o(\Delta y^2) \tag{26}$$

$$W_j^{n+1}=-W_j^{n-1}+2\,W_j^n+o(\Delta x^2) \tag{27}$$

and

$$y_{j+1}-y_j=-(y_{j-1}-y_j)r_y=r_y\Delta y_j \tag{28}$$

where W can represent either T or T_p or u or u_p or $v_p$or v or ρ_p.

A typical three-point representation of $\frac{\partial W}{\partial y}$ on a non-uniform grid is employed here to achieve the minimal truncation error.

Equations (15) through (21) are transformed into difference equations in accordance with the methodology proposed by Mishra and Tripathy [33] as follows:

$$v_j^{n+1}=-\frac{1}{2}\,\frac{\Delta y}{\Delta x}\,[\,(0.5\,u_j^{n-1}-2\,u_j^n+1.5\,u_j^{n+1})+(0.5\,u_{j-1}^{n-1}-2\,u_{j-1}^n+1.5\,u_{j-1}^{n+1})]+v_{j-1}^{n+1} \tag{29}$$

$$a_j u_{j-1}^{n+1}=d_j-b_j u_j^{n+1}-c_j u_{j+1}^{n+1} \tag{30}$$

$$a_j^* u_{p_{j-1}}^{n+1} = d_j^* - b_j^* u_{p_j}^{n+1} - c_j^* u_{p_{j+1}}^{n+1} \tag{31}$$

$$a_j^{**} v_{p_{j-1}}^{n+1} = d_j^{**} - b_j^{**} v_{p_j}^{n+1} - c_j^{**} v_{p_{j+1}}^{n+1} \tag{32}$$

$$a_j^{+} T_{j-1}^{n+1} = d_j^{+} - b_j^{+} T_j^{n+1} - c_j^{+} T_{j+1}^{n+1} \tag{33}$$

$$a_j^{++} T_{p_{j-1}}^{n+1} = d_j^{++} - b_j^{++} T_{p_j}^{n+1} - c_j^{++} T_{p_{j+1}}^{n+1} \tag{34}$$

$$a_j^{\blacksquare} \rho_{p_{j-1}}^{n+1} = d_j^{\blacksquare} - b_j^{\blacksquare} \rho_{p_j}^{n+1} \; c_j^{\blacksquare} \rho_{p_{j+1}}^{n+1} \tag{35}$$

Where:

$$a_j = \frac{1}{\Delta x}\left[-q - pr_y\right] \tag{36}$$

$$b_j = \frac{1}{\Delta x}\left[p\left(r_y - \frac{1}{r_y}\right) + 1.5\ \left(2\,u_j^n - u_j^{n-1}\right) + \frac{1}{1-\varphi}\frac{FL}{U}\alpha\Delta x\left(2\,\rho_{p_j}^{\,n} - \rho_{p_j}^{\,n-1}\right) + q\left(1 + \frac{1}{r_y}\right)\right] \tag{37}$$

$$c_j = \frac{1}{\Delta x}\left[\frac{1}{r_y}(p-q)\right] \tag{38}$$

$$d_j = \frac{1}{\Delta x}\begin{bmatrix} \frac{Gr\left(2T_j^n - T_j^{n-1}\right)}{Re^2}\Delta x + \left(-u_j^{n-1} + 2\,u_j^n\right)\left(-0.5\,u_j^{n-1} + 2\,u_j^n\right) \\ -\frac{\varphi}{1-\varphi}\frac{FL}{U}\,\alpha\left(2\,\rho_{p_j}^{\,n} - \rho_{p_j}^{\,n-1}\right)\left(-\,2\,u_{p_j}^{\,n} + \,u_{p_j}^{\,n-1}\right)\Delta x \end{bmatrix} \tag{39}$$

$$a_j^* = \frac{1}{\Delta x}\left[-\epsilon q - pr_y\right] \tag{40}$$

$$b_j^* = \frac{1}{\Delta x}\left[1.5\ \left(2\,u_{p_j}^{\,n} - u_{p_j}^{\,n-1}\right) + \epsilon q\left(1 + \frac{1}{r_y}\right) + \frac{FL}{U}\,\Delta x + \,p\left(r_y - \frac{1}{r_y}\right)\right] \tag{41}$$

$$c_j^* = \frac{1}{\Delta x}\left[\frac{1}{r_y}(-\epsilon q + p)\right] \tag{42}$$

$$d_j^* = \frac{1}{\Delta x}\left[\left(2\,u_{p_j}^{\,n} - \,u_{p_j}^{\,n-1}\right)\left(2\,u_{p_j}^{\,n} - \,0.5\,u_{p_j}^{\,n-1}\right) + \frac{1}{Fr}\left(1 - \frac{1}{\gamma}\right)\Delta x + \frac{FL}{U}\,\Delta x\,u_j^{n+1}\right] \tag{43}$$

$$a_j^{**} = \frac{1}{\Delta x}\left[-\epsilon q - pr_y\right] \tag{44}$$

$$b_j^{**} = \frac{1}{\Delta x}\left[\frac{FL}{U}\,\Delta x + 1.5\ u_{p_j}^{\,n+1} + \,\epsilon q\left(1 + \frac{1}{r_y}\right) + \,p\left(r_y - \frac{1}{r_y}\right)\right] \tag{45}$$

$$c_j^{**} = \frac{1}{\Delta x}\left[\frac{1}{r_y}(-\epsilon q + p)\right] \tag{46}$$

$$d_j^{**} = \frac{1}{\Delta x}\left[\frac{FL}{U}\,\Delta x\,v_j^{n+1} + u_{p_j}^{\,n+1}\left(2\,v_{p_j}^{\,n} - 0.5\,v_{p_j}^{\,n-1}\right)\right] \tag{47}$$

$$a_j^{+} = \frac{1}{\Delta x}\left[-q\left(\frac{1}{Pr} + 0.5\,r_y\,\Delta y\,v_j^{n+1}\right)\right] \tag{48}$$

$$b_j^{+} = \frac{1}{\Delta x}\left[0.5\,q\,\Delta y\,v_j^{n+1}\left(r_y - \frac{1}{r_y}\right) + 1.5\,u_j^{n+1} + \frac{2\alpha}{3\,Pr}\,\frac{1}{1-\varphi}\,\frac{FL}{U}\,\Delta x\,\rho_{p_j}^{\,n+1} + \frac{q\,(1+r_y)}{Pr.r_y}\right] \tag{49}$$

$$c_j^{+} = \frac{1}{\Delta x}\left[\frac{q}{r_y}\left(-\frac{1}{Pr} + 0.5\,\Delta y\,v_j^{n+1}\right)\right] \tag{50}$$

$$d_j^{+} = \frac{1}{\Delta x}\begin{bmatrix} \frac{2\alpha}{3\,Pr}\,\frac{1}{1-\varphi}\,\frac{FL}{U}\,\rho_{p_j}^{\,n+1}\left(2\,T_{p_j}^{\,n} - \,T_{p_j}^{\,n-1}\right)\Delta x \\ +u_j^{n+1}\left(2\,T_j^n - 0.5\,T_j^{n-1}\right) + \Delta x.\,Ec\left(\frac{u_{j+1}^{n+1} - u_j^{n+1}}{\Delta y}\right)^2 \end{bmatrix} \tag{51}$$

$$a_j^{++} = \frac{1}{\Delta x}\left[\frac{\epsilon}{Pr} - q\left(\frac{1}{2}\,\Delta y\,r_y\,v_{p_j}^{\,n+1}\right)\right] \tag{52}$$

$$b_j^{++} = \frac{1}{\Delta x}\left[\,1.5\,u_{p_j}^{\,n+1} + \frac{\epsilon\,q\,(1+r_y)}{Pr.r_y} + \,\frac{FL}{U}\,\Delta x\, + 0.5\,q\,\Delta y\,v_{p_j}^{\,n+1}\left(r_y - \frac{1}{r_y}\right)\right] \tag{53}$$

$$c_j^{++} = \frac{1}{\Delta x}\left[\frac{q}{r_y}\left(-\frac{\epsilon}{Pr} + 0.5\Delta y.\,v_{p_j}^{\,n+1}\right)\right] \tag{54}$$

$$d_j^{++} = \frac{1}{\Delta x}\left[\begin{array}{c}\frac{FL}{U}\ T_j^{n+1}\Delta x + u_{p_j}^{n+1}\left(2\,T_{p_j}^{n} - 0.5\,T_{p_j}^{n-1}\right) \\ +\frac{3}{2}Pr.\epsilon.Ec.\Delta x\left\{\left(\frac{u_{p_{j+1}}^{n+1} - u_{p_j}^{n+1}}{\Delta y}\right)^2 + 2u_{p_j}^{n+1}\left(\frac{u_{p_{j-1}}^{n+1} - \left(1+\frac{1}{r_y}\right)u_{p_j}^{n+1} + \frac{1}{r_y}u_{p_{j+1}}^{n+1}}{(1+r_y)\ \Delta y^2}\right)\right\}\end{array}\right] \tag{55}$$

$$a_j^{\blacksquare} = -2\epsilon\, r_y\ -\ v_{p_j}^{n+1} r_y^2\,\Delta y \tag{56}$$

$$b_j^{\blacksquare} = 2\epsilon\left(1 + r_y\right) -\ v_{p_j}^{n+1}\left(1 - r_y^2\right)\Delta y + \frac{1.5\,p^{\blacksquare}\,u_{p_j}^{n+1}}{\Delta x} \tag{57}$$

$$c_j^{\blacksquare} = -2\epsilon + p^{\blacksquare}\,v_{p_j}^{n+1}\Delta y \tag{58}$$

$$d_j^{\blacksquare} = p^{\blacksquare}\,u_{p_j}^{n+1}\frac{-\,0.5\,\rho_{p_j}^{n-1} + 2\rho_{p_j}^{n}}{\Delta x} \tag{59}$$

$$p = \left(2\,v_j^n -\ v_j^{n-1}\right)\frac{\Delta x}{(1+r_y)\Delta y} \tag{60}$$

$$q = \frac{2\,\Delta x}{\left(1 +\ r_y\right)\Delta y^2}$$

$$p^{\blacksquare} = r_y\left(r_y + 1\right)\Delta y^2 \tag{61}$$

The equations (30) to (35) cannot be applied at $j = 1$ or $j = jmax$ due to the boundary conditions (22) and (23). Therefore,

$a_2 = 0$ as $u_1 = 0$ at $j = 2$
$c_j = 0$ at $j = j_{max} - 1$
$d_2^* = d_2^* - a_2^* v_{pw}$ at $j = 2$
$c_j^* = 0$ at $j = j_{max} - 1$
$a_2^{**} = 0$ at $j = 2$
$c_j^{**} = 0$ at $j = j_{max} - 1$
$d_2^+ = d_2^+ - a_2^+$ at $j = 2$
$c_j^+ = 0$ at $j = j_{max} - 1$
$d_2^{++} = d_2^{++} - a_2^{++} T_{pw}$ at $j = 2$
$c_j^{++} = 0$ at $j = j_{max} - 1$
$d_2^{\blacksquare} = d_2^{\blacksquare} - a_2^{\blacksquare}\rho_{pw}$ at $j = 2$
$d_j^{\blacksquare} = d_j^{\blacksquare} - c_j^{\blacksquare}$ at $j = j_{max} - 1$

Computation of u_{pw} at $y = 0$:
Since u_{pw} depends solely on x, we can derive from equation (18) that

$$u_{p1}^{n+1} = +\frac{2}{3}\frac{\Delta x}{Fr}\left(1 - \frac{1}{\gamma}\right) + \frac{4}{3}u_{p1}^{n} - \frac{1}{3}u_{p1}^{n-1} - \frac{2}{3}\frac{FL}{U}\Delta x \tag{62}$$

Computation of T_{pw} at y= 0:
As T_{pw} depends solely on x, we can derive from equation (18) that

$$T_{p_1}^{n+1} = \frac{\frac{FL}{U}\frac{\Delta x}{u_{p_1}^{n+1}} + 2T_{p_1}^{n} - 0.5T_{p_1}^{n-1}}{1.5 + \frac{FL}{U}\frac{\Delta x}{u_{p_1}^{n+1}}} \tag{63}$$

Heat transfer:
The Nusselt number, defined as follows, represents the qualities of heat transfer:

$$Nu^{\,n+1} = -\sqrt{Re}\left[\frac{\partial T}{\partial y}\right]_{y=0}^{n+1} = -\sqrt{Re}\left[\frac{T_{j+1}^{n+1} - r_y^2 T_{j-1}^{n+1} - \left(1 - r_y^2\right)T_j^{n+1}}{r_y(1+r_y)\Delta y}\right]_{j=2} = -\sqrt{Re}\left[\frac{-r_y^2 T_1^{n+1} + T_3^{n+1} - (1 - r_y^2)T_2^{n+1}}{r_y(r_y+1)\Delta y}\right] \tag{64}$$

Computation of skin friction coefficient:

$$C_f = \frac{\tau_w}{0.5\rho U^2} = \frac{2}{U^2\sqrt{Re}}\left.\frac{\partial u}{\partial y}\right]_{y=0}$$

Through the application of finite differences, the equation above simplifies to

$$C_f^{n+1} = \frac{2}{U^2\sqrt{Re}}\left[\frac{u_{j+1}^{n+1} - r_y^2 u_{j-1}^{n+1} - (1-r_y^2)u_j^{n+1}}{r_y(1+r_y)\Delta y}\right]_{j=2} = \frac{2}{U^2\sqrt{Re}}\left[\frac{u_3^{n+1} - r_y^2 u_1^{n+1} - (1-r_y^2)u_2^{n+1}}{r_y(1+r_y)\Delta y}\right] \quad (65)$$

Figure 3 illustrates the grid independence analysis, demonstrating the convergence of the Nusselt number as the number of grid points increases. A grid independence test was performed using grid sizes ranging from 20 to 192 points. The Nusselt number exhibits monotonic convergence, and variations beyond 190 grid points are negligible. Hence, a grid size of 192 points was selected for all subsequent computations.

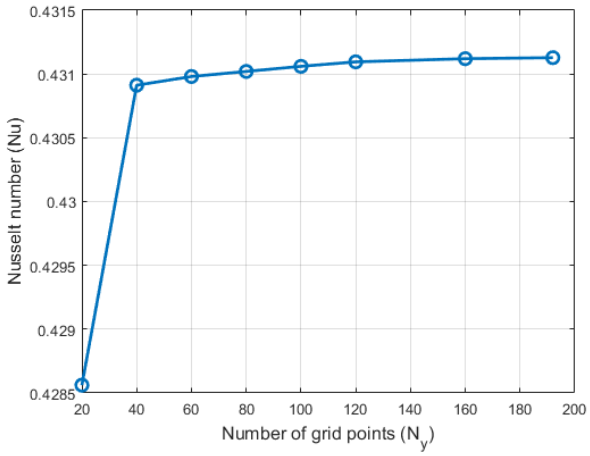

Figure 3. Grid independence study showing convergence of the Nusselt number with increasing number of grid points

4. DISCUSSION OF THE RESULTS

This study examines the essential characteristics of two-phase momentum and thermal boundary layer flow across a semi-infinite flat plate, using the finite difference method for its analysis.

We chose the subsequent values for the different parameters involved.

$\varphi = 0.01, 0.05, 0.1$; $Pr = 0.71, 1.0, 7.0$; $U = 0.45\ m/sec$; $\epsilon = 0.1$;

$\rho = 0.913\ \ kg/m^3$; $\rho_p = 800\, kg/m^3$; $D = 50\ \mu m$; $\alpha = 0.1$;

$L = 0.3048\, m$; $Ec = 0.1$; $\mu = 1.5415 \times 10^{-5}\ kg/m\, sec$.

The primary aim of this study is to investigate the influence of the volume fraction (φ) and Prandtl number (Pr) on the flow dynamics and heat transfer processes involving suspended particulate matter. A numerical solution is obtained using a computational algorithm that employs a non-uniform grid, and the scheme was implemented in MATLAB (Shampine and Kierzenka [34]). The numerical outcomes are examined in the form of graphs for various values of φ and Pr. The heat transfer rate, expressed as the Nusselt number (Nu), and the shear stress, represented by the skin friction coefficient (C_f), are calculated due to their physical relevance.

A specific limiting case of the present model has been validated by comparing the numerical values of the Nusselt number with those reported by Mishra et al. [15], as summarized in Table 1. An excellent agreement is observed over the entire range of Prandtl numbers considered. The absolute differences between the two sets of results are of the order of 10^{-5}, while the corresponding relative errors remain well below 0.005%, indicating negligible numerical deviation. For instance, at $Pr = 0.72$ and $Pr = 1.0$, the relative errors are approximately 0.0009% and 0.0038%, respectively, whereas even at higher Prandtl numbers such as $Pr = 10.0$, the discrepancy remains extremely small. This consistently minimal error confirms the numerical stability, accuracy, and convergence of the present computational scheme. Moreover, the close match across both low and high Prandtl number regimes demonstrates that the present formulation reliably captures the underlying heat transfer physics without introducing spurious numerical artifacts. Hence, the error analysis strongly substantiates the correctness of the numerical implementation and establishes the present results as a trustworthy extension of the existing literature.

The accuracy of the present numerical results is further illustrated through the graphical representation of Table 1, as shown in Fig. 4. The near-perfect overlap between the present results and those reported by Mishra et al. [15] in the figure clearly confirms the precision, consistency, and reliability of the numerical methodology adopted in this study.

Table 1. Comparison of numerical results for Nu

Pr	Nu (Mishra et al. [15])	Nu (Present results)
0.72	1.0884	1.08841
1.0	1.3333	1.33335
3.0	2.5097	2.50976
10.0	4.7969	4.79693

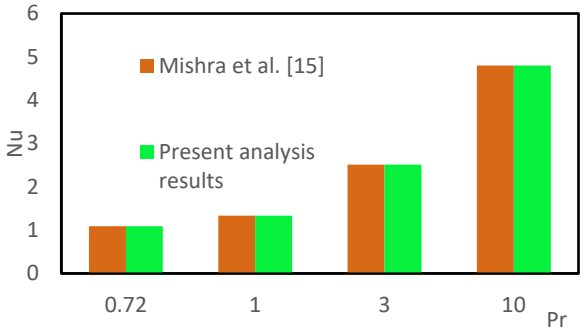

Figure 4. Graphical comparison of present analysis with Mishra et al. [15]

It is important to emphasize that Figures 5-12 display the numerical results for velocity and temperature profiles, which closely resemble those reported in previously published studies on natural convective flows. This similarity serves to validate the accuracy of the numerical findings presented in this investigation.

The velocity and temperature fields for different φ are depicted in Fig 5-8. Figures 5 and 6 illustrate that as the concentration of particles per unit volume in the mixture rises, the velocities of both the carrier fluid and the particle phase decrease.

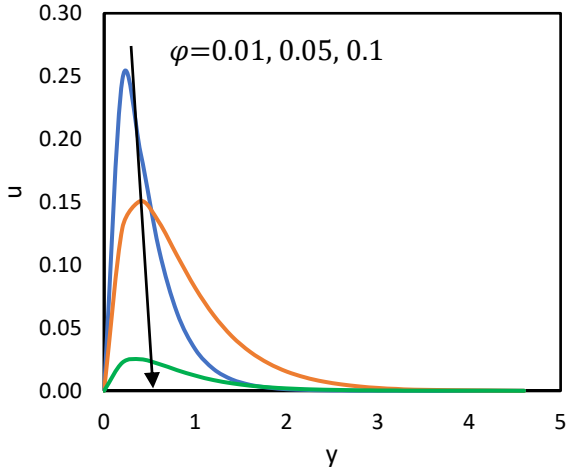

Figure 5. Variation of u with φ

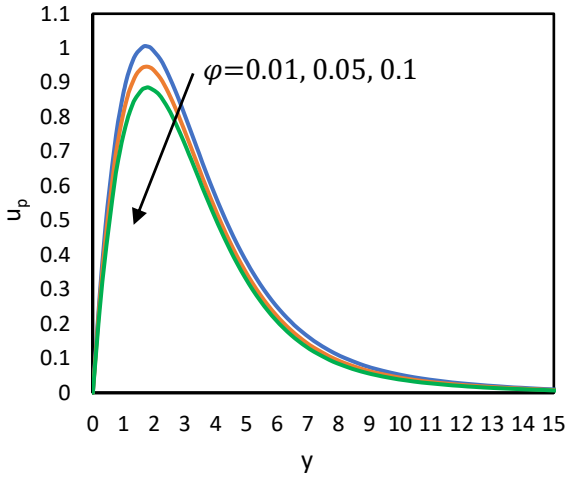

Figure 6. Variation of u_p with φ

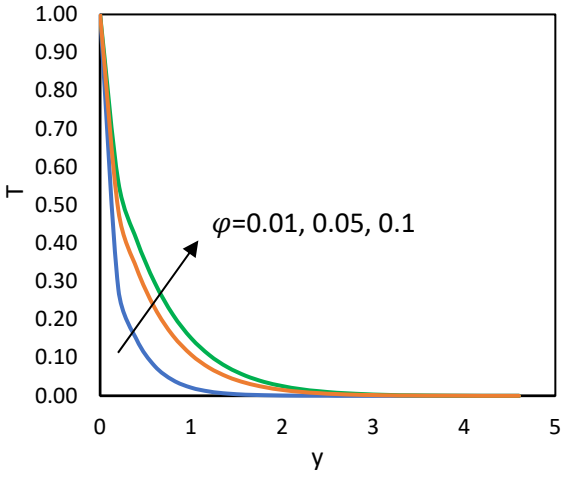

Figure 7. Variation of T with φ

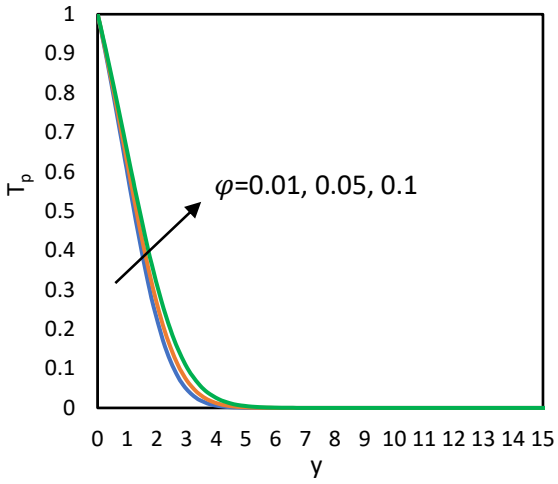

Figure 8. Variation of T_p with φ

In contrast, Figures 7 and 8 indicate that a higher particle concentration results in an increase in the temperatures of both the carrier fluid and particle phases. Additionally, the boundary layer thickness for the particle phase is greater than that of the carrier fluid in both the velocity and temperature distributions. The variation in velocity and temperature

distribution for different values of Pr with respect to y is illustrated in Figures 9 to 12. An increase in Pr values does not influence the velocity of the carrier fluid; however, it leads to an increase in the velocity of the particle phase, as shown in Figures 9 and 10. It is observed that as the Pr value increases, the temperature of the carrier fluid decreases, while the particle phase temperature rises. The rise in Pr results in a reduction in the carrier fluid's temperature distribution. This occurs because lower Pr values correspond to higher thermal conductivity, allowing heat to diffuse more rapidly away from the heated surface compared to higher Prandtl numbers. Consequently, the temperature decreases more quickly for water than for air as the carrier fluid. Moreover, the boundary layer thickness of the particle phase is greater than that of the carrier fluid in terms of both velocity and temperature distributions.

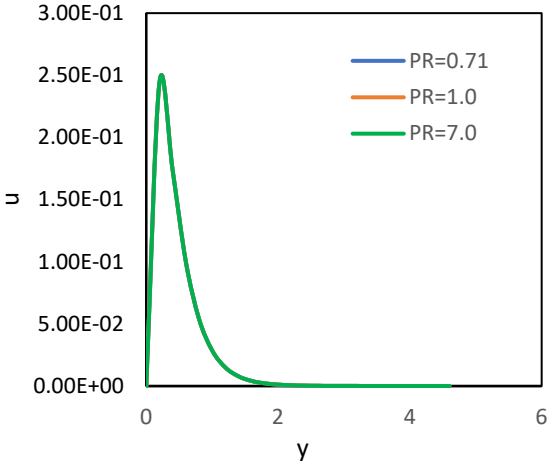

Figure 9. Variation of u with Pr

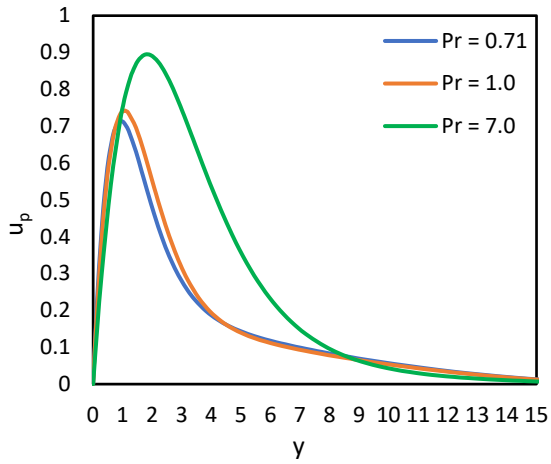

Figure 10. Variation of u_p with Pr

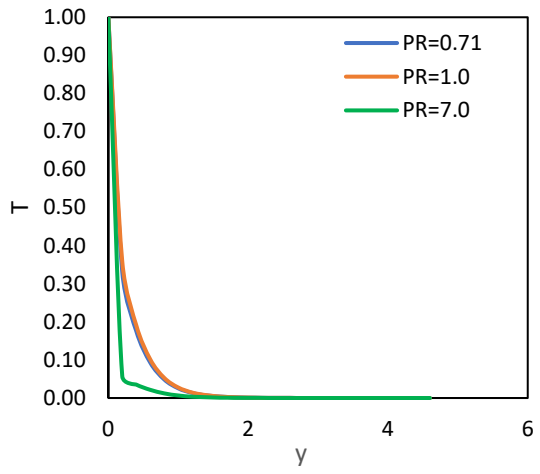

Figure 11. Variation of T with Pr

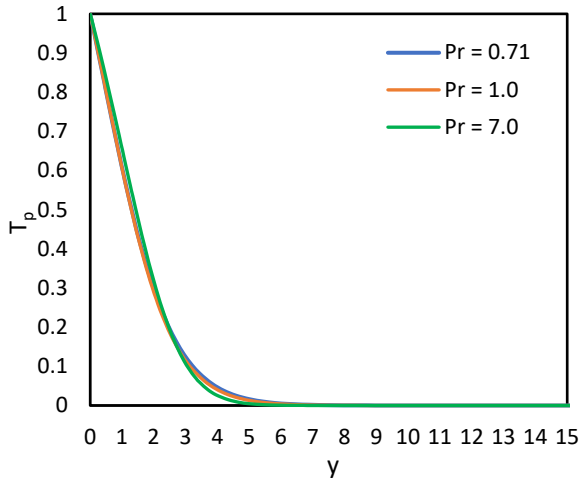

Figure 12. Variation of T_p with Pr

Figure 13 illustrates the streamline patterns of the flow field generated from the velocity components u and v, with color contours representing the magnitude of the velocity field, in the presence of suspended particulate matter for two different Prandtl numbers, namely (a) $Pr = 0.71$ and (b) $Pr = 7.0$, thereby highlighting the influence of thermal diffusivity on the flow structure and momentum transport.

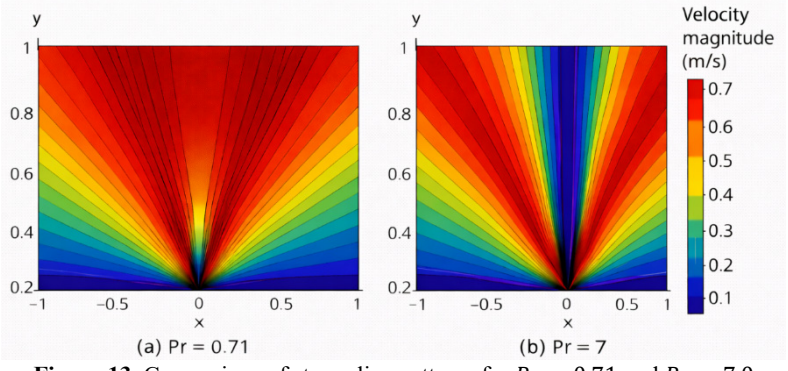

Figure 13. Comparison of streamline patterns for $Pr = 0.71$ and $Pr = 7.0$

For $Pr = 0.71$, which is characteristic of air, the streamlines are relatively more dispersed and smoothly distributed throughout the flow domain. This behavior indicates that thermal diffusion is moderately dominant compared to momentum diffusion, allowing heat to spread efficiently across the fluid. Consequently, the temperature gradients are weaker, resulting in a reduced coupling between the thermal and velocity fields. This leads to broader streamline spacing, gentler curvature, and a less pronounced flow acceleration in the central region, as evidenced by the gradual colour transitions. In contrast, when the Prandtl number is increased to $Pr = 7.0$, corresponding to fluids such as water, the streamline patterns become significantly denser and more concentrated toward the central vertical region. The higher Prandtl number signifies lower thermal diffusivity relative to momentum diffusivity, causing heat to be confined within a thinner thermal boundary layer. This confinement enhances the temperature gradients near the surface, which strengthens buoyancy-induced forces and intensifies the flow circulation. As a result, the streamlines exhibit sharper curvature and closer spacing, particularly near the core region, indicating higher velocity magnitudes and stronger shear effects. The colour contours further corroborate this trend by displaying steeper gradients and elevated peak values compared to the $Pr = 0.71$ case.

The combined influence of φ and Pr on C_f and Nu is illustrated in Figures 14 and 15, respectively. As shown in Figure 14, C_f decreases as the volume fraction (φ) increases across different values of Pr. Conversely, for varying values of φ, the skin friction coefficient C_f exhibits an upward trend with increasing Prandtl number (Pr). This indicates that the highest skin friction is observed when lower values of the volume fraction parameter are combined with higher values of the Prandtl number. This finding underscores the crucial role that the Prandtl number plays in shaping the behavior of skin friction. The interaction between these parameters reveals a complex relationship, where the Prandtl number's influence becomes increasingly dominant, emphasizing its importance in understanding and predicting skin friction coefficient.

Similarly, Figure 15 demonstrates that the Nu values diminish with an increase in φ across various Pr values. In contrast, for different φ values, the Nusselt number (Nu) tends to increase with rising Prandtl numbers. The findings indicate that the highest heat transfer coefficient is achieved when the volume fraction parameter is maintained at relatively lower values, while the Prandtl number is elevated to higher levels. This observation underscores the pivotal role of the Prandtl number in governing heat transfer dynamics, emphasizing its substantial impact on the efficiency and behavior of heat transfer processes.

At a fixed Prandtl number ($Pr \approx 3$), increasing the particle volume fraction from $\varphi = 0.01$ to 0.10 leads to a reduction in C_f from approximately 1.12 to 1.07, corresponding to a decrease of about 4-5%. A similar suppressing trend is observed for heat transfer, where Nu decreases from nearly 0.41 to 0.385, indicating an approximate 6% reduction. This behavior is attributed to enhanced effective viscosity and particle–fluid interactions, which thicken the momentum and thermal boundary layers and weaken wall gradients. In contrast, at a fixed particle volume fraction ($\varphi \approx 0.05$), increasing the Prandtl number from 0.7 to 7 enhances the skin friction coefficient by nearly 6-7% and the Nusselt number by about 10%. Higher Prandtl numbers reduce thermal diffusivity, resulting in a thinner thermal boundary layer and steeper temperature gradients at the wall, thereby intensifying heat transfer. Overall, particle loading tends to suppress transport processes, whereas increasing the Prandtl number significantly improves thermal performance in buoyancy-driven two-phase flows with suspended particulate matter. The boundary layer thickness is set to an optimized value of 15.0 to ensure accurate and reliable numerical results.

These observations indicate a complex interaction between φ and Pr, highlighting their significant roles in influencing both heat transfer and skin friction characteristics in the flow system.

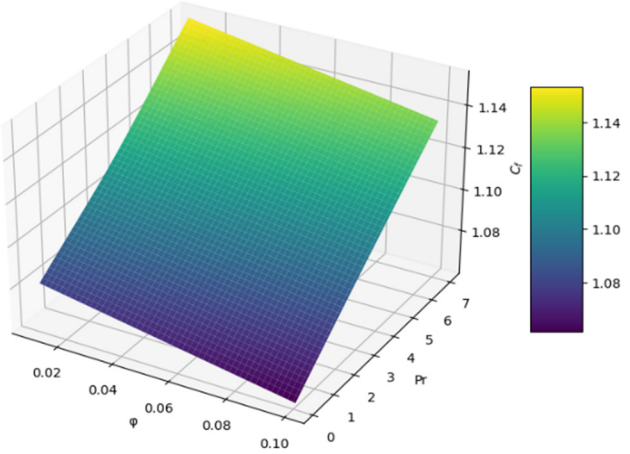

Figure 14. Combined effects of φ and Pr on skin friction coefficient

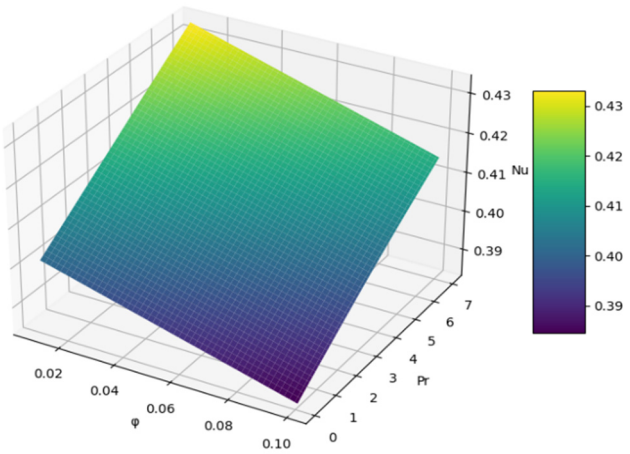

Figure 15. Combined effects of φ and Pr on Nusselt number

5. CONCLUSIONS

This study examines the impact of volume fraction parameter (φ) and Prandtl number (Pr) on the boundary layer properties, skin friction, and heat transfer in a steady, laminar, incompressible natural convective two-phase flow past a vertical plate with suspended particles. The key results are outlined below:

i. The volume fraction decreases the velocities of both the particle phase and carrier fluid, but it increases the temperatures of both the carrier fluid and particle phase within the boundary layer region.

ii. Pr has no significant impact on the velocity of the carrier fluid; however, it enhances the velocity of the particle phase within the boundary layer region.

iii. Pr leads to a reduction in the temperature of the carrier fluid while simultaneously raising the temperature of the particle phase within the boundary layer region.

iv. An increase in φ results in a decrease in both the Nusselt number and the skin friction coefficient. Conversely, a rise in Pr enhances both the Nusselt number and the skin friction coefficient.

v. Since the Prandtl number is 6.2 for pure water and 0.71 for air, heat transfer occurs at a much higher rate in fluids like pure water than in air.

vi. An increase in the Prandtl number enhances the rate of heat transfer from the plate surface to the surrounding fluid. This improvement, influenced by the Prandtl number effect, promotes more efficient heat dissipation into the cooler fluid, thereby aiding in the cooling of the plate. The enhanced thermal performance of fluids containing suspended particles, driven by this effect, proves particularly beneficial in manufacturing processes involving plane wall-shaped products, which are prone to high temperatures during production. By improving heat transfer efficiency, the Prandtl number effect supports better temperature regulation, leading to reduced product temperatures, improved manufacturing efficiency, and enhanced product quality.

This study demonstrates that the volume fraction is a key factor in diminishing both resistance and the efficiency of heat transfer within a system. In contrast, the Prandtl number exerts a positive effect on fluid flow properties and enhances thermal performance. A higher Prandtl number typically indicates that momentum diffusivity is lower compared to thermal diffusivity, resulting in a thinner thermal boundary layer. This leads to improved thermal gradients and more efficient heat exchange. Gaining a comprehensive understanding of these relationships is essential for the effective optimization of heat transfer processes in various engineering applications like metal casting, glass production, and chemical processing, where maintaining optimal thermal conditions ensures product quality, process stability, and energy efficiency. By optimizing heat transfer characteristics through control of the Prandtl number, industries can achieve better thermal management, reduce energy consumption, and improve the overall performance of thermal systems.

ORCID

Sasanka Sekhar Bishoyi, https://orcid.org/0000-0003-0760-9460; **Sakambari Mishra,** https://orcid.org/0009-0007-9088-7571
Aditya Kumar Pati, https://orcid.org/0000-0003-0966-5773; **Prasanta Kumar Rath,** https://orcid.org/0000-0002-3869-9705

REFERENCES

[1] M.A. Arabi, and B. Sakr, "Natural convection heat transfer from inclined isothermal plates", International J. Heat Mass Transfer," **31**(3), 559-565 (1988). https://doi.org/10.1016/0017-9310(88)90037-3

[2] W. Lin, S.W. Armfield, and P.L. Morgan, "Unsteady natural convection boundary-layer flow along a vertical isothermal plate in a linearly stratified fluid with Pr>1," International J. Heat Mass Transfer, **45**, 451-459 (2002). https://doi.org/10.1016/s0017-9310(01)00154-5

[3] F. Kimura, K. Kitumara, M. Yamaguchi, and T. Asami, "Fluid flow and heat transfer of natural convection adjacent to upward-facing inclined heated plates," Heat Transfer-Japanese Research, **32**(3), 278-291 (2003). https://doi.org/10.1002/htj.10091

[4] S. Siddiqa, M.A. Hossain, and S.C. Saha, "Two-phase natural convection flow of a dusty fluid," International Journal of Numerical Methods for Heat & Fluid Flow, **25**(7), 1542-1556 (2015). https://doi.org/10.1108/hff-09-2014-0278

[5] H. Gasmi, U. Khan, A. Zaib, A. Ishak, S.M. Eldin, and Z. Raizah, "Analysis of mixed convection on two-phase nanofluid flow past a vertical plate in Brinkman-extended Darcy porous medium with Nield conditions," Mathematics, **10**(20), 3918 (2022).

[6] A. Kitagawa, R. Kobayashi, P. Denissenko, and Y. Murai, "Natural convection heat transfer enhancement using bubble injection between vertical parallel plates," International Journal of Heat and Mass Transfer, **202**, 123658 (2023). https://doi.org/10.1016/j.ijheatmasstransfer.2022.123658

[7] D. Khan, G. Ali, P. Kumam, M.Y. Almusawa, and A.M. Galal, "Time fractional model of free convection flow and dusty two-phase couple stress fluid along vertical plates," ZAMM-Journal of Applied Mathematics and Mechanics/Zeitschrift für Angewandte Mathematik und Mechanik, **103**(5), e202200369 (2023). https://doi.org/10.1002/zamm.202200369

[8] A.M. Obalalu, M.O. Oni, U. Khan, A. Abbas, T. Muhammad, and A. Zaib, "Two-phase numerical simulation for the heat and mass transfer evaluation across a vertical deformable sheet with significant impact of solar radiation and heat source/sink," Arabian Journal for Science and Engineering, **49**(8), 11053-11071 (2024). https://doi.org/10.1007/s13369-023-08585-z

[9] R.H. Hameed, Q.R. Al-Amir, H.K. Hamzah, F.H. Ali, and A. Alahmer, "Enhancing Natural Convection Heat Transfer Through Dome-Shaped Nanofluid Enclosures: Two-Phase Simulation Analysis," Heat Transfer Engineering, **46**(15), 1331-1356 (2024). https://doi.org/10.1080/01457632.2024.2378562

[10] M. Shi, Z. Duan, X. Zhao, Z. Wang, S. Liu, and H. Xue, "Experimental investigation on two-phase flow instability induced by direct contact condensation in open natural circulation," Energy, **292**, 130547 (2024). https://doi.org/10.1016/j.energy.2024.130547

[11] S. Akter, A. Hossain, M.M. Islam, and M.M. Molla, "Finite difference simulation of natural convection of two-phase hybrid nanofluid along a vertical heated wavy surface," Journal of Taibah University for Science, **18**(1), 2358548 (2024). https://doi.org/10.1080/16583655.2024.2358548
[12] N.H. Zamri, A.R.M. Kasim, M.H. Hassan, T.L. Hassan, S.M. Zokri, N.S. Arifin, and A.A. Taofeeq, "Theoretical Analysis of Two-Phase Mixed Convection Flow: Effects of Fluid-particle Interaction and Mass Concentration on Velocity, Temperature and Skin Friction. Journal of Advanced Research in Computing and Applications, **38**(1), 23-38 (2025). https://doi.org/10.37934/arca.38.1.2338
[13] S.L. Soo, *Fluid Dynamics of Multiphase Systems*, (Blaisdell Publishing co., Waltham MA, 1967)
[14] P.K. Tripathy, T. Samantara, and S. Kanungo, "Radiation effect on convective boundary layer dusty flow over a stretching surface," AIP Advances, **14**(3), 035151 (2024). https://doi.org/10.1063/5.0188957
[15] J. Mishra, T. Samantara, and P.K. Tripathy, "Effects of Electrification and Transverse Force on Dusty Flow over a Linear Stretching Sheet," CFD Letters, **16**(2), 151-161 (2024). https://doi.org/10.37934/cfdl.16.2.151161
[16] S.J. Li, L.T. Zhu, X.B. Zhang, and Z.H. Luo, "Recent advances in CFD simulations of multiphase flow processes with phase change," Industrial & Engineering Chemistry Research, **62**(28), 10729-10786 (2023). https://doi.org/10.1021/acs.iecr.3c00706
[17] X. Wu, J. Huang, Y. Zhuang, Y. Liu, J. Yang, H. Ouyang, and X. Han, "Prediction Models of Saturated Vapor Pressure, Saturated Density, Surface Tension, Viscosity and Thermal Conductivity of Electronic Fluoride Liquids in Two-Phase Liquid Immersion Cooling Systems: A Comprehensive Review," Applied Sciences, **13**(7), 4200 (2023). https://doi.org/10.3390/app13074200
[18] P. Barnoon, D. Toghraie, and S. Rostami, "Optimization of heating-cooling generators with porous components/cryogenic conductors on natural convection in a porous enclosure: Using different two-phase models and single-phase model and using different designs," International Communications in Heat and Mass Transfer, **111**, 104472 (2020). https://doi.org/10.1016/j.icheatmasstransfer.2019.104472
[19] S. Alapati, "Simulation of natural convection in a concentric hexagonal annulus using the lattice Boltzmann method combined with the smoothed profile method," Mathematics, **8**(6), 1043 (2020). https://doi.org/10.3390/math8061043
[20] O.R. Alomar, R.R. Mohammed, M.A. Mendes, S. Ray, and D. Trimis, "Numerical investigation of two-phase flow in anisotropic porous evaporator," International Journal of Thermal Sciences, **135**, 1-16 (2019). https://doi.org/10.1016/j.ijthermalsci.2018.08.026
[21] O.R. Alomar, "Analysis of variable porosity, thermal dispersion, and local thermal non-equilibrium on two-phase flow inside porous media," Applied Thermal Engineering, **154**, 263-283 (2019). https://doi.org/10.1016/j.applthermaleng.2019.03.069
[22] O.R. Alomar, M.A. Mendes, D. Trimis, and S. Ray, "Numerical simulation of complete liquid–vapour phase change process inside porous media: A comparison between local thermal equilibrium and non-equilibrium models," International journal of thermal sciences, **112**, 222-241 (2017). https://doi.org/10.1016/j.ijthermalsci.2016.09.014
[23] A.K. Rauta, "Modelling of two-phase flow over a stretching sheet with analysis of boundary layer flow and heat transfer characteristics," International Journal of Mathematics Trends and Technology-IJMTT, 41 (2017). https://doi.org/10.14445/22315373/ijmtt-v41p519
[24] A.K. Pati, and P. Jena, "Optimizing thermal performance of chemically reactive and thermally radiative nanofluid flow with convective heating and triboelectric effect of nanoparticles," Multiscale and Multidisciplinary Modeling, Experiments and Design, **8**(7), 336 (2025). https://doi.org/10.1007/s41939-025-00923-y
[25] A.K. Pati, A. Misra, and S.K. Mishra, "Thermal analysis of Ag-water nanofluid flow induced by a horizontally stretching cylinder with electrified nanoparticles," Sigma Journal of Engineering & Natural Sciences, **43**(4), (2025). https://doi.org/10.14744/sigma.2025.00111
[26] A.K. Pati, A. Misra, and S.K. Mishra, "Heat and mass transfer analysis on natural convective boundary layer flow of a Cu-water nanofluid past a vertical Flat plate with electrification of nanoparticles," Advances and Applications in Fluid Mechanics, **23**(1), 1-15 (2019). https://doi.org/10.17654/fm023010001
[27] S.S. Bishoyi, A.K. Pati, S. Mishra, A. Misra, and S.K. Mishra, "Lie group analysis of triboelectric nanoparticle influence on heat and mass transfer in buoyancy-driven nanofluid flow with multiple slip effects," Journal of Electrostatics, **139**, 104220 (2026). https://doi.org/10.1016/j.elstat.2025.104220
[28] A.K. Pati, A. Misra, and S.K. Mishra, "Effect of electrification of nanoparticles on natural convective boundary layer flow and heat transfer of a Cu-Water nanofluid past a vertical flat plate," International Journal of Engineering, Science and Mathematics, **6**(8), 1254-1264 (2017).
[29] S. Mishra, A.K. Pati, A. Misra, and S.K. Mishra, "Thermal performance of nanofluid flow along an isothermal vertical plate with velocity, thermal, and concentration slip boundary conditions employing Buongiorno's revised non-homogeneous model," East European Journal of Physics, (4), 98-106(2024). https://doi.org/10.26565/2312-4334-2024-4-09
[30] A.K. Pati, M.M. Rout, R. Sahu, I.S. Ramakoti, K.K. Panda, and K.C. Sethi, "Chemical reaction, electrification, Brownian motion and thermophoresis effects of copper nanoparticles on nanofluid flow with skin friction, heat and mass transfer," East European Journal of Physics, (4), 152-158 (2024). https://doi.org/10.26565/2312-4334-2024-4-14
[31] B. Otterman, "Particle migrations in laminar mixing of a suspension with a clear fluid", ZAMP, 20, 730-749 (1969). https://doi.org/10.1007/bf01590631
[32] A. Misra, S.K. Mishra, and J. Prakash, "Modeling electrification of suspended particulate matter (SPM) in a two-phase laminar boundary layer flow and heat transfer over a semi-infinite flat plate," Int. Commun. Heat Mass Transf. **38**(8), 1110-1118 (2011). https://doi.org/10.1016/j.icheatmasstransfer.2011.05.015
[33] S.K. Mishra and P.K. Tripathy, "Mathematical and Numerical modeling of two-phase flow and heat transfer using non-uniform grid", Far East journal of Applied Mathematics, **54**(2), 107-126 (2011).
[34] L.F. Shampine, and J. Kierzenka, "A BVP Solver based on residual control and the MATLAB PSE," ACM Trans. Math. Softw. **27**(3), 299-316 (2001). https://doi.org/10.1145/502800.502801

АНАЛІЗ МЕТОДОМ СКІНЧЕННИХ РІЗНИЦЬ ВПЛИВУ ЧИСЛА ПРАНДТЛЯ ТА ОБ'ЄМНОЇ ЧАСТКИ ЧАСТИНОК НА ТЕРТЯ ПО ПОВЕРХНІ ТА ПЕРЕНОС ТЕПЛА У ДВОФАЗНОМУ ПОТОЦІ, ОБУМОВЛЕНОМУ ПЛАВУЧІСТЮ, ЗІ ЗВАЖЕНИМИ ЧАСТИНКАМИ (SPM)

Сасанка Сехар Бішоїї[1], Сакамбарі Мішра[2], Адітья Кумар Паті[3]*, Прасанта Кумар Рат[3]

[1]Університет NIST, Берхампур, Ганджам, Одіша, Індія

2Коледж фундаментальних наук та гуманітарних наук, Університет сільського господарства та технологій Одіші, Бхубанешвар, Одіша, Індія

[3]Університет технологій та менеджменту Центуріон, Паралакхемунді, Одіша, Індія

Було проведено числове дослідження нестисливого, ламінарного двофазного потоку, що залежать від плавучості, що містить зважені частинки навколо вертикальної пластини. Незважаючи на актуальність таких систем, попередні дослідження значною мірою ігнорували природні конвекційні двофазні потоки з твердими частинками, особливо щодо ролі таких параметрів, як число Прандтля та об'ємна частка. Заповнення цієї прогалини в дослідженнях є критично важливим, оскільки ці параметри суттєво впливають на поведінку потоку та теплопередачу, які є життєво важливими в екологічних, промислових та теплових застосуваннях. Це дослідження зосереджено на вивченні впливу об'ємної частки та числа Прандтля на характеристики двофазного потоку за допомогою неявного методу скінченних різниць, застосованого до неоднорідної сітки. Аналіз оцінює поведінку прикордонного шару, швидкість теплопередачі та коефіцієнти тертя поверхневого шару. Картини ліній струму проілюстровано для різних значень числа Прандтля, тоді як контурні топології представлені для демонстрації комбінованого впливу числа Прандтля та об'ємної частки на тертя поверхневого шару та швидкість теплопередачі. Результати показують, що збільшення об'ємної частки зменшує як число Нуссельта, так і коефіцієнт тертя поверхневого шару, тоді як вище число Прандтля посилює обидва. Покращена теплова реакція, що спостерігається при вищих числах Прандтля, особливо корисна у виробничих процесах, що включають плоскі стінкоподібні структури, схильні до термічних напружень. Ці висновки мають практичне значення для проектування та оптимізації теплообмінників, систем змащення та рішень для терморегулювання в електронних пристроях.

Ключові слова: *теплопередача; потік, зумовлений плавучістю; число Прандтля; об'ємна частка частинок; зважені тверді частинки; неявний метод скінченних різниць*

East European Journal of Physics. 1. 460-472 (2026)
DOI:10.26565/2312-4334-2026-1-53 ISSN 2312-4334

A STUDY ON THERMO-VISCOUS STEADY FLUID MOTION THROUGH A MOVING RECTANGULAR FLAT PLATE-A NUMERICAL APPROACH

N. Pothanna[1], P. Raja Shekar[1]*, Jyotsna Cherukuri[2], L. Srinivasa Rao[3], Adigoppula Raju[4], Devunuri Suresh[5]

[1]*Department of Mathematics, VNR Vignana Jyothi Institute of Engineering and Technology, Hyderabad, Telangana, India-500090*
[2]*Department of Chemistry, VNR Vignana Jyothi Institute of Engineering and Technology, Hyderabad, Telangana, India-500090*
[3]*Centre for Nanoscience and Technology, Department of Physics, VNR Vignana Jyothi Institute of Engineering and Technology, Bachupally, HYD., TG, India -500 090*
[4]*Department of Applied Sciences, Symbiosis Institute of Technology, Symbiosis International (Deemed University), Pune-412115, India*
[5]*Department of Automobile Engineering, VNR Vignana Jyothi Institute of Engineering and Technology, Hyderabad, Telangana, India-500090*
**Corresponding author E-mail: rajoct25@gmail.com*
Received November 19, 2025; revised December 25, 2025; accepted January 21, 2026

This study presents a novel numerical approach for analysis on thermo-viscous steady fluid motion through a moving rectangular flat plate. The numerical results have been found employing the Runge-Kutta method of order 6 shooting techniques developed in *Mathematica* software. Numerical differentiation (ND) solves for the flow-adaptable equations comprising temperature and velocity. The flow behavior and the impacts of material constraints on the flow region for governed equations have been analyzed and deliberated, taking the help from the generated graphs. The nonlinear coupled Partial differential equations (PDE's) in terms of temperature and velocity, subject to the corresponding boundary conditions, control the fluid motion. The numerical computations of Runge-Kutta(R-K) 6^{th} order results are presented in form of tables and also represented for numerous thermophysical coefficient values. The variations of these flow fields have been studied for wide spectrum of physical characteristics which influences the nature of thermo-viscous fluid. The impact of suction/injection parameter, dimensionless viscosity factor, constant pressure and temperature gradients, thermophysical factors and the Prandtl parameter effect on flow region have explored using graphical illustrations with the wide range of values. The Explicit numerical calculations also been calculated and results are associated through the current outcomes in the literature. To improve heat transfer rates in systems such as heat exchangers and aerospace components, engineers can optimize surface textures and flow conditions by taking coefficients effects on flow considerations into account.
Keywords: *Thermo-viscous fluid; ND Solve; R-K 6^{th} order Method; Permeability; Thermal Conductivity*
PACS: 02.30. Hq, 02.30.Jr, 02.60.Cb, 02.60.Lj

Nomenclature

$\alpha_1 = -p$	Pressure of Fluid	d_{ij}	Deformation rate tensor
$\alpha_3 = 2\mu$	Viscosity Coefficient	b_{ij}	Thermal gradient bi-vector
$\alpha_5 = 4\mu_c$	Cross model viscosity parameter	t_{ji}	Stress tensor
α_6	Thermo interaction stress coefficient	h	Thermo bi-gradient of vector
α_8	Thermal viscosity stress parameter	T	Temperature (non-dimensional)
$\beta_1 = k$	Fourier and thermal conductivity Coefficient	U	Dimensionless velocity
β_3	Thermal strain factor of conductivity	V	Dimensionless injection/ suction parameter
a_6	Thermal interaction stress factor (non-dimensional)	C_1	Pressure gradient that is constant
b_3	Thermal strain coefficient of conductivity(non-dimensional)	C_2	Temperature gradient that is constant
v_o	Injection/suction parameter		**Greek Symbols**
p_r	Prandtl number	ρ	Fluid Density
c	Specific heat	γ	External Source energy per unit mass
f_i	i^{th} component of external force per unit mass	η	Temperature of a Fluid
q_i	i^{th} component of heat flux bi-vector	α_i's	Coefficient of viscosity
u_i	i^{th} velocity component	β_i's	Coefficient of thermal conductivity

1. INTRODUCTION

The features of non-Newtonian fluid have been a subject of substantial investigation for centuries. However, it is only during the last six to seven decenniums particularly since the second world war time, the significant research efforts have been undertaken to expand these evaluates into the non-linearity domain. The non-linear thermo-viscoelasticity

Cite as: N. Pothanna, P.R. Shekar, C. Jyotsna, L.S. Rao, A. Raju, D. Suresh, East Eur. J. Phys. 1, 460 (2026), https://doi.org/10.26565/2312-4334-2026-1-53

fundamentals were considered by Koh and Eringen [1]. Yamamoto et al. [2] investigated convective acceleration in flow through a porous wall. Conditions near a naturally porous wall's boundaries were considered by Beavers et al. [3]. In thermodynamics, the existence of caloric equations of state was examined by Coleman et al. [4]. A few incompressible viscometric flows of thermo viscous fluids were described by Kelly [5]. A thermo-viscous fluid of second-order flowing steadily across an endless plate was examined by Rao et al. [6]. Unsteady thermo viscous movement over a staggering horizontal plate in a permeable slab was investigated by Pothanna and Aparna [7]. In this work they demonstrated the analytical expressions and solutions for the governed flow equations. The effect of heat production during flow of nanofluids across a shrieking sheet was inspected by Jithender Reddy et al. [8]. Thermo-viscous liquid movement in a permeable wedge enclosed by the comparative mobility of two impermeable extending equal plates was examined by Pothanna et al. [9]: four-stage algorithmic methodology. Employing this methodology, the external forces applied and internal energy sources generated have been calculated in this work. Considering a viscous effect, chemical response, and Soret-Dufour constraints, Kumar et al. [10] examined the behavior of heat-mass transfer in a 2-D forchheimer permeable region on casson mhd fluid flow across a disposed non-linear surface. Pothanna [11] used an analytical and numerical method to study an unsteady fluid flow around an oscillating sphere. The casson mhd nanofluid and the impact of thermal radiation with the presence of chemical reaction on the flow over a non-linear elongating sheet was described by Shekar et al. [12]. Using artificial neural networks, Pothanna et al. [13] investigated instable thermo viscid liquid transport among two indefinitely stretched impervious straight plates. This work compares to other literature works related to the flow between parallel plates is analyzed deeply with the statistical analysis on the required flow fields with the data-driven neural networks approach. Nalimela et al. [14] used artificial neural network techniques to forecast and assess an instable liquid flow over a horizontal oscillating plate in an absorbent slab. The radially inflow and outflow of a viscous hydromagnetic fluid concerning two narrow flat disks were investigated by Naeem et al. [15]. The entropy creation in heated joule radiation viscous fluid flow over a permeable radially extending disk was investigated numerically by Tahir et al. [16]. The mhd electronic effect on Darrcy-Forchheimer fluid flow on a stretchy surface was investigated by Zeeshan et al. [17] using an integrated intelligent neuro-evolutionary computing technique. The incompressible viscous fluid flow determined by a pressure differential in a specific channel was examined by Hranislav et al. [18]. The heat-mass transfer case study for a viscous fluid flow in a double layer caused by ciliate channel was completed by Nahid et al. [19]. The influence of blowing or suction on the temperature distribution and flow velocity across a flat plate is observed by Ahmed et al. [20]. The effects of chemical reactions and diffusion on heat transmission in casson nano-fluid flowing across a plane plate with accretion were investigated by Jayaprakash et al. [21]. The compressible mhd flow on plane plate boundary layer flow with somewhat exclusive effects was investigated by Shunhao et al. [22]. The use of a multi-test technique to simultaneously determine the adiabatic temperature near the wall and heat transfer effect in a shock channel for transonic flow across a flat plate was described by Wei et al. [23]. The Buongiorno nano fluid model's numerical calculations for the viscoelastic boundary layer flow of a towards a non-linear extending sheet were completed by Sohail et al. [24]. The study of magnetic fields and temperature radiation on dusty tangent hyperbolic fluid flow on an elongating sheet with a high prandtl number were investigated by Ali et al. [25]. The effects of Newtonian heating and slip conditions on mhd flow of a casson fluid across a nonlinearly stretching sheet saturated in a porous media were examined by Imran et al. [26]. In mhd casson fluid flow via a wavering vertical plate absorbed in a porous region with ramping wall temperature, Hari et al. [27] described heat-mass transfer. The impact of a heat cause and chemical response on the dissipative mhd mixed convection flow of a casson nano fluid across a non-linear permeable stretch sheet was examined by Ibrahim et al. [28]. The maxwell fluid through an infinite plate was explored with a novel exact solution by Fetecau et al. [29]. Dholey [30] investigated the first Stokes issue, which is flow caused by an infinite flat plate that abruptly starts moving in a viscoelastic fluid.

The thermo-viscous incompressible flows typically satisfy the succeeding governing equations:

Continuity equation formula: $v_{i,i} = 0$

Momentum equation formula:

$$\rho\left[\frac{\partial \mathrm{v_i}}{\partial \mathrm{t}} + \mathrm{v_k v_{i,k}}\right] = \rho \mathrm{f_i} + \mathrm{t_{ji,j}}$$

and the energy calculation formula:

$$\rho c\dot{\theta} = t_{ij} d_{ij} - q_{i,i} + \rho\gamma$$

where $\mathrm{f_k}$ is external forces per mass unit (k^{th} Component), t_{ij} is the stress component tensor and d_{ij} is components rate deformation tensor.

A fluid that is viscous in a thermal state, known as a thermo-viscous fluid, is defined by a pair of equations that constitute: one for heat and another for stress. The kinematic tensor's polynomial functions are the heat flux bi-vector (h) and stress tensor (t), which also includes deformation rate of tensor d, thermo bi-gradient of vector b, density ρ and the temperature θ

$$b \equiv \|b_{ij}\| \equiv \|\varepsilon_{ijk}\, \theta_{,k}\|$$

$$h \equiv \|h_{ij}\| \equiv \|\varepsilon_{ijk}\, q_{,k}\|$$

where ε_{ijk} illustrating the sign for permutation.

Stated differently, for thermo-viscous liquids,

$$\overrightarrow{t} = \overrightarrow{t}(d, b, \rho, \theta), \text{ and } \overrightarrow{h} = \overrightarrow{h}(d, b, \rho, \theta)$$

The mechanical equivalences for the heat flux bivector and stress tensor provided by Koh and Eringen [1] are

$$t = \alpha_1 I + \alpha_3 d + \alpha_5 d^2 + \alpha_6 b^2 + \alpha_8 (db - bd) + \alpha_{12} (db^2 - b^2 d) + \alpha_{15} (bd^2 - d^2 b) + \alpha_{17}(d^2 b^2 - b^2 d^2) + \alpha_{20}(dbd^2 - d^2 bd) + \alpha_{22}(bdb^2 - b^2 db) + \alpha_{24}(bd^2 b^2 - b^2 d^2 b)$$

and

$$h = \beta_1 b + \beta_3(bd + db) + \beta_6(db^2 - b^2 d) + \beta_9(bd^2 + d^2 b) + \beta_{12}(d^2 b^2 - b^2 d^2) + \beta_{19}(db^2 d^2 - d^2 b^2 d)$$

the constitutive coefficient $\alpha_i^{'s}$ and $\beta_i^{'s}$. These polynomials in the d and b invariants along these lines:

$$tr\, d\,, tr\, d^2, tr\, d^3, tr\, b^2$$

$$tr\, db^2, tr\, d^2 b^2, tr\, bdb^2 d^2$$

with coefficients depending on ρ and θ only.

The combined degree is N+P where N and P represent the maximum of the degrees of d and b in the aforementioned fundamental formulas.

In this illustration, Max |N+P|=2. The constitutive fundamental formulas are therefore joined in d and b as

$$t = \alpha_1 I + \alpha_3 d + \alpha_5 d^2 + \alpha_6 b^2 + \alpha_8 (db - bd)$$

and

$$h = \beta_1 b + \beta_3(bd + db)$$

with the deformation rate tensor: $d_{ij} = (u_{i,j} + u_{j,i})/2$ and bivector gradient 'b': $b_{ij} = \in_{ijk} \theta_k$

where u_i is the i^{th} fluid's velocity component and θ is the fluids temperature.

The constants α_i and β_i are polynomial expressions in terms of d and b are coefficients that are entirely be contingent on θ and ρ. The constants such as α_1 and α_3 can be determined as pressure of fluid and viscosity constant coefficient correspondingly and α_5 is the cross-viscosity coefficient. The expressions for the constitutional coefficients $\alpha_i^{'s}$ and $\beta_i^{'s}$ in the second order concept can be attained as

$$\alpha_1 = \alpha_{1000} + \alpha_{1010} tr\, d + \alpha_{1020} tr\, d^2 + \alpha_{1002}\, tr\, b^2\,, \alpha_3 = \alpha_{3010} + \alpha_{3020} tr\, d,$$

$$\alpha_5 = \alpha_{5020}\,, \alpha_6 = \alpha_{6002}\,, \alpha_8 = \alpha_{8011}\,, \beta_1 = \beta_{1001} + \beta_{1011} tr\, d \text{ and } \beta_3 = \beta_{1011}$$

the second order coefficients α_{isrt} and β_{isrt} are functions in terms of ρ and η.

In this work, the properties of different material characteristics on the thermo-viscous steady flow fields of a fluid through a horizontal moving flat plate are attempted to be studied. The current study was greatly helpful to the scientist and researchers to resolve their engineering and research study problems. The last several years have seen a huge increase in interest in the investigation of the flow features of these formations due to the vast range of applications.

1.1 Novelty and Research gap

This study investigates a novel numerical approach for analysis on thermo-viscous steady fluid motion through a moving rectangular flat plate for application of non-Newtonian fluids in aerospace engineering. Analysis has been done on the effects of different thermo-viscous characteristics with the development of ND solve developed algorithms. These fluids were the subject of earlier attempts in the literature, but the non-linear nature of the studies they included was not taken into consideration. The non-linear fluid behavior with various impacts have been studied and analyzed with the development of this algorithm. This present work developed to study the non-linear nature of the fluid using Mathematica software ND solve. The literature has not yet addressed this present work.

2. MATHEMATICAL MODELING

Consider the thermo-viscous steady fluid flow through permeable stretched infinite plate bounded in a impermeable medium as shown in Fig. (1). A study is conducted on the movement of the plate in the flow direction, moving at a specific velocity u_0. In the system of coordinates O(XYZ), the plates can be denoted by $y = 0$ and $y = \infty$. The points on x-axis are in the plate movement direction, the y-axis is vertical to the plates, and the origin is on the fixed plate. Further, a constant temperature of θ_0 and θ_1 is maintained accordingly.

Consider the fluid velocity $[u(y), v_0, 0]$ also fluid temperature θ(y) define the steady constant motion through a moving flat plate. The continuity calculation is fulfilled with this velocity choice.
The fundamental equations that describe the flow as follows:
along the X-direction:

$$\rho v_0 \frac{\partial u}{\partial y} = -\frac{\partial p}{\partial x} + \mu \frac{\partial^2 u}{\partial y^2} - \alpha_6 \frac{\partial \theta}{\partial x}\frac{\partial^2 \theta}{\partial y^2} + \rho F_x \tag{1}$$

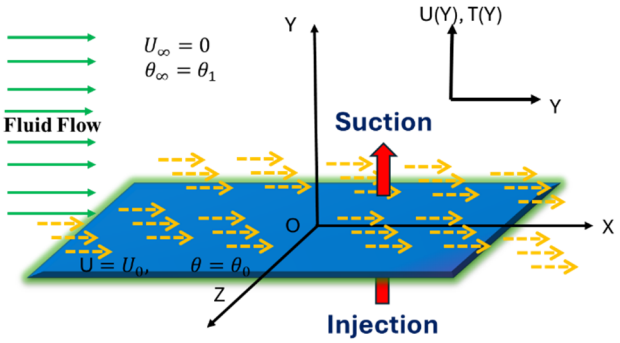

Figure 1. Flow Configuration

The fluid in the x-direction by the rate of change of fluid velocity with effect of plate suction/injection is represented by the term $\rho v_0 \frac{\partial u}{\partial y}$. The fluid is pushed in the x-direction by the rate of change of fluid pressure, with regard to the term $\frac{\partial p}{\partial x}$. Momentum diffusion caused by viscosity is represented by the viscous term $\mu \frac{\partial^2 u}{\partial y^2}$. Because of the internal resistance that shifts momentum from high to low regions, this attempts to smooth out velocity gradients. Boundary-layer growth, flow separation, vortex formation, and shock boundary layer interaction on wings are all governed by changes in temperature, which are represented by the second order nonlinear convective acceleration term ($\alpha_6 \frac{\partial \theta}{\partial x}\frac{\partial^2 \theta}{\partial y^2}$).

Along the Y-direction:

$$0 = \mu_c \frac{\partial}{\partial y}\left(\frac{\partial u}{\partial y}\right)^2 + \rho F_y \tag{2}$$

Along Z- direction:

$$0 = \alpha_8 \frac{\partial}{\partial y}\left(\frac{\partial \theta}{\partial y}\frac{\partial u}{\partial y}\right) + \rho F_z \tag{3}$$

and energy equation is

$$\rho c\left(u\frac{\partial \theta}{\partial x} + v_0 \frac{\partial \theta}{\partial y}\right) = \mu\left(\frac{\partial u}{\partial y}\right)^2 - \alpha_6 \frac{\partial \theta}{\partial x}\frac{\partial u}{\partial y}\frac{\partial \theta}{\partial y} + k\frac{\partial^2 \theta}{\partial y^2} + \beta_3 \frac{\partial \theta}{\partial x}\frac{\partial^2 u}{\partial y^2} + \rho\gamma \tag{4}$$

The convective expression $\rho c\left(u\frac{\partial \theta}{\partial x} + v_0 \frac{\partial \theta}{\partial y}\right)$ illustrates how heat is transported by a flowing fluid. The thermal conduction through the fluid is given by the conductive term $k\frac{\partial^2 \theta}{\partial y^2}$. The internal heat generation resulting from fluid friction is represented by the viscous dissipation term $\mu\left(\frac{\partial u}{\partial y}\right)^2$. The effects of thermal conductivity(β_3) and thermo-viscosity(α_6) on fluid flow are caused by the terms $\beta_3 \frac{\partial \theta}{\partial x}\frac{\partial^2 u}{\partial y^2}$ and $\alpha_6 \frac{\partial \theta}{\partial x}\frac{\partial u}{\partial y}\frac{\partial \theta}{\partial y}$ respectively.

In high-speed or high-shear regions, the second-order nonlinearities become significant because they couple velocity and temperature through viscous dissipation, thermal conductivity, and thermo viscosity factors. Accurate modeling of these nonlinear terms is crucial for predicting performance, guaranteeing structural integrity, and optimizing wing shapes in transonic and supersonic regimes because they dictate how aerodynamic heating, temperature gradients, and compressibility effects interact with the flow field for aircraft wings, influencing lift, drag, thermal loads, and material limits.

The boundary limitations assumed are:

$u = u_0$, $\theta = \theta_0$ at $y = 0$

and

$$u = 0, \theta = \theta_1 \text{ at } y = \infty \tag{5}$$

It is assumed that the plate velocity is constant. There are many real-world and useful uses for this in the field of aerospace engineering. This condition often applies at the wing surfaces to evaluate air flow over wings, which is crucial

for aircraft design in order to efficiently forecast flow behavior. Shear stress and viscosity-related energy losses in turbine and compressor jet engines are predicted by this condition. The boundary conditions for temperature are considered to be constants. These boundary conditions are essential for simulating conduction, convection, and radiation because they specify how temperature changes at the fluid-surface contact.

The dimensionless quantities were introduced as follows:

$$y = hY\ ,\ u = \frac{\mu}{\rho h}U\ ,\ u_0 = (\frac{\mu}{\rho h})\ U_0,\ T = \frac{\theta-\theta_0}{\theta_1-\theta_0}\ ,\ \frac{\partial\theta}{\partial x} = \frac{\theta_1-\theta_0}{h}C_2,\ \frac{\partial p}{\partial x} = \frac{\mu^2}{\rho h^3}C_1,\ p_r = \frac{\mu c}{k},\ b_3 = \frac{\beta_3}{\rho h^2 c}\ ,\ a_6 = \frac{\alpha_6\rho(\theta_1-\theta_0)^2}{\mu^2}$$

and $V = \frac{v_0\rho h}{\mu}$

where C_1 and C_2 are dimensionless pressure and temperature gradients respectively. V is the injection/ suction parameter.

When the pressure gradient, outside forces, and internal energy source are removed, the aforementioned non-dimensional quantities can be used to reduce equations (1) and (4) to

$$V\frac{dU}{dY} = -C_1 + \frac{d^2U}{dY^2} - a_6C_2\frac{d^2T}{dY^2} \tag{6}$$

$$UC_2 + V\frac{dT}{dY} = a_1\left[\left(\frac{dU}{dY}\right)^2 - A_6C_2\frac{dU}{dY}\frac{dT}{dY}\right] + b_3C_2\frac{d^2U}{dY^2} + \frac{1}{p_r}\frac{d^2T}{dY^2} \tag{7}$$

in addition to the boundary limitations:

$$U(0) = 1\ ,T(0) = 0 \tag{8}$$

and

$$U(\infty) = 0\ ,T(\infty) = 1 \tag{9}$$

3. NUMERICAL SCHEME

The second order linear ordinary differential equations (6 and 7) which have been obtained are coupled with velocity and temperature fields. The solutions of differential equations governed by the equations (6 and 7) by employing the b. c's (8 and 9) for velocity and temperature were measured using the MATHEMATICA ND solver tool package via. shooting technique with 6th order R-K methods and its solution flow chart is presented in Fig. 2. Following the introduction of dimensional-less quantities into the fluid equations, the infinite distance from the plate is represented by the units "h" for temperature and velocity (i.e., y→h) has been reduced to a finite value of 10. The solution's convergence was confirmed to meet the problem's boundary circumstances. Tables and illustrations have been used to display the impact of diverse material constants for the velocity and temperature of the fluid, including the suction/injection(V), coefficient of thermal interaction stress coefficient(a_6), thermal strain coefficient of conductivity (b_3), cross viscosity parameter (μ_c) , Prandtl parameter(p_r), non dimensional viscosity (a_1), specific heat (c), density (ρ), constant pressure gradient (C_1) and constant temperature gradient (C_2).

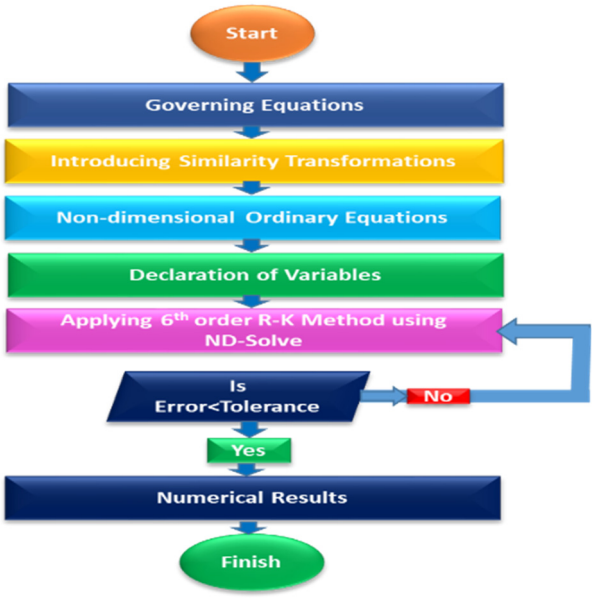

Figure 2. Flow Chart

3.1. Tables

The numerical outcomes related with the several substantial properties are shown in table.1 and table.2 and deliver the governing equations' explanations of fluid ascribed in temperature also velocity fields. The MATHEMATICA ND solver tool has yielded the numerical results of the equations that govern (6) and (7) with regard to the b.c.'s (8–9).

Table 1. Numerical computations for the velocity $U(Y)$ and temperature $T(Y)$ for V

Y	$U(Y)$ $a_6 = 0.01, b_3 = 0.10, C_1 = 0.2, C_2 = 0.2, a_1 = 0.1, p_r = 0.77$				$T(Y)$ $a_6 = 0.01, b_3 = 0.10, C_1 = 0.2, C_2 = 0.2\ a_1 = 0.1, p_r = 0.77$			
	V=0.10	V=0.25	V=0.50	V=0.75	V=0.10	V=0.25	V=0.50	V=0.75
0.00	1.00000	1.00000	1.00000	1.00000	0.00000	0.00000	0.00000	0.00000
1.00	0.16455	0.16537	0.1719	0.18216	1.05873	1.26153	2.25314	3.18553
2.00	-0.54864	-0.54699	-0.53375	-0.51286	2.01654	2.4126	4.35037	6.17665
3.00	-1.12689	-1.1245	-1.10532	-1.07494	2.7891	3.34351	6.05701	8.61842
4.00	-1.55611	-1.55319	-1.52961	-1.49213	3.31694	3.97622	7.20413	10.25492
5.00	-1.82073	-1.81753	-1.79165	-1.75046	3.56478	4.26379	7.68744	10.92698
6.00	-1.90345	-1.90028	-1.87462	-1.83373	3.52108	4.18983	7.46673	10.57118
7.00	-1.78512	-1.7823	-1.75955	-1.72326	3.19746	3.76812	6.56592	9.22002
8.00	-1.44451	-1.44238	-1.42515	-1.39767	2.62823	3.04228	5.07363	7.0035
9.00	-0.85814	-0.85697	-0.84755	-0.83253	1.86981	2.08546	3.14432	4.15189
10.0	0.00000	0.00000	0.00000	0.00000	1.00000	1.00000	1.00000	1.00000

Table 2. Numerical computations for the velocity $U(Y)$ and temperature $T(Y)$ for C_1

Y	$U(Y)$ $a_6 = 0.01, b_3 = 0.10, V = 0.25, C_2 = 0.2, a_1 = 0.1, p_r = 0.77$				$T(Y)$ $a_6 = 0.01, b_3 = 0.10, V = 0.25, C_2 = 0.2, a_1 = 0.1, p_r = 0.77$			
	C1=0.10	C1=0.30	C1=0.50	C1=0.70	C1=0.10	C1=0.30	C1=0.50	C1=0.70
0.00	1.00000	1.00000	1.00000	1.00000	0.00000	0.00000	0.00000	0.00000
1.00	0.67627	0.67629	0.67612	0.67575	0.23401	0.24724	0.25737	0.26278
2.00	0.37421	0.37456	0.37491	0.37523	0.46711	0.58511	0.69733	0.80071
3.00	0.09993	0.10079	0.10205	0.10364	0.67938	0.93542	1.18349	1.41936
4.00	-0.13867	-0.13728	-0.13502	-0.13197	0.85647	1.23978	1.61362	1.97292
5.00	-0.33148	-0.32965	-0.32653	-0.32221	0.98924	1.45772	1.91614	2.35907
6.00	-0.4655	-0.46342	-0.45979	-0.4547	1.07335	1.56549	2.04804	2.51576
7.00	-0.52403	-0.52197	-0.51834	-0.51321	1.1092	1.55568	1.99408	2.41995
8.00	-0.48562	-0.48392	-0.48089	-0.47661	1.10182	1.43739	1.76726	2.08826
9.00	-0.32274	-0.32173	-0.31995	-0.31742	1.06079	1.23709	1.41057	1.57961
10.0	0.00000	0.00000	0.00000	0.00000	1.00000	1.00000	1.00000	1.00000

4. COMPARISON OF PRESENT RESULTS WITH EXISTING SOLUTIONS

The second order linear ordinary differential equations (6 and 7) which have been obtained are coupled with velocity and temperature fields. The results of differential equations governed by the equations (6 and 7) by employing the b. c's (8 and 9) for velocity and temperature were measured using the MATHEMATICA ND solver tool package via. shooting technique with 6th order R-K methods. The solution's convergence was confirmed to meet the problem's boundary circumstances. Tables and illustrations have been used to display the impact of diverse material constants for the velocity and temperature of the fluid.

4.1 Tables

Table 3. Comparison of velocity $U(Y)$ and temperature $T(Y)$ results for b_3

Y	$U(Y)$ $V = 0, a_6 = 0.01, C_1 = 0.2, C_2 = 0.2, a_1 = 0.1, p_r = 0.77$				$T(Y)$ $V = 0, a_6 = 0.01, C_1 = 0.2, C_2 = 0.2, a_1 = 0.1, p_r = 0.77$			
	Present Results		Results of P. N. Rao *et al.* [6]		Present Results		Results of P. N. Rao *et al.* [6]	
	b3=0.10	b3=0.10	b3=0.10	b3=0.10	b3=0.10	b3=0.10	b3=0.10	b3=0.10
0.00	1.00000	1.00000	1.00000	1.00000	0.00000	0.00000	0.00000	0.00000
1.00	0.45014	0.45017	0.45011	0.45016	0.23518	0.26635	0.23520	0.26634
2.00	0.00029	0.00034	0.00020	0.00033	0.48544	0.54084	0.48545	0.54083
3.00	-0.34958	-0.3495	-0.34953	-0.34950	0.72307	0.79577	0.72300	0.79578
4.00	-0.59947	-0.59939	-0.59942	-0.59940	0.92656	1.00963	0.92655	1.00964
5.00	-0.74942	-0.74933	-0.74941	-0.74934	1.08052	1.16705	1.08049	1.16700
6.00	-0.79942	-0.79934	-0.79944	-0.79933	1.17574	1.2588	1.17575	1.25870

7.00	-0.74949	-0.74942	-0.74950	-0.74944	1.20914	1.28183	1.20913	1.28184
8.00	-0.59962	-0.59956	-0.59959	-0.59957	1.18381	1.2392	1.18379	1.23919
9.00	-0.34979	-0.34976	-0.34981	-0.34975	1.10897	1.14013	1.10900	1.14014
10.0	0.00000	0.00000	0.00000	0.00000	1.00000	1.00000	1.00000	1.00000

Table 4. Comparison of velocity $U(Y)$ and temperature $T(Y)$ results for a_6

Y	$U(Y)$				$T(Y)$			
	$V=0, b_3=0.10, C_1=0.2, C_2=0.2, a_1=0.1, p_r=0.77$				$V=0, b_3=0.10, C_1=0.2, C_2=0.2, a_1=0.1, p_r=0.77$			
	Present Results		Results of P.N. Rao *et al.* [6]		Present Results		Results of P.N. Rao *et al.* [6]	
	a6=0.01	a6=0.05	a6=0.01	a6=0.05	a6=0.01	a6=0.05	a6=0.01	a6=0.05
0.00	1.00000	1.00000	1.00000	1.00000	0.00000	0.00000	0.00000	0.00000
1.00	0.45014	0.45015	0.45015	0.45016	0.23518	0.23520	0.23519	0.23519
2.00	0.00029	0.00030	0.00030	0.00029	0.48544	0.48539	0.48545	0.48543
3.00	-0.34958	-0.34959	-0.34960	-0.34950	0.72307	0.72306	0.72308	0.72300
4.00	-0.59947	-0.59944	-0.59948	-0.59948	0.92656	0.92661	0.92659	0.92658
5.00	-0.74942	-0.74943	-0.74945	-0.74941	1.08052	1.08060	1.08060	1.08058
6.00	-0.79942	-0.79940	-0.79944	-0.79942	1.17574	1.17577	1.17579	1.17576
7.00	-0.74949	-0.74950	-0.74950	-0.74951	1.20914	1.20915	1.20918	1.20918
8.00	-0.59962	-0.59957	-0.59961	-0.59962	1.18381	1.18379	1.18380	1.18383
9.00	-0.34979	-0.34978	-0.34980	-0.34981	1.10897	1.10899	1.10898	1.10890
10.0	0.00000	0.00000	0.00000	0.00000	1.00000	1.00000	1.00000	1.00000

5. DISCUSSION ON RESULTS

The numerically obtained computations using ND solve developed in MATHEMATICA software are graphically depicted in Figs. 3–12. The problem's physical perception was seen by examining the velocity$(U(Y))$ and temperature$(T(Y))$ field results, which were acquired by assigning various values to various physical factors such suction/injection(V), coefficient of thermal interaction stress coefficient(a_6), thermal strain coefficient of conductivity (b_3), cross viscosity parameter (μ_c), Prandtl parameter(p_r), non dimensional viscosity (a_1), specific heat (c), density (ρ), constant pressure gradient (C_1) and constant temperature gradient (C_2) which characterize the flow occurrence. Graphical illustrations have been produced to show the impact of each of these coefficients on the temperature and velocity fields.

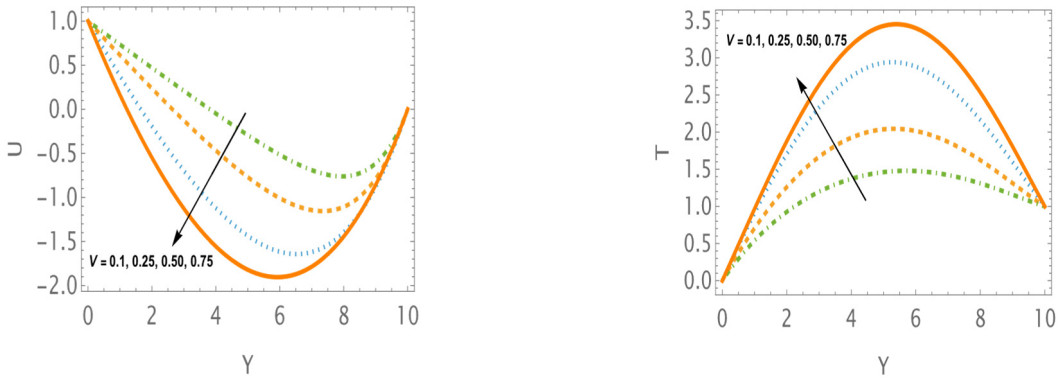

(a) (b)

Figure 3. (a) Velocity (b) Temperature contours for V with $a_6 = 0.01$ and $b_3 = 0.1$

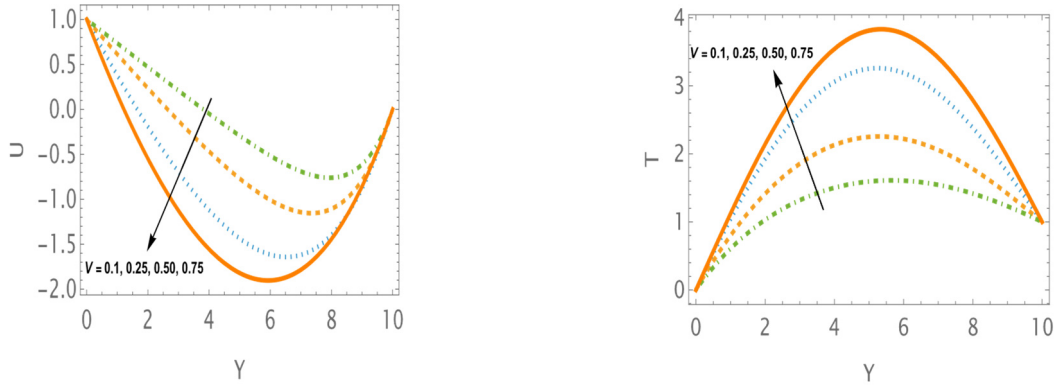

(a) (b)

Figure 4. (a) Velocity (b) Temperature contours for V with $a_6 = 0.05$ and $b_3 = 1$

In Figs. (3), (4) and (5), the variations in both $U(Y)$ and $T(Y)$ have been studied with the impact of suction/injunction parameter. The $U(Y)$ profiles are shown to decrease up to the center channel, after which they alternately decrease till the infinite distance. However, for the temperature profiles, the opposite effect has been noted. Fig. (3a and 3b) depicts the variations of $U(Y)$ besides $T(Y)$ thru the very small amount of a_6 and b_3. Fig. (4a and 4b) depicts the variations of $U(Y)$ in addition $T(Y)$ by the small rates of a_6 and b_3. Fig. (5a and 5b) depicts the variations of $U(Y)$ and $T(Y)$ with the very big values of a_6 and $T(Y)$. It is identified from the Figs. (3a 4a and 5a) that , the $U(Y)$ variations decreases as the values of V increases but as the values of b_3 increases from very small values to very large values ($i.e.0.1\ to\ 10$) there is no much variations is observed among the $U(Y)$ profiles. This effect of variation can also be observed in the Fig.(6(a)) It is depicted from the Figs. (3b, 4b and 5b) that, the $T(Y)$ variations increase as the values of V increases. For small values of b_3, the $T(Y)$ variations increase at the small rate and very large values of b_3 $T(Y)$ variations increase at the faster rate.

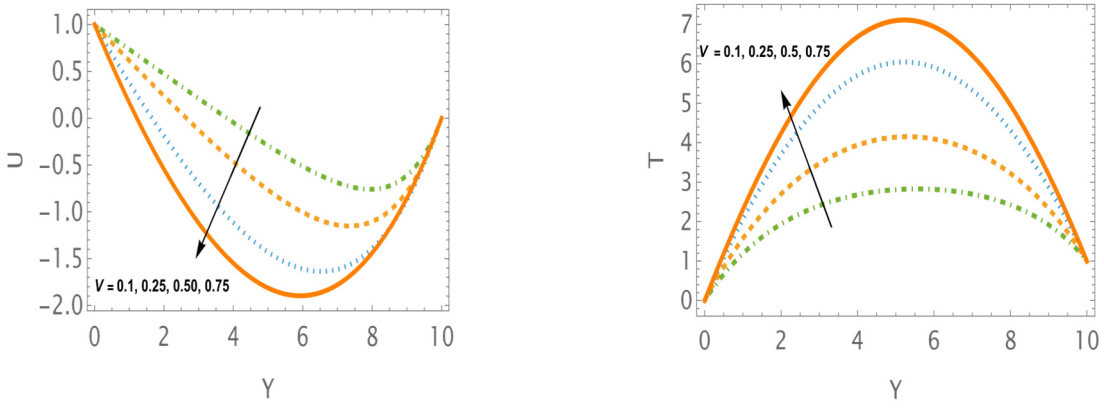

(a) (b)

Figure 5. (a) Velocity (b) Temperature contours for V with $a_6 = 0.10$ and $b_3 = 10$

The variation of $U(Y)$ also $T(Y)$ profiles in relation to b_3 effect is observed in the Figs. (6(a) and 6(b)). In Fig. 6(a), it is observed that all the $U(Y)$ profiles are coinciding. In Fig. 6(b), it is noticed that, the temperature, as the fluid move away from the plate is increasing at the faster rate up to certain distance and suddenly takes the turn and decreases to take the max. assumed temperature at the infinite distance from the plate boundary.

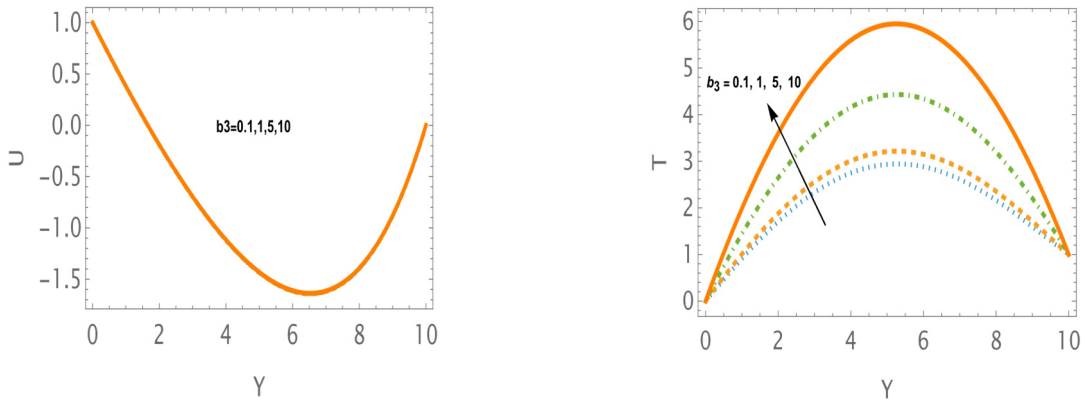

(a) (b)

Figure 6. (a) Velocity (b) Temperature contours for b_3 with $a_6 = 0.01$ and $V = 0.25$

The velocity at the center of the plates continues to decrease as the injection/suction parameter magnitude increases. This is because the non-Newtonian fluid in question has non-linear properties. Higher injection/suction parameter magnitudes will therefore lower the fluid velocity in the first half. But in the second half, these are counterbalanced by higher velocities, thus the overall impact of velocity is felt throughout the fluid's passage. Conversely, with lower magnitudes, the velocity increases more in the first half and less in the second. Additionally, it should be noted that the curves join at the bottom and top in all cases. This is due to the condition that prevails on the surfaces as the fluid flows.

The effect of a_6 on the $U(Y)$ and $T(Y)$ profiles is noted in the Figs. (7(a) and 7(b)). In Fig. 7(a), it is noted that all the $U(Y)$ profiles are overlaps each other. After decreasing till the centre, the velocity steadily increases until it influences the endless flow area. The temperature of the fluid is drastically increasing up to middle distance and suddenly drops then decreases to take the max. temperature.

The result of constant pressure gradient on $U(Y)$ and $T(Y)$ with different values for small values of b_3 and V have been shown in Figs. 8(a) and 8(b). Completely opposite effects have been observed on $U(Y)$ and $T(Y)$ profiles. The velocity reduced and the temperature raised as the constant pressure gradient values increases with the small values. The

velocity variations are completely drifting down the plate where as the temperature variations are drifting up from surface of the plate.

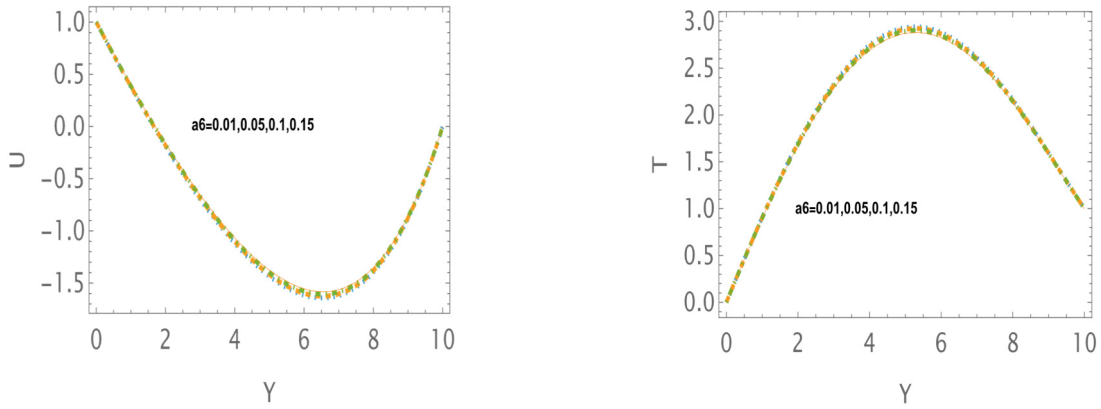

(a) (b)

Figure 7. (a) Velocity (b) Temperature contours for a_6 with $b_3 = 0.1$ and $V = 0.25$

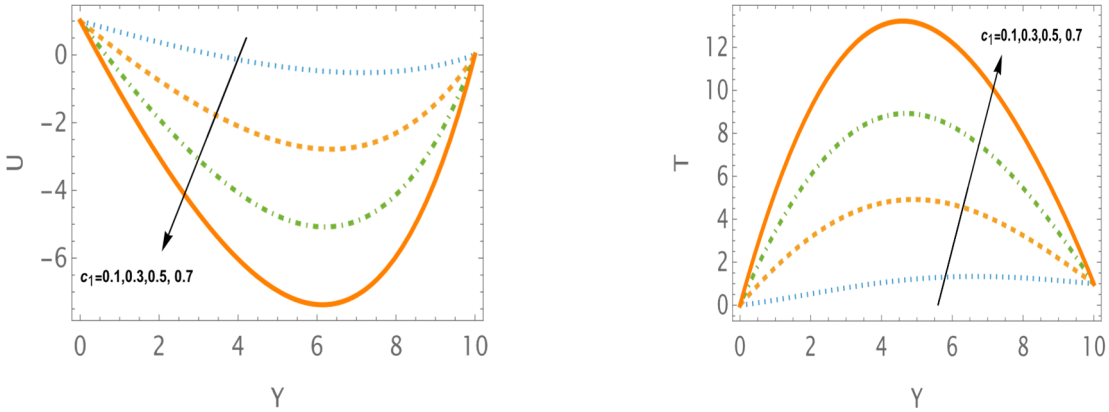

(a) (b)

Figure 8. (a) Velocity (b) Temperature contours for C_1 with $b_3 = 0.1$ and $V = 0.25$

The impact of constant temperature gradient on $U(Y)$ besides $T(Y)$ by different values for small values of b_3 and V have been shown in Figs. 9(a) and 9(b). All the velocity variations overlap for the values of constant temperature gradient increases. Completely opposite effects have been observed on $U(Y)$ and $T(Y)$ profiles. As the constant temperature gradient values rise with the very small values, the temperature rises and the velocity falls. Whereas the temperature variations are migrating upward from the plate's surface, the velocity variations are entirely drifting downward.

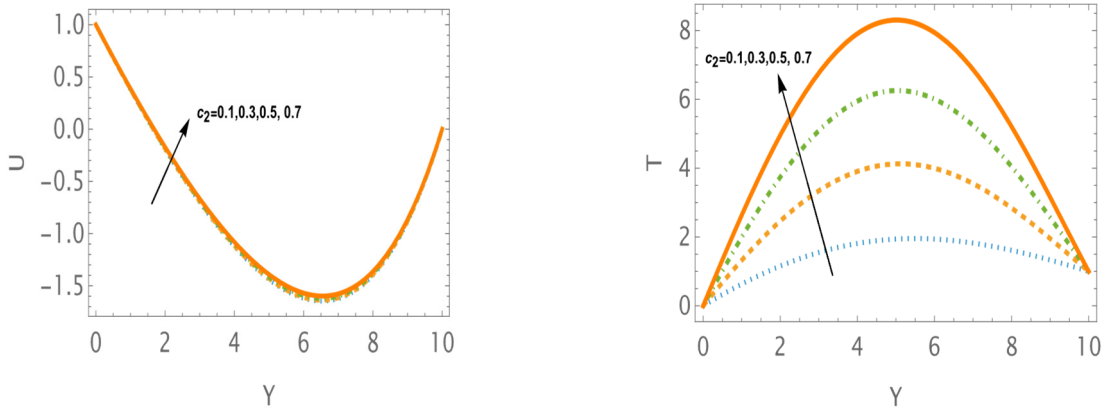

(a) (b)

Figure 9. (a) Velocity (b) Temperature contours for C_2 with $b_3 = 0.1$ and $V = 0.25$

The dimensionless viscosity coefficient(a_1) influence on both $U(Y)$ and $T(Y)$ is shown in Figs. 10(a), 10(b) and 10(c). The $T(Y)$ profiles rise strongly until the middle flow zone, after which they fall to reach the maximum temperature far from the plate surface, while the $U(Y)$ profiles coincide. When b_3 is large, the rate of temperature increase is higher; when b_3 is small, the rate of temperature increase is lower.

The influence of small Prandtl (p_r) number values on $U(Y)$ and $T(Y)$ is shown in Figs. 11(a) to 11(d). The variation of (p_r) values on velocity also not shown much effect and all $U(Y)$ profiles coincide with this effect. The $T(Y)$ variations with increase of small p_r values increase and is observed in figs. 11(b) to 11(d). It is also noted that, the temperature variations increase with the increase of very small values of b_3 to the very large values of b_3 .

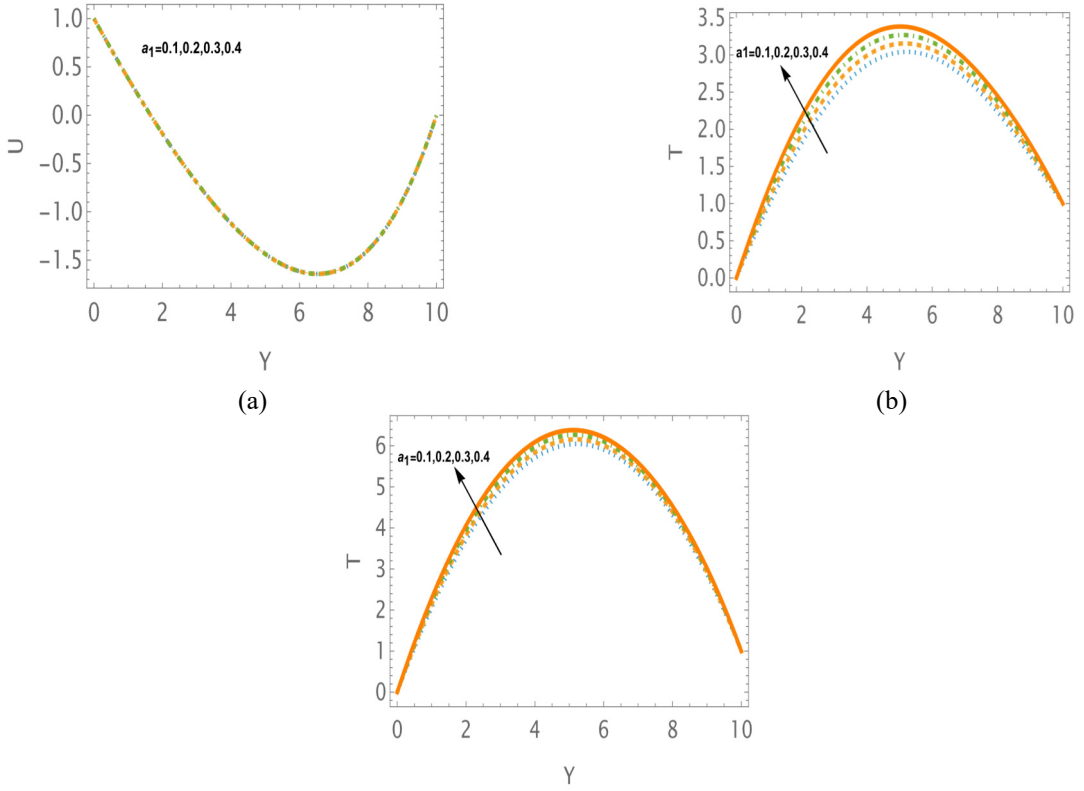

Figure 10. (a) Velocity for $b_3 = 0.1$ and (b), (c) Temperature for $b_3 = 0.1$ and $b_3 = 10$

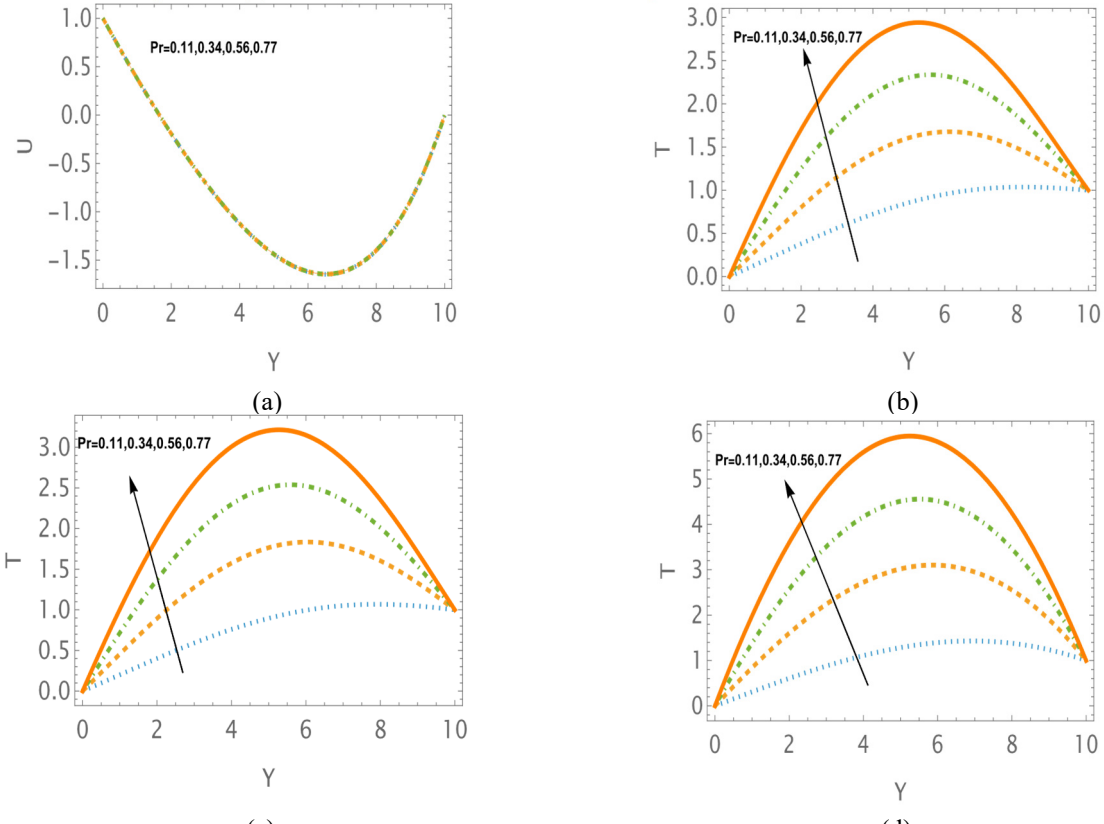

Figure 11. (a) Velocity for $b_3 = 0.1$ and (b), (c) , (d) Temperature for small p_r with $b_3 = 0.1$, $b_3 = 1$ and $b_3 = 10$

The maximum temperature parameter has consistently produced a high thermal conductivity, albeit to varied degrees. Accordingly, it is possible to say that the thermal conductivity of non-Newtonian materials is directly proportional to the Y-location. However, this is only part of the reality. According to the fluid domain's overall spatial view, temperature variations were shifted from the upper triangle to the lower triangle as the thermal conductivity factor grew from 0.1 to 10.0. This is because the fluid under consideration is non-homogeneous and anisotropic. The thermal conductivity influence will differ depending on the location due to the anisotropic nature. The associated figures clearly show this.

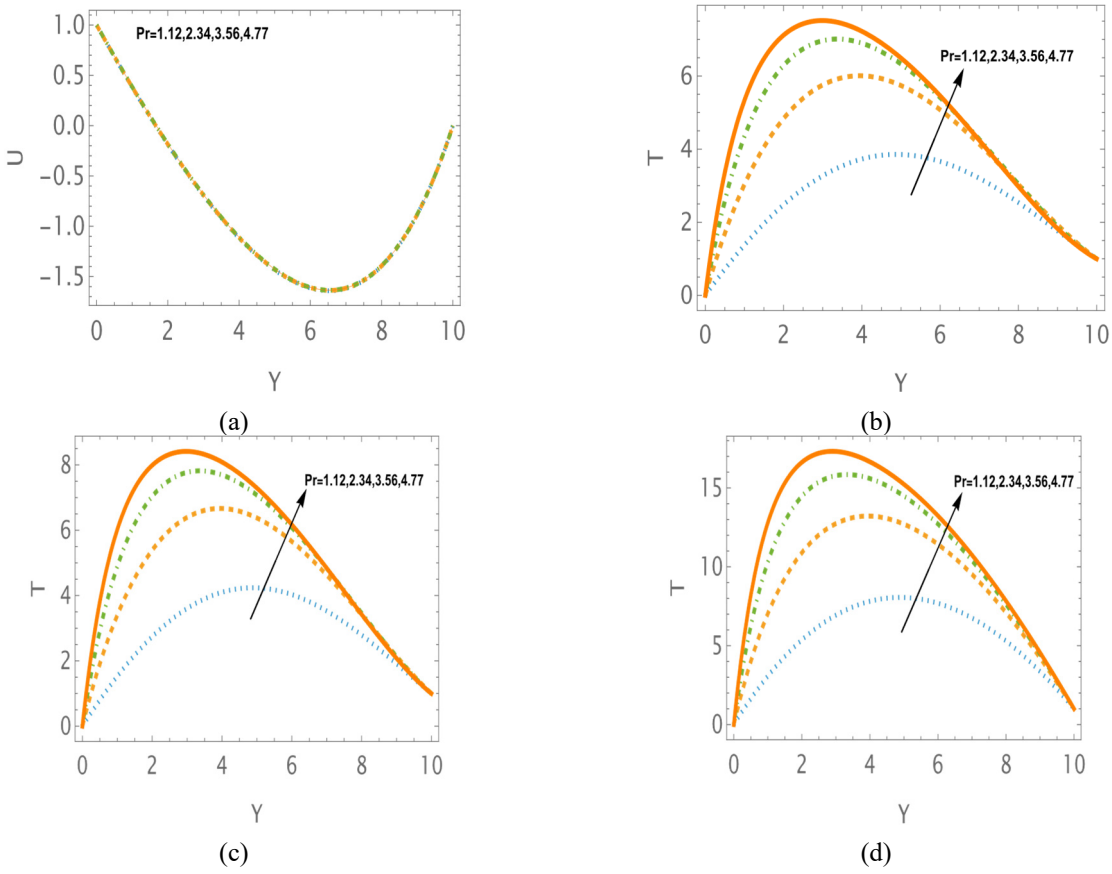

Figure 12. (a) Velocity for $b_3 = 0.1$ and (b), (c), (d) Temperature for big p_r with $b_3 = 0.1$, $b_3 = 1$ and $b_3 = 10$

The influence of big Prandtl (p_r) number values on $U(Y)$ and $T(Y)$ is shown in Figs. 12(a) to 12(d). Additionally, there is little effect of the changing of p_r values on velocity, and all $U(Y)$ profiles coincide with this effect. The $T(Y)$ variations with increase of small p_r values increase and is observed in figs. 12(b) to 12(d). It is also noted that, the temperature variations increase with the increase of very small values of b_3 to the very large values of b_3 . The temperature increases more quickly when the p_r values rise from modest to big levels.

In the design of aircraft wings, the behavior of the thermo-viscous boundary layer across a flat plate is greatly influenced by temperature dependent material qualities, such as viscosity, thermal conductivity, and specific heat. Because of the friction with the wing surface, the air usually becomes less viscous as it heats up, changing the velocity profile and perhaps postponing flow separation. The thermal boundary layer forms concurrently, and its thickness is determined by the air's specific heat and thermal conductivity. While a fluid with a greater specific heat can absorb more heat before its temperature increases noticeably, a fluid with a higher thermal conductivity can dissipate heat more quickly.

6. CONCLUSIONS

This study presents a novel numerical approach for analysis on thermo-viscous steady fluid motion through the moving rectangular plate for an application of aircraft wing design in aerospace engineering. The governing equations numerical solution has been found, and the MATHEMATICA ND solver tool with 6th order R-K techniques has used to solve the resulting governing equations. For a range of physical values of different parameters, as well as for some fixed values of other coefficients, the solutions are implemented.

- The suction parameter/ injection (V) factor decreases the fluid's velocity and increases the temperature. The opposite effects have been noted on both the velocity and the temperature.
- When the coefficient of heat conductivity (b_3) grows to large levels, the fluid velocity increases more quickly.

- Thermal conductivity (b_3) and thermal stress mechanical interaction (a_6) decreases the fluid's velocity and increases the temperature.
- The dimensionless viscosity coefficient (a_1), constant pressure and temperature gradients increase the temperature. There is no variation in velocity with these parameters' effects.
- The small and big values of the Prandtl number (p_r) increases both the velocity and the temperature.
- The derived numerical solutions show an excellent agreement with the available analytical solutions in the literature.
- The parameters of heat transport and the boundary layer over aircraft surfaces are greatly influenced by the temperature-dependent material properties of thermo-viscous fluids.

ORCID

N. Pothanna, https://orcid.org/0000-0003-3983-3125; **P. Raja Shekar,** https://orcid.org/0000-0003-4028-4688; **Jyotsna Cherukuri,** https://orcid.org/0000-0002-9861-7978; **L. Srinivasa Rao,** https://orcid.org/0000-0001-9249-1713; **Adigoppula Raju**, https://orcid.org/0000-0002-8927-3376, **Devunuri Suresh**, https://orcid.org/0000-0002-0533-8604

REFERENCES

[1] S.L. Koh, and A.C. Eringen, "On the foundations of non-linear thermo-viscoelasticity," International Journal of Engineering Science, **1**(2), 199-229 (1963). https://doi.org/10.1016/0020-7225(63)90034-X
[2] K. Yamamoto, and Z.-I. Yoshida, "Flow through a porous wall with convective acceleration," Journal of the Physical Society of Japan, **37**(3), 774-779 (1974). https://doi.org/10.1143/JPSJ.37.774
[3] S.B. Gordon, and D.D. Joseph, "Boundary conditions at a naturally permeable wall, Journal of fluid mechanics," **30**(1), 197-207 (1967). https://doi.org/10.1017/S0022112067001375
[4] D.C. Bernard, and J.V. Mizel, "Existence of caloric equations of state in thermodynamics," The Journal of Chemical Physics, **40**(4), 1116-1125 (1964). https://doi.org/10.1063/1.1725257
[5] P.D. Kelly, "Some viscometric flows of incompressible thermo viscous fluids," International Journal of Engineering Science, **2**(5), 519-533 (1965). https://doi.org/10.1016/0020-7225(65)90007-8
[6] P.N. Rao, and N.Ch. Pattabhiramacharyulu, "Steady flow of a second-order thermo-viscous fluid over an infinite plate," in: *Proceedings of the Indian Academy of Sciences-Mathematical Sciences*. **88**, 157-161 (1979). (Springer India). https://doi.org/10.1007/BF02871612
[7] N. Pothanna, and P. Aparna, "Unsteady thermo viscous flow in a porous slab over an oscillating flat plate," J. Porous Media, **22**, 531–543 (2019). https://doi.org/10.1615/JPorMedia.2019028871
[8] G.J. Reddy, P. Mangathai, and N. Pothanna, "Analysis of heat generation impact on nanofluid flow over a stretching sheet," Partial Differential Equations in Applied Mathematics, **11**, 100852 (2024). https://doi.org/10.1016/j.padiff.2024.100852
[9] N. Pothanna, P. Aparna, M.P. Reddy, R.A. Reddy, and M.C.J. Anand, "Thermo-viscous fluid flow in porous slab bounded between two impermeable parallel plates in relative motion: Four stage algorithm approach," Applications of Mathematics, **69**, 807–827 (2024). https://doi.org/10.21136/AM.2024.0144-23
[10] M.A. Kumar, N. Pothanna, and G.J. Reddy, "Analyzing the heat and mass transfer behavior in a 2-D forchheimer porous medium on MHD Casson fluid flow over an inclined non-linear surface with viscous dissipation, chemical reaction, and Soret–Dufour parameters," Multiscale and Multidiscip. Model. Exp. and Des. **8**, 176 (2025). https://doi.org/10.1007/s41939-025-00767-6
[11] N. Pothanna, "Investigation on unsteady fluid flow around an oscillating sphere-A numerical and analytical approach," Hybrid Advances, **6**, 100257 (2024). https://doi.org/10.1016/j.hybadv.2024.100257
[12] P.R. Shekar, G.J. Reddy, and N. Pothanna, "Influence of Thermal Radiation on MHD Casson Nanofluid Flow over a Non-Linear Stretching Sheet with the Presence of Chemical Reaction," East European Journal of Physics, (1), 101-111 (2025). https://doi.org/10.26565/2312-4334-2025-1-09
[13] N. Pothanna, J. Srinivas, C. Thirmal, G.R. Chandra, and L.S. Raj, "Unsteady thermo viscous fluid motion between two infinitely extended impermeable horizontal plates-an artificial neural networks approach," Thermal Science and Engineering Progress, **62**, 103617 (2025). https://doi.org/10.1016/j.tsep.2025.103617
[14] P. Nalimela, C. Thirmal, V.G. Kumar, and G.J. Reddy, "Artificial neural networks analysis of an unsteady fluid flow through a horizontal oscillating flat plate in a porous slab," Physics of Fluids, **37**, (2025). https://doi.org/10.1063/5.0253605
[15] A. Naeem, Z. Abbas, and M.Y. Rafiq, "Radially inflows and outflows of hydromagnetic viscous fluid between two narrowly flat disks," Results in Engineering, **25**, 103924 (2025). https://doi.org/10.1016/j.rineng.2025.103924
[16] T. Naseem, F. Mebarek-Oudina, H. Vaidya, N. Bibi, K. Ramesh, and S.U. Khan, "Numerical Analysis of Entropy Generation in Joule Heated Radiative Viscous Fluid Flow over a Permeable Radially Stretching Disk," CMES - Computer Modeling in Engineering and Sciences, **143**(1), 351-371 (2025). https://doi.org/10.32604/cmes.2025.063196
[17] Z.I. Butt, I. Ahmad, M. Shoaib, H. Ilyas, and M.A.Z. Raja, "Electro-magnetohydrodynamic impact on Darrcy-Forchheimer viscous fluid flow over a stretchable surface: Integrated intelligent Neuro-evolutionary computing approach," International Communications in Heat and Mass Transfer, **137**, 106262 (2022). https://doi.org/10.1016/j.icheatmasstransfer.2022.106262
[18] H. Milosevic, N.A. Geydarov, Y.N. Zakharov, and S. Stevovic, "Model of incompressible viscous fluid flow driven by pressure difference in a given channel," International Journal of Heat and Mass Transfer, **62**, 242-246 (2013). https://doi.org/10.1016/j.ijheatmasstransfer.2013.02.059
[19] N. Fatima, K.S. Nisar, S. Shaheen, M.B. Arain, N. Ijaz, T. Muhammad, "A case study for heat and mass transfer of viscous fluid flow in double layer due to ciliated channel," Case Studies in Thermal Engineering, **45**, 102943 (2023). https://doi.org/10.1016/j.csite.2023.102943
[20] A.M. Saleem, N.M. Basher, and A.A. Yousif, "Effect of suction or blowing on velocity and temperature distribution of flow over a flat plate," Materials Today: Proceedings, **42**(5), 2859-2865 (2021). https://doi.org/10.1016/j.matpr.2020.12.735

[21] J. Jayaprakash, and V. Govindan, "Impacts of diffusion and chemical reaction on heat transfer in Casson nanofluids flow over a flat plate with accretion," Case Studies in Thermal Engineering, **72**, 106309 (2025). https://doi.org/10.1016/j.csite.2025.106309
[22] S. Peng, T. Peng, Y. Feng, and X. Zheng, "Compressible magnetohydrodynamic flat plate boundary layer flow with slightly rarefied effects," European Journal of Mechanics-B/Fluids, **113**, 204281 (2025). https://doi.org/10.1016/j.euromechflu.2025.204281
[23] W. Zeng, Y. Fang, and H. Ma, "Use of Multi-Test Strategy to Obtain Heat Transfer Coefficient and Adiabatic Wall Temperature Simultaneously in Shock Tunnel for Transonic Flow over a Flat Plate," Aerospace Science and Technology, **160**, 110057 (2025). https://doi.org/10.1016/j.ast.2025.110057
[24] S. Nadeem, W. Fuzhang, F.M. Alharbi, F. Sajid, N. Abbas, A.S. El-Shafay, and F.S. Al-Mubaddel, "Numerical computations for Buongiorno nano fluid model on the boundary layer flow of viscoelastic fluid towards a nonlinear stretching sheet," Alexandria Engineering Journal, **61**(2), 1769-1778 (2022). https://doi.org/10.1016/j.aej.2021.11.013
[25] A.A. Azar, "Thermal radiation and magnetic field effects on dusty hyperbolic tangent fluid flow over a stretching sheet with high Prandtl number," International Communications in Heat and Mass Transfer, **165**, Part A, 109040 (2025). https://doi.org/10.1016/j.icheatmasstransfer.2025.109040
[26] I. Ullah, S. Shafie, and I. Khan, "Effects of slip condition and Newtonian heating on MHD flow of Casson fluid over a nonlinearly stretching sheet saturated in a porous medium," Journal of King Saud University – Science, **29**(2), 250-259 (2017). https://doi.org/10.1016/j.jksus.2016.05.003
[27] H.R. Kataria, and H.R. Patel, "Heat and mass transfer in magnetohydrodynamic (MHD) Casson fluid flow past over an oscillating vertical plate embedded in porous medium with ramped wall temperature," Propulsion and Power Research, **7**(3), 257-267 (2018). https://doi.org/10.1016/j.jppr.2018.07.003
[28] S.M. Ibrahim, G. Lorenzini, P.V. Kumar, and C.S.K. Raju, "Influence of chemical reaction and heat source on dissipative MHD mixed convection flow of a Casson nanofluid over a nonlinear permeable stretching sheet," International Journal of Heat and Mass Transfer, **111**, 346-355 (2017). https://doi.org/10.1016/j.ijheatmasstransfer.2017.03.097
[29] C. Fetecau, and C. Fetecau, "A new exact solution for the flow of a Maxwell fluid past an infinite plate," International Journal of Non-Linear Mechanics, **38**(3), 423-427 (2003). https://doi.org/10.1016/S0020-7462(01)00062-2
[30] S. Dholey, "Flow due to an infinite flat plate suddenly set into motion in a viscoelastic fluid: first Stokes problem," Sadhana, **44**, 118 (2019). https://doi.org/10.1007/s12046-019-1098-9

ДОСЛІДЖЕННЯ ТЕРМО-В'ЯЗКОГО СТАЦІОНАРНОГО РУХУ РІДИНИ ЧЕРЕЗ РУХОМУ ПРЯМОКУТНУ ПЛОСКУ ПЛАСТИНУ – ЧИСЛОВИЙ ПІДХІД

Н. Потханна[1], П. Раджа Шекар[1], Джйотсна Черукурі[2], Л. Срінівас Рао[3], Адігоппула Раджу[4], Девунурі Суреш[5]

[1]Кафедра математики, Інженерно-технологічний інститут ім. ВНР Віньяна Джйоті, Хайдерабад, Телангана, Індія-500090
[2]Кафедра хімії, Інженерно-технологічний інститут ім. ВНР Віньяна Джйоті, Хайдерабад, Телангана, Індія-500090
[3]Центр нанонауки та технологій, кафедра фізики, Інженерно-технологічний інститут ім. ВНР Віньяна Джйоті, Бачупаллі, ГІД., ТГ, Індія-500 090
[4]Кафедра прикладних наук, Технологічний інститут Симбіозу, Symbiosis International (вважається Університет), Пуне-412115, Індія
[5]Кафедра автомобільної інженерії, Інститут інженерії та технологій VNR Віньяна Джйоті, Хайдерабад, Телангана, Індія-500090

Це дослідження представляє новий числовий підхід до аналізу руху термов'язкої стаціонарної рідини через рухому прямокутну плоску пластину. Числові результати були отримані з використанням методу Рунге-Кутти 6-го порядку, розробленого в програмному забезпеченні Mathematica. Числове диференціювання розв'язує адаптивні рівняння потоку, що включають температуру та швидкість. Поведінка потоку та вплив матеріальних обмежень на область потоку для керованих рівнянь були проаналізовані та розглянуті за допомогою згенерованих графіків. Нелінійні зв'язані диференціальні рівняння з частинними похідними (ДРП) щодо температури та швидкості, з урахуванням відповідних граничних умов, керують рухом рідини. Числові розрахунки результатів Рунге-Кутти (Р-К) 6-го порядку представлені у вигляді таблиць, а також для численних значень теплофізичних коефіцієнтів. Варіації цих полів потоку були досліджені для широкого спектру фізичних характеристик, які впливають на природу термов'язкої рідини. Вплив параметра всмоктування/впорскування, безрозмірного коефіцієнта в'язкості, постійних градієнтів тиску та температури, теплофізичних факторів та впливу параметра Прандтля на область потоку було досліджено за допомогою графічних ілюстрацій з широким діапазоном значень. Також були проведені чіткі числові розрахунки, результати яких пов'язані з сучасними результатами в літературі. Для покращення швидкості теплопередачі в таких системах, як теплообмінники та аерокосмічні компоненти, інженери можуть оптимізувати текстури поверхні та умови потоку, враховуючи вплив коефіцієнтів на міркування потоку.

Ключові слова: *термов'язка рідина; розв'язання ND; метод R-K 6-го порядку; проникність; теплопровідність*

East European Journal of Physics. 1. 473-483 (2026)
DOI:10.26565/2312-4334-2026-1-54 ISSN 2312-4334

FDM SIMULATION OF Cu–Al_2O_3/WATER CASSON HYBRID NANOFLUID FLOW AND THERMAL TRANSPORT IN A COUETTE SYSTEM

Khasim Ali[1], Ramesh Alluguvelli[2], Swatmaram[3], Chandra Shekar Balla[4]*, K. Praveen Kumar[5], E. Jagathprabhav[6]

[1]*Department of Mathematics, Nawab Shah Alam Khan College of Engineering and Technology, Hyderabad, Telangana, 500024, India*
[2]*Department of Mathematics, Geethanjali College of Engineering and Technology, Keesara, Hyderabad, Telangana, 501303, India*
[3]*Department of Mathematics, Chaitanya Bharathi Institute of Technology, Hyderabad, Telangana, 500075, India*
[4]*Government Junior College, Amangal, Ranga Reddy, Telangana, 509321, India*
[5]*Department of Humanities and Science, Government Polytechnic, Hyderabad, Telangana, 500028, India*
[6]*Department of Humanities and Science, Government Polytechnic, Shadnagar, Telangana, 509216, India*
**Corresponding author's email: shekar.balla@gmail.com*
Received December 2, 2025; revised January 19, 2026; accepted January 27, 2026

This paper numerically inspects the unsteady Couette Casson hybrid nanofluid (HNF) containing copper (Cu) and aluminum oxide (Al_2O_3) nanoparticles dissolved in water. The upper wall is set in uniform motion, and the lower wall is taken as stationary and stretchable. Finite difference method (FDM) is used to integrate the governed nonlinear partial differential equations. The results are explored through streamlines, isotherms, Nusselt number and skin friction. The impact of key dimensionless numbers such as Grashof number, Biot number, stretching parameter, Casson parameter, and Eckert number on Cu-Al_2O_3-water HNF is discussed. The results disclose that the flow and heat transfer(HT) can be controlled considerably by the key parameters.
Keywords: *Couette flow; Variable viscosity; Al_2O_3-H_2O nanofluid; Biot number; Stretching parameter*
PACS: 47.11.-j, 47.50.-d, 47.61.-k, 44.25.+f

1. INTRODUCTION

In recent years, substantial attention has been garnered by non-Newtonian fluid flows because of their extensive applications in engineering, biomedical, and industrial processes. Casson fluid model is one to describe non-Newtonian behaviour and captures effectively the yield-stress characteristics of materials like paints, polymer solutions, blood, and printing inks. This model was first introduced by Casson [1] in 1959. Mukhopadhyay[2] analysed HT in Casson flow over a stretchable surface. Abd El-Aziz and Afify [3] inspected MHD Casson flow with entropy generation. Previous investigations [4-8] have addressed Casson fluid flow over stretching surfaces, porous media, and boundary layers under the influence of magnetic fields, thermal radiation, viscous dissipation, and entropy generation. Several authors [9-13] confirmed Casson rheology's role in predicting realistic non-Newtonian flow behaviour in different configurations. These studies demonstrate the effectiveness of the Casson model in capturing realistic non-Newtonian behaviour, however, most are restricted to steady or external boundary-layer flows.

In parallel, nanofluid technology introduced to enhance thermal transport properties by dispersing nanoparticles into base fluids, has become a significant development in modern HT enhancement[14]. Tiwari and Das [15] studied the nanofluid flow in square cavity. Mono-nanofluids have been widely explored for various geometries and thermal conditions [16–20]. More recently, HNFs are made by combining two or more types of nanoparticles. Due to the synergistic effects between different particle materials, they exhibit improved thermal performance. Such hybrid suspensions exhibit superior HT capability, stability, and regulable viscosity. Unlike mono-nanoparticle nanofluids, HNFs highly associated to cooling systems, energy systems, and process engineering. Studies on Al_2O_3–Cu/water and related hybrid nanofluids with radiation and porous effects have reported notable enhancements in thermal efficiency [21–25].

Couette flow, representing the motion of a viscous fluid lying in two parallel plates with one or both plates in relative motion, serves as a fundamental configuration for studying shear-driven transport phenomena. Attia et al. [26] studied how temperature dependent viscosity and thermal conductivity influence unsteady hydromagnetic Couette flow. Couette flow is further studied by several researchers [27-33]. Existing studies have largely focused on steady-state flows or single-nanoparticle suspensions. In many practical applications, including lubrication systems and transient electronic cooling, the flow and temperature fields are naturally unsteady. Therefore, unsteadiness is incorporated to capture the transient evolution of the system. These transient effects are particularly important for accurately describing the behaviour of non-Newtonian hybrid nanofluids. Zeeshan et al. [34] studied MHD Casson hybrid nanofluid over the shrinking sheet. Although recent works have investigated Casson hybrid nanofluids in various geometries [35–42], the combined effects of unsteadiness, Casson and hybrid nanoparticle dispersion within an internal Couette geometry remain insufficiently explored.

Recent research [43-47] has focused on Casson hybrid nanofluids, where two or more distinct nanoparticles are dispersed in a Casson base fluid to achieve superior thermophysical performance. However, most prior studies have been

Cite as: K. Ali, R. Alluguvelli, Swatmaram, C.S. Balla, K.P. Kumar, E. Jagathprabhav, East Eur. J. Phys. 1, 473 (2026), https://doi.org/10.26565/2312-4334-2026-1-54

limited to steady, external boundary-layer configurations such as stretching sheets or porous media, neglecting unsteady internal geometries like Couette channels. The effects of unsteadiness and HT for Casson HNF in a Couette configuration are still not well understood. Therefore, present study aims to address this gap by investigating unsteady Casson HNF flow and HT between parallel plates. This analysis contributes new insights into non-Newtonian hybrid thermal transport under confined geometries.

Motivated by this gap, the current work examines the unsteady Couette flow of a Casson HNF consisting of Copper (Cu) and alumina (Al_2O_3) nanoparticles dispersed in water. The upper wall of the channel is moving uniformly, while the lower wall is stationary and stretchable. A comprehensive mathematical formulation incorporating the impact of key dimensionless parameters such as the Casson parameter, Grashof number, Biot number, stretching parameter, and Eckert number is developed. The governing nonlinear partial differential equations are solved using a finite difference method (FDM) to elucidate the fluid flow and HT characteristics.

2. MATHEMATICAL FORMULATION

An unsteady, laminar, incompressible Casson HNF flow of Cu-Al_2O_3-H_2O confined within two parallel plates is taken into account. The viscosity of the fluid is considered to be a function of temperature. To configure the model geometry, x-axis is aligned with the plate and the y-axis is oriented perpendicular to the plates, as shown in Figure 1. The lower plate is located at y =0, possesses a stretching velocity U_0. The upper plate had convective cooling at y = h. And this flow is driven by a uniform pressure gradient located at the ends of the channel.

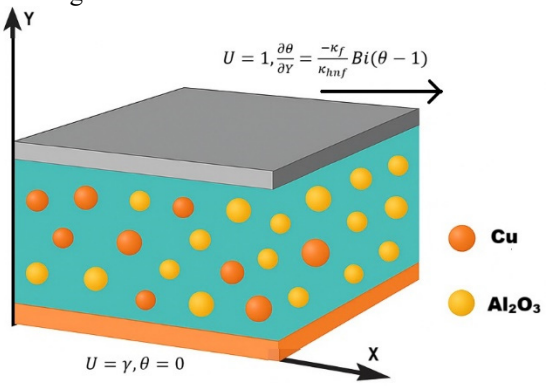

Figure 1. Physical configuration

Based on Tiwari and Das [15] nanofluid model for nanofluid, the governing equations are given by,
Momentum equation:

$$\rho_{hnf}\frac{\partial u}{\partial \tau} = -\frac{\partial p}{\partial x} + \left(1 + \frac{1}{\lambda}\right)\frac{\partial}{\partial y}\left(\mu_{hnf}(T)\frac{\partial u}{\partial y}\right) + (\rho\beta_T)_{hnf} g(T - T_0) \tag{1}$$

Temperature equation:

$$\frac{\partial T}{\partial \tau} = \alpha_{hnf}\frac{\partial^2 T}{\partial y^2} + \frac{\mu_{hnf}(T)\,\alpha_{hnf}}{\kappa_{hnf}}\left(\frac{\partial u}{\partial y}\right)^2 \tag{2}$$

The dynamic viscosity is presumed to be an exponential declining function that depends on temperature [28], expressed as,

$$\mu_f(T) = \mu_0 e^{-m(T - T_0)} \tag{3}$$

Constraints at the boundary are:

When $\tau = 0$, $u = 0, T = 0$ at $y = 0,\ y = h$

$$\text{When } \tau > 0, \quad \left.\begin{array}{ll} u = U_0, & T = T_0 \quad \text{at} \quad y = 0 \\ u = U_h, & -\kappa_{hnf}\frac{\partial T}{\partial y} = h_f(T - T_\infty) \quad \text{at} \quad y = h \end{array}\right\} \tag{4}$$

where U_0 corresponds to stretching velocity of bottom plate, U_h denotes velocity of top plate, T_∞ depicts the ambient temperature, P represents nanofluid pressure. μ_0 symbolizes dynamic viscosity of nanofluid at reference temperature T_0 and m represents parameter of viscosity, h_f symbolizes coefficient of HT. Volume fraction of comprised nanoparticles, density, thermal conductivity, thermal diffusivity and heat capacitance are described below. The subscripts f, s, nf and hnf refer to base fluid, solid nanoparticles, nanofluid and hybrid nanofluid. Relationships indicating the physical characteristics of nanofluids are expressed as:

$$\mu_{hnf} = \frac{\mu_f}{(1-\phi_1)^{2.5}(1-\phi_1)^{2.5}} \tag{5}$$

$$\rho_{hnf} = \left\{(1-\phi_2)\left((1-\phi_1)+\phi_1\frac{\rho_{s1}}{\rho_f}\right)+\phi_2\frac{\rho_{s2}}{\rho_f}\right\}\rho_f \tag{6}$$

$$(\rho C_P)_{hnf} = \left\{(1-\phi_2)\left((1-\phi_1)+\phi_1\frac{(\rho C_P)_{s1}}{(\rho C_P)_f}\right)+\phi_2\frac{(\rho C_P)_{s2}}{(\rho C_P)_f}\right\}(\rho C_P)_f \tag{7}$$

$$\kappa_{hnf} = \frac{(\kappa_{s2}+2\kappa_f)-2\phi_2(\kappa_f-\kappa_{s2})}{(\kappa_{s2}+2\kappa_f)+\phi_2(\kappa_f-\kappa_{s2})}\kappa_{nf} \tag{8}$$

$$\kappa_{nf} = \frac{(\kappa_{s1}+2\kappa_f)-2\phi_1(\kappa_f-\kappa_{s1})}{(\kappa_{s1}+2\kappa_f)+\phi_1(\kappa_f-\kappa_{s_1})}\kappa_f \tag{9}$$

$$\alpha_{hnf} = \frac{\kappa_{hnf}}{(\rho C_P)_{hnf}} \tag{10}$$

Table 1. Thermophysical characteristics of Copper, Alumina and Water

Physical characteristics	Cu	Al_2O_3	H_2O
C_p (J/KgK)	385	765	4179
ρ (Kg/m^3)	8933	3970	997.1
k (W/mK)	400	40	0.613

The following dimensionless quantities and parameters are invoked to change governing equations into non-dimensional form.

$$\left.\begin{aligned} X=\frac{x}{h}, Y=\frac{y}{h},\ U=\frac{hu}{\nu_f}, t=\frac{\tau\nu_f}{h^2},\ \theta=\frac{T-T_0}{T_\infty-T_0}, Pr=\frac{\nu_f}{\alpha_f} \\ \bar{P}=\frac{Ph^2}{\rho_f{\nu_f}^2}, \beta=m(T_\infty-T_0),\ Ec=\frac{{\nu_f}^2}{C_P(T_\infty-T_0)h^2}, Bi=\frac{h\,h_f}{\kappa_f}, \gamma=\frac{U_0}{h} \end{aligned}\right\} \tag{11}$$

The converted dimensionless equations could be written as:

$$\frac{\partial U}{\partial t} = \frac{\rho_f}{\rho_{hnf}}\left\{-\frac{\partial \bar{P}}{\partial X}+\left(1+\frac{1}{\lambda}\right)\frac{\mu_{hnf}}{\mu_f}e^{-\beta\theta}\left[\frac{\partial^2 U}{\partial Y^2}-\beta\frac{\partial\theta}{\partial Y}\frac{\partial U}{\partial Y}\right]\right\}+Gr\,\theta \tag{12}$$

Temperature equation:

$$\frac{\partial\theta}{\partial t} = \frac{(\rho C_P)_f}{(\rho C_P)_{hnf}}\left\{\frac{1}{Pr}\frac{\kappa_{hnf}}{\kappa_f}\frac{\partial^2\theta}{\partial Y^2}+\frac{\mu_{hnf}}{\mu_f}e^{-\beta\theta}Ec\left(\frac{\partial U}{\partial Y}\right)^2\right\} \tag{13}$$

Boundary conditions are:

When $t=0$, $\quad U=0,\ \theta=0 \quad$ at $\quad Y=0,\ Y=1$

$$\left.\begin{aligned} &U=\gamma, \theta=0 && \text{at}\quad Y=0 \\ &U=1, \frac{\partial\theta}{\partial Y}=\frac{-\kappa_f}{\kappa_{hnf}}Bi(\theta-1) && \text{at}\quad Y=1 \end{aligned}\right\} \tag{14}$$

When $t>0$,

Local coefficients of skin friction and Nusselt for lower and upper plates are given by

$$\left.\begin{aligned} C_{f0}=\frac{\mu_{hnf}}{\mu_f}e^{-\beta\theta}\frac{\partial U}{\partial Y}_{Y=0},\ C_{f1}=\frac{\mu_{hnf}}{\mu_f}e^{-\beta\theta}\frac{\partial U}{\partial Y}_{Y=1} \\ Nu_0=-\frac{\kappa_{hnf}}{\kappa_f}\frac{\partial\theta}{\partial Y}_{Y=0}, Nu_1=-\frac{\kappa_{hnf}}{\kappa_f}\frac{\partial\theta}{\partial Y}_{Y=1} \end{aligned}\right\} \tag{15}$$

3. METHODOLOGY

The nonlinear coupled partial differential equations (12-13), with constraints (14), are evaluated numerically using finite difference method. Time derivative is computed with forward difference scheme and spatial derivatives of first and second order with central difference scheme. Convergence of the scheme is assumed when the values of unknowns U, θ of two consecutive iterations differ by less than 10^{-5} i.e., $|\varphi^{n+1}-\varphi^n| \le 10^{-5}$, where n specifies number of loops and φ stands for $[U,\theta]^T$. Table 2 shows the comparison of Cf_{avg} and Nu_{avg} of current study with previous works and found satisfactory.

Equations (12-13) could be written as:

$$\frac{\partial U}{\partial t} = A_1 + A_2\,e^{-\beta\theta}\frac{\partial^2 U}{\partial Y^2} - A_3 e^{-\beta\theta}\frac{\partial\theta}{\partial Y}\frac{\partial U}{\partial Y} + A_4\,\theta \tag{15}$$

$$\frac{\partial \theta}{\partial t} = B_1 \frac{\partial^2 \theta}{\partial Y^2} + \mathrm{B}_2\, e^{-\beta\theta} \left(\frac{\partial U}{\partial Y}\right)^2 \tag{16}$$

The explicit FDM scheme is given by,

$$U_i^{n+1} = U_i^n + \Delta t A_1 + \Delta t A_2 e^{-\beta\theta_i^n} \frac{U_{i+1}^n - 2U_i^n + U_{i-1}^n}{(\Delta Y)^2} - \Delta t A_3 e^{-\beta\theta_i^n} \left(\frac{\theta_{i+1}^n - \theta_{i-1}^n}{2\Delta Y}\right)\left(\frac{U_{i+1}^n - U_{i-1}^n}{2\Delta Y}\right) + \Delta t A_4 \theta_i^n \tag{17}$$

$$\theta_i^{n+1} = \theta_i^n + \Delta t \left[B_1 \frac{\theta_{i+1}^n - 2\theta_i^n + \theta_{i-1}^n}{(\Delta Y)^2} + B_2 e^{-\beta\theta_i^n} \left(\frac{U_{i+1}^n - U_{i-1}^n}{2\Delta Y}\right)^2\right] \tag{18}$$

Here

$$A_1 = -\frac{\rho_f}{\rho_{hnf}}\frac{\partial \bar{P}}{\partial X}, A_2 = \frac{\rho_f}{\rho_{hnf}}\left(1 + \frac{1}{\lambda}\right)\frac{\mu_{hnf}}{\mu_f}, A_3 = \frac{\rho_f}{\rho_{hnf}}\left(1 + \frac{1}{\lambda}\right)\frac{\mu_{hnf}}{\mu_f}\beta,$$

$$A_4 = Gr, B_1 = \frac{(\rho C_P)_f}{(\rho C_P)_{hnf}}\frac{1}{Pr}\frac{\kappa_{hnf}}{\kappa_f}, B_2 = \frac{(\rho C_P)_f}{(\rho C_P)_{hnf}}\frac{\mu_{hnf}}{\mu_f}Ec$$

Table 2. Comparison of Skin friction(Cf_{avg}) and Nusselt number(Nu_{avg}).

β	Bi	Ec	Cf_{avg}			Nu_{avg}		
			Ali and Makinde [28]	Karim et al. [29]	Current study	Ali and Makinde [28]	Karim et al. [29]	Current study
0.1	1	1.0	0.397	0.395	0.3962	0.512	0.511	0.5121
0.1	3	1.0	0.406	0.405	0.4058	0.790	0.784	0.7883
0.5	1	1.0	0.145	0.146	0.1443	0.223	0.221	0.2227
0.1	1	0.5	0.435	-	0.4347	0.039	-	0.0401
0.1	7	1.0	0.411	-	0.4106	0.943	-	0.9428

4. DISCUSSION OF RESULTS

The governing nonlinear partial differential equations describing the unsteady Casson hybrid nanofluid flow were evaluated numerically using FDM. The impact of various non-dimensional numbers, namely the Casson parameter (λ), Eckert number (Ec), Biot number (Bi), viscosity parameter (β), nanoparticle volume fraction (φ), stretching parameter (γ), and Grashof number (Gr) on velocity, temperature, skin friction, and Nusselt number are presented and interpreted in this section.

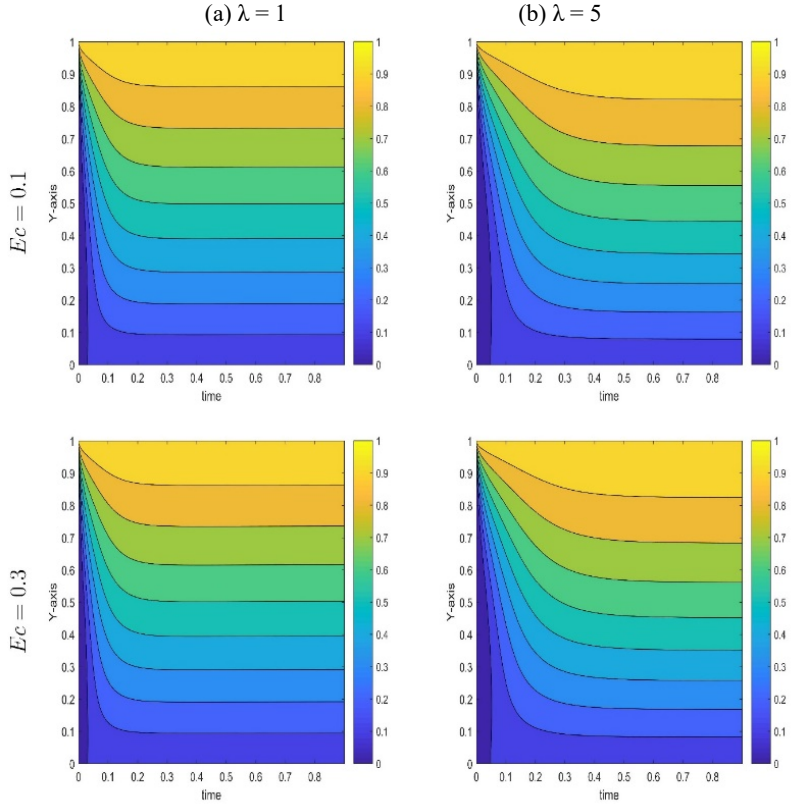

Figure 2. Streamlines for (a) $\lambda = 1$ (b) $\lambda = 5$ and $Ec = 0.1, 0.3$

Figures 2 and 3 illustrate the streamline and isotherm patterns for different values of the Casson parameter λ and Eckert number Ec. It is noticed that with increasing λ (i.e., higher Casson parameter implying stronger yield stress), the flow resistance increases and the velocity gradients near the walls become weaker. Consequently, the flow field becomes more uniform and shear layers are reduced. The isotherm contours reveal that higher λ suppresses heat generation near the moving wall, leading to a more uniform temperature field. An increase in Ec enhances the internal viscous dissipation, which thickens the boundary layer of temperature and raises thermal profile throughout the channel.

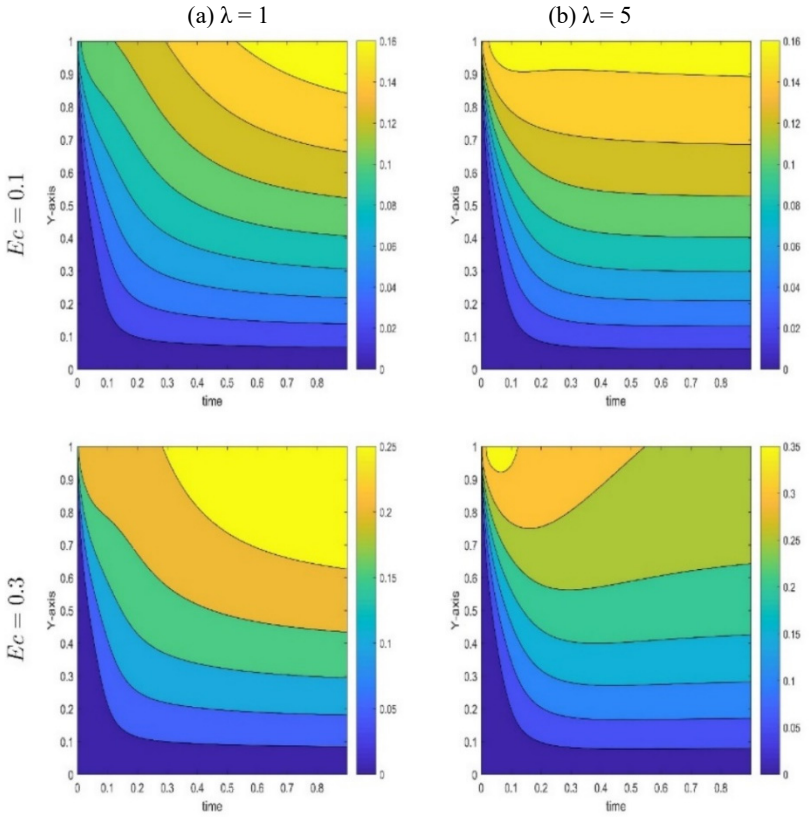

Figure 3. Isotherms for (a) $\lambda = 1$ (b) $\lambda = 5$ and $Ec = 0.1, 0.3$

Figure 4 illustrates that increasing the Biot number decreases slightly the velocity but boosts temperature in the channel. Physically, a larger Bi indicates to enhanced convective heat exchange at the wall. So, there is an increase in wall temperature and consequently the buoyancy-induced motion. As Bi rises, the velocity boundary layer thickens while the temperature gradient near the wall intensifies. This indicates improved heat transfer between the surface and the fluid.

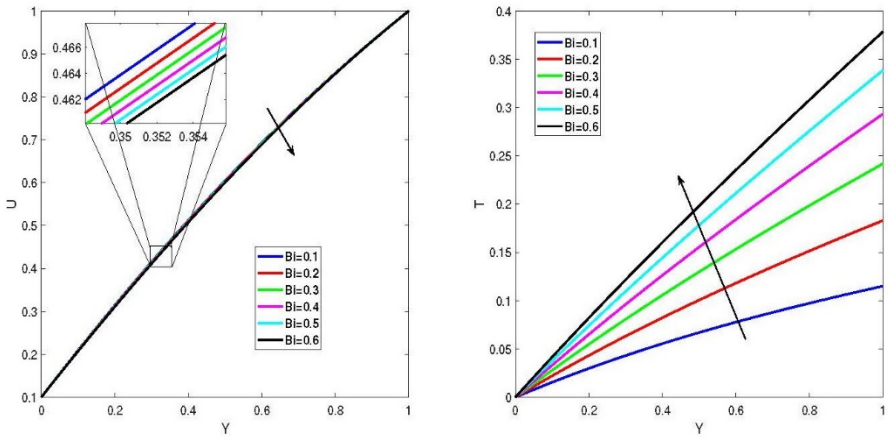

(a) (b)

Figure 4. Effect of Bi on (a) velocity (b) temperature

Eckert number quantifies the conversion of kinetic energy into internal energy due to viscous dissipation. As shown in Figure 5, with higher Ec, the fluid experiences greater frictional heating. This leads to elevated temperature profiles and reduced velocity near the walls. The increase in thermal energy promotes stronger thermal stratification across the channel. This behaviour is consistent with the energy dissipation effects in high-shear flows.

Figure 6 shows that velocity decreases with the increase in β. This is due the increase in effective viscosity, particularly near the lower wall with considerable temperature gradient. Temperature distribution rises with β, as higher viscous resistance dissipates more energy into heat. This trend emphasizes the competing influence between viscous drag and thermal conduction in HNF systems.

Figure 7 shows that increasing the nanoparticle concentration enhances thermal conductivity of the Casson HNF. This leads to higher temperatures throughout the channel. The velocity, however, decreases with increased φ. This is due to the rise in viscosity induced by the additional solid particles. The improved HT demonstrates the synergistic effect of Cu–Al_2O_3 nanoparticles. They provide a better balance between viscosity increase and conductivity improvement compared to single-particle nanofluids.

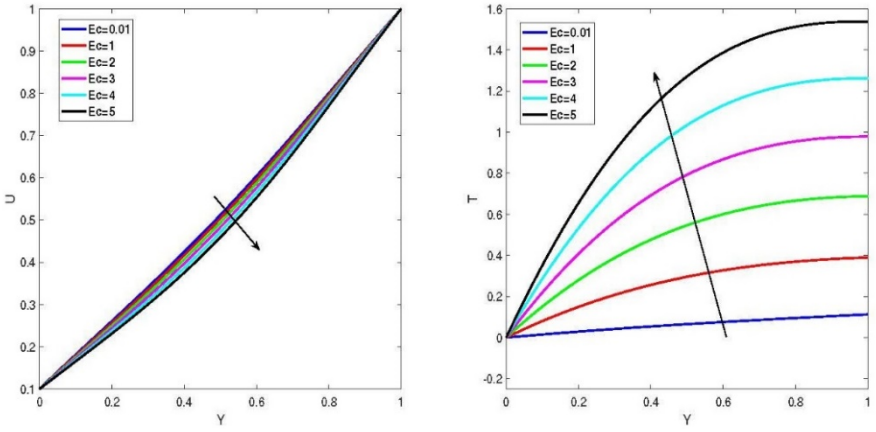

(a) (b)

Figure 5. Effect of Ec on (a) velocity (b) temperature

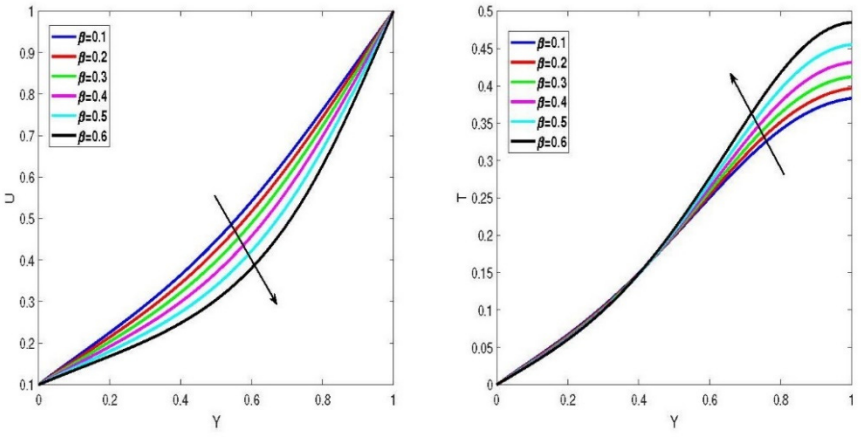

(a) (b)

Figure 6. Effect of β on (a) velocity (b) temperature

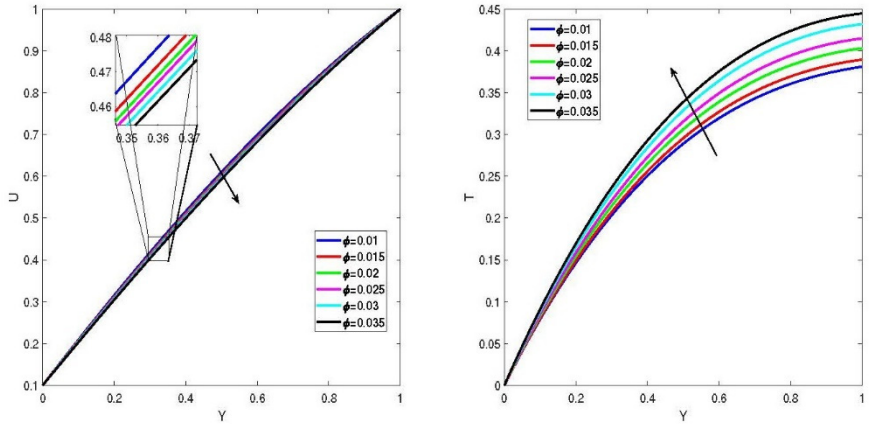

(a) (b)

Figure 7. Effect of ϕ on (a) velocity (b) temperature

From Figure 8, it is evident that increasing γ (the wall stretching rate) accelerates the fluid motion near the lower plate. This leads to higher velocity and thinner velocity boundary layer. The temperature decreases with the increase in γ.

From Figure 9, it is evident that rise in λ values, significantly reduces the fluid velocity and increases temperature. This is due to stronger non-Newtonian effect and higher yield stress. The suppression of motion due to yield stress restricts convective transport, and allows heat to accumulate within the fluid. This behaviour differentiates Casson fluids from Newtonian ones. It also emphasises the significance of rheology concerning HNF performance.

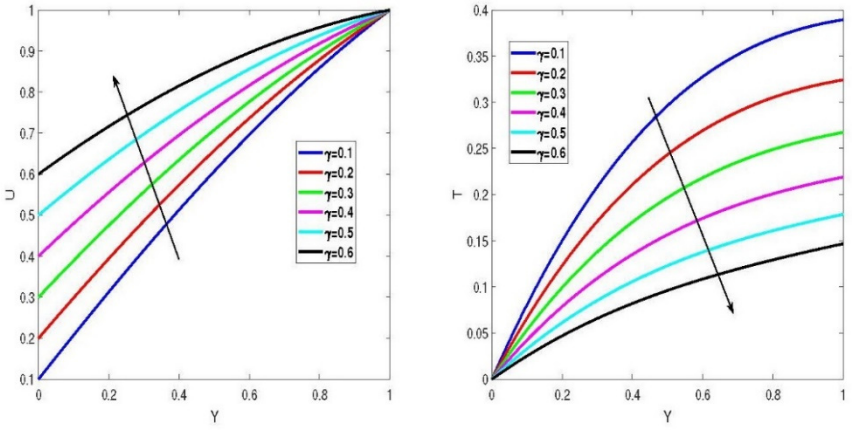

(a) (b)

Figure 8. Effect of γ on (a) velocity (b) temperature

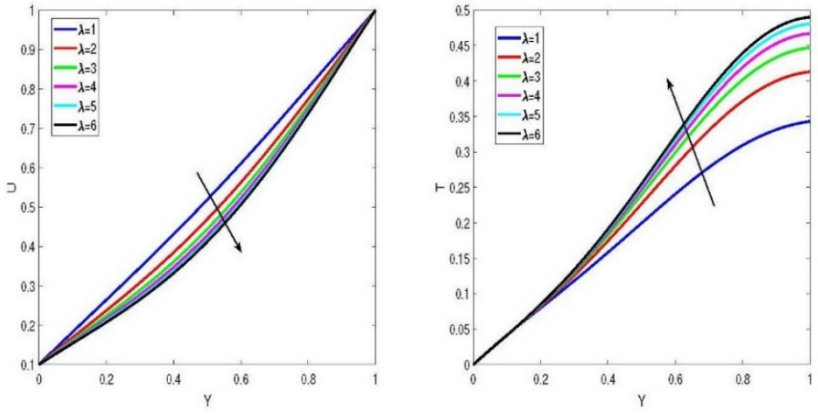

(a) (b)

Figure 9. Effect of λ on (a) velocity (b) temperature

As shown in Figure 10, increasing Gr enhances velocity but decreases temperature field. This happens due to the buoyancy-driven flow formed by temperature gradients. Larger Gr values decrease the temperature slightly. When buoyancy become stronger, the warm fluid is carried away more quickly. This improves cooling effect in the channel of HNF.

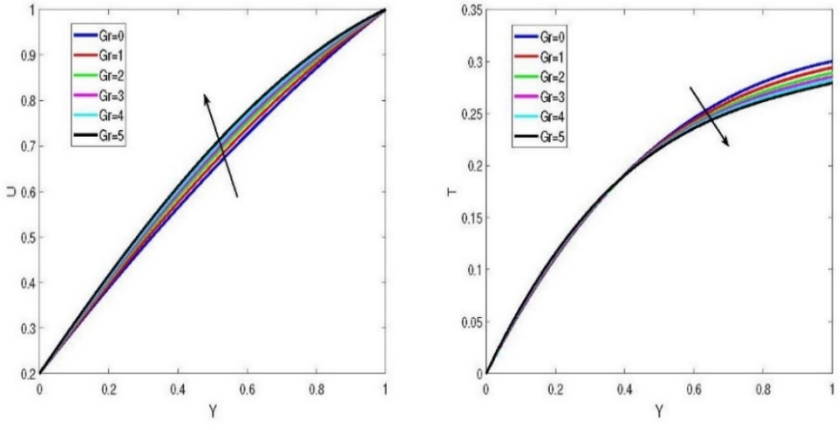

(a) (b)

Figure 10. Effect of Gr on (a) velocity (b) temperature

Figure 11(a) shows that Cf_0 decreases as the Casson parameter increases, while Cf_1 rises. This means that, as the yield-stress increases weaker shear is observed at lower wall but stronger shear at upper wall. Figure 11(b) shows that Nu_0 increases slightly with λ, while the upper wall value Nu_1 decreases. This indicates that higher yield stress enhances HT at the lower plate but reduces it at the upper plate.

Figure 12(a) depicts that, as the Grashof number increases, Cf_0 increases steadily while Cf_1 decreases. Figure 12(b) reveals that Nu_0 increases slightly with Gr, while Nu_1 stays almost same with a tiny downward trend.

Figure 13 reveals that, increasing the Casson parameter λ raises average skin friction but reduces average Nusselt number. Increasing the Grashof number barely affects average friction but slightly boosts average heat transfer.

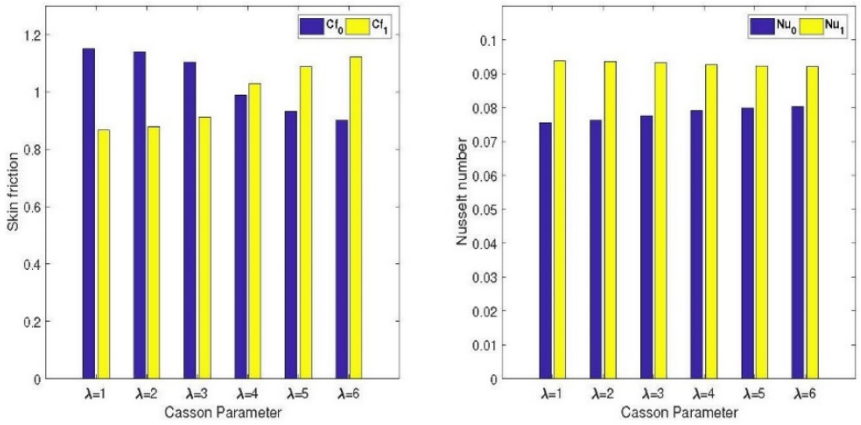

(a) (b)

Figure 11. Effect of λ on (a) Skin friction (b) Nusselt number

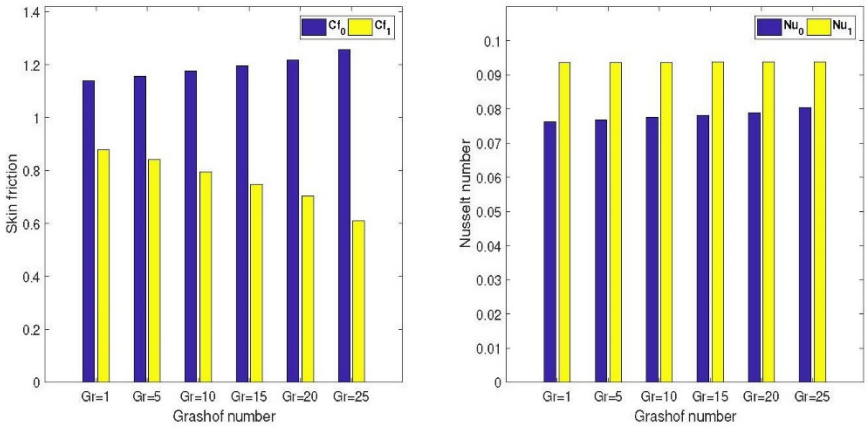

(a) (b)

Figure 12. Effect of Gr on (a) Skin friction (b) Nusselt number

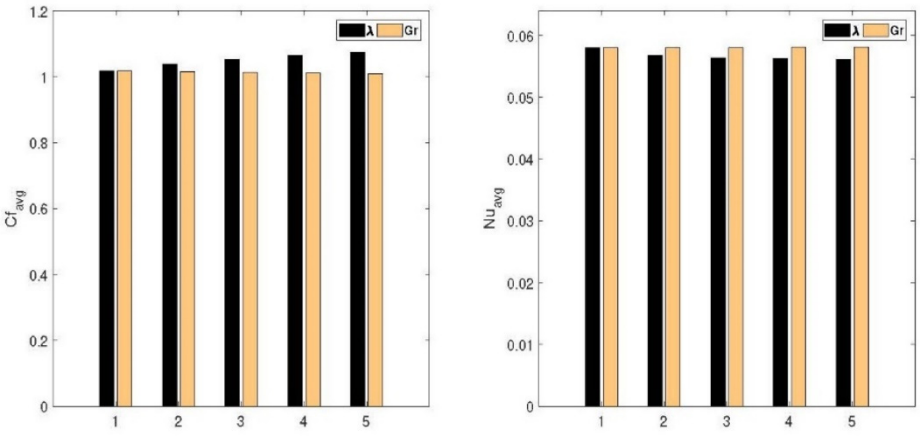

(a) (b)

Figure 13. Variation of average (a) Skin friction (b) Nusselt number for λ and Gr

Figure 14 illustrates the effect of time on the skin friction coefficient (Cf) and Nusselt number (Nu) for $\lambda = 1$ and $\lambda = 2$ over the time interval $t = 0.01 - 1.05$. It is observed that both Cf and Nu exhibit significant variations at early times, indicating transient behaviour. However, as time progresses, the variations gradually diminish, and both quantities approach constant values beyond $t = 1$. Therefore, in the present study, t = 1 is considered as the steady state time. The time step was chosen sufficiently small $dt = 1.3605 \times 10^{-4}$ to ensure convergence of the solution, and further reduction in the time step did not lead to any noticeable change in Cf and Nu.

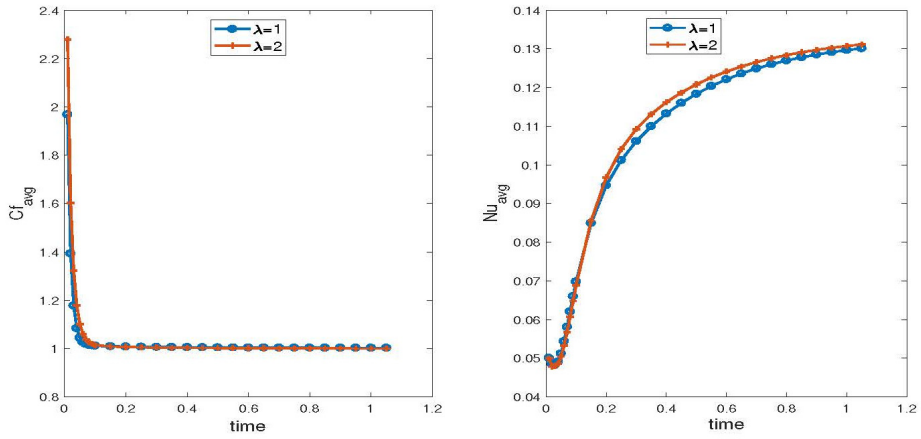

(a) (b)

Figure 14. (a) Skin friction (b) Nusselt number for time variation and $\lambda = 1, 2$

5. CONCLUSIONS

An analysis of unsteady Couette flow and HT behaviour of a Casson HNF composed of copper (Cu) and alumina (Al_2O_3) nanoparticles suspended in water, was carried out through numerical study. Non-dimensional governing equations were evaluated using FDM to study the effects of significant physical parameters for instance, Casson parameter (λ), Grashof number (Gr), Biot number (Bi), Eckert number (Ec), viscosity parameter (β), nanoparticle volume fraction (φ), and wall stretching parameter (γ).

The findings from the study are as follows:

- The momentum field is primarily controlled by rheological and viscous parameters. Casson (λ) and viscosity parameter (β) exert the strongest influence on velocity and skin friction. Higher values of λ significantly suppress fluid motion due to increased yield stress, while larger β enhances viscous resistance. This indicates that non-Newtonian effects dominate momentum transport when λ and β are large.
- The thermal field is mainly governed by the Eckert (Ec) and Biot (Bi) numbers. At low Ec, HT is conduction-dominated, whereas higher Ec leads to dominant viscous dissipation, increased internal heating, thicker thermal layers, and reduced Nusselt numbers. Increasing Bi enhances wall to fluid convection, causing surface convection to dominate thermal transport.
- Buoyancy effects become important at high Grashof numbers (Gr), where natural convection speeds up the flow and improves cooling.
- Nanoparticle volume fraction(ϕ) improve heat transfer by increasing thermal conductivity but reduce fluid velocity because they increase viscosity.
- Stretching parameter(γ) helps control the flow by increasing velocity near wall and reducing fluid temperature, offering useful design control for practical applications.
- From a practical perspective, the results suggest that flow resistance in HNF systems can be effectively controlled through rheological parameters λ and β, whereas thermal performance can be optimized by managing Ec and Bi. These findings provide useful design guidelines for engineering applications such as polymer processing, thermal management systems, and cooling technologies involving non-Newtonian HNFs.

Funding Declaration
The authors declare that no funds, grants, or other financial support were received during the preparation of this manuscript.

ORCID
Khasim Ali, https://orcid.org/0000-0001-8449-7090; **Ramesh Alluguvelli,** https://orcid.org/0000-0002-5075-4375
Chandra Shekar Balla, https://orcid.org/0000-0002-1919-1367

REFERENCES

[1] N. Casson, "A flow equation for the PIGMENT-oil suspensions of the printing ink type," in: *Rheology of Disperse Systems*, edited by C.C. Mill, (Pergamon, 1959), pp. 84–102.

[2] Mukhopadhyay, S., "Casson fluid flow and heat transfer over a nonlinearly stretching surface," Chinese Physics B, **22**(7), 074701 (2013). https://doi.org/10.1088/1674-1056/22/7/074701
[3] M. Abd El-Aziz, and A.A. Afify, "MHD Casson fluid flow over a stretching sheet with entropy generation analysis and Hall influence," Entropy, **21**(6), 592 (2019). https://doi.org/10.3390/e21060592
[4] K. Gangadhar, D.N. Bhargavi, and V.S.R. Munagala, "Steady Boundary Layer Flow of Casson Fluid over a Nonlinear Stretched Sheet in Presence of Viscous Dissipation Using the Spectral Relaxation Method," Mathematical Modelling of Engineering Problems, **7**(3), 351-358 (2020). https://doi.org/10.18280/mmep.070304
[5] I.A. Tantry, S. Wani, and B. Agrawal, "Study of MHD boundary layer flow of a casson fluid due to an exponentially stretching sheet with radiation effect," Int. J. Stat. Appl. Math, **6**, 138-144 (2021). https://doi.org/10.13140/RG.2.2.33054.41286
[6] M.M. Nandeppanavar, "Flow and Heat Transfer Analysis of Casson Fluid due to a stretching sheet: An Analytical Solution," Advances in Physics theories and Applications, **50**, 2224-2225 (2015).
[7] M.B. Ashraf, T. Hayat, and A. Alsaedi, "Mixed convection flow of Casson fluid over a stretching sheet with convective boundary conditions and Hall effect," Boundary Value Problems, **2017**(1), 137 (2017). https://doi.org/10.1186/s13661-017-0869-7
[8] J. Qing, M.M. Bhatti, M.A. Abbas, M.M. Rashidi, and M.E.S. Ali, "Entropy generation on MHD Casson nanofluid flow over a porous stretching/shrinking surface," Entropy, **18**(4), 123 (2016). https://doi.org/10.3390/e18040123
[9] Walawender, W.P., Chen, T.Y. and Cala, D.F., "An approximate Casson fluid model for tube flow of blood," Biorheology, **12**(2), 111-119 (1975). https://doi.org/10.3233/bir-1975-12202
[10] Batra, R.L. and Jena, B., "Flow of a Casson fluid in a slightly curved tube," International journal of engineering science, **29**(10), 1245-1258 (1991). https://doi.org/10.1016/0020-7225(91)90028-2
[11] Pramanik, S., "Casson fluid flow and heat transfer past an exponentially porous stretching surface in presence of thermal radiation," Ain shams engineering journal, **5**(1), 205-212 (2014). https://doi.org/10.1016/j.asej.2013.05.003
[12] Mustafa, M., Hayat, T., Pop, I. and Aziz, A., "Unsteady boundary layer flow of a Casson fluid due to an impulsively started moving flat plate, "Heat Transfer—Asian Research, **40**(6), 563-576 (2011). https://doi.org/10.1002/htj.20358
[13] Shashikumar, N.S., Kumara, B.P., Gireesha, B.J. and Makinde, O.D., "Thermodynamics analysis of MHD Casson fluid slip flow in a porous microchannel with thermal radiation," Diffusion foundations, **16**, 120-139 (2018). https://doi.org/10.4028/www.scientific.net/df.16.120
[14] Choi, S.U.S. "Enhancing thermal conductivity of fluids with nanoparticles," in: *Development and Applications of Non-Newtonian Flows*, edited by D. Singer, and H. Wang, (American Society of Mechanical Engineers, New York, 1995), pp. 99-106.
[15] Tiwari, R.K. and Das, M.K., "Heat transfer augmentation in a two-sided lid-driven differentially heated square cavity utilizing nanofluids," International Journal of heat and Mass transfer, **50**(9-10), 2002-2018 (2007). https://doi.org/10.1016/j.ijheatmasstransfer.2006.09.034
[16] Khan, U., Zaib, A., Pop, I., Waini, I. and Ishak, A., "MHD flow of a nanofluid due to a nonlinear stretching/shrinking sheet with a convective boundary condition: Tiwari–Das nanofluid model," International Journal of Numerical Methods for Heat & Fluid Flow, **32**(10), 3233-3258 (2022). https://doi.org/10.1108/hff-11-2021-0730
[17] Kumar, M., Reddy, G.J., Kumar, N.N. and Bég, O.A., "Computational study of unsteady couple stress magnetic nanofluid flow from a stretching sheet with Ohmic dissipation," Proceedings of the Institution of Mechanical Engineers, Part N: Journal of Nanomaterials, Nanoengineering and Nanosystems, **233**(2-4), 49-63 (2019). https://doi.org/10.1177/2397791419843730
[18] Bao, H.X., Arain, M.B., Shaheen, S., Khan, H.I., Inc, M. and Yao, S.W., "Boundary-layer flow of heat and mass for Tiwari-Das nanofluid model over a flat plate with variable wall temperature," Thermal Science, **26**(Spec. issue 1), 39-47 (2022). https://doi.org/10.2298/tsci22s1039b
[19] Mustafa, M., Khan, J.A., Hayat, T. and Alsaedi, A., "Numerical solutions for radiative heat transfer in ferrofluid flow due to a rotating disk: Tiwari and Das model," International Journal of Nonlinear Sciences and Numerical Simulation, **19**(1), 1-10 (2018). https://doi.org/10.1515/ijnsns-2015-0196
[20] Shekar, B. C., & Kishan, N. "Finite element analysis of natural convective heat transfer in a porous square cavity filled with nanofluids in the presence of thermal radiation," Journal of Physics: Conference Series, **662**(1), 012017 (2015). https://doi.org/10.1088/1742-6596/662/1/012017
[21] Suresh, S., Venkitaraj, K.P., Selvakumar, P. and Chandrasekar, M., "Effect of Al2O3–Cu/water hybrid nanofluid in heat transfer," Experimental Thermal and Fluid Science, **38**, 54-60 (2012). https://doi.org/10.1016/j.expthermflusci.2011.11.007
[22] Waqas, H., Farooq, U., Liu, D., Abid, M., Imran, M. and Muhammad, T., "Heat transfer analysis of hybrid nanofluid flow with thermal radiation through a stretching sheet: A comparative study," International Communications in Heat and Mass Transfer, **138**, 106303 (2022). https://doi.org/10.1016/j.icheatmasstransfer.2022.106303
[23] Muneeshwaran, M., Srinivasan, G., Muthukumar, P. and Wang, C.C., "Role of hybrid-nanofluid in heat transfer enhancement–A review," International Communications in Heat and Mass Transfer, **125**, 105341 (2021). https://doi.org/10.1016/j.icheatmasstransfer.2021.105341; Jha, B. K. "Natural convection in unsteady MHD Couette flow," Heat and mass transfer, **37**(4), 329-331(2001). https://doi.org/10.1007/pl00013295
[24] Rajesh, V. and Öztop, H.F., "Conjugate MHD natural convection in a chamber filled by ternary hybrid nanofluid with entropy generation," Numerical Heat Transfer, Part A: Applications, **86**(19), 6671-6692 (2025). https://doi.org/10.1080/10407782.2024.2344201
[25] Hansda, S., Chattopadhyay, A., Goswami, K.D., Pandit, S.K., Öztop, H.F. and Sheremet, M.A., "Optimizing entropy production in bi-diffusive convection within trapezoidal porous enclosure using radiative trihybrid nanofluids and T-shaped baffle," European Journal of Mechanics-B/Fluids, **113**, 204268 (2025). https://doi.org/10.1016/j.euromechflu.2025.204268
[26] Attia, H. A. "Unsteady hydromagnetic Couette flow of dusty fluid with temperature dependent viscosity and thermal conductivity," International Journal of Non-Linear Mechanics, **43**(8), 707-715 (2008). https://doi.org/10.1016/j.ijnonlinmec.2008.03.007
[27] Ghara, N., Maji, S. L., Das, S., Jana, R., & Ghosh, S. K. "Effects of Hall current and ion-slip on unsteady MHD Couette flow," Open Journal of Fluid Dynamics, **2**(01), 1 (2012). https://doi.org/10.4236/ojfd.2012.21001
[28] K. Jha, B., & A. Apere, C. "Combined effect of hall and ion-slip currents on unsteady mhd couette flows in a rotating system," Journal of the Physical Society of Japan, **79**(10), 104401 (2010). https://doi.org/10.1143/jpsj.79.104401
[29] Guria M, Jana RN, Ghosh SK, "Unsteady Couette flow in a rotating system," Int. J. Non-Linear Mech. **41**, 838–843 (2006). https://doi.org/10.1016/j.ijnonlinmec.2006.04.010

[30] Ali, A. O., & Makinde, O. D. "Modelling the Effect of Variable Viscosity on Unsteady Couette Flow of Nanofluids with Convective Cooling," Journal of Applied Fluid Mechanics, **8**(4), 793-802 (2015). https://doi.org/10.18869/acadpub.jafm.67.223.22967
[31] Karim, M. E., Samad, M. A., & Ferdows, M. "Numerical study of the effect of variable viscosity on unsteady pulsatile nanofluid flow through a Couette channel of stretching wall with convective heat transfer," AIP Conference Proceedings, **2121**(1), 070005 (2019). https://doi.org/10.1063/1.5115912
[32] Hajmohammadi, M. R. "Cylindrical Couette flow and heat transfer properties of nanofluids; single-phase and two-phase analyses," Journal of Molecular Liquids, **240**, 45-55 (2017). https://doi.org/10.1016/j.molliq.2017.05.043
[33] Wakif, A., Boulahia, Z., Ali, F., Eid, M. R., & Sehaqui, R. "Numerical analysis of the unsteady natural convection MHD Couette-nanofluid flow in the presence of thermal radiation using single and two-phase nanofluid models for Cu-water nanofluids," International Journal of Applied and Computational Mathematics, **4**(3), 1-27 (2018). https://doi.org/10.1007/s40819-018-0513-y
[34] Zeeshan, A., Khan, M.I., Ellahi, R. and Marin, M., "Computational intelligence approach for optimising MHD Casson ternary hybrid nanofluid over the shrinking sheet with the effects of radiation," Applied Sciences, **13**(17), 9510 (2023). https://doi.org/10.3390/app13179510
[35] Akbar, N.S., Hussain, M.F., Alghamdi, M. and Muhammad, T., "Thermal characteristics of magnetized hybrid Casson nanofluid flow in a converging–diverging channel with radiative heat transfer: A computational analysis," Scientific Reports, **13**(1), 21891 (2023). https://doi.org/10.1038/s41598-023-49397-3
[36] Das, S., Ali, A. and Jana, R.N., "Insight into the dynamics of magneto-casson hybrid nanoliquid caused by a plate rotation," World Journal of Engineering, **18**(1), 66-84 (2021). https://doi.org/10.1108/wje-07-2020-0261
[37] Krishna, M.V., "Hall and ion slip effects on the MHD flow of Casson hybrid nanofluid past an infinite exponentially accelerated vertical porous surface," Waves in Random and Complex Media, **34**(5), 4658-4687 (2024). https://doi.org/10.1080/17455030.2021.1998727
[38] Mishra, S.R., Mathur, P. and Pattnaik, P.K., "Hybrid nanofluid flow of non-Newtonian Casson fluid for the analysis of Entropy through a permeable medium," Journal of Nanofluids, **11**(3), 328-339 (2022). https://doi.org/10.1166/jon.2022.1846
[39] Rehman, A., Khan, D., Mahariq, I., Elkotb, M.A., and Elnaqeeb, T., "Viscous dissipation effects on time-dependent MHD Casson nanofluid over stretching surface: A hybrid nanofluid study," Journal of Molecular Liquids, **408**, 125370 (2024). https://doi.org/10.1016/j.molliq.2024.125370
[40] Varatharaj, K., Tamizharasi, R., Sivaraj, R. and Vajravelu, K., "Simulation of MHD-Casson hybrid nanofluid dynamics over a permeable stretching sheet: effects of heat transfer and thermal radiation," Journal of Thermal Analysis and Calorimetry, **149**(15), 8693-8711 (2024). https://doi.org/10.1007/s10973-024-13347-6
[41] Balla, C.S., Ali, K. and Rajashekhar Reddy, Y., "Effectiveness of silver-magnesium oxide-water hybrid nanofluid in Couette channel," Proceedings of the Institution of Mechanical Engineers, Part N: Journal of Nanomaterials, Nanoengineering and Nanosystems, **239**(1-2), 3-10 (2025). https://doi.org/10.1177/23977914231196379
[42] Ali, K., Reddy, Y.R. and Shekar, B.C., "Thermo-fluidic transport process in magnetohydrodynamic Couette channel containing hybrid nanofluid," Partial Differential Equations in Applied Mathematics, **7**, 100468 (2023). https://doi.org/10.1016/j.padiff.2022.100468
[43] Raza, A., Almusawa, M.Y., Ali, Q., Haq, A.U., Al-Khaled, K. and Sarris, I.E., "Solution of water and sodium alginate-based casson type hybrid nanofluid with slip and sinusoidal heat conditions: A prabhakar fractional derivative approach," Symmetry, **14**(12), 2658 (2022). https://doi.org/10.3390/sym14122658
[44] Paul, A., Sarma, N. and Patgiri, B., "MHD Al2O3/Cu-water Casson hybrid nanofluid flow across a porous exponentially stretching sheet," Latin American Applied Research-An international journal, **54**(4), 467-476 (2024). https://doi.org/10.52292/j.laar.2024.3282
[45] Reddy, V.S., Kandasamy, J. and Sivanandam, S., "Impacts of casson model on hybrid nanofluid flow over a moving thin needle with dufour and soret and thermal radiation effects," Mathematical and Computational Applications, **28**(1), 2 (2022).
[46] Sarkar, A., Mondal, H. and Nandkeolyar, R., "Mixed convective hydromagnetic unsteady Casson hybrid nanofluid flow analysis and entropy optimization over an inclined surface with viscous dissipation," Discover Molecules, **2**(1), 10 (2025).
[47] Ishaq, M., Khan, S.U., Garalleh, H.A., Sowayan, A.S. and Tlili, I., "Thermal performance of casson hybrid nanofluid with radiative effects and convective conditions: applications to energy systems and industrial heat transfer," Multiscale and Multidisciplinary Modeling, Experiments and Design, **8**(2), 141 (2025). https://doi.org/10.1007/s41939-024-00720-z

FDM-МОДЕЛЮВАННЯ ПОТОКУ ТА ТЕПЛОПЕРЕНОСУ ГІБРИДНОЇ НАНОРІДИНИ КАССОНА Cu–Al_2O_3/ВОДА В СИСТЕМІ КУЕТТА

Хасім Алі[1], Рамеш Аллугувеллі[2], Сватмарам[3], Чандра Шекар Балла[4], К. Правін Кумар[5], Е. Джагатпрабхав[6]
[1]Кафедра математики, інженерно-технологічний коледж імені Наваба Шаха Алама Хана, Хайдерабад, Телангана, 500024, Індія
[2]Кафедра математики, інженерно-технологічний коледж імені Гітанджалі, Кісара, Хайдерабад, Телангана, 501303, Індія
[3]Кафедра математики, технологічний інститут Чайтаньї Бхаратхі, Хайдерабад, Телангана, 500075, Індія
[4]Урядовий молодший коледж, Амангал, Ранга Редді, Телангана, 509321, Індія
[5]Кафедра гуманітарних наук та природничих наук, державний політехнічний інститут, Хайдарабад, Телангана, 500028, Індія
[6]Кафедра гуманітарних наук та природничих наук, державний політехнічний інститут, Шаднагар, Телангана, 509216, Індія

У цій статті чисельно досліджується нестаціонарна гібридна нанорідина Куетта-Кассона (HNF), що містить наночастинки міді (Cu) та оксиду алюмінію (Al_2O_3), розчинені у воді. Верхня стінка приводиться в рівномірний рух, а нижня стінка вважається нерухомою та розтяжною. Для інтегрування керованих нелінійних диференціальних рівнянь з частинними похідними використовується метод скінченних різниць (FDM). Результати досліджуються за допомогою ліній струму, ізотерм, числа Нуссельта та поверхневого тертя. Обговорюється вплив ключових безрозмірних чисел, таких як число Грасгофа, число Біо, параметр розтягування, параметр Кассона та число Екерта, на HNF Cu-Al_2O_3-вода. Результати показують, що потік та теплопередача (HT) можуть значною мірою контролюватися ключовими параметрами.

Ключові слова: *потік Куетта; змінна в'язкість; нанорідина Al_2O_3-H_2O; число Біо; параметр розтягування*

East European Journal of Physics. 1. 484-489 (2026)
DOI:10.26565/2312-4334-2026-1-55 ISSN 2312-4334

IMPLEMENTATION OF HARMONIC MAPPING TO A CLOAK PHENOMENON

Najma Abdul Rehman[1], Muhammad Raza[1], Oleg Rybin[2]*, Sergey Shulga[2]
[1]*Department of Mathematics, COMSATS University Islamabad, Sahiwal Campus, Sahiwal, Pakistan*
[2]*School of Radio Physics, Biomedical Electronics & Computer Systems,*
V.N. Karazin Kharkiv National University, Kharkiv, Ukraine
**Corresponding Author email: oleg.rybin@karazin.ua*
Received November 11, 2025; revised February 7, 2026; accepted February 24, 2026

In this work, a novel physical transformation-based approach has been employed to realize the cloak effect. The transformation mapping is derived for the first time by minimizing the energy functional subject to specified geometric constraints on the scatterer's boundaries. This variational problem has been solved using a physics-informed neural network to solve the boundary-value problem for the Laplace equation. Numerical analysis and graphical visualization of the obtained results clearly demonstrate weak scattering and distortion, as well as negligible perturbation to exterior fields. Furthermore, we show that the proposed mapping achieves considerably improved performance compared with conventional transformation-based cloaking methods, which can be used to mask compact radiating devices, particularly patch antennas.
Keywords: *Harmonic maps; Physics-informed neural network; Cloaking; Laplace equation; Energy functional minimization*
PACS: 41.20.Cv; 02.70.-c

1. INTRODUCTION

Research on harmonic maps originated from the study of harmonic functions and the Dirichlet principle. Indeed, Joseph Sampson [1], James Eells, and L. Lemaire [2] formally introduced harmonic maps as a generalization of harmonic functions to maps between Riemannian manifolds, defining them as the critical points of an associated energy functional [2]. Harmonic maps have a strong mathematical foundation because they preserve both the shape and the continuity of the underlying objects. Due to its analytical and geometric properties, the theory of harmonic maps has a wide range of applications in physics, including quantum physics, fluid dynamics, gravitation, electrostatics, image processing, and learning-based studies [3-7].

Transformation optics is a fundamental approach for designing invisibility cloaks by using coordinate transformations to control physical fields across a wide range of subjects [8-10]. In electromagnetic and Optics, Transformation optics (TO) aims to map the behaviour of light around an object/scatterer from virtual space to a transformed physical space, thereby controlling the bending and propagation of light to achieve cloaking invisibility [11-13]. In fact, the main idea behind cloaking is that an appropriate coordinate transformation maps a virtual space into a physical space, and the material parameters required for field guidance are derived from the transformation's Jacobian. Initially, the method was applied to the transformation of Maxwell's equations; later, this framework was extended to other governing equations under various coordinate transformations [10, 14-18]. This, in turn, shows that developing mapping approaches is a direct path toward establishing TO as a multidisciplinary research subject.

In this study, we model the cloak phenomenon using harmonic maps rather than a conventional coordinate transformation. We show that harmonic maps, as critical points of an energy functional, naturally yield smooth, regularized cloaking transformations. Furthermore, the elements of the tensor of material parameters derived from this transformation are generally bounded, which leads to a low distortion field manipulation. By employing harmonic maps, undesirable scattering can be considerably reduced. Moreover, the harmonic maps are combined with transformation optics and a physics-informed neural network (PINN) based approach to achieve the desired invisibility effect. Fig. 1 illustrates the main steps of the proposed methodology.

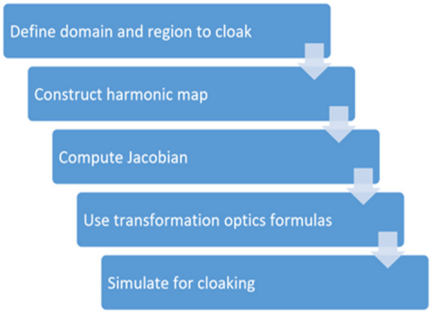

Figure 1. Flow chart of the proposed method

Cite as: N.A. Rehman, M. Raza, O. Rybin, S. Shulga, East Eur. J. Phys. 1, 484 (2026), https://doi.org/10.26565/2312-4334-2026-1-55

According to Fig. 1, the transformation domain and cloaked region are first defined. Using these, transformed coordinates are obtained through a harmonic map with appropriate boundary conditions. The corresponding Jacobian matrices are then computed at domain points, and the tensor field matrices are derived using transformation optics formulas. Finally, the cloaking configuration is simulated.

METHODS AND RESULTS

The main target of this study is to design a transformation from virtual space to physical space providing the cloak invisibility for a circular region. The appropriate transformation F is based on harmonic mapping.

The cloak phenomenon in a region is going to be confirmed in this study by absence or minimization of the energy of field coming to the region from outside. Accepting that the Laplace equation as a governing one in the study, one can estimate the above field energy by the energy functional $EN(F)$ given by

$$EN(F)=\frac{1}{2}\int_{\Omega}\|\nabla F\|^2 d^3\vec{r}\,, \tag{1}$$

where Ω is the virtual space.

The Problem Statement

Consider three circles C_i ($i=0,1,2$) with radius r_i respectively with centers at the origin $(0,0)$ in 2-D Cartesian coordinate system (x,y). Let R_i be the region inside the circles C_i. Define the annular regions $\Omega=R_2\setminus R_0$ and $D=R_2\setminus R_1$, and construct a harmonic map $F:\Omega\to D$ defined as:

$$F(x,y)=(F_1(x,y),F_2(x,y))\,, \tag{2.1}$$

where $\forall(x,y)\in\Omega$ the following boundary conditions are imposed:

$$\left.\begin{aligned}&\forall(x,y)\in C_2:(F_1,F_2)\in C_2,\\&\forall(x,y)\in\left\{(x,y)\,|\,r_0^2\le x^2+y^2\le r_1^2\right\}:(F_1,F_2)\in C_1.\end{aligned}\right\} \tag{2.2}$$

For the sake of clarity, we assume in this study the that: $r_0=0.3$, $r_1=1$, $r_2=2$. It is assumed that a domain around of the origin is to be cloaked. In order to succeed, we are going to minimize the functional $EN(F)$ subject to constraints in the form of Eqs. (2), to further compute the desired transformation.

The setup of the study in the form of Eqs. (2a) is presented in Fig. 2 where the domain region depicted in the Figure part (a) is the virtual domain. Figure 2(b) shows the target region (the physical domain) which is to be achieved after applying the optimized (minimized) functional $EN(F)$.

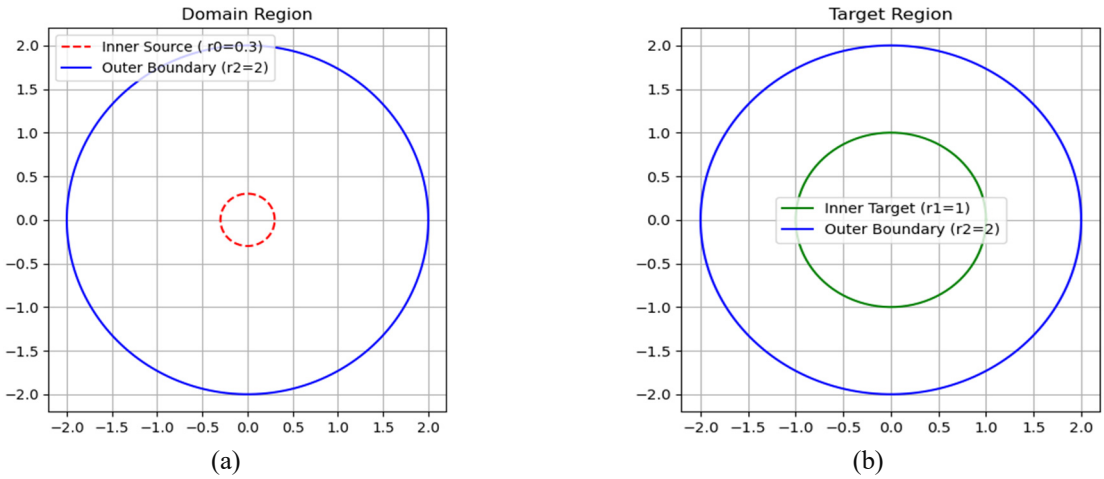

Figure 2. Setup of study for (a) virtual space, (b) physical space.

In the next section, as one of the targets of our study, we use neural network computations and get the transformation based on harmonicity of the functional $EN(F)$.

PINNs Setup

To minimize energy functional (1) subject to constraints (2), we setup a neural network of four layers with two hidden layers, one input and one output layer. Input (x,y) and output $F(x,y)=(F_1(x,y),F_2(x,y))$ layers have two

neurons. Each hidden layer has 32 neurons. We have used here the function $\sigma = \tanh(\cdot)$ as an activation function. Layers relations can be represented by the system:

$$\left.\begin{aligned} &U_{n+1} = \sigma(W_n U_n + b_n),\ n = 1,2, \\ &U_1 = (x,y)^T, \\ &U_4 = W_3 U_3 + b_3 = (F_1(x,y),\ F_2(x,y))^T. \end{aligned}\right\} \tag{3}$$

The output of the previous layer is the input of next layer. W_1 is weight matrix of order 32×2, W_2 and W_3 are weight matrices of order 32×32, W_4 is a weight matrix of order 2×32. We take the weight matrix entries as random normal distribution to minimize loss as suggested for PINNs, [19-21]. Bias matrix b_n, $(n = 1,2,3)$ each of order 32×1, b_4 is of order 2×1, with constant entries 0. We take collocation points $N_\Omega = 1000$ in annular region Ω, boundary points on C_2 as $N_2 = 200$, points on $\{(x,y) \mid 0.09 \le x^2 + y^2 \le 1\}$ as $N_0 = 300$.

Under the above assumptions, the mean square error or loss has been computed in this study by the formula:

$$\begin{aligned} MSE &= MSE_{\text{annular region }\Omega} + MSE_{\{0.3\le x^2+y^2\le 1\}} + MSE_{\text{boundary } C_2} \\ &= \frac{1}{N_1}\sum_{i=1}^{N_1}\left[\left(\frac{\partial^2 F_1}{\partial x^2}\right)_i + \left(\frac{\partial^2 F_1}{\partial y^2}\right)_i\right]^2 + \left[\left(\frac{\partial^2 F_2}{\partial x^2}\right)_i + \left(\frac{\partial^2 F_2}{\partial y^2}\right)_i\right]^2 + \frac{1}{N_0}\sum_{j=1}^{N_0}\left|norm\left(F_{\{0.3\le x^2+y^2\le 1\}}\right)_j - 1\right|^2 \\ &+ \frac{1}{N_2}\sum_{k=0}^{N_2}\left|\left(F_{\text{outer boundary}}\right)_k - (x,y)_k\right| = 0.02. \end{aligned} \tag{4}$$

The graph showing loss during training of our PINN for obtaining the optimal value of the MSE is depicted in Fig. 3.

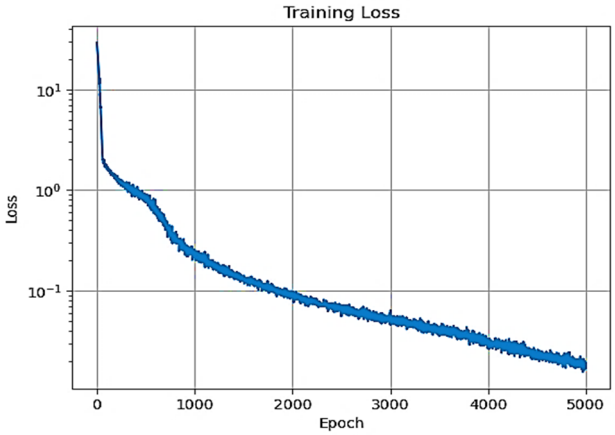

Figure 3. Graph of loss curve obtained during training PINN

The results of prediction of the map F during training PINN are shown Figure 4: the graph (a) shows original grid in domain Ω while the graphs (b) stands for the already mapped (target) domain after applying the map F to the grid depicted in graphs (a).

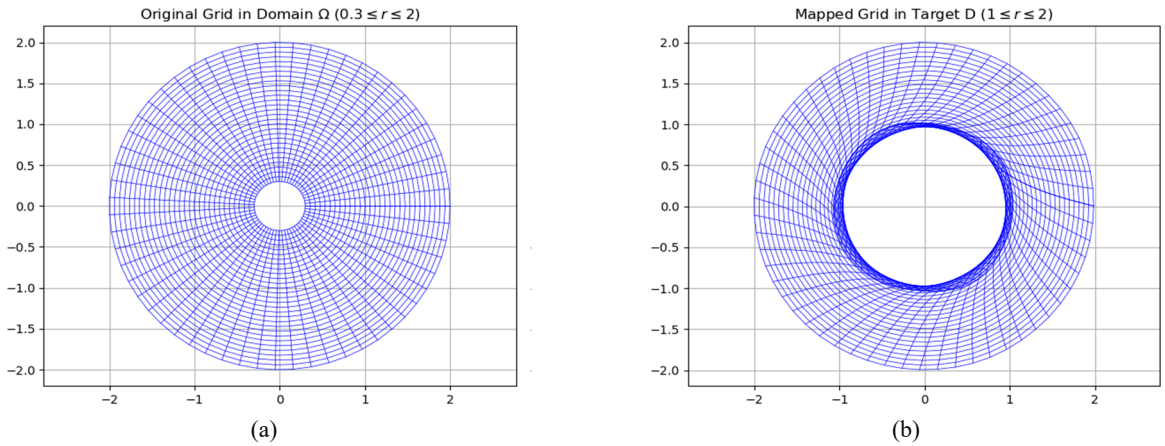

Figure 4. Transforming domain Ω by using the obtained optimized map F.

As a next step (as per the flow chart of Fig.1), we evaluate the Jacobean J_F based on the predicted values of map $F(x,y)$:

$$J_F = \begin{bmatrix} \dfrac{\partial F_1}{\partial x} & \dfrac{\partial F_1}{\partial y} \\ \dfrac{\partial F_2}{\partial x} & \dfrac{\partial F_2}{\partial y} \end{bmatrix}, \tag{5}$$

where partial derivatives of $F(x,y)$ have been computed by calling *tf.gradient* function in tensor flow by above neural setup.

Then material tensor $A(x,y)$ given by

$$A = \frac{J_F J_F^T}{\det J_F}, \tag{6}$$

has been computed at all domain points.

We get symmetric positive definite material tensor $A(x,y)$ of order 2×2, $\forall (x,y)\in \Omega$.

Cloak Setup

Throughout the study, the field distribution in the region Ω is defined by the two-dimensional potential $u(x,y)$. This means that the govern equation of the original region/domain is the isotropic Laplace equation:

$$\nabla^2 u = 0, \tag{7}$$

while the governing equation of the target region/domain is already the anisotropic Laplace equation:

$$\nabla(A\nabla u) = 0. \tag{8}$$

due to the tensor *A*.

Notice that physically material tensor *A* shows directional conductivity, the flux or flow vector which can be defined as $\vec{q} = -A\nabla u$.

Taking into account the definition of the harmonic map (2) leads to Dirichlet's problem for the potential $u(x,y)$ in the target domain:

$$\left.\begin{aligned} &\nabla(A\nabla u) = 0, \\ &\begin{cases} u(x,y) = 0 & \forall (x,y)\in C_1 \\ u(x,y) = 1 & \forall (x,y)\in C_2 \end{cases}. \end{aligned}\right\} \tag{9}$$

where C_1 and C_2 are the inner and outer boundaries of already transformed region introduced in the Problem Statement section.

We solve Eqs. (9) using a neural setup. For this reason, we set up a five-layer neural network with three hidden layers, one input layer, and one output layer. Input (x,y) and output $u(x,y)$ layers have two and one neurons respectively. Each hidden layer has 125 neurons. The activation function is $\sigma = \tanh(\cdot)$. The layers' relation mathematically is the same as explained in the PINNs Setup section. Thus, the mean square error/loss has been computed as:

$$MSE = MSE_{PDE} + MSE_{boundary\ C_2} = 0.2, \tag{10}$$

while Fig. 5 shows the plot of the solution.

One can see from the figure that Fig. 5(a) clearly reflects the Dirichlet boundary conditions, value of potential $u(x,y)$ is high at outer boundary and smoothly decreases up to inner boundary. At the same time, Fig. 5(b) shows the symmetry about an axis, say *z*-axis, reflecting the symmetry of material tensor. The surface curves are smoothly showing nonlinear variation of potential which is the result of anisotropic material tensor computed from transformation based on harmonicity of the mapping. Thus, both figures (a) and (b) show the effeteness of gradient distribution clearly showing a successful achieving the cloak phenomenon.

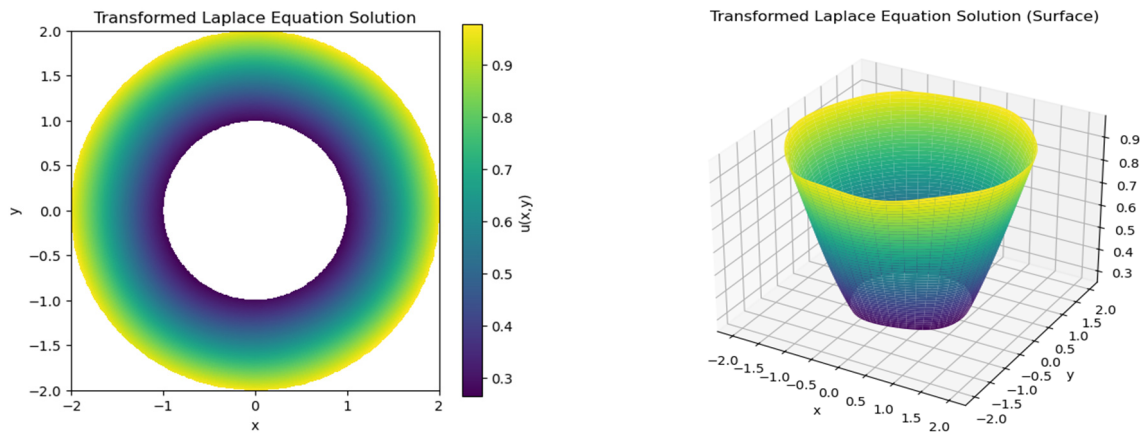

(a) (b)

Figure 5. (a) Clocked region and boundary. **(b)** Surface plot of anisotropic Laplace equation.

DISCUSSION AND ANALYSIS

Further to show the effectiveness of proposed method based on harmonicity and neural computations, the gradient magnitude behaviour on transformed grid and radial profile have been plotted in Fig. 6. Smoothness and continuity show a weak distortion outside the cloaked region and there is smooth transition between cloaked and uncloaked region.

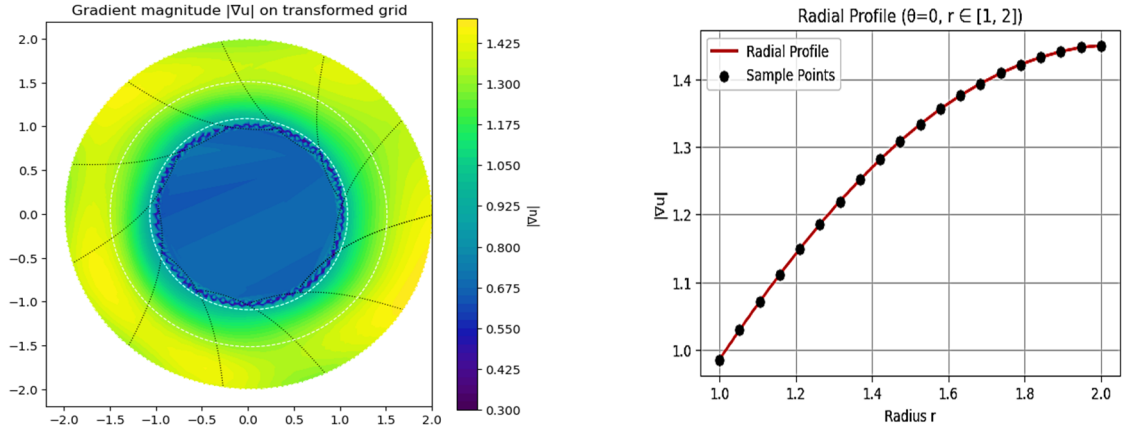

(a) (b)

Figure 6. (a) Gradient magnitude of potential on transformed grid. **(b)** Radial profile of Gradient magnitude of potential.

Resuming the results of previous section, one can clearly observe that Fig. 5-6 show how the transformation affects the gradient by compressing the potential variation near the inner region, making it appear as if the solution is smoothly pushed upward. This behaviour is consistent with cloaking mappings, where the anisotropic tensor redistributes the flow around the cloaked region without allowing penetration. It, in fact, enable to use the proposed method for masking the objects situated in the origin.

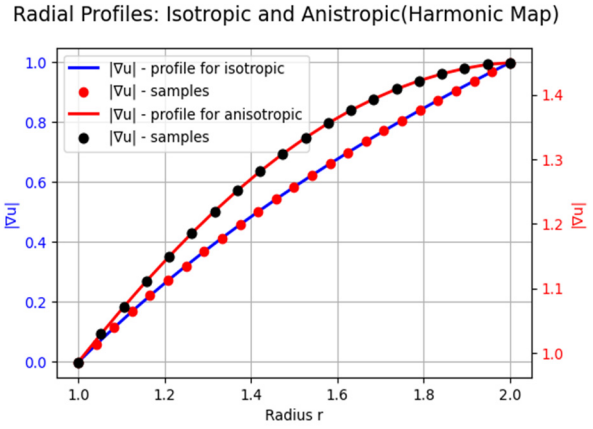

Figure 7. Radial Profile of gradient magnitude.

In Fig. 7, the radial profile of the magnitude of has been compared for isotropic and anisotropic cases (with harmonic transformation). In both cases, the radial profile increases with respect to radius *r,* however, in the anisotropic case, the gradient grows more rapidly. For the isotropic case, the magnitude of ∇u for origin domain increases approximately linearly with r while in the anisotropic case (this is, in fact, rather relative to $A\nabla u$), the harmonic map based transformation modifies the radial scaling, resulting in an amplified gradient magnitude. Physically, this implies that the gradient exhibits stronger behavior near the outer boundary in the transformed medium which is important with a viewpoint of masking applications, in particular patch antenna masking.

CONCLUSIONS

In this study, a new transformation model based on harmonic mapping has been created for designing 2-D circular cloaking structures. The model provides an alternative to conventional radial-based coordinate transformations widely used in applications of trans-formative optics. While computing the transformation coordinates under boundary constraints composed on the mapping, the resulting tensor field remains smooth. Numerical simulations of the transformed governing equation have confirmed that the proposed framework achieves effective field redirection with extremely weak scattering and distortion as well as stronger behaviour of the transformed field near the outer boundary. This new approach may be further adapted to diverse applications including object masking, in particular patch antennas.

The study shows the prospects for joint use harmonic mapping and methods of transformation optics as multidisciplinary subject.

Acknowledgments

O. Rybin, and S. Shulga are grateful to the National Research Foundation of Ukraine for support of this work through the project grant (No. 2025.06/0108).

ORCID

Najma Abdul Rehman, https://orcid.org/0000-0001-8952-8968; **Muhammad Raza**, https://orcid.org/0000-0002-1026-0856
Oleg Rybin, https://orcid.org/0000-0002-4472-6861; **Sergey Shulga,** https://orcid.org/0000-0002-9392-9366

REFERENCES

[1] J. H. Samson, Annales scientifiques de l'É.N.S. 4e série. **11**(2), 211-228 (1978). https://doi.org/10.24033/asens.1344
[2] J. Eells, and L. Lemaire, Bull, London Math. Soc. **20**, 385-524. https://doi.org/10.1112/blms/10.1.1
[3] C.W. Misner, Physical Review D, **18**(12), 4510-4524 (1978). https://doi.org/10.1103/PhysRevD.18.4510
[4] X Zhai, C. Huang, & G. Ren, Scientific Reports, **10**, 18281 (2020). https://doi.org/10.1038/s41598-020-75211-5
[5] Q. Zhao, J. Liang, and Z. Xu, The Journal of Chemical Physics, **149**, 084111 (2018), https://doi.org/10.1063/1.5044438
[6] E. Chong, L. Zhang, and V.J. Santos, The International Journal of Robotics Research, **40**(2-3), 534-537 (2020). https://doi.org/10.1177/0278364920962205
[7] M. Kazemia, and Y.J. Moghaddam, Journal of Finsler Geometry and its Applications, **6**(1), 23-25 (2025). https://doi.org/10.22098/jfga.2024.16018.1140
[8] J.B. Pendry, *et al*. Science, **312**(5781), 1780-1782 (2006). https://doi.org/10.1126/SCIENCE.1125907
[9] L. Zhou, Brazilian Journal of Physics, **46**(1), 35-40 (2016). https://doi.org/10.1007/s13538-015-0378-z
[10] L. Zeng, and W. Xie, Modern Physics Letters B, **32**(21) 1850237 (2018). https://doi.org/10.1142/S0217984918502378
[11] J.B. Pendry, Y. Luo, & R. Zhao, Science, **348**(6234), 521-524 (2015). https://doi.org/10.1126/science.1261244
[12] H. Kan, L. Xu, Y. Xu, and H. Chen, Europhysics Letters, **117**(3), 34002 (2017). https://doi.org/10.1209/0295-5075/117/34002
[13] M.S. Khan, R.A. Shakoor, O. Fayyaz, and E.M. Ahmed, Optik, **297**, 171575 (2024). https://doi.org/10.1016/j.ijleo.2023.171575
[14] J.-H. Huang, H.-J. Ren, & T.-Y. Huang, Scientific Reports, **15**, 9427 (2025). https://doi.org/10.1038/s41598-025-94344-z
[15] M. Raza, Materials Research Express, **7**(5), 055802 (2020). https://doi.org/10.1088/2053-1591/ab8fba
[16] M. Raza, M. Ahsan, W.B. Alonazi, S.A. Naqvi, and B. Braaten, Physica Scripta, **98**(11), 115029 (2023). https://doi.org/10.1088/1402-4896/acfc6e
[17] J. Zhan, K. Li, Y. Zhou, X. Liu, and Y. Ma, ACS Applied Materials & Interfaces, **13**(14), 17104-17109 (2021). https://doi.org/10.1021/acsami.1c02117
[18] O. Rybin, M. Raza, S. Shulga, and N.A. Rehman, Zeitschrift für Naturforschung A, **80**(5), 335-344 (2025). https://doi.org/10.1515/zna-2024-0206
[19] M. Raissi, and G.E. Karniadakis, Journal of Computational Physics, **357**, 125–141 (2018). https://doi.org/10.1016/j.jcp.2017.11.039
[20] Z. Fang, and J. Zhan, IEEE Access, **8**, 24506–24513 (2019). https://doi.org/10.1109/ACCESS.2019.2963375
[21] A. Farea, O. Yli-Harja, and F. Emmert-Streib, Artificial Intellect, **5**(3), 1534-1557 (2024). https://doi.org/10.3390/ai5030074

ВПРОВАДЖЕННЯ ГАРМОНІЧНОГО ЗОБРАЖЕННЯ ДЛЯ ФЕНОМЕНА НЕВИДИМОСТІ

Найма Абдул Рехман[1], Мухаммед Раза[1], Олег Рибін[2], Сергій Шульга[2]
[1]Кафедра математики, Ісламабадський університет інформаційних технологій, Сагівальський кампус, Сагівал, Пакистан,
[2]Факультет радіофізики, біомедичної електроніки та комп'ютерних систем, Харківський національний університет імені В.Н. Каразіна, Харків, Україна

У даній роботі для реалізації феномену маскування було застосовано новий підхід, заснований на фізичній трансформації. Вперше було отримано трансформаційне відображення шляхом мінімізації енергетичного функціоналу з урахуванням заданих геометричних обмежень, накладених на межі розсіювача. Ця варіаційна задача була вирішена шляхом застосування фізично-інформованої нейронної мережі для вирішення граничної задачі для рівняння Лапласа. Чисельний аналіз і графічна візуалізація отриманих результатів чітко демонструють слабке розсіювання і спотворення, а також незначне збурення зовнішніх полів. Крім того, ми показуємо, що запропоноване відображення дозволяє досягти значно кращих результатів у порівнянні з традиційними методами маскування на основі перетворення.

Ключові слова: *гармонічне відображення; фізично-інформованої нейронної мережі; невидимість; рівняння Лапласа; мінімізація енергетичного потенціалу*

EAST EUROPEAN JOURNAL OF PHYSICS. 1. 490-495 (2026)
DOI:10.26565/2312-4334-2026-1-56 ISSN 2312-4334

OPTIMIZATION OF THE OPTICAL PROPERTIES OF BLACK SILICON SOLAR CELL

M. Azouza[1]*, N. Mekkakia-Maaza[1,2], R. Dussart[2], T. Tillocher[2], P. Lefaucheux[2]
[1]LMSE, Microsystems and Embedded Systems Laboratory, University of Sciences and Technology of Oran Mohamed Boudiaf, BP1505 El Mnaouer, 31000, Oran, Algeria.
[2]GREMI, Université d'Orléans, 14 Rue d'Issoudun BP 6744, 45067 Orléans, France
**Corresponding Author e-mail: maamar.azouza@univ-usto.dz*
Received August 27, 2025; revised February 2, 2026; accepted February 22, 2026

Black silicon (BSi) is an important texturized form of a semiconducting material used in photovoltaic solar cell technology. It is characterized by surface structuration of silicon with very low reflectance. In this paper, we study the optical properties of black silicon in the visible-near infrared wavelength range. Our work focuses on texturing the silicon surface using cryogenic etching in an inductively coupled plasma (ICP) system. The surface structure of black silicon is formed by varying several parameters of the cryo-etching process, like wafer temperature, SF_6/O_2 ratio and bias voltage. The microstructure surfaces of BSi can be formed in various shapes (Pyramids, Columns, and Cones forms). The optical properties of the micro-structures were studied by spectrophotometer measurements. The results obtained show that columnar microstructures (CMS) exhibit different texturing shapes under different plasma etching process conditions. The CMS obtained without HF chemical treatment process have a reflectance value as high as about 14%. However, the surface reflectance is reduced to less than 2% in the VIS-NIR range by processing the samples in HF solution.
Keywords: *Black silicon; Surface texturing; Vis-NIR reflectance; Solar cell; HF process*
PACS: 78.67.−n / 78.68.+m /52.70.Kz

I. INTRODUCTION

Silicon is the second-most-abundant element on Earth, after oxygen. Its abundance and ease of processing make it a cost-effective, readily available material for various semiconductor applications. Crystalline silicon (c-Si) solar cells dominate more than 90% of the photovoltaic (PV) industry [1]. And its flat surface has a high natural reflectance around 35% in 300-1100nm spectral region [1]. Using Black silicon (BSi) as a surface texturing approach has shown promising results in improving the performance of c-Si solar cells and holds great potential for enhancing the efficiency of solar energy conversion. Black silicon (BSi) is an active candidate in the renewable energy area due to its potential applications in solar cells, its applications cover different fields such as photonic sensors and biosensors [2]. Black silicon (BSi) can be produced by several methods, such as electrochemical etching of macro porous silicon (macP-Si) [3, 4], metal assisted chemical etching (MACE) [5-6], femto-second laser [7], and inductively coupled plasma reactive ion etching (ICP-RIE) [8]. A Harvard University group has developed a process (Mazur's Method) in which Black silicon (BSi)is produced by irradiating Si with femto-second laser pulses. The reflectance of Black silicon (BSi), obtained by Mazur's process, is less than 5% and the absorbance is about 97%in the visible region [7]. Black silicon (BSi) is a surface modification of silicon where a nanoscale surface structure is formed bysilicon plasma etching. The resulting nanoscale structure provides an extremely low reflectivity. Because the Black silicon (BSi) surface nanostructure exhibits high absorption over a wide spectral range (250–2500 nm) [9], it offers an ideal solution as an Anti-reflective coating (ARC) for solar cells [9-10], as well as applications in photodetectors. The nanoscale structure may be in the form of inverted nanoscale cones (i.e. with the tip of the cones pointing upward away from the silicon surface) or a series of nanoscale pores of varying depths and diameters extending into the surface. Both types of nanoscale structures are distributed randomly over the silicon surface [11].

In this study, we used an inductively coupled plasma reactive ion etching (ICP-RIE) system. Which can be used to form Columns of different dimensions on a mask less silicon.

II. EXPERIMENT

II.1 Experimental device

Experiments and optimization settings are conducted using a commercial ICP reactor (Alcatel 601E). The source plasma is generated by an inductively coupled coil supplied by a 13.56 MHz R.F. generator. A 13.56 MHz generator powers the substrate holder electrode, allowing independent control of the bias potential. The substrate chuck is cooled with liquid nitrogen and maintained at a very low temperature (~-100°C) using resistances. To enhance the thermal conductivity between the substrate and the chuck, the wafer is electrostatically clamped to the chuck, and helium gas is injected under the wafer.

The standard cryogenic etching process uses SF_6/O_2 gas mixture to achieve deep silicon etching. For the experiments presented in this paper, the SF_6 flow rate was set to 200 sccm, and the total pressure was about 9 Pa.

Cite as: M. Azouza, N. Mekkakia-Maaza, R. Dussart, T. Tillocher, P. Lefaucheux, East Eur. J. Phys. 1, 490 (2026), https://doi.org/10.26565/2312-4334-2026-1-56

The Black silicon was obtained by the DRIE process with varying parameters at cryogenic temperature. The black silicon samples were produced on 6-inch-diameter maskless (100) silicon wafers with a thickness of 400 μm.

II.2. Black silicon formation mechanism:

Figure 1 shows the effect of O_2on the Etch profiles of maskless silicon after 10 min of process (source power 1500W, bias -50V, SF_6= 300 sccm, pressure 9 Pa, T: -100°C, Ar: 75sccm, at O_2flow rate of: 00, 30, 42, 60 sccm, respectively).

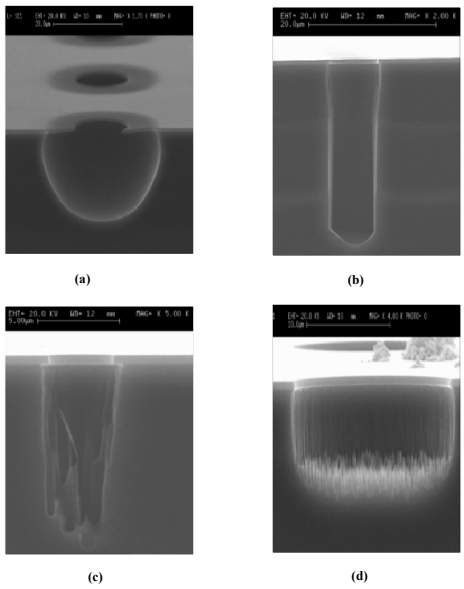

Figure 1. Etch profiles of mask-less silicon at different O_2 flow rate
(a): 00sccm, (b): 30sccm, (c): 42sccm, (d): 60sccm [13].

Black silicon, which is a grasslike structure, appears only at the bottom of the trench for high oxygen content as shown in Figure 1 (d), for an O_2/SF_6 ratio of 20%, indicating that we have reached the overpassivating regime, in this case, the increase of the oxygen flow rate tends to reinforce the passivation layer$S_iO_xF_y$, and the etching rate tends to a minimum value around 0.8 µm/min. In Figure 1 (a) dark areas correspond to the bottom of the structure and the white part corresponds to the top of the hole. [12].

The cryogenic etching process uses SF_6 / O_2 gas mixture to achieve a deep silicon etching at a very low temperature. The average diameter and height of black silicon (BSi) structures can be determined through precise measurements using advanced imaging and analysis techniques. To measure the diameter and height of black silicon structures, we first need high-resolution images of the sample surface. In our study, this is done using SEM. SEM provides a detailed view of BSi structures at micro- or nanometer scales. Structures are usually imaged from the top view to measure their base diameters or from a tilted angle to measure varying diameters along their height.

III- RESULTS AND DISCUSSION

1. Columnar Microstructures of Silicon (CMS)

The wafer temperature, O_2/SF_6 The flow rate ratio and bias voltage are the main parameters that play an important role in the formation of the black silicon. Basically, the microstructure appears in an overpassivating regime, i.e., for high O_2 / SF_6 ratios and at cryogenic temperature. Pressure process and voltage bias also play a role in its appearance [14]. The evolution of the typical microstructural dimensions (diameter and mean height) is studied as a function of wafer temperature and bias voltage. The images SEM of the textured silicon samples are shown in Figure 2.

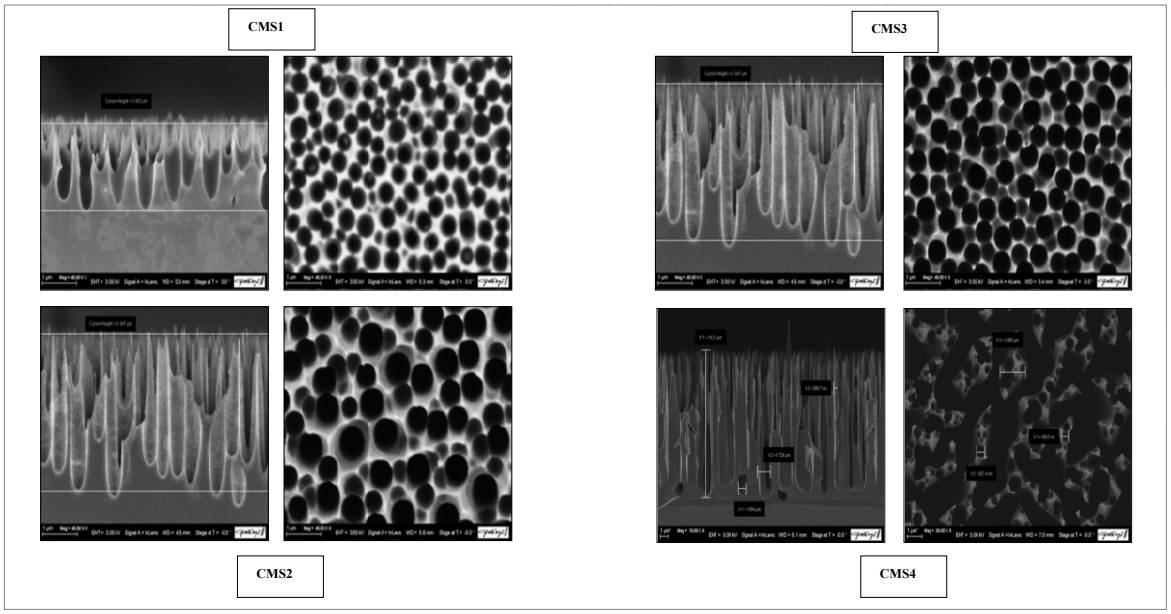

Figure 2. Image SEM with Top and Side views of samples with different Bias voltages (CMS1: -10V, CMS2: -15V, CMS3: -20V, CMS4: -25V [13]

A. Effect of Bias voltage on columnar formation

The influence of the bias voltage on the formation of Black silicon will be studied by varying its value from-10V to -25V (Table 1) under the following fixed conditions: ICP power 1000 W, SF_6 flow rate = 200 sccm, T = -120°C, pressure = 3 Pa, T = 10 min, O_2 flow rate = 16 sccm. Figure 2 summarizes the SEM observations of these samples showing different types of BSi structure.

Table 1. Variable parameters for the cryogenic process

Samples	V Bias (V)	T(°C)
CMS 1	-10	-120
CMS 2	-15	-120
CMS 3	-20	-120
CMS 4	-25	-120
CMS 5	-20	-105
CMS 6	-20	-110
CMS 7	-20	-115

From −10V to −20V of bias voltage, the mean height slightly increases from less than 1.8μm to about 3.47μm as shown in Figure 3, at the bias voltage of -25V; a significant increase in the average column height is obtained around 6.21µm. Thus, it seems that for such bias value and beyond, the ion energy is efficient enough to avoid the silicon passivation by a $S_iO_xF_y$ layer [12]. In cryogenic etching process, the bias voltage controls the energy and direction of the ions which arrive at the silicon surface. The BSi is formed for a bias voltage value between -10V and -25V. Figure 3 and Figure 4 show the morphological evolution of black silicon structures when the bias voltage varied from -10V to -25V.

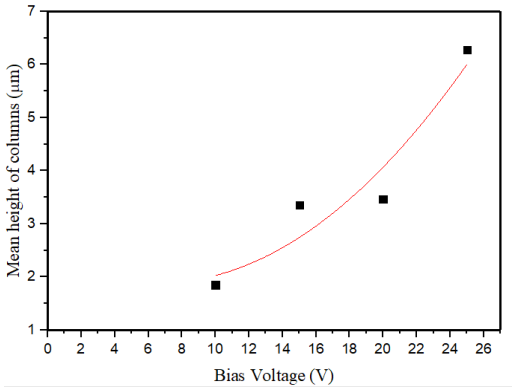

Figure 3. Mean column height versus bias voltage

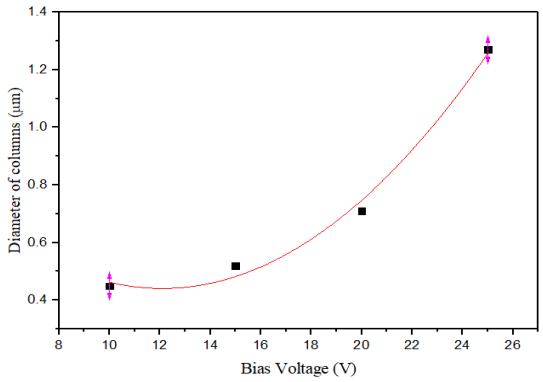

Figure 4. Mean column Diameter versus bias voltage

B. Effect of wafer temperature on column formation

We study the effect of wafer temperature on column formation under etching conditions of: power=1000W, SF_6 flow rate =200sccm, O_2 flow rate = 16sccm, pressure=3Pa, etching time=10 min, Bias voltage =-20V, and wafer temperature range from [-105°to-115°C] as shown on Table1. Figure 5 summarizes the SEM observations of samples showing different types of BSi structure.The formation of black silicon is very sensitive to the temperature gradient.

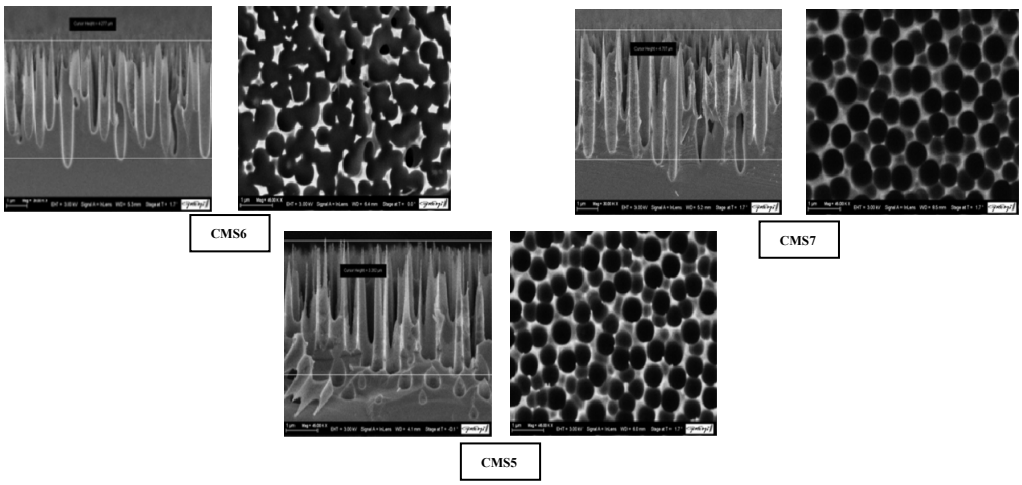

Figure 5. SEM with Top and Side view of samples with Wafer temperature (CMS5: -105°C, CM6: -110°C, CMS7: -115°C [13]

The cryogenic temperature also has very significant effects on the slope of the etching profile. For a temperature of -115°C (CMS7), we obtain a large increase of mean height column around 4.7µm as shown in Figure 6.

Figure 7 shows the morphological evolution of black silicon structures when the wafer temperature ranges from -105°C to-115°C.

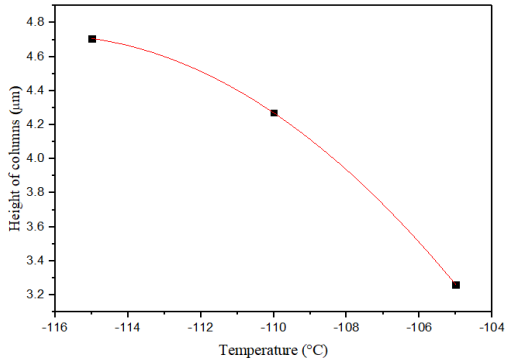

Figure 6. Column Mean height versus wafer Temperature

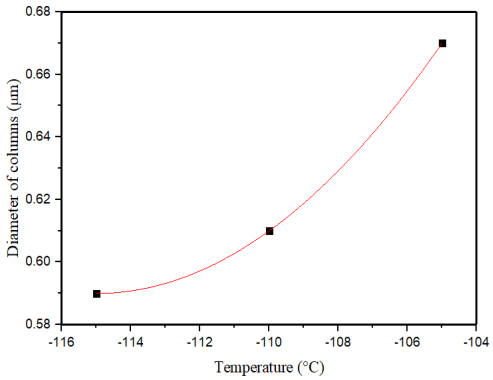

Figure 7. Column Mean diameter versus Wafer Temperature

2. OPTICAL PROPERTIES OF BLACK SILICON

We have started our work to characterize the optical properties for all black silicon samples by measuring their reflectance in the Vis-NIR range [300, 1100] nm. Spectrum acquisition is provided by the software Win ASPECT PLUS. The software Aspect Plus is windows-based and offers a variety of options for data acquisition and analysis. In our case we choose the curve which analyzes the reflectance as a function of the wavelength. The reflectance spectrum of black silicon samples is shown in Figure 8 for silicon process etching parameters of bias voltage. All reflectance measurements were performed using a Specord 210 spectrophotometer**,** without an integrating sphere. The measurements were performed using air as the reference standard, and the reported values represent the average reflectance over the **3**00-1100 nm spectral range**.**

Several samples have been studied to determine the influence of different parameters on the etching process on optical properties; certain parameters were fixed for all measurements, such as ICP power, gas pressure, and SF_6,O_2 gas flow, to 1000 W, 3 Pa, 200 sccm, and 16 sccm, respectively. The variable parameters are the bias voltage and the temperature; all these parameters are illustrated in theTable 1.

After the silicon DRIE etching, the samples are etched dipped in polypropylene beaker containing HF:$H_2O_2$with 1:5 volume ratio aqueous solution for 60s at room temperature. H_2O_2 participates in the oxidation reaction, and can be added to control of aqueous concentration of HF. Reflectance measurements have been performed in the VIS-NIR range for wavelengths between 300nm and 1100nm using the spectrophotometer SPECORD 210.

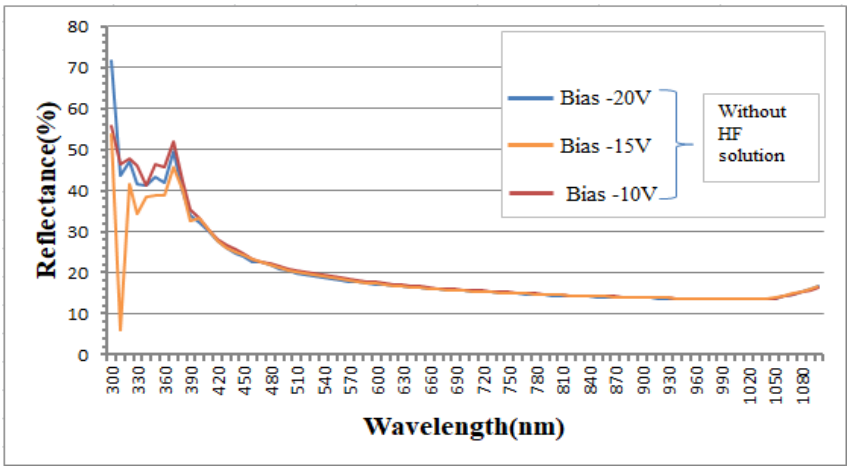

Figure 8. Reflectance of BSi at different Bias voltage value without HF solution

Figure 8 and Figure 9 shows the reflectance spectrum of the black silicon obtained by DRIE process etching before and after HF process etching. We choose three samples of BSi (CMS1, CMS2, and CMS3) for study the reflectance by variation parameters of bias voltage. In the first one, samples that are not processed in HF hydrofluoric acid bath have a decrease reflectance value of 14% from 600nm to 1000nm. The low reflectance of black silicon surface using mask-less DRIE etching is due to dense columns, which improves light trapping. [15]. Figure 8 shows the evolution of the reflectance spectrum of DRIE etched black silicon before HF etching which has almost the same curve

by changing the value of bias voltage from -10V to-20V. In second step, the DRIE etched black silicon of all samples (CMS1, CMS2, and CMS3) is then etched in HF solution process with volume ratio of 1:5.

Figure 9 shows a decrease of the reflectance of the black silicon textured using HF solution process etching, the average of reflectivity is around 1% in the wavelength range of 300nm to 1100nm. After Black silicon HF etching, the reflectance of the black silicon wafers decreases dramatically with the plasma etching conditions from CMS1 to CMS3. The Black silicon wafer etched at a -20V Bias voltage in an HF solution process has the lowest reflectance compared to other Bias voltages, such as -10V and -15V, in the VIS-NIR range. The average reflectance of the samples etched in an HF solution decreases to 1% as the Bias voltage increases from -10V (CMS1) to -20V (CMS3). The decreased reflectance of black silicon is a result of its unique structure. The unique microstructure causes multiple reflections of incoming light [16]. The bias voltage used during plasma etching significantly influences the reflectance of the resulting surface; first the high Bias voltage leads to deeper, sharper, and denser nanostructures [17]. These features enhance light trapping by increasing multiple scattering and absorption, reducing reflectance. In the other side the low bias voltage produces shallow and less pronounced nanostructures. These structures may not trap light efficiently, resulting in higher reflectance.

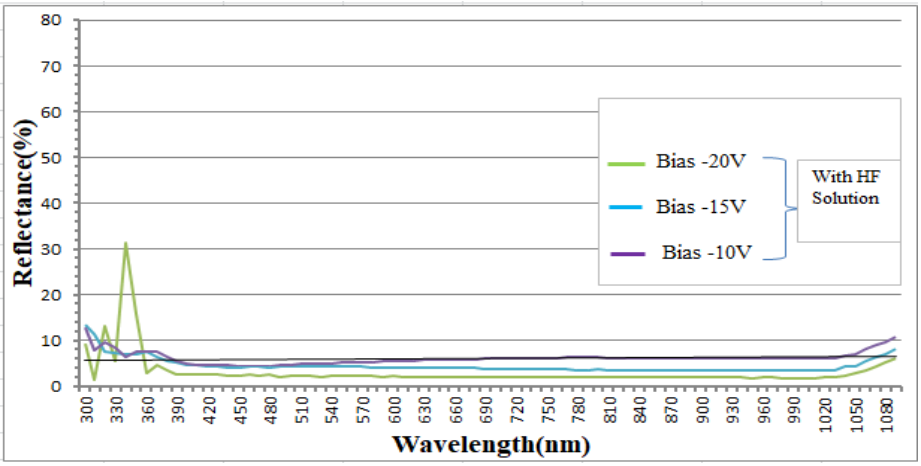

Figure 9. Reflectance of BSi at different Bias voltage value with HF solution

CONCLUSIONS

In this paper, we present a process of measuring of reflectance of black silicon. The process involves using ICP (Inductively Coupled plasma) plasma cryogenic etching and (HF/H_2O_2) process etching. We investigated the influence of various parameters such as wafer temperature and bias voltage on both of surface morphology and optical properties of the black silicon samples.

The combination of black silicon produced by plasma etching and HF/H_2O_2 treatment results in a surface texturing that significantly enhances light absorption, the nanostructures (plasma) and micropores (HF/H_2O_2) work synergistically to create a surface that traps light through multiple internal reflections, this effectively reduces reflectance and ensures that more light is absorbed by the silicon.

The results indicate that black silicon samples obtained through ICP plasma etching technique had a reflectance of approximately of 14% in the visible to near-infrared (VIS-NIR) range, however, the black silicon samples created using their proposed structure with (HF/H_2O_2) process etching exhibited superior anti-reflective and light-trapping properties, leading to a significantly lower reflectance of around of 1.75%in the same of range.

Author Contributions:
All authors contributed to the study.
N. Mekkakia conceived of the presented idea.
M. Azouza, N. Mekkakia, and R. Dussart, T. Tillocher, P. Lefaucheux carried out the experiment
M. Azouza, N. Mekkakia wrote the manuscript with support from R. Dussart.
R. Dussart author contributed to the final version of the manuscript.

Data Availability:
All the data and information mentioned in this article are related to this research.

Ethical Approval: Not applicable.
Consent to participate: Not applicable
Consent for Publication: Not applicable
Competing Interests: No competing interests.
Funding: Not applicable

ORCID
M. Azouza, https://orcid.org/0009-0002-4610-553X; **N. Mekkakia-Maaza,** https://orcid.org/0000-0002-9868-1427;
T. Tillocher, https://orcid.org/0000-0002-9160-5595; **Philippe Lefaucheux,** https://orcid.org/0000-0001-7889-8891

REFERENCES

[1] N.A.M. Noor, and M.Z. Pakhuruddin, "Investigation on surface morphological and optical properties of black silicon fabricated by metal-assisted chemical etching with different etchant concentrations," IOP Conf. Ser.: Earth Environ. Sci. **268**, 012064 **(**2019). https://doi.org/10.1088/1755-1315/268/1/012064
[2] J.Y.-H. Chai, B.T. Wong, and S. Juodkazis, "Black-silicon assisted photovoltaic cells for better conversion efficiencies: A review on recent research and development efforts," Materialstoday Energy, **18**, (2020). https://doi.org/10.1016/j.mtener.2020.100539
[3] K. Omar, and K.A. Salman, "Effects of Electrochemical Etching Time on the Performance of Porous Silicon Solar Cells on Crystalline n-Type (100) and (111)," Journal of Nano Research, **46**, 45-56 (2017). https://doi.org/10.4028/www.scientific.net/JNanoR.46.45
[4] B. Gesemann, R. Wehrspohn, A. Hackner, and G. Müller, "Large-scale fabrication of ordered silicon nanotip arrays used for gas ionization in ion mobility spectrometers," IEEE transactions on nanotechnology, **10**(1), 50-52 (2011). https://doi.org/10.1109/TNANO.2010.2053046
[5] A.A. Leonardi, M.J.L. Faro, and A. Irrera, "Silicon Nanowires Synthesis by Metal-Assisted Chemical Etching: A Review," Nanomaterials, **11**(2), 383 (2021). https://doi.org/10.3390/nano11020383
[6] R. Akan, and U. Vogt, "Optimization of Metal-Assisted Chemical Etching for Deep Silicon Nanostructures," Nanomaterials, **11**(11), 2806 (2021). https://doi.org/10.3390/nano11112806
[7] S.R. Marthi, S. Sekhri, and N.M. Ravindra, "Optical properties of Black silicon: An analysis," The Minerals, Metals & Materials Society, **67**, 2154–2159 (2015). https://doi.org/10.1007/s11837-015-1527-0
[8] X. Liu, B. Radfar, K. Chen, O.E. Setälä, T. Pasanen, M. Yli-Koski, H. Savin, Hele; and V. Vähänissi, "Perspectives on Black Silicon in Semiconductor Manufacturing: Experimental Comparison of Plasma Etching, MACE and Fs-Laser Etching," IEEE Transactions on Semiconductor Manufacturing, **35**(3), 504-510 (2022). https://doi.org/10.1109/TSM.2022.3190630
[9] M. Arias, M. Briceño, A. Marzo, and A. Zárate, "Optical and electrical properties of silicon solar cells by wet chemical etching," J. Chil. Chem. Soc., 64**(1)**, **(**2019**).** http://dx.doi.org/10.4067/s0717-97072019000104268
[10] P. Spinelli, M.A. Verschuuren, and A. Polman, "Broadband omnidirectional antireflection coating based on subwavelength surface mie resonators," Nature Communications, **3**, 692 (2012). https://doi.org/10.1038/ncomms1691
[11] C.-H. Hsu, J.-R. Wu, Y.-T. Lu, D.J. Flood, A.R. Barron, and L.-C. Chen, "Fabrication and characteristics of black silicon for solar cell applications: An overview," Materials Science in Semiconductor Processing, **25**, 2-17 (2014). http://dx.doi.org/10.1016/Jmssp.2014.02.005
[12] R. Dussart, X. Mellhaoui, T. Tillocher, P. Lefaucheux, M. Volatier, C. Socquet-Clerc, P. Brault, *et al*., "Silicon columnar microstructures induced by an SF_6/O_2 plasma," J. Phys. D: Appl. Phys. **38**, 3395-3402 (2005). https://doi.org/10.1088/0022-3727/38/18/012
[13] N Mekkakia-Maaza, R. Dussart, T. Tillocher, P. Lefaucheux, and P. Ranson, "A novel amorphization–etch alternating process for Si(1 0 0)," J. Micromech. Microeng. **23**, 045023 (2013). https://doi.org/10.1088/0960-1317/23/4/045023
[14] R. Dussart, M. Boufnichel, G. Marcos, P. Lefaucheux, A. Basillais, R. Benoit, T. Tillocher, *et al*., "Passivation mechanisms in cryogenic SF6/O_2 etching process," J. Micromech. Microeng. **14**, 190–196 **(**2003). https://doi.org/10.1088/0960-1317/14/2/004
[15] N. Nguyen, D. Abi-Saab, P. Basset, E. Richalot, M. Malak, N. Pavy, F. Flourens, *et al*., "Study of black silicon obtained by cryogenic plasma etching: approach to achieve the hot spot of a thermoelectric energy harvester," Microsyst. Technol. **18**, 1807-1814 (2012). https://doi.org/10.1007/s00542-012-1486-0
[16] X. Yang, L. Bangwu, L. Jie, S. Zenan, and L. Chaobo, "A novel method to produce black silicon for solar cells," Solar Energy, **85**, 1574–1578 (2011). https://doi.org/10.1016/j.solener.2011.03.012
[17] A. Miakonkikh, and V. Kuzmenko, "Formation of Black Silicon in a Process of Plasma etching with Passivation in a SF_6/O_2 Gas Mixture," Nanomaterials, **14**, 945 (2024). https://doi.org/10.3390/nano14110945

ОПТИМІЗАЦІЯ ОПТИЧНИХ ВЛАСТИВОСТЕЙ ЧОРНОГО КРЕМНІЄВОГО СОНЯЧНОГО ЕЛЕМЕНТА

М. Азуза[1], Н. Меккакія-Мааза[1,2], Р. Дюссар[2], Т. Тіллоше[2], П. Лефоше[2]
[1]LMSE, Лабораторія мікросистем та вбудованих систем, Університет наук і технологій Орана Мохамед Будіаф, BP1505 Ель-Мнауер, 31000, Оран, Алжир.
[2]GREMI, Університет Орлеана, 14 Rue d'Issoudun BP 6744, 45067 Орлеан, Франція

Чорний кремній (BSi) – це важлива текстурована форма напівпровідникового матеріалу, що використовується в технології фотоелектричних сонячних елементів. Він характеризується поверхневою структурою кремнію з дуже низьким коефіцієнтом відбиття. У цій статті ми вивчаємо оптичні властивості чорного кремнію у діапазоні довжин хвиль від видимого до ближнього інфрачервоного. Наша робота зосереджена на текстуруванні поверхні кремнію за допомогою кріогенного травлення в системі індуктивно зв'язаної плазми (ICP). Поверхнева структура чорного кремнію формується шляхом зміни кількох параметрів процесу кріотравлення, таких як температура пластини, співвідношення {SF}_6/O_2 та напруга зміщення. Мікроструктурні поверхні BSi можуть бути сформовані в різних формах (піраміди, колони та конуси). Оптичні властивості мікроструктур вивчали за допомогою спектрофотометричних вимірювань. Отримані результати показують, що стовпчасті мікроструктури (CMS) демонструють різні форми текстурування за різних умов процесу плазмового травлення. CMS, отримані без процесу хімічної обробки HF, мають значення коефіцієнта відбиття до 14%. Однак, поверхневе відбиття знижується до менш ніж 2% у діапазоні VIS-NIR шляхом обробки зразків у розчині HF.

Ключові слова: *чорний кремній; текстурування поверхні; відбивна здатність у видимому та ближньому інфрачервоному діапазонах; сонячний елемент; ВЧ-процес*

East European Journal of Physics. 1. 496-506 (2026)
DOI:10.26565/2312-4334-2026-1-57 ISSN 2312-4334

REDUCTION OF AMPLITUDE AND DURATION OF POST-PULSE OSCILLATIONS IN BOW-TIE ACTIVE RADIATING ANTENNA

Gennadiy P. Pochanin[1], Mikhail V. Nesterenko[2]*, Oleksandr A. Orlenko[1], Tetiana M. Ogurtsova[1], Iryna Ye. Pochanina[1], Vadym P. Ruban[1]
[1]O.Ya. Usikov Institute for Radiophysics and Electronics of the National Academy of Sciences of Ukraine, 12, Ac. Proskura St., Kharkiv, Ukraine, 61085
[2]V.N. Karazin Kharkiv National University, 4, Svobody Sq., Kharkiv, Ukraine, 61022
**Corresponding Author e-mail: mikhail.v.nesterenko@gmail.com*
Received October 10, 2025; revised January 25, 2026; accepted February 7, 2026

The paper investigates one of the ways of suppressing post-pulse oscillations in ultra-wideband (UWB) electromagnetic pulses radiated by a bow-tie type antenna excited in active mode (the pulse generator is located directly on the radiator). Since this excitation method does not require balancing or other elements that match the impedances, conditions are created for increasing the radiated power with the same power consumption. To suppress post-pulse oscillations in the radiated field, resistive elements with high resistance are used. They are located near the excitation region in order to absorb the non-radiated part of the excitation signal energy accumulated in the antenna. The influence of the antenna form factor and load resistance on the shape of the radiated signal is experimentally analyzed.
Keywords: *UWB signal; Bow-Tie antenna; Radiated electromagnetic field; Post-pulse oscillations; Active antenna*
PACS: 02.70.Pt; 78.70Gq; 84.37.+q; 84.40.Ba

INTRODUCTION

One of the main applications of ultra-wideband(UWB) technologies is subsurface radar (ground penetrating radar (GPR)), which is widely used for such purposes as mine detection, detection of people by optically opaque obstacles, search for people under rubble, non-destructive testing of objects, environmental monitoring, monitoring the condition of subsurface communications, pipelines and many others (see, for example, [1]-[5] and references in them). Special requirements for the antenna system are imposed on GPR that use video pulses as UWB probing signals. The antenna must create in space a short single useful pulse of an electromagnetic field of the required amplitude, shape and duration. The presence of additional pulses in the probing signal (they are called post-pulse oscillations or ringing) complicates the interpretation of sounding results and deteriorates the information and accuracy characteristics of the GPR.

The most general is the use of dipole-type structures for impulse radiation. The prerequisite for the occurrence of post-pulse oscillations of the probing signal in such structures is the peculiarity of the very process of radiation of a single pulse by the antenna. The exciting signal goes from the exciting area to the ends of the dipole and back from the ends to the exciting area. Each propagation cycle in the antenna produces one impulse in the radiated field. It is impossible to create conditions under which all the energy supplied to the antenna is spent on radiating a single pulse during one pass of the exciting signal through the radiator [1]. Therefore, the portion of the non-radiated energy of the exciting signal propagating through the radiator and radiating at each cycle causes an appearance of post-pulse oscillations in the field created by the antenna. Depending on the geometry of the radiating elements and the electrophysical characteristics of the material from which they are made, a greater or lesser part of the energy supplied to the radiator is separated from the antenna, going into space. The remaining part continues to move along the radiator in the form of an electrical pulse, reflecting off the boundaries of the radiator and making oscillatory movements until the energy of the exciting signal is spent on the radiation of post-pulse oscillations, as well as on heating due to ohmic losses in the radiator and the return of part of the energy back to sources of the exciting signal.

One of the possible options for antenna structures for radiating UWB pulses are biconical dipoles, patented in 1898 by Lodge [6]. These can be symmetrical biconical dipoles with symmetrical excitation [7]-[19], asymmetrical biconical dipoles [20], [21] as well as biconical dipoles with asymmetrical excitation [22]. Calculations have shown that the use of specially formed resistive loading allows excluding post-pulse oscillations in radiated (received) signals. However, creating in practice such loadings is difficult.

A planar analogue of a biconical dipole is a dipole with triangular arms which is bow-tie antenna (BTA), also patented in [6]. It can be used both to generate harmonic electromagnetic fields [9], [23]-[34] and to radiate electromagnetic pulses [21], [35], [42]. Possible approach to prevent appearing of post-pulse oscillations and provide single pass propagation of exciting impulse by the antenna radiator is absorption of extra part of excitation energy by resistive or resistive-capacitive loads near the ends of dipole [35], [38].

The next update is the resistor-loaded bow-tie antenna, which is covered with a rectangular conducting cavity with inner walls partially or fully coated with a ferrite absorber [43]. This antenna is designed for GPR use. However, the

Cite as: G.P. Pochanin, M.V. Nesterenko, O.A. Orlenko, T.M. Ogurtsova, I.Ye. Pochanina, V.P. Ruban, East Eur. J. Phys. 1, 496 (2026), https://doi.org/10.26565/2312-4334-2026-1-57

authors concluded that the ferrite absorber cannot significantly improve the antenna characteristics of the GPR system. The appearance of additional impulses in the radiated field is noted in the paper [39]. The dependence of the shape of the waveform of radiated impulse on the direction of radiation was also noted. It should be considered when designing an antenna for GPR.

The authors of the paper [21] show how the dimensions of a biconical antenna influence the radiation pattern and shape of radiated/received signals. The least influence is when the antenna dimensions are much bigger or much smaller than the central frequency of the signal. However, both of these cases have disadvantages from the practical point of view [44]. In [45], it was shown that cylindrical slots can radiate impulse signals due to an extensive working frequency band. Authors of [46] studied cylindrical radiator with six slots incusing resistors. Specially designed distribution of resistors has shown to be a good performance in terms of absorbing ability at lower frequency, reflected pulse energy. However, the radiated/received pulses have long ringing after main pulse. Such signals require additional compressing to be applicable in GPR.

Active antennas, whose design includes active elements [47], are of particular interest to radar system developers. This approach improves the antenna's energy characteristics because it allows the abandonment of matching devices and significantly reduces signal energy losses at transmission from the generator to the radiator. It should be noted that the first radiators of electromagnetic (EM) waves, for example, [6], were active.

Earlier studies [48] showed that if the radiating elements of a BTA are used as a capacitive energy store for the further formation of a radiated pulse, then, in contrast to the passive method of antenna excitation, with the same parameters of the radiated pulse, in the case of active excitation, the energy consumed by the radiator, turns out to be an order of magnitude smaller.

Experiments for dipole allowed us to analyze the physical processes responsible for the radiation of EM fields. It was demonstrated that the area of excitation and the ends of the antenna are the main sources of intense radiation. By placing energy-absorbing resistors in the slots near the ends of the antenna arms, we reduce the radiated energy by absorbing the electric current as it travels to the ends. Therefore, it makes sense to absorb the excess energy from the exciting signals after they have been radiated from the ends of the antenna arms [2].

This paper proposes a design of a BTA that provides efficient radiation and simultaneously suppresses post-pulse oscillations. Electrodynamic characteristics of UWB bow-tie radiators of various shapes with resistive loads of different values are theoretically and experimentally investigated.

FDTD SIMULATION

1. Problem Formulation

Unfortunately, active antennas are difficult to model mathematically. The result is influenced not only by the geometry and material of the radiator but also by the electrical parameters of the excitation circuit, together with active electronic elements (usually semiconductor diodes, transistors, etc.), and the feedback caused by these parameters. With this in mind, we will first find out the main regularities of pulse radiation caused by the geometry of the radiating elements based on the results of finite-difference time-domain (FDTD) modeling. Then, in the experimental part of the work, we will connect the radiator to the circuit generating exciting pulses and select its parameters that provide the desired radiation mode. In contrast to the approach of using a resistive load proposed in [38], in this study, a resistive load designed to suppress after-pulse oscillations is moved to the excitation region of the radiator.

Consider a BTA (Fig. 1) located in free space. Triangular conductors are located in the xz -plane. The dipole axis is oriented in the x -direction. The antenna dimensions: length is h_1, width is h_2. The antenna is excited by a unipolar pulse through the terminals "1". The exciting source is located in the center of the Cartesian coordinate system in the gap between the antenna conductors. Connected to the terminals "2" the load is resistive elements, the resistances of which are selected during the study in the range from 100 Ohms to 1000 Ohms.

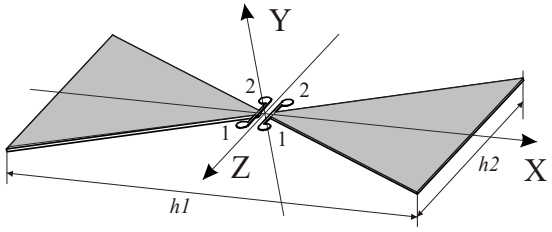

Figure 1. BTA: 1, 2 - antenna feeding and load terminals

Let us analyze the amplitude-time characteristics of the EM field registered at some distance h from the radiator in the direction of the y axis, depending on the dimensions h_1, h_2 and the value of the resistive load.

2. Solution Method

The mathematical statement of the problem includes the main equations, which are Maxwell's equations and initial and boundary conditions (to limit the calculation area and effectively use numerical methods). One of the most universal

and common methods of numerically solving non-stationary electrodynamics problems is the FDTD method [49]. We will use the specially developed program SEMP (Software for ElectroMagnetic Profiling) [50] for computer simulation which implements it. Computer simulation of the radiation of fully three-dimensional antennas using the FDTD method is a task that requires large amounts of calculations and resources. However, there are "optimization techniques" that allows to increase the speed of calculations, namely: 1) the use of a point model of the antenna excitation source, which simplifies the calculation algorithm and allows to use a larger size of the discretization grid than in the case of a full 3D model; 2) application of effective absorbing boundary conditions (ABC) [51].

3. Simulation Parameters

When limiting the computational domain in the FDTD method, the following two conditions must be considered:
1) the calculation area should have as small a volume as possible to increase the speed of calculations and reduce the amount of memory used;
2) the dimensions of the calculation area should be chosen so that reflections from its boundaries (taking into account the application of ABC) do not distort the investigated electromagnetic process.
The simulation parameters related to the features of the implementation of the FDTD algorithm are given in Table I.

Table I. Simulation Parameters

Parameter	Value
Dimensions of the calculation area in space, m^3	0.7×0.35×0.35
The size of the spatial grid, m	0.0025
Time window (observation time), ns	6
The time step, ns	10^{-2}

4. Simulation Results

Fig. 2 visualizes the distribution of the EM field radiated by the investigated rectangular (h_1=2 h_2=130 mm) unloaded antenna in space in discrete time intervals. Field distributions at different moments are presented on images in the xz-plane. The color scale shows the amplitudes of the field strengths.

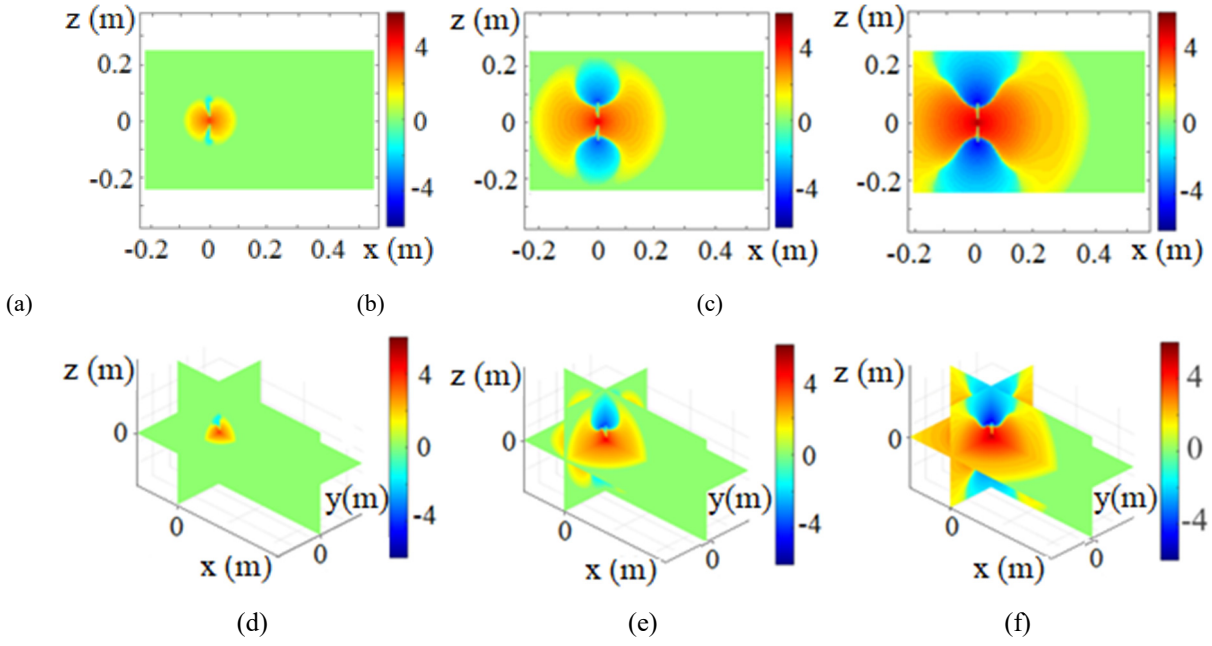

Figure 2. Distribution of the EM field radiated by a rectangular (h_1 =2 h_2 =130 mm) unloaded BTA in the xz-plane (a), (b), (c) and in space (d), (e), (f) for some t :(a), (d) – 0.5 ns; (b), (e) – 1.0 ns; (c), (f) – 1.5 ns

Fig. 2 illustrates that the amplitudes of EM field pulses near the center of the antenna and at its edges are the most significant. This confirms the thesis that the primary sources of EM field radiation are the areas where the charges excited by the source receive the greatest acceleration.

Fig. 3 shows that an unloaded antenna radiates pulses with post-pulse oscillations of much higher intensity than a loaded one. An increase in the antenna length from 110 mm to 150 mm leads to an increase in the intensity of the radiated field (see the amplitude in Fig. 3a at the time interval of 1 ns–3 ns). This part of the pulse is formed during radiation directly from the excitation area. Since the length of the antenna is less than the spatial duration of the exciting pulse, the fields radiated by the edges of the antenna and having the opposite polarity arrive at the observation point at a time when the intensity of the field radiated by the excitation area has not yet reached its maximum. As a result of such

synchronization in time, the fields radiated by the excitation area and the edges of the dipole mutually compensate each other, limiting the intensity of the field at the observation point. The process of forming the field pulse at the point of observation is similar to forming the radiated pulse by a dipole radiator [2]. Post-pulse oscillations are observed in the time interval 2.5 ns÷6.0 ns. The parameters of these oscillations weakly depend on the length of the radiator.

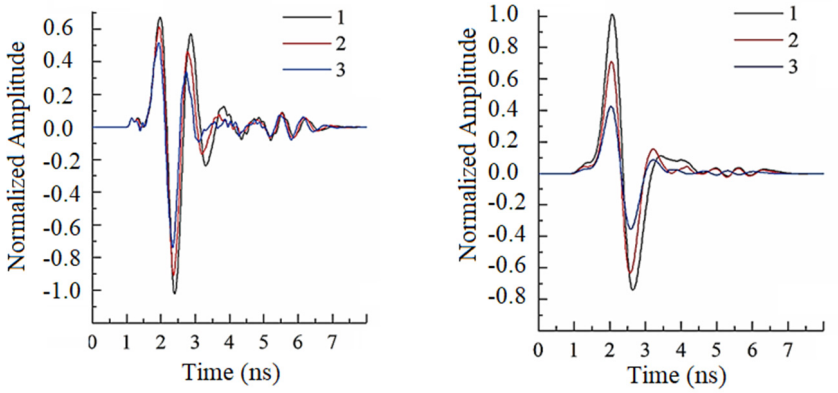

(a) (b)

Figure 3. Plots of pulses radiated by a rectangular (h_1 =2 h_2) BTA: FDTD simulation for unloaded (a) and loaded by the 200 Ohm resistance (b) antennas: 1 – 150×75 mm; 2 – 130x65 mm; 3 – 110×55 mm

However, such synchronization, in addition to the increase in field strength at the point of observation, creates conditions for the occurrence of post-pulse oscillations that follow this (negative) amplitude peak. As a result, the radiated field takes the form of a damped oscillation (Fig. 3a, 3 ns÷5 ns). Despite the increase in amplitude, this form of probing signal is inconvenient for use in ground-penetrating radars. With this in mind, this paper proposes suppressing post-pulse oscillations by connecting a load resistor in the excitation region parallel to the excitation signal's source. The result of applying such a load in FDTD modeling is shown in Fig. 3b. A significant decrease in the amplitude of post-pulse oscillations in the radiated pulse is clearly visible. The resistive load connected in the excitation region reduces the Q-factor of the oscillations in the antenna. Despite the coincidence of the length of the antenna with the spatial duration of the pulse, there are no fading oscillations in the radiation field of the antenna with a length of h_1=150 mm.

EXPERIMENTAL RESEARCH

The object of research in this paper is an active radiating antenna that is excited without the use of a feeder line between the generator and the radiator (Fig. 4a). It is obvious that the addition of elements of electric circuits to the excitation region of the dipole significantly affects the shape of the radiated pulse. Therefore, the influence of the electrical parameters of the pulse generator output on the processes of formation and flow of the exciting current in the antenna should be taken into account.

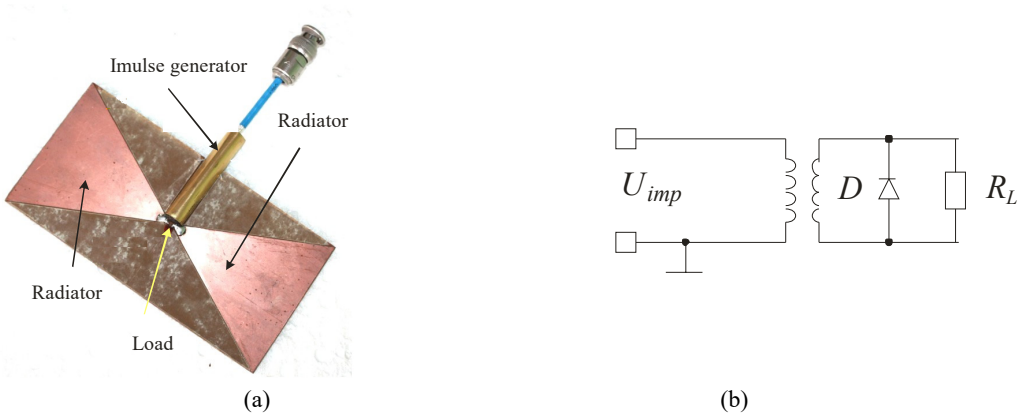

(a) (b)

Figure 4. Appearance of an active antenna with a radiator of rectangular configuration (a); the output part of the pulse generator with a resistive load (b)

To find out the conditions under which both a large amplitude of the radiated field and a minimization of post-pulse oscillations are simultaneously achieved, it is advisable to conduct direct experiments on the radiation of short pulses of the EM field by active BTA with different radiator geometries. The study considered two configurations of the radiator - rectangular (h_1=2 h_2) and square (h_1= h_2). Let's analyze the influence of the load resistance, which is connected to the excitation area, on the pulse parameters of the radiated field. To do this, we connect the arms of the dipole in the region of excitation with resistance R_L (Fig. 4b). Resistors whose resistance is 100 Ohm÷1000 Ohm are used as load elements.

1. Measuring equipment

Fig. 5a contains an oscilloscope with a sweep block unit and an amplifier working in the 0÷3.5 GHz frequency range; timing generator, which generates a signal with an amplitude of +5 V and a duration of at least 20 ns to start the antenna excitation pulse generator and the oscilloscope synchronization signal; the power supply unit of the excitation pulse generator, which provides a voltage of +12 V and a current of 25 mA.

A ferrite antenna [52] was used as a receiving antenna, which allows receiving pulse signals with a rise time of more than 0.4 ns and a pulse duration of less than 2.5 ns without distortion. Registration of radiated pulses of the EM field is carried out at a distance of 0.5 m from the investigated antenna at a height of 1.8 m from the floor surface. This combination of distances makes it possible to exclude pulses reflected from surrounding objects (floor, walls, ceiling of the laboratory, measuring equipment) from the observation time window. Thus, the conditions of the experiment make it possible to analyze the structure of the radiated field and the effect on it of the design parameters of the radiator.

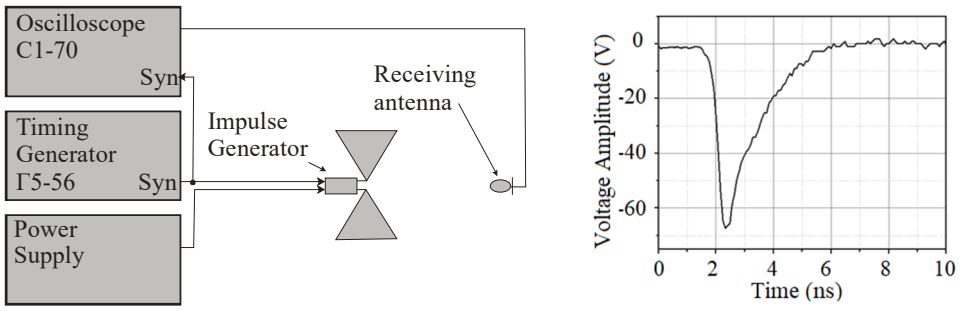

(a) (b)

Figure 5. Block diagram of the experimental equipment (a) and exciting pulse at the output of the generator load 50 Ohm (b)

To excite the radiator, a pulse generator was developed [53] using a diode КД513А, which acts as a drift diode with a sharp recovery of resistance [54] and allows forming of a pulse with a front duration of 0.5 ns and amplitude of 70 V at a load of 50 Ohm (Fig. 5b). Structurally, the generator is made in the form of a shielded printed circuit board with dimensions of 50x10 mm^2, located directly on the radiator (Fig. 4a). Since the generator has its own timing circuits, as well as a stabilized power source, the parameters of the generated voltage pulse do not depend on the duration of the start signal. The input signal for starting the generator is a pulse of positive polarity with an amplitude of 5 V and an arbitrary duration (from 20 ns or more). The supply voltage is +12 V, and the average current consumption is 25 mA at a pulse repetition rate of 100 KHz.

2. Radiation of pulses of EM fields

For experiments (antenna with a dipole aspect ratio of 2:1), radiators with dimensions h_1 of 150 mm, 140 mm, 130 mm, 120 mm, and 110 mm were made. During the experiments, the time dependences of electromagnetic field pulses radiated by unloaded and loaded (R_L =200 Ohm) antennas were recorded (Fig. 6). The plots of the received signals clearly demonstrate that the load connection practically eliminates the post-pulse oscillations. However, the amplitude of the radiated pulse decreases by almost 1.5 times. The first two half-waves of the signal, which have the maximum amplitude, will be considered a "useful" signal. Let's define its amplitude as $V_A = V(t)_{\max} + |V(t)_{\min}|$. Consider it as the value of the amplitude for the useful signal (range $t \in \{1, 3, 5\}$ ns in Fig. 6a) and the amplitude of after-pulse oscillations (range $t \in \{3, 5, 12\}$ ns in Fig. 6b).

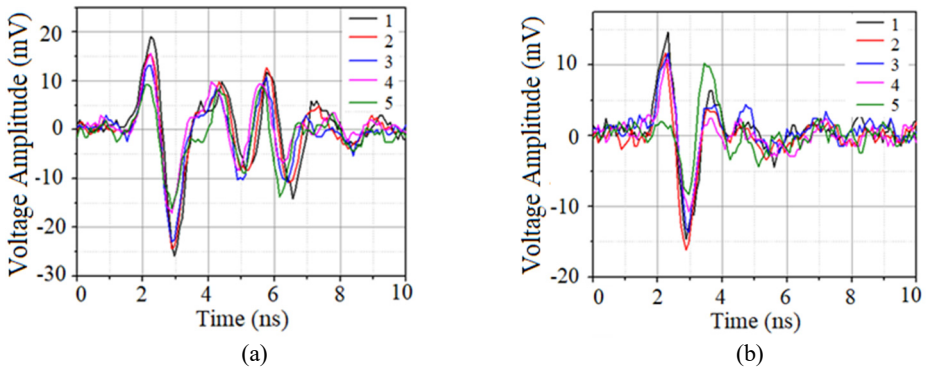

(a) (b)

Figure 6. Plots of pulses radiated by an antenna of a rectangular configuration without load (a) and with load (b) R_L = 200 Ohm: 1 – 150 mm; 2 – 140 mm; 3 – 130 mm; 4 – 120 mm; 5 – 110 mm

3. Effect of antenna size and load magnitude

From Fig. 6, it can be seen that with each decrease in the size of h_1 by 10 mm, the amplitude of the useful signal decreases by approximately 4 mV for an unloaded antenna (Fig. 6a) and by 2 mV for a loaded antenna (Fig. 6b) for h_1 sizes of the radiator from 150 mm to 110 mm. This means that the dependence of the amplitude of the useful signal on the size of h_1 in these cases is linear (Fig. 7) and has the form:

$V_A \approx 0.4\,h_1 - 0.015$ –for the unloaded antenna;

$V_A \approx 0.2\,h_1$ – for the loaded antenna.

In addition, from Fig. 6, it can be seen that the amplitude of post-pulse oscillations changes slightly for both unloaded (Fig. 6a) and loaded (Fig. 6b) antennas, while signal amplitudes change significantly when the radiator size changes (Fig. 7).

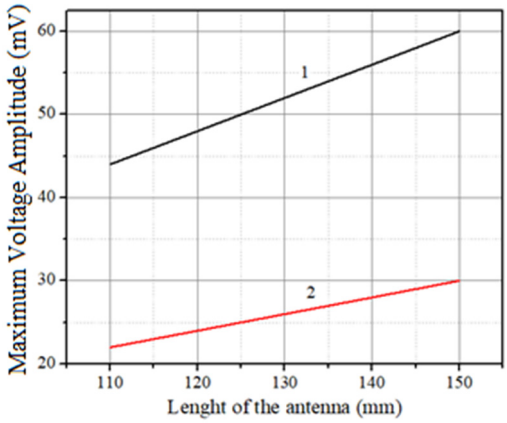

Figure 7. The amplitude of the useful signal depending on the size of the antennas (1 - no load, 2 – with a load R_L = 200 Ohm)

Compare the plots of pulses emitted by rectangular antennas with a load magnitude (R_L =200 Ohm) and without a load at the same size as the radiators in the time interval from 5 ns to 9 ns (see Fig. 6).To quantify the impact of the load on the radiated signal, consider the amplitude of the first two half-waves that follow the radiated useful pulse. Fig. 8 shows the dependence of the amplitude of the useful pulse and two half-waves of post-pulse oscillations on the load resistance of the antennas, which was changed from 100 Ohm to 1000 Ohm in steps of 100 Ohm. A radiator of length h_1=130 mm was chosen for this experiment.

From Fig. 8, it follows that when the load resistance increases from 100 Ohm to 300 Ohm, the amplitude of the useful signal increases faster than the amplitude of post-pulse oscillations. When the load increases from 300 Ohm to 1000 Ohm, the amplitudes of the useful pulse and post-pulse oscillations change similarly. Moreover, the amplitude of the first half-wave decreases (Fig. 8, curve 2), and the amplitude of the second half-wave (Fig. 8, curve 3) increases. When the resistance increases to 1000 Ohm, the amplitude of the useful pulse and post-pulse oscillations slowly increases to the values formed by the antenna without load. Thus, by applying a resistive load (from 200 Ohm to 300 Ohm) in active BTA with a rectangular configuration, it is possible to significantly (up to -20 dB) reduce the amplitude of after-pulse oscillations, while the amplitude of the useful signal decreases by only $(20 \div 30)$ %.

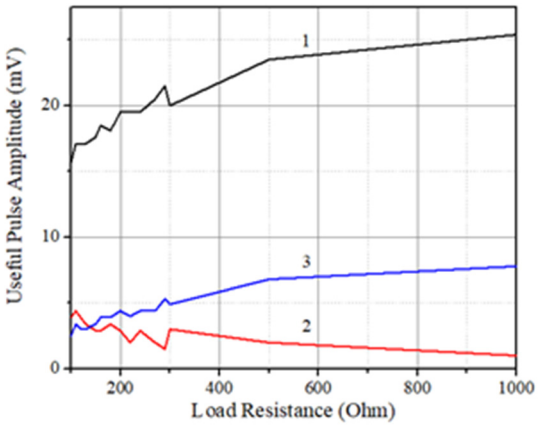

Figure 8. Dependence of the amplitude of the useful pulse and two half-waves of after-pulse oscillations on the antenna load: 1 is the amplitude of useful signal, 2 is the amplitude of the first half-wave, 3 is the amplitude of the second half-wave

4. Antenna with a 1:1 aspect ratio

For this series of experiments, radiators with dimensions $h_1 = h_2$ of 150 mm, 140 mm, 130 mm, 120 mm, and 110 mm were manufactured. The experiments recorded the time dependences of EM field pulses radiated by unloaded and loaded (R_L =200 Ohm) antennas. Fig. 9 illustrates the results of the measurements. As can be seen, the characteristic features of the pulses radiated by the antenna with a rectangular configuration (Fig. 6) are repeated in the antenna with a square configuration (Fig. 9). Amplitudes of the useful signal (range $t \in \{1, 4\}$ ns shown in Fig. 9a) and post-pulse oscillations (range $t \in \{4, 20\}$ ns in Fig. 9b). From Fig. 9, it follows that the amplitude of post-pulse oscillations changes slightly within the certain limits of the change in size h_1 for both unloaded (a) and loaded (b) antennas.

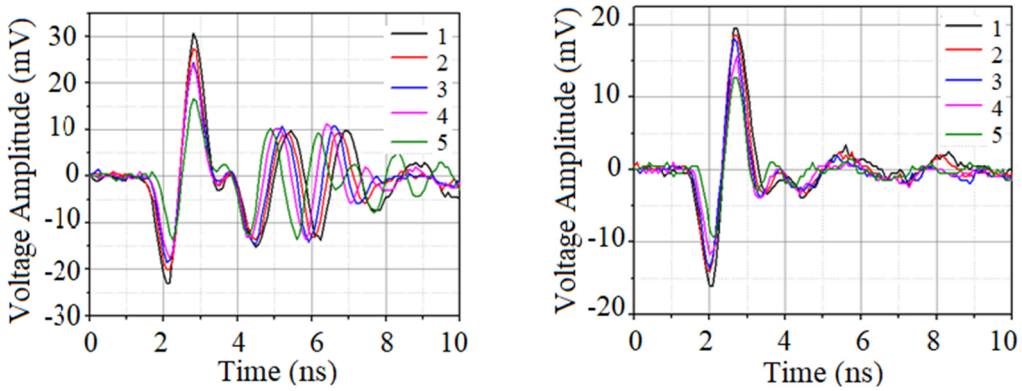

Figure 9. Plots of pulses radiated by a square antenna: without load (a), with load R_L = 200 Ohm (b): 1 – 150 mm; 2 – 140 mm; 3 – 130 mm; 4 – 120 mm; 5 – 110 mm

5. Effect of antenna size and load magnitude

From Fig. 10, it follows that with a decrease in the size of h_1 by 10 mm, the maximum amplitude V_A of the useful signal decreases by about 6 mV for the unloaded antenna and by 4 mV for the loaded antenna in the range of sizes h_1 of the radiator from 150 mm to 110 mm. This means that the dependence of the amplitude of the useful signal on the size of h_1 within the limits of the change in the size of h_1 is linear (Fig. 10) and is described by the expressions:

$V_A \approx 0.6h_1 - 0.036$ – for the unloaded antenna;

$V_A \approx 0.4h_1 - 0.014$ – for the loaded antenna.

Comparing the waveforms of Fig. 9 in the time interval from 5 ns to 9 ns reveals that the use of a resistor of R_L =200 Ohm allows significantly reducing the amplitude of the EM wave reflected from the ends of the antenna (up to -20 dB). Still, simultaneously, the amplitude of the radiated pulse also decreases by $(20 \div 40)$ %.

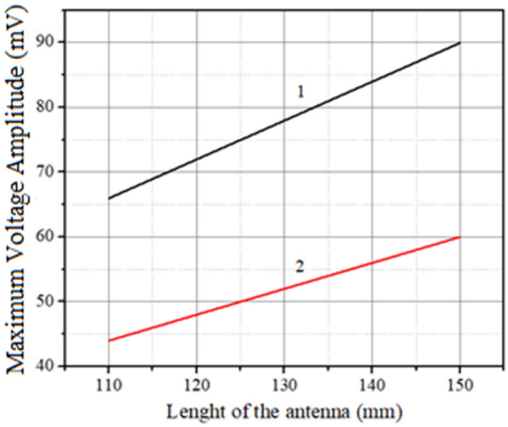

Figure 10. The amplitude of the useful signal depending on the dimensions of the antenna: 1 is for the unloaded antenna, 2 is for the antenna loaded by R_L =200 Ohm

6. Comparison of radiators of rectangular and square configurations

Fig. 11 shows the dependence of the amplitudes of the useful pulse on the antenna load for radiators of rectangular and square configurations. Measurements were made for the radiators with a length of h_1=130 mm. As you can see, that when using a resistive load, a square-shaped antenna radiates pulses of the EM field of greater amplitude than a rectangular

antenna with the same size h_1. With an increase in the load in the range of $(100 \div 500)$ Ohm, the amplitude of the pulses radiated by a square-shaped antenna increases faster than that of a rectangular-shaped antenna. With a load close to 1000 Ohm, both antennas radiate pulses with the same useful pulse amplitude as an unloaded antenna of the corresponding size and shape.

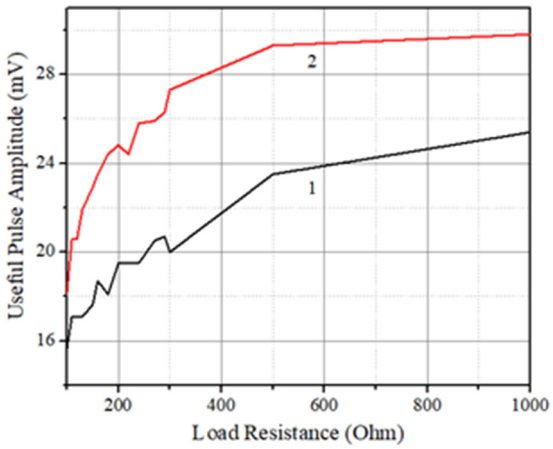

Figure 11. Dependence of the amplitude of the useful pulse on the antenna load for radiators of rectangular and square configurations: 1 is for the rectangular h_2=65 mm; 2 is for the square with h_2=130 mm

From a comparison of the graphs shown in Fig. 6 and Fig. 9, it is evident that when the size of the radiator changes, the amplitude of the useful pulse changes significantly more than the amplitude of the after-pulse oscillations. This again confirms that field radiation is formed by areas where the charges excited in the antenna receive maximum acceleration - in the area of antenna excitation and at the edges of the radiator. In the case of an increase in the size of the antenna and a constant load, the radiating edges of the antenna move apart, and the time interval between radiation from the feeding region of the antenna and from the edge increases, this delays the appearance of the pulse radiated by the edge in the observation point. Since the electric field strength vectors radiated by the feeding region and the edge of the radiator have mutually opposite directions [48] and mutually compensate each other, increasing the time interval between these pulses makes it possible to increase the field strength of the pulse radiated by the feeding region to greater values before a compensating pulse arrives at the point of observation from the edge of the radiator. This is an explanation for the increase in the amplitude of the radiated field when the size of the radiator increases.

Since nothing changes in the feeding region with such changes in the antenna geometry, the after-pulse oscillations, most likely caused by radiation from this region, remain unchanged. However, if a resistor is included in the gap between the conductors of the dipole, which absorbs the energy of the excitation field wave reflected from the edge of the radiator, the energy of the excitation signal is mostly dissipated on this resistor and is not radiated.

COMPARISON OF FDTD SIMULATION RESULTS AND EXPERIMENTAL DATA

The impulse signals registered in the experiments demonstrate the regularities revealed in the numerical simulation. Some discrepancy in the forms of program simulated and experimentally obtained pulses is explained by the presence of additional structural elements in experimental antenna samples that are not taken into account in numerical modeling (in particular, the "physical presence" of the generator, its imagined part of impedance and variable output resistance, a thin dielectric substrate on which the metal parts of the dipole are located, etc.).

The experiments revealed the following patterns:

1) with an increase in the size h_1 of the antenna, the amplitude of the radiated signal increases more than the amplitude of post-pulse oscillations;

2) using resistors as a load significantly reduces the amplitude of the EM wave, which excites oscillations in the antenna; at that, the amplitude of the radiated pulse decreases slightly.

CONCLUSIONS

The complex approach used in the paper (consideration of "simplified" theoretical and "full" experimental models) has its advantages. Simplification makes the theoretical model more universal and allows studying the basic regularities of signal formation and radiation without the influence of distorting factors. Considering the "full" experimental model allows for obtaining and analyzing the real spatial-temporal distributions of EM fields created by the antenna system under study. Thus, a complex approach, including theoretical (modeling) and experimental analysis, provides the most complete and effective study of the given experimental task. The mutual close correspondence of the results of calculations and experiments confirms the correctness of the chosen model and, as a result, opens up the possibility of an in-depth study of the dynamics of the change in the UWB pulse fields both in the near and far zones of the antenna.

As a result of the research, it was concluded:

1) from the point of view of practical use, square-shaped radiators are better than rectangular ones because the amplitude of the useful signal radiated by them is about 30% larger, and the post-pulse oscillations are the same as those of a rectangular-shaped radiator;
2) the largest efficiency of radiation at the minimum level of post-pulse oscillations is achieved if a load resistance of $(200 \div 300)$ Ohm;
3) when using a square radiator without load, the amplitude of the useful pulse depends only on the length of the dipole. In contrast, the amplitude of post-pulse oscillations is almost independent on the length of the dipole.

Thanks to the active mode of antenna excitation, the need to match the impedance of the feeder and the radiator can be abandoned. So, there are no mismatch losses. This also opens the possibility of using resistive elements with arbitrary resistance to suppress oscillations in the radiator. So, it is possible to select the optimal load under which the post-pulse oscillations are minimal, and the amplitude of the radiated field pulse remains large.

ORCID

Gennadiy P. Pochanin, https://orcid.org/0000-0002-1977-2217; **Mikhail V. Nesterenko**, https://orcid.org/0000-0002-1297-9119;
Oleksandr A. Orlenko, https://orcid.org/0000-0002-3287-9692; **Tetiana M. Ogurtsova**, https://orcid.org/0000-0002-3211-4390;
Iryna Ye. Pochanina, https://orcid.org/0009-0002-3229-662X; **Vadym P. Ruban**, https://orcid.org/0000-0002-9008-7466

REFERENCES

[1] E. K. Miller, and J. A. Landt, "Direct time-domain techniques for transient radiation and scattering from wires," Proc. IEEE, **68**, (11), 1396-1423 (1980). https://doi.org/10.1109/PROC.1980.11881
[2] G. P. Pochanin, and I. Ye. Pochanina, "Radiation of UWB pulses by thin wire monopole," in Proc. 6th Int. Conf. Ultra Wideband and Ultra Short Impulse Signals, 133-136 (2012). https://doi.org/10.1109/UWBUSIS.2012.6379757
[3] L. A. Varyanitsa-Roshchupkina, and G. P. Pochanin, "Optimization of a sounding ultra wide-band (UWB) pulsed signal in subsurface object detection," Telecom. Radio Eng. **71**, 1159-1182 (2012). https://doi.org/10.1615/telecomradeng.v71.i13.20
[4] G. P. Pochanin, and S. A. Masalov, "Large current radiators: problems, analysis, and design," in Ultrawideband radar applications and design. Ed. by J. D. Taylor. CRC Press. 325-372 (2012). https://doi.org/10.1201/b12356
[5] O. A. Pryshchenko, V. A. Plakhtii, O. M. Dumin, G. P. Pochanin, V. P. Ruban, L. Capineri, and F. Crawford, "Implementation of an artificial intelligence approach to GPR systems for landmine detection," Remote Sensing, **14**, No. 17, 4421 (2022). https://doi.org/10.3390/rs14174421
[6] O. Lodge, "Electric Telegraphy," U.S. Patent 609 154, Aug. 15, 1898.
[7] S. A. Schelkunoff, "Theory of antennas of arbitrary size and shape," Proc. IRE, **29**, 493-521 (1941). https://doi.org/10.1109/JRPROC.1941.231669
[8] C. T. Tai, "On the theory of biconical antennas," Journal Applied Phys. **19**, 1155-1160 (1948). https://doi.org/10.1063/1.1715036
[9] G. H. Brown, and O. M. Woodward, "Experimentally determined radiation characteristics of conical and triangular antennas," RCA Rev., **13**, 425-452 (1952).
[10] J. Ga1ejs, "Capacitor type biconical antennas," Radio Science, **68**, No. 2, 165-172 (1964).
[11] T. T. Wu, and R. W. P. King, "The tapered antenna and its application to the junction problem for thin wires," IEEE Trans. Antennas Propag. **24**, 42-45 (1976). https://doi.org/10.1109/TAP.1976.1141274
[12] S. A. Saoudy, and M. Hamid, "Input admittance of a biconical antenna with wide feed gap," IEEE Trans. Antennas Propag. **38**, 1784-1790 (1990). https://doi.org/10.1109/8.102740
[13] S. S. Sandler, and R. W. P. King, "Compact conical antennas for wide-band coverage," IEEE Trans. Antennas Propag. **42**, 436-439 (1994). https://doi.org/10.1109/8.280735
[14] K.-L. Wong, and S.-L. Chien, "Wide-band cylindrical monopole antenna for mobile phone," IEEE Trans. Antennas Propag. **53**, 2756-2758 (2005). https://doi.org/10.1109/TAP.2005.851784
[15] A. K. Amert, and K. W. Whites, "Miniaturization of the biconical antenna for ultrawideband applications," IEEE Trans. Antennas Propag. **57**, 3728-3735 (2009). https://doi.org/10.1109/TAP.2009.2026667
[16] C. S. Rao, and A. Sudhakar, "Analysis of edge terminated wide band biconical antenna," ACES J. **30**, 804-809 (2015).
[17] M. V. Nesterenko, A. V. Gomozov, V. A. Katrich, S. L. Berdnik, and V. I. Kijko, "Scattering of electromagnetic waves by impedance biconical vibrators in a free space and in a rectangular waveguide," Prog. Electromagn. Res. C, **119**, 275-285 (2022). http://dx.doi.org/10.2528/PIERC22020304
[18] F. F. Dubrovka, S. Piltyay, M. Movchan, and I. Zakharchuk, "Ultrawideband compact lightweight biconical antenna with capability of various polarizations reception for modern UAV applications," IEEE Trans. Antennas Propag. **71**, 2922-2929 (2023). https://doi.org/10.1109/TAP.2023.3247145
[19] J. M. Platt, L. B. Boskovic, and D. S. Filipovic, "Wideband biconical antenna with embedded band-notch resonator," IEEE Trans. Antennas Propag. **72**, 2921-2925 (2024). https://doi.org/10.1109/TAP.2024.3349785
[20] S. N. Samaddar, and E. L. Mokole, "Biconical antennas with unequal cone angles," IEEE Trans. Antennas Propag. **46**, 181-193, (1998). https://doi.org/10.1109/8.660962
[21] D. Ghosh, and T. K. Sarkar, "Design of a wide-angle biconical antenna for wideband communications," Prog. Electromagn. Res. B, **16**, 229–245 (2009). https://doi.org/10.2528/PIERB09061508
[22] M. V. Nesterenko, V. A. Katrich, and S. V. Pshenichnaya, "Multiband asymmetric biconical dipole antenna with distributed surface impedance and arbitrary excitation," East European J. Physics, (2), 450-455 (2024). https://doi.org/10.26565/2312-4334-2024-2-59
[23] Y.-D. Lin, and S.-N. Tsai, "Coplanar waveguide-fed uniplanar bow-tie antenna," IEEE Trans. Antennas Propag. **45**, 305-306 (1997). https://doi.org/10.1109/8.560350

[24] Y.-D. Lin, and S.-N. Tsai, "Analysis and design of broadside-coupledstriplines-fed bow-tie antennas," IEEE Trans. Antennas Propag. **46**, 459-460 (1998). https://doi.org/10.1109/8.662667
[25] K. Kiminami, A. Hirata, and T. Shiozawa, "Double-sided printed bow-tie antenna for UWB communications," IEEE Antennas Wireless Propag. Lett. **3**, 152-153 (2004). https://doi.org/10.1109/LAWP.2004.832126
[26] G. Wang, J. Liu, J. Xia, and L. Yang, "Coaxial-fed double-sided bow-tie antenna for GSM/CDMA and 3G/WLAN communications," IEEE Trans. Antennas Propag. **56**, 2739-2742 (2008). https://doi.org/10.1109/TAP.2008.927571
[27] A. C. Durgun, C. A. Balanis, C. R. Birtcher, and D. R. Allee, "Design, simulation, fabrication and testing of flexible bow-tie antennas," IEEE Trans. Antennas Propag. **59**, 4425-4435 (2011). https://doi.org/10.1109/TAP.2011.2165511
[28] H.-W. Liu, H. Jiang, X. Guan, J.-H. Lei, and S. Li, "Single-feed slotted bowtie antenna for triband applications," IEEE Antennas Wireless Propag. Lett. **12**, 1658-1661 (2013). https://doi.org/10.1109/LAWP.2013.2294751
[29] X. Li, M. Jalilvand, Y. L. Sit, and T. Zwick, "A compact double-layer on-body matched bowtie antenna for medical diagnosis," IEEE Trans. Antennas Propag. **62**, 1808-1816 (2014). https://doi.org/10.1109/TAP.2013.2297158
[30] T. Li, H. Zhai, X. Wang, L. Li, andC. Liang, "Frequency-reconfigurable bow-tie antenna for Bluetooth, WiMAX, and WLAN applications," IEEE Antennas Wireless Propag. Lett. **14**, 171-174 (2015). https://doi.org/10.1109/LAWP.2014.2359199
[31] X. Zhang, C.-J. Chung, S. Wang, H. Subbaraman, Z. Pan, Q. Zhan, and R. T. Chen, "Integrated broadband bowtie antenna on transparent silica substrate," IEEE Antennas Wireless Propag. Lett. **15**, 1377-1381 (2016). https://doi.org/10.1109/LAWP.2015.2510361
[32] J. Wang, Z. Shen, and L. Zhao, "Wideband dual-polarized antenna for spectrum monitoring systems," IEEE Antennas Wireless Propag. Lett. **16**, 2236-2239 (2017). https://doi.org/10.1109/LAWP.2017.2709938
[33] Y. Shafiq, J. Henricks, C. P. Ambulo, T. H. Ware, and S. V. Georgakopoulos, "A battery-free temperature sensor with liquid crystal elastomer switching between RFID chips," IEEE Access, **8**, 87870-87883 (2020).
[34] I. D. Chiele, M. Donelli, J. Iannacci, and K. Guha, "On chip modulated scattering tag operating at millimetric frequency band," Prog. Electromagn. Res. C, **124**, 71-77 (2024). http://dx.doi.org/10.2528/PIERM23102707
[35] K. L. Shlager, G. S. Smith, and J. G. Maloney, "Optimization of bow-tie antennas for pulse radiation," IEEE Trans. Antennas Propag. **42**, 975-982 (1994). https://doi.org/10.1109/8.299600
[36] Y. Nishioka, O. Maeshima, T. Uno, and S. Adachi, "FDTD analysis of resistor-loaded bow-tie antennas covered with ferrite-coated conducting cavity for subsurface radar," IEEE Trans. Antennas Propag. **47**, 970-977 (1999). https://doi.org/10.1109/8.777119
[37] A. A. Lestari, A. G. Yarovoy, and L. P. Ligthart, "Ground influence on the input impedance of transient dipole and bow-tie antennas," IEEE Trans. Antennas Propag. **52**, 1970-1975 (2004). https://doi.org/10.1109/TAP.2004.832371
[38] A. A. Lestari, A. G. Yarovoy, and L. P. Ligthart, "RC-loaded bow-tie antenna for improved pulse radiation," IEEE Trans. Antennas Propag. **52**, 2555-2563 (2004). https://doi.org/10.1109/TAP.2004.834444
[39] F. Sagnard, D.-L. Ton, and J. Badet, "Analysis of the transient waveforms radiated bya combination of thin-wire antennas—part II: simulation results" IEEE Antennas Wireless Propag. Lett. **5**, 213-216 (2006). https://doi.org/10.1109/LAWP.2006.875278
[40] D. Caratelli, and A. Yarovoy, "Unified time- and frequency-domain approach for accurate modeling of electromagnetic radiation processes in ultrawideband antennas" IEEE Trans. Antennas Propag. **58**, 3239-3255 (2010). https://doi.org/10.1109/TAP.2010.2055800
[41] D. Lee, G. Shaker, and W. Melek, "A Broadband wrapped bowtie antenna for UWB pulsed radar applications," IEEE Trans. Antennas Propag. **68**, 7803-7812 (2020). https://doi.org/10.1109/TAP.2020.3000556
[42] O. Fiser, V. Hruby, J. Vrba, T. Drizdal, J. Tesarik, J. Vrba Jr., and D. Vrba, "UWB bowtie antenna for medical microwave imaging applications," IEEE Trans. Antennas Propag. **70**, 5357-5372 (2022). https://doi.org/10.1109/TAP.2022.3161355
[43] Y. Nishioka, O. Maeshima, T. Uno, and S. Adachi, "FDTD analysis of resistor-loaded bow-tie antennas covered with ferrite-coated conducting cavity for subsurface radar," IEEE Trans. Antennas Propag. **47**, 970-977 (1999). https://doi.org/10.1109/8.777119
[44] G. P. Pochanin, "UWB/SP antennas classification," in: *Proc. Int. Symp. Physics and Engineering of Millimeter and Submillimeter Waves*, **3**, 549-550 (1994).
[45] G. P. Pochanin and P. V. Kholod, "Cylindrical slot radiator of non-sinusoidal waves. Use of radio waves of millimeter and submillimeter ranges," Collection of scientific papers, Kharkiv: Institute for Radiophysics and Electronics of the National Academy of Sciences of Ukraine, 112-119 (1993).
[46] D. Lee, G. Shaker, and W. Melek, "A broadband wrapped bowtie antenna for UWB pulsed radar applications," IEEE Trans. Antennas Propag. **68**, 7803-7812 (2020). https://doi.org/10.1109/TAP.2020.3000556
[47] V. P. Prokhorenko, V. E. Ivashchuk, and S. V. Korsun, "Electromagnetic impulse radiator,". in Proc. 2nd Int. Conf. Ultra Wideband and Ultra Short Impulse Signals, 244-245 (2004). https://doi.org/10.1109/UWBUS.2004.1388115
[48] A.A. Orlenko, and P. V. Kholod, "Two modes of excitation of the UWB/SP transmitting antenna," in: *Proc. 3rd Int. Conf. Ultra Wideband and Ultra Short Impulse Signals*, (Sevastopol, Ukraine, 2006), pp. 185-187. https://doi.org/10.1109/UWBUS.2006.307197
[49] A. Taflove, *Computational electrodynamics: The finite – difference time – domain method*, (New York: Artech House, 1995).
[50] L. A. Varyanitza-Roshchupkina, "Software for image simulation in ground penetrating radar problems," in: *Proc. 3rd Int. Conf. Ultra Wideband and Ultra Short Impulse Signals*, (Sevastopol, Ukraine, 2006), pp. 150-155. https://doi.org/10.1109/UWBUS.2006.307172
[51] M. V. Nesterenko, S. L. Berdnik, A. V. Gomozov, D. V. Gretskih, and V. A. Katrich, "Approximate boundary conditions for electromagnetic fields in electromagnetics," Radioelectronic and Computer Systems, (3), 141-160 (2022). https://doi.org/10.32620/reks.2022.3.11
[52] T.N. Ogurtsova, P.V. Kholod, and G.P. Pochanin, "Sensitivity of UWB ferrite receiving antennas," in: *Proc. 2nd Int. Conf. Ultra Wideband and Ultra Short Impulse Signals*, (Sevastopol, Ukraine, 2004), pp. 279-281. https://doi.org/10.1109/UWBUS.2004.1388129

[53] O.A. Orlenko, "UWB pulse generators," in: *Proc. 6th Int. Conf. Ultra Wideband and Ultra Short Impulse Signals*, (Sevastopol, Ukraine, 2012), pp. 75-77. https://doi.org/10.1109/UWBUSIS.2012.6379737
[54] V. Prokhorenko, V. Ivashchuk, S. Korsun, "Drift step recovery devices utilization for electromagnetic pulse radiation," in: *Proc. 10th Int. Conf. on Ground Penetrating Radar*, 195-198 (Piscataway, NJ, 2004). https://doi.org/10.1109/ICGPR.2004.179954

ЗМЕНШЕННЯ АМПЛІТУДИ ТА ТРИВАЛОСТІ ПІСЛЯІМПУЛЬСНИХ КОЛИВАНЬ В АКТИВНІЙ ВИПРОМІНЮВАЛЬНІЙ АНТЕНІ ТИПУ "BOW-TIE"

Геннадій П. Почанін[1], Михайло В. Нестеренко[2], Олександр А. Орленко[1], Тетяна М. Огурцова[1], Ірина Є. Почаніна[1], Вадим П. Рубан[1]

[1]Інститут радіофізики та електроніки ім. О.Я. Усикова Національної академії наук України, вул. Ак. Проскури, 12, м. Харків, Україна, 61085

[2]Харківський національний університет імені В.Н. Каразіна, майдан Свободи, 4, м. Харків, Україна, 61022

У статті досліджується один із способів придушення післяімпульсних коливань у надширокосмугових (НШС) електромагнітних імпульсах, що випромінюються антеною типу «Bow-Tie», збудженою в активному режимі (генератор імпульсів розташований безпосередньо на випромінювачі). Оскільки цей метод збудження не вимагає балансування або інших засобів, необхідних для узгодження антени, створюються умови для збільшення випромінюваної потужності при тій самій споживаній потужності. Для придушення післяімпульсних коливань у випромінюваному полі використовуються резистивні елементи з високим опором. Вони розташовуються поблизу джерела збудження, щоб поглинати накопичену в антені невипромінену частину енергії. Експериментально проаналізовано вплив форм-фактора антени та опору навантаження на форму сигналу, що випромінюється.

Ключові слова: *надширокосмуговий сигнал; антена типу «Bow-Tie»; випромінюване електромагнітне поле; післяімпульсні коливання; активна антена*

EAST EUROPEAN JOURNAL OF PHYSICS. 1. 507-519 (2026)
DOI:10.26565/2312-4334-2026-1-58 ISSN 2312-4334

QUANTUM-CHEMICAL CALCULATIONS OF TECHNETIUM RADIOPHARMACEUTICALS

K. Vus*, V. Trusova, V. Romashyna, U. Malovytsia, O. Zhytniakivska, G. Gorbenko
Department of Medical Physics and Biomedical Nanotechnologies, V.N. Karazin Kharkiv National University
4 Svobody Sq., Kharkiv, 61022, Ukraine
**Corresponding Author email: kateryna.vus@karazin.ua*
Received January 5, 2026, revised February 15, 2026; accepted February 19, 2026

The synthesis of radiopharmaceuticals is a major task of nuclear medicine, and Technetium-99m (^{99m}Tc) has ideal nuclear properties for non-invasive nuclear medical diagnostics by single-photon emission computed tomography (SPECT) – a cheaper method than CT, MRI, and PET, suitable for developing countries. Of particular relevance today is the design of various covalently labelled ^{99m}Tc radiopharmaceuticals for the diagnosis and theranostics of oncological diseases. However, the correct selection of ligands and the development of high-quality ^{99m}Tc-based imaging agents that will not disrupt the functions of biologically active molecules requires a good understanding of the coordination chemistry of group 7 transition metals. In this work, the quantum-chemical characteristics of ten ^{99m}Tc radiopharmaceuticals were calculated using *ab initio* (a combined basis set: SBKJC on the Tc atom and 6-31G (d,p)/DFT – on other atoms, Gamess) and semi-empirical (PM6, MOPAC) methods. Negative (for Tc-Exametazime, Tc-ECD) and positive (for other ^{99m}Tc complexes) values of the E_{LUMO} parameter indicated the electrophilic and nucleophilic properties of the radiopharmaceuticals, respectively. Analysis of the absolute hardness values of the complexes revealed that the studied radiopharmaceuticals are soft reagents, with Pertechnetate having the lowest reactivity, which is consistent with the literature data. Dipole moments of most of the ^{99m}Tc radiopharmaceuticals were similar or up to one order of magnitude greater as compared to that of a water molecule. Finally, a strong correlation was established between the ground state dipole moments, lipophilicity and the percentage of nonspecific binding of five radiopharmaceuticals (Tc-Exametazime, Tc-MAG3, Tc-MDP, Tc(III)-DMSA, Tc-DTPA) to plasma proteins (Pearson's correlation coefficients were *ca.* -0.719 and 0.611, respectively). The obtained results could be employed for the design of new ^{99m}Tc-based theranostic agents suitable for cancer treatment, in particular those with high nonspecific binding to plasma proteins.
Keywords: *^{99m}Tc radiopharmaceuticals; Quantum-chemical calculations; Nonspecific protein binding; Dipole moment; Lipophilicity*
PACS: 87.14.C++c, 87.16.Dg

Development of the current nuclear medicine is associated with the design of new radiolabeled agents, and technetium-99m (^{99m}Tc) is a component of more than 80% of radiopharmaceuticals employed for the imaging of function and physiological/ pathological changes in organs by the non-invasive single-photon emission computed tomography (SPECT) [1, 2]. Broad application of ^{99m}Tc in nuclear medicine is explained by its ideal characteristics, i.e.: i) low production cost [3, 4]; ii) high specificity, rapid elimination from the blood and low toxicity [5]; iii) the half-life of ^{99m}Tc is 6.01 h and the gamma photon energy is about 140 keV, allowing the synthesis and transportation of the radionuclide over long distances, a reduction in the internal radiation hazard compared to other radioisotopes, as well as the study of tissues at any depth from the body surface [1, 6, 7]. Moreover, ^{99m}Tc plays an important role in molecular imaging, since SPECT has similar spatial resolution with positron emission tomography (PET) [7]. The first radiopharmaceutical of ^{99m}Tc, Pertechnetate (TcO_4^-), is widely employed for brain and thyroid gland imaging, because it distributes within the body to a similar extent as iodine [8, 9]. Pertechnetate is obtained by the beta decay of molybdenum (^{99}Mo), although chemical reduction of the ^{99m}Tc oxidation state +7 is required to allow formation of stable complexes of ^{99m}Tc radiopharmaceuticals with organic ligands or biomolecules [1]. Thus, in the last decades synthesis of ^{99m}Tc coordination complexes has been accompanied by binding of the radionuclide to the so-called "core", allowing the incorporation of ^{99m}Tc into bioactive molecules without affecting their bioactivity [7]. The physicochemical properties, concentration of the reducing agent and the coordinating ligand, pH, etc. significantly affect the stability of the resulting ^{99m}Tc radiopharmaceuticals in the bloodstream [10]. There is an urgent need to design theranostic agents based on ^{99m}Tc radiopharmaceuticals for cancer early diagnosis and treatment, real time monitoring of the therapy progress, which would improve treatment outcomes and life quality of patients [10 − 14]. For example, Tc(V)-DMSA, typically used for medullary thyroid cancer diagnostics, was proved to be efficient in lung cancer detection [15], and the myocardial perfusion SPECT radiotracer, Tc-Sestamibi, appeared to be suitable for breast cancer imaging [10, 16]. Notably, new theranostic agents based on ^{99m}Tc radiopharmaceuticals should be characterized by high affinity for blood plasma proteins, which would increase their biological half-life and thus prolong the therapeutic effect. Good understanding of the coordination chemistry of transition metals with an oxidation state of +7, as well as deep investigating the influence of various coordinating ligands on the physicochemical properties of the resulting complexes, are required for successful development of new ^{99m}Tc radiopharmaceuticals [7]. Quantum-chemical calculations are believed to facilitate the search for coordinating ligands suitable for synthesizing new, more thermodynamically stable ^{99m}Tc radiopharmaceuticals, characterized by certain molecular interactions and biological

Cite as: K. Vus, V. Trusova, V. Romashyna, U. Malovytsia, O. Zhytniakivska, G. Gorbenko, East Eur. J. Phys. 1, 507 (2026), https://doi.org/10.26565/2312-4334-2026-1-58

activity. The density functional theory (DFT) method is largely used to study the influence of various ligands on the spectroscopic properties, NMR chemical shifts, stability and electronic structure of ^{99m}Tc complexes [17, 18]. In view of the above, this work was aimed at investigating the quantum-chemical characteristics of ten ^{99m}Tc radiopharmaceuticals: Tc-MAG3, Tc-Medronate, Tc(III)-DMSA, Tc-DTPA, Tc-Exametazime, Tc-DISIDA, Tc-ECD, Pertechnetate, Tc-Sestamibi and Tc-Mebrofenin. To achieve this goal, the following tasks were performed: i) *ab initio* and semi-empirical quantum-chemical calculations of the ^{99m}Tc radiopharmaceuticals using the combined basis set: SBKJC on the Tc atom and 6-31G (d,p)/DFT – on other atoms (Gamess), and the PM6 method (MOPAC), respectively; ii) characterizing HOMO and LUMO orbitals, the electron density distribution, solvation energy and the lowest singlet excited state energy of the optimized structures of the ^{99m}Tc complexes; iii) accession of the reliability of the obtained results by comparing them with available literature data; iv) establishing the correlation between the calculated quantum-chemical descriptors of the geometric and electronic structure, electronic and thermodynamic properties of the ^{99m}Tc complexes [19] and the nonspecific binding of radiopharmaceuticals to plasma proteins.

MATERIALS AND METHODS

Nine largely used radiopharmaceuticals for nuclear medicine containing coordinating ligands for the ^{99m}Tc atom combined with the core of the complex (Tc-MAG3 (^{99m}Tc-Mercaptoacetyltriglycine), Tc-Medronate, Tc(III)-DMSA, Tc-DTPA, Tc-Exametazime, Tc-DISIDA (Tc-Disofenin), Tc-ECD (Tc-Ethylene cysteine dimer), Tc-Sestamibi and Tc-Mebrofenin), as well as Pertechnetate (which does not contain any coordination ligand) [7], were employed in the present study.

Tc-MAG3 is a tetradentate monooxocomplex of Tc(V) and mercaptoacetyltriglycine, which is used for the diagnosis of renal failure and urinary tract obstruction, as well as for assessing kidney function in a donor before transplantation [20, 21]. This radiopharmaceutical has low affinity for plasma proteins and thus is rapidly excreted from the body of a healthy person by glomerular filtration through the kidneys, but provides quantitative characterization of impaired renal function in sick patients [20, 21]. Tc-ECD, a five-coordinate square pyramidal complex of the Tc(V) atom with N,N′-1,2-ethenediylbis-L-cysteine diethylester, acts in a similar way to Tc-MAG3, and therefore is used as an imaging agent for renal function and brain perfusion (notably, high lipophilicity allows Tc-ECD to pass through the blood-brain barrier) [7, 9]. Radioactive half-life of Tc-ECD is about 50 minutes in patients with normal renal function, but may be prolonged in renal failure [7, 9]. Tc-Exametazime is a five-coordinate square pyramidal complex of Tc(V) with a hexamethyl-functionalized derivative of propylene amine oxime, employed for radioactive labeling of leukocytes [9], as well as a brain perfusion imaging agent (due to its high lipophilicity and affinity for blood plasma proteins) [22]. Tc-DTPA is a six-coordinate complex of the Tc(IV) atom with three N atoms and three O atoms for coordination [9, 23]. After intravenous administration it is rapidly eliminated from the bloodstream by glomerular filtration and is used to assess the glomerular filtration rate of the kidneys [9, 23]. Tc(IV)-Medronate, like Tc(IV)-DTPA, is formed by reduction of Pertechnetate with tin chloride in the presence of a coordinating ligand [9]. Tc-Medronate contains medronic acid and thus, is highly bound to albumin, transporting the radiopharmaceutical to the liver and then localizing it in the bones (due to high affinity of Tc-Medronate for hydroxyapatite crystals in the bones), thereby making Tc-Medronate suitable for visualization of areas of altered osteogenesis [9]. Tc(III)-DMSA is a dimeric complex that forms at low pH, and after intravenous administration slowly accumulates in the renal cortex (due to its high affinity for plasma proteins), binding the proximal convoluted tubule cells. Tc(III)-DMSA is used to assess renal parenchymal diseases [9].

Tc-DISIDA and Tc-Mebrofenin are analogues of Tc-Iminodiacetic acid (IDA), hexacoordination complexes of Tc(III), stabilized by two N atoms and four O atoms of two IDA ligands, which are employed to assess hepatobiliary function in acute and chronic cholecystitis [9] due to their high affinity for plasma proteins [24 – 27]. After intravenous administration, these radiopharmaceuticals are rapidly extracted from the blood into the bile by active transport through the anionic site on the hepatocyte membrane, which is the same site for bilirubin transport [9].

Tc-Sestamibi is an octahedral, cationic Tc(I) complex containing six isonitrile ligands, characterized by low affinity for plasma proteins [28– 30] and used for visualization of myocardial perfusion, cardiac ischemia and necrosis, as well as breast cancer [31 – 33].

The main physicochemical properties of the ^{99m}Tc radiopharmaceuticals studied in this work are summarized in Table 1.

The three-dimensional structures of the ^{99m}Tc radiopharmaceuticals were drawn in MarvinSketch (version 24.1.2) [34], followed by modification of the total charge of each complex to reach that shown in Table 1, pre-optimization and generation input files for Gamess in Avogadro (version 1.97.0).

Quantum-chemical calculations of the ground state S_0 free energy (E_g), the ground state dipole moment (μ_g) and its projections on the X, Y and Z axes (μ_{gx}, μ_{gy} and μ_{gz}, respectively), the partial charge on the Tc atom in the ground state (q_g) were performed in the gas phase using the Gamess software package (version 30 SEPT 2017 (R2)). Free energy in water (E_{H2O}) and the solvation energy (E_{solv}) of the radiopharmaceuticals were also estimated. For all *ab initio* calculations, the combined basis set: SBKJC on the Tc atom [35] and 6-31G (d,p) – on other atoms [36], as well as density functional theory (DFT) and B3LYP functional [35, 37], were used. The SBKJC basis set (unlike 6-31G (d,p)) can be employed in Gamess for heavy elements: it takes into account only the valence electrons of the atom, and

replaces the inner electrons with the effective nuclear potential [37, 38]. To estimate the energy characteristics of the ^{99m}Tc complexes in water, we used the optimized geometry in the gas phase, the PCM theory, and the covalent radius of Tc – 1.47 Å [39]. All other quantum-chemical descriptors of the ^{99m}Tc radiopharmaceuticals (except for E_{H2O} and E_{solv}) were calculated in the gas phase. To estimate the free energy (E_e), the partial charge on the Tc atom (q_e) and dipole moment (μ_e) of the non-relaxed excited state S_1 (the lowest singlet excited state formed immediately after photon absorption), the excited state energy (ΔE_e) and oscillator strength (f) of the $S_0 \rightarrow S_1$ electronic transition, we used the optimized ground state geometry in the gas phase, density functional theory (TDDFT=EXCITE) and B3LYP functional [35, 37]. The calculation of the absorption wavelength (λ_{abs}) of the ^{99m}Tc radiopharmaceuticals in the excited state was also performed using the ΔE_e values.

The ALOGPS 2.1 online server (http://www.vcclab.org/) was used to calculate the lipophilicity of the ^{99m}Tc complexes (*CLogP*), their molecular weight (*Mol. wt.*), and water solubility (*LogS*).

To estimate the geometric parameters of the ^{99m}Tc radiopharmaceuticals (length, width, thickness, molecular volume, solvent-accessible surface area (*SASA*), as well as the *heat of formation*, semi-empirical PM6 method and the MOPAC program (version 23.1.2 Linux) were used, although the accuracy of semi-empirical calculations for transition metal complexes is low [40]. The number of hydrogen bond donors (*No. of H-bond donors*) and acceptors (*No. of H-bond acceptors*), as well as the number *of rotatable bonds* were calculated using the SwissADME online server: http://www.swissadme.ch/ .

Table 1. Physico-chemical properties of ^{99m}Tc radiopharmaceuticals

№	Name	*Charge of the complex*	*Core of the complex*	^{99m}Tc oxidation state	Stability	References
1	Tc-MAG3 (^{99m}Tc-Mercaptoacetyltriglycine, ^{99m}Tc-Mertiatide)	-1	Tc=O3+	+5	Stable in water	9
2	Tc-Medronate (or Tc-MDP)	-2	Tc4+	+4	Stable	9
3	Tc(III)-DMSA (or Tc(III)-Succimer)	-3	Tc3+	+3	Has a lability to oxidation	9
4	Tc-DTPA (or Tc-pentetate)	-2	Tc4+	+4	Stable	9, 32
5	Tc-Exametazime (or Tc-HMPAO)	0	Tc=O3+	+5	Lipophilic, unstable in water	9
6	Tc-DISIDA (Tc-Disofenin)	-1	Tc3+	+3	Kinetically inert	9
7	Tc-ECD (Tc-Ethylene cysteine dimer)	0	Tc=O3+	+5	Lipophilic	7, 9
8	Pertechnetate	-1	[Tc+7O4] –	+7	Stable in water	9
9	Tc-Sestamibi	+1	Tc+	+1	Lipophilic	9
10	Tc-Mebrofenin (Tc-BRIDA)	-1	Tc3+	+3	Kinetically inert	9

To visualize the obtained results (geometry of the ^{99m}Tc complexes, their electron density distribution, HOMO and LUMO orbitals), the wxMacMolPlt program (version 7.7.2) [41] was employed.

Absolute hardness (η) of the ^{99m}Tc radiopharmaceuticals was calculated using the formula [42, 43]:

$$\eta = ½ (E_{nvmo} - E_{vzmo}) \quad (1),$$

where E_{HOMO} and E_{LUMO} are the energies of the lowest unoccupied and highest occupied molecular orbitals in the gas phase, respectively.

According to Koopmans' theorem, the following parameters were estimated: *the ionization potential* is the E_{HOMO} parameter, taken with the opposite sign, and the electron *affinity* is equivalent to the E_{LUMO} parameter [42,43].

20 quantum-chemical descriptors and five ^{99m}Tc complexes (Tc-Exametazime, Tc-MAG3, Tc-MDP, Tc(III)-DMSA, Tc-DTPA) were selected for correlation analysis in order to establish the correspondence between theoretical calculations and the percentage of nonspecific binding of the ^{99m}Tc radiopharmaceuticals to plasma proteins. By fitting the quantum-chemical descriptor value dependence on percentage of protein binding, estimation of the Pearson's correlation (*Pearson's r*) and determination (*Adj.* R^2) coefficients were carried out in the OriginPro software (version 9.1).

RESULTS AND DISCUSSION

In the first stage of our study the quantum-chemical characteristics of ten ^{99m}Tc radiopharmaceuticals were evaluated. Fig. 1 shows the optimized structures of the ^{99m}Tc radiopharmaceuticals. It is worth noting that after geometry optimization of Tc-Sestamibi, atoms of the Tc-C-N chain, linked by a coordination (Tc-C) and a covalent C≡N bonds of the complex, lay on one straight line (Fig. 1I), which is consistent with the literature data [9].

Tables 2 and 3 comprise the results of quantum-chemical calculations of the ^{99m}Tc radiopharmaceuticals in Gamess and MOPAC, respectively. Interestingly, the Mulliken charge on the Tc atom (q_g) in all the ^{99m}Tc complexes ranged from -0.67 (in Tc-Sestamibi) to 1.38 (in Pertechnetate), although the supposed values of the partial charges on the Tc atom are +1 and -1 for the above two radiopharmaceuticals, respectively (*Core of the complex*, Table 1). Furthermore, other eight ^{99m}Tc complexes most likely would have partial charge values close to +3 – +4 because these

are the charges of their cores (*Core of the complex*, Table 1). Unfortunately, Gamess, unlike Gaussian, has low accuracy in calculating partial charges on atoms, so the obtained charges on the Tc atom were far from the correct ones [9]. However, the Tc partial charge values (Table 2) increased in a similar manner to those taken from other sources (*Pearson's* $r = 0.828$, *Adj.* $R^2 = 0.646$), highlighting the possibility of comparing the relative values for different ^{99m}Tc complexes calculated using the combined basis set (SBKJC on the Tc atom and 6-31G (d,p) – on other atoms). Furthermore, the total charges of the complexes obtained from quantum-chemical calculations matched the literature data (*Charge of the complex*, Table 1).

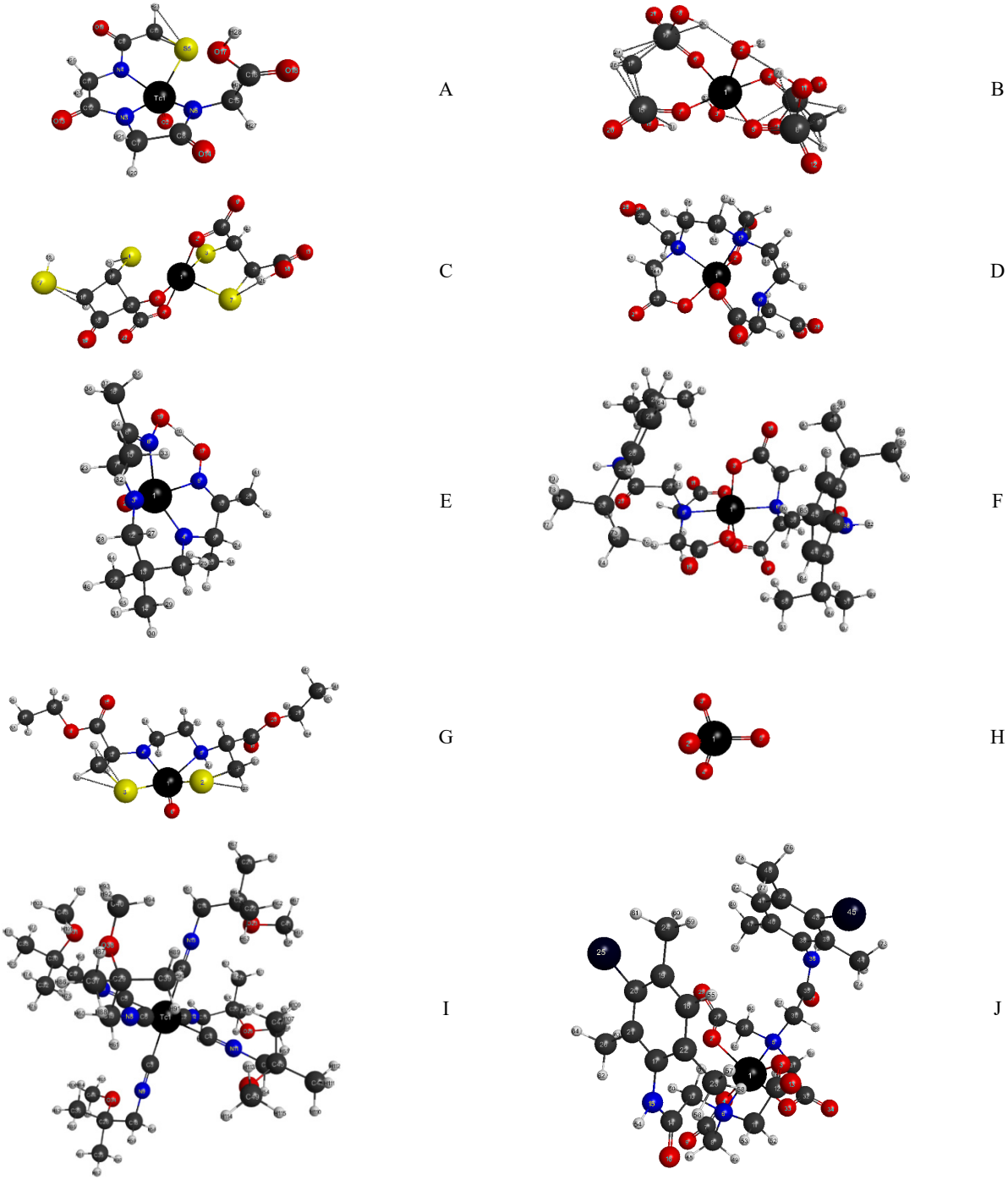

Figure 1. Optimized structures of Tc-MAG3 (A), Tc-Medronate (B), Tc(III)-DMSA (C), Tc-DTPA (D), Tc-Exametazime (E), Tc-DISIDA (F), Tc-ECD (G), Pertechnetate (H), Tc-Sestamibi (I), Tc-Mebrofenin (J) in the gas phase.

As seen in Figs. 2 and 3, the HOMO orbitals of Tc-MAG3, Tc(III)-DMSA, Tc-DTPA, Tc-DISIDA, Tc-Mebrofenin and Tc-Sestamibi are localized on the Tc atom, and that for Tc-MAG3 – additionally on the O and N atoms. In contrast, the LUMO orbitals are localized mainly on the Tc atom for Tc-MAG3, Tc(III)-DMSA, Tc-DISIDA, Tc-Mebrofenin and Tc-DTPA (in Tc-DTPA additionally – on four O atoms of the two carboxyl groups), and in Tc-Sestamibi – only on C and N forming coordinate bonds with the Tc atom.

Table 2. Quantum-chemical characteristics of ^{99m}Tc radiopharmaceuticals calculated in Gamess (using combined basis set: SBKJC on the Tc atom and 6-31G (d,p) – on other atoms)

Parameter, units	Tc-MAG3	Tc-Medronate	Tc(III)-DMSA	Tc-DTPA	Tc-Exametazime	Tc-DISIDA	Tc-ECD	Pertechnetate	Tc-Sestamibi	Tc-Mebrofenin
E_g, Hartree	-1404	-2581	-2621	-1541	-1035	-2451	-1832	-381	-2270	-7362
E_g, kcal/mol	-38211	-1619640	-1644620	-966799	-649494	-1538254	-1149522	-239315.85	-61779	-4619689
E_e, Hartree	-1404	-2581	nd	-1541	-1035	-2451	-1832	-38	-2270	-7362
ΔE_e, eV	2.717	0.276	nd	0.516	2.606	0.252	2.106	3.862	4.305	0.273
E_{H2O}, kcal/mol	-881234	-1619791	-1644938	-966954	-649504	-1538310	-1149536	-239371.18	-1424711	-4619748
λ_{abs}, nm	456	4492	nd	2403	476	4920	589	321	288	4542
f	0.0033	0.000	nd	0.0003	0.0004	0.0000	0.0012	0.0000	0.0002	0.0000
E_{solv}, kcal/mol	-48.47	-153.43	-324.82	-161.15	-12.83	-60.98	-17.24	-55.137	-33.90	-63.82
E_{HOMO}, Hartree	-0.0976	0.0429	0.1976	0.0255	-0.2048	-0.0621	-0.2053	-0.1038	-0.2645	-0.0627
E_{LUMO}, Hartree	0.0546	0.0842	0.2702	0.1091	-0.0599	0.0233	-0.0764	0.0950	-0.0671	0.0224
η, eV	2.07	0.56	0.99	1.14	1.97	0.60	1.75	2.71	2.69	1.16
Ionization potential, eV	2.66	-1.17	-5.38	-0.69	5.57	1.69	5.59	2.82	7.2	1.71
Electron affinity, eV	1.49	2.29	7.35	2.97	-1.63	0.63	-2.08	2.59	-1.83	0.61
μ_{gx}, D	1.55	0.322	-2.45	3.11	1.05	-13.18	5.77	0.003	0.65	0.38
μ_{gy}, D	0.67	0.70	-1.02	5.80	-1.77	2.23	-2.70	-0.003	0.87	12.06
μ_{gz}, D	-0.80	0.34	-0.84	7.88	4.73	-3.69	2.64	0.002	1.83	12.13
μ_g, D	1.87	0.84	2.78	10.26	5.16	13.87	6.90	0.004	2.13	17.11
μ_e, D	1.78	0.95	nd	10.30	5.67	13.91	6.97	0.13	2.14	17.00
q_g, a.u.	0.90	0.92	0.36	0.91	1.07	0.79	0.55	1.38	-0.67	0.78
q_e, a.u.	0.98	0.95	nd	0.93	1.16	0.91	0.59	1.26	-0.62	0.88

nd — not determined

Table 3. Quantum-chemical characteristics of ^{99m}Tc radiopharmaceuticals calculated in MOPAC (PM6) and by the ALOGPS 2.1 online server

Parameter, units	Tc-MAG3	Tc-Medronate	Tc(III)-DMSA	Tc-DTPA	Tc-Exametazime	Tc-DISIDA	Tc-ECD	Pertechnetate	Tc-Sestamibi	Tc-Mebrofenin
CLogP	-1.35	0.17	1.07	-1.17	1.71	2.53	0.97	-0.59	1.32	2.11
LogS	-0.67	-1.57	-2.86	-2.71	-1.43	-6.33	-2.00	0.51	-4.89	-6.03
Mol. wt., Da	418.2	480.9	469.3	487.2	384.3	795.7	436.3	162.9	776.0	869.3
Length, Å	8.6	9.2	11.6	10.6	9.7	14.0	15.3	2.9	15.2	12.6
Width, Å	7.4	5.5	6.1	7.7	8.7	12.5	6.2	2.9	14.7	11.0
Thickness, Å	4.7	4.9	4.9	6.8	4.8	9.9	4.6	2.0	14.0	8.6
SASA, Å^2	264	291	313	336	312	598	353	105	699	572
Volume, Å^3	305	339	382	432	383	878	408	93	1046	824
Heat of formation, kcal/mol	-289	-789	-227	-424	-22	-427	-189	-167	-88	-416
No. of H-bond donors	2	6	1	0	4	2	1	0	6	2
No. of H-bond acceptors	7	14	8	10	9	10	8	4	12	10
No. of rotatable bonds	3	0	1	4	1	12	7	0	30	8

The LUMO orbitals of Pertechnetate and Tc-Medronate are localized mainly on the Tc atom, and the HOMO orbitals – on the O atoms (belonging to two OH groups in the case of Tc-Medronate). The LUMO orbital of Tc-Exametazime is localized mainly on the Tc atom, on one of the N atoms and on the O atom of the Tc=O3+ core, and the HOMO orbital is localized on the Tc and O atoms of the Tc=O3+ core. The LUMO orbital of Tc-ECD is localized mainly on the Tc atom and on one of the S atoms, and the HOMO orbital is localized on the Tc atom and on the O atoms of the Tc=O3+ core. Thus, orbitals of the Tc and sometimes N, O, S atoms (forming covalent/ coordinate bonds with Tc) participate in the formation of the HOMO and LUMO orbitals of the ^{99m}Tc complexes. Negative (for Tc-Exametazime, Tc-ECD) and positive (for all other studied ^{99m}Tc radiopharmaceuticals) values of the E_{LUMO} parameter determine the electrophilic (with a negative sign of *the electron affinity* value, because according to Koopmans' theorem, the electron affinity energy is equal to the LUMO energy) and nucleophilic properties of the ^{99m}Tc complexes, respectively (Table 2) [42, 43].

As seen in Table 2, the absolute rigidity (η) of radiopharmaceuticals fall in the range of 0.56 eV (Tc-Medronate) to 2.71 eV (Pertechnetate), indicating that they will react with soft reagents, e.g. aromatic chemical compounds and alkaline amino acids. At the same time, Tc-Medronate and Tc-DISIDA, possessing the highest reactivity and high affinity for blood plasma proteins [24 – 26], showed the lowest value of the η parameter. In turn, Pertechnetate and Tc-Sestamibi, possessing the lowest reactivity (Pertechnetate) [1] and the lowest ability to associate with proteins and lipid bilayers (Tc-Sestamibi) [28 – 30], showed the highest value of the η parameter. The obtained results indicate the reliability of using the selected combined basis set for calculating the HOMO and LUMO energies of the ^{99m}Tc radiopharmaceuticals.

Fig. 4 shows the electron density distribution of the ^{99m}Tc complexes. The electrostatic charge +1 of Tc-Sestamibi is uniformly distributed between the atoms of the complex, while the charge -1 of Tc-MAG3 is concentrated on the O and S atoms, so the second complex should have better solubility in water, which is consistent with the literature data [44, 45]. Pertechnetate has a positive/ negative partial charge on the Tc/ O atom, which is consistent with the results of other authors [9]. Tc-Medronate, Tc(III)-DMSA and Tc-DTPA, possessing the highest absolute charge (-2 for Tc-Medronate, Tc-DTPA, and -3 for Tc(III)-DMSA), also had the most irregular electron density distribution than other complexes (Table 2). Also, high net charge values and irregular charge distribution of the above three ^{99m}Tc complexes should induce their high solubility in water, which is confirmed by the literature data (Table 1), but is not confirmed by semi-empirical calculations (Tc(III)-DMSA, Tc-DTPA have the lowest *LogS* values, lower than those of lipophilic Tc-Exametazime and Tc-ECD, Table 3), emphasizing the inaccuracy of semi-empirical calculations for the ^{99m}Tc radiopharmaceuticals [7, 9, 33]. The most negative partial charge of Tc-Medronate, Tc(III)-DMSA and Tc-DTPA is

localized on the O atoms (these atoms are most abundant in these three complexes compared to others), while the Tc atom has a positive partial charge (Figure 4). Tc-Mebrofenin and Tc-DISIDA have a net charge of -1 and a similar distribution of electron density: a positive charge on the Tc atom and negative charges on the O atoms (Figure 4). The charges of Tc-Exametazime and Tc-ECD are distributed uniformly (Figure 4), which is probably due to zero net charge of these radiopharmaceuticals (Table 1).

The dipole moment (μ_g) of Pertechnetate was close to zero, in Tc-Medronate (Tc-MAG3 and Tc-Sestamibi) – less than (close to) that of a water molecule, in other radiopharmaceuticals – 1.5–9 times higher than the μ_g of water (Table 2). Furthermore, no significant changes in the dipole moments (μ_e) of the ^{99m}Tc radiopharmaceuticals were observed in the excited state as compared to the ground state (Table 2). It should be noted that the estimated dipole moment values are not very precise, since e.g., for neutral Tc-Exametazime and Tc-ECD they were several times higher than those for the charged ^{99m}Tc complexes, while the lowest μ_g value was obtained for Tc-Medronate possessing a charge of -2 (Table 2).

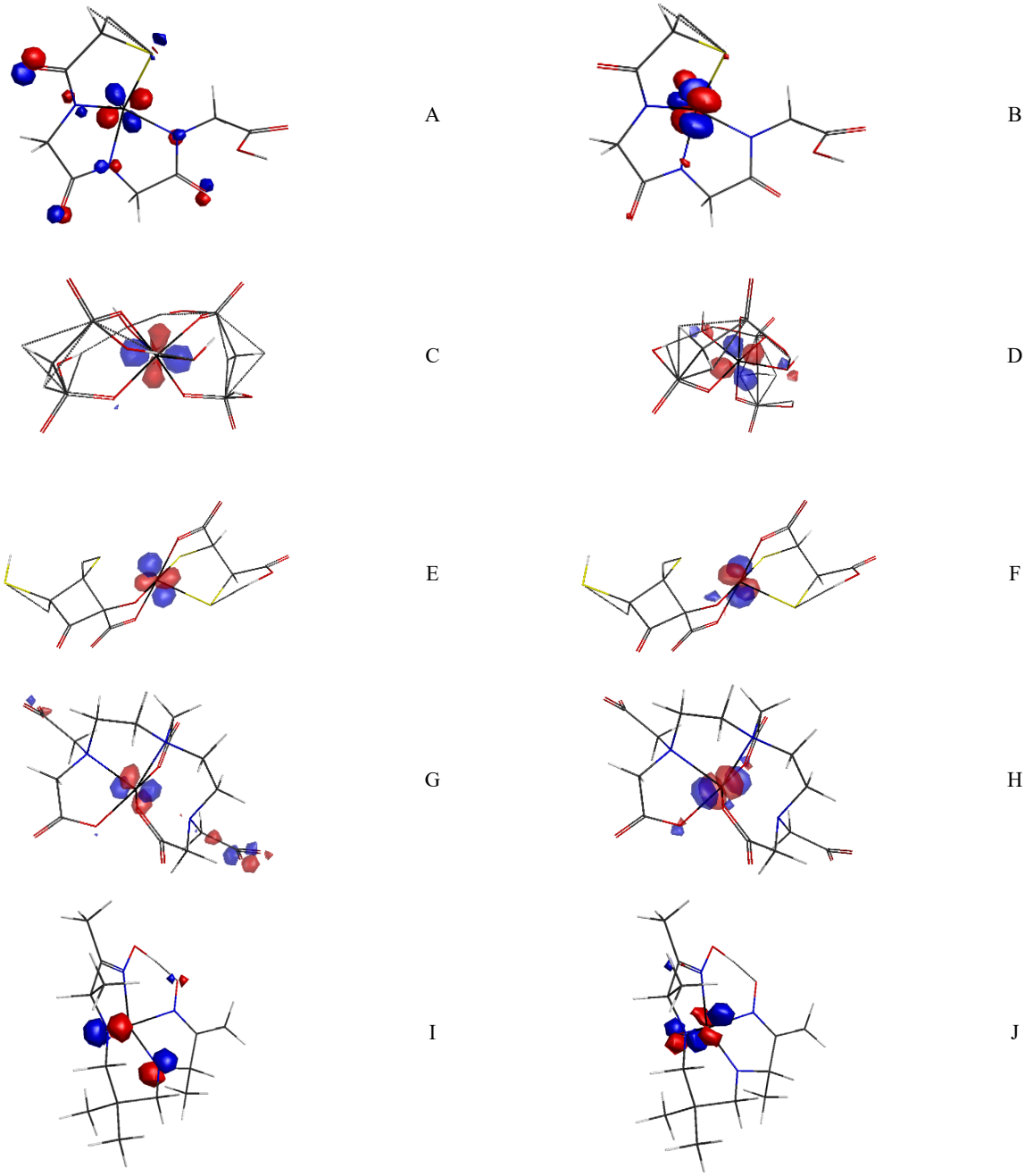

Figure 2. HOMO (A – 79, C – 106, E – 103, G – 110, I – 85) and LUMO (B – 80, D – 107, F – 104, H – 111, J – 86) orbitals of the optimized structures of Tc-MAG3 (A, B), Tc-Medronate (C, D), Tc(III)-DMSA (E, F), Tc-DTPA (G, H), Tc-Exametazime (I, J) in the gas phase.

The solvation energy (E_{solv}) of the ^{99m}Tc radiopharmaceuticals ranged between -12.8 kcal/ mol (Tc-Exametazime) and -324.8 kcal/ mol (Tc(III)-DMSA), with the highest values of this parameter obtained for neutral Tc-Exametazime and Tc-ECD, and the lowest – for the most charged complexes (Tc(III)-DMSA, Tc-DTPA, Tc-Medronate), which is consistent with the high water solubility of the latter complexes (Table 2) [7, 9, 33]. Interestingly, the E_{solv} value of Tc-MAG3 was lower than that of Tc-Sestamibi, which is consistent with higher water solubility of Tc-MAG3 [44 , 45].

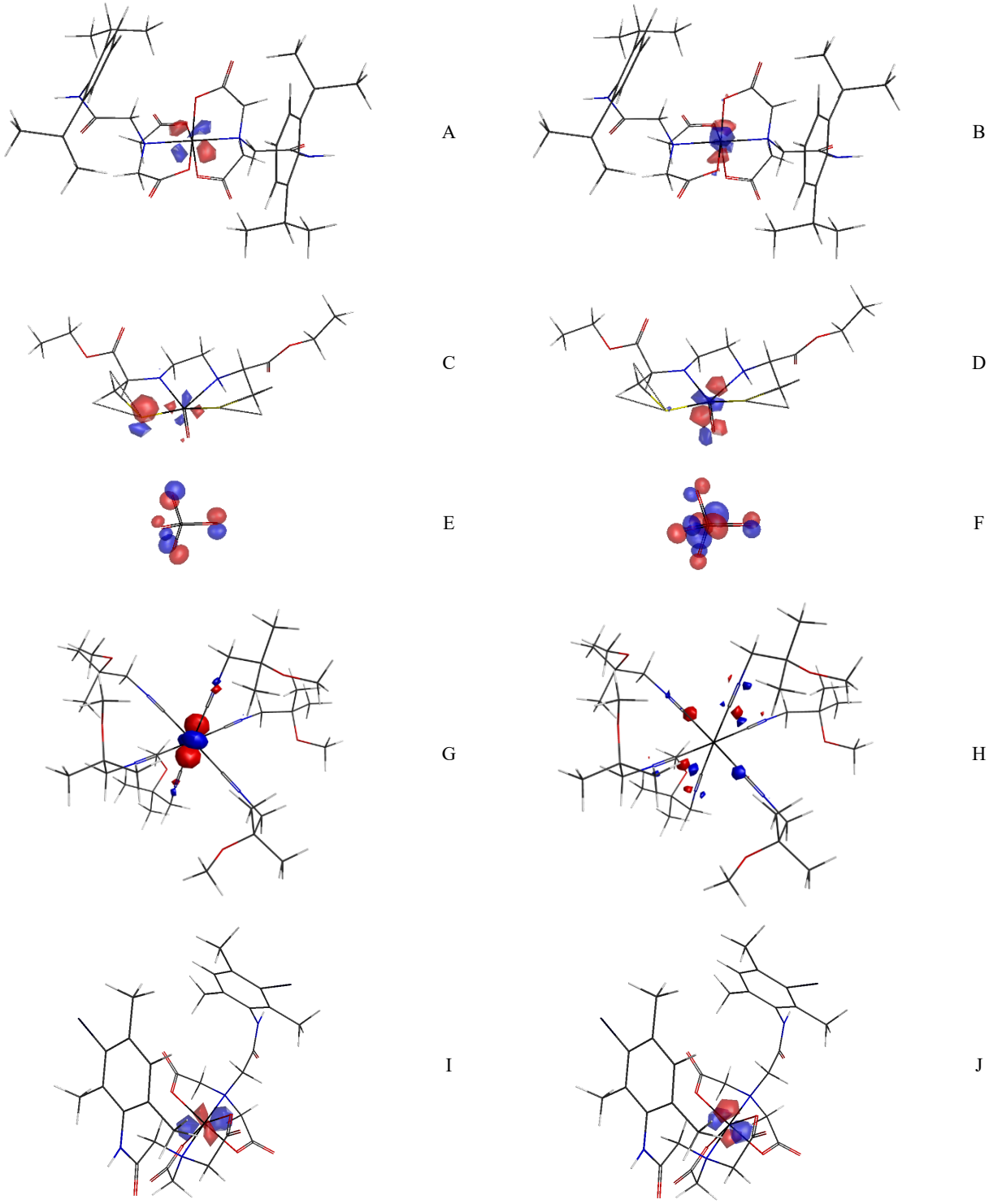

Figure 3. HOMO (A – 194, C – 97, E – 24, G – 193, I – 204) and LUMO (B – 195, D – 98, F – 25, H – 194, J – 205) orbitals of the optimized structures of Tc-DISIDA (A, B), Tc-ECD (C, D), Pertechnetate (E, F), Tc-Sestamibi (G, H), Tc-Mebrofenin (I, J) in the gas phase.

The oscillator strength *f* (that is proportional to the fluorescence quantum yield, Table 2) for all the ^{99m}Tc complexes was about zero (the highest value was 0.0012, indicating a weak fluorescence of Tc-ECD, followed by light

absorption at 589 nm). Notably, Tc-Sestamibi, Pertechnetate, Tc-MAG3, Tc-Exametazime and Tc-ECD had absorption wavelengths (λ_{abs}) in the ultraviolet and visible (288 nm, 321 nm, 456 nm, 476 nm and 589 nm, respectively), Tc-Medronate, Tc-DISIDA and Tc-Mebrofenin – in the far-infrared (4500 – 5000 nm), and Tc-DTPA – in the mid-infrared (2500 nm) regions of the electromagnetic spectrum. Interestingly, λ_{abs} of Tc-Sestamibi in the gas phase was in the ultraviolet region, similar to that of its MIBI ligand in water (Table 2) [33]. For Tc-MAG3, the predicted value of λ_{abs} was 456 nm, which is consistent with the data on the high light sensitivity of the TechnescanMAG3 kit used for the preparation of Tc-MAG3 [21, 46]. The above results indicate the reliability of calculation of the physicochemical characteristics of the ^{99m}Tc radiopharmaceuticals in the excited state using the combined basic set. It is worth noting that Tc-ECD, a renal imaging agent, possessing low protein binding and low liver activity [47, 48], may, according to our data, have a slight absorption of visible light in the same region as the hemoglobin molecule [49]. Interestingly, after excitation of the ^{99m}Tc radiopharmaceuticals (except Pertechnetate), the charge q_e on the Tc atom slightly increased compared to its value in the ground state (q_g, Table 2).

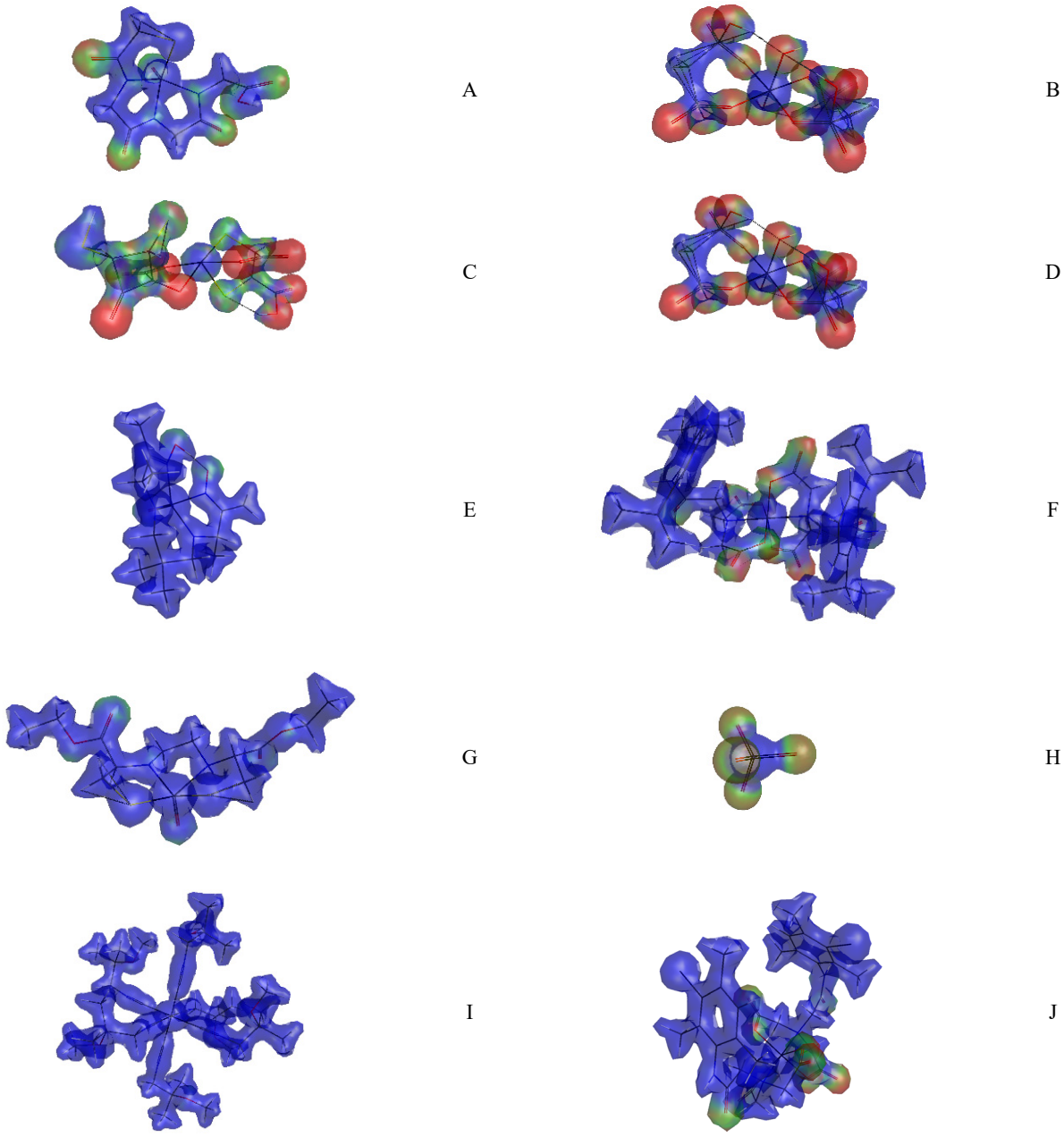

Figure 4. Electron density distribution of Tc-MAG3 (A), Tc-Medronate (B), Tc(III)-DMSA (C), Tc-DTPA (D), Tc-Exametazime (E), Tc-DISIDA (F), Tc-ECD (G), Pertechnetate (H), Tc-Sestamibi (I), Tc-Mebrofenin (J) in the gas phase. Positive and negative values of the electron density are colored in blue and red, respectively.

ALOGPS 2.1 online server revealed negative *CLogP* values of Tc-MAG3, Tc-DTPA and Pertechnetate (Table 3), suggesting high hydrophilicity of these radiopharmaceuticals [9, 33]. For other ^{99m}Tc complexes *CLogP* values ranged

from 0.17 (Tc-Medronate) to 2.53 (Tc-DISIDA), and were the highest for the lipophilic Tc-DISIDA, Tc-Mebrofenin and Tc-Exametazime, possessing high affinity for plasma proteins [25, 26, 50].

The *heat of formation* value (Table 3) of Tc-MAG3 was 3.3 times lower than that of Tc-Sestamibi, showing a greater thermodynamic stability of the first complex [51]. Similarly, the *heat of formation* values of Tc-Medronate, Tc-DISIDA, Tc-DTPA and Tc-Mebrofenin were 1.4–35 times lower than those of Tc-MAG3, Tc(III)-DMSA, Tc-ECD, Pertechnetate, Tc-Sestamibi and Tc-Exametazime, showing a greater thermodynamic stability of the first four complexes [51]. Notably, according to *ab initio* calculations, Tc-Exametazime and Tc-Medronate had one of the largest and lowest values of η (i.e. one of the smallest and largest reactivity), respectively (Table 2). However, the *heat of formation* values revealed that Tc-Exametazime was the least and Tc-Medronate was the most thermodynamically stable, presumably due to low accuracy of the PM6 method.

In the next step of our study, the compliance of the quantum-chemical characteristics of the studied radiopharmaceuticals with Lipinski's "rule of five" was assessed, which would allow prediction of passive intestinal absorption, side effects and pharmacokinetics of the new ^{99m}Tc complexes [52]. For drug-like substances, the following conditions should be met: i) ≤ 5 *hydrogen bond donors* (OH- and NH- bonds) in the molecular structure; b) ≤ 5 *hydrogen bond acceptors* (O and N atoms) in the molecular structure; c) *molecular weight* < 500 Da; d) octanol-water partition coefficient (*CLogP*) ≤ 5; e) number of *rotatable bonds* ≤ 5 – 10. The results obtained (Table 4) showed that the best/ worst compliance with Lipinski's "rule of five" was observed for Pertechnetate, Tc-MAG3, Tc(III)-DMSA, Tc-DTPA, Tc-Exametazime, Tc-ECD/ Tc-Sestamibi, Tc-Medronate, Tc-DISIDA, Tc-Mebrofenin. Indeed, Pertechnetate has been used in the diagnosis of a wide range of diseases by SPECT [8], while e.g., Ts-Sestamibi and Tc-Medronate are nuclear myocardial perfusion and bone imaging agents, respectively [20, 28]. Furthermore, Tc-DISIDA and Tc-Mebrofenin are typically employed to measure the function of liver and gallbladder (they do not need to penetrate the blood-brain barrier, so they are "allowed" to have high *Mol. wt.* values) [24, 25]. Notably, all ^{99m}Tc complexes, except Pertechnetate, possessed *No. of H-bond acceptors* higher than 5.

Table 4. Complience of ^{99m}Tc radiopharmaceuticals with Lipinski's "rule of 5"

Criterion	Tc-MAG3	Tc-Medronate	Tc(III)-DMSA	Tc-DTPA	Tc-Exametazime	Tc-DISIDA	Tc-ECD	Pertechnetate	Tc-Sestamibi	Tc-Mebrofenin
No. of H-bond donors ≤ 5	+	–	+	+	+	+	+	+	–	+
No. of H-bond acceptors ≤ 5	–	–	–	–	–	–	–	+	–	–
Mol. wt. < 500	+	+	+	+	+	–	+	+	–	–
CLogP ≤ 5	+	+	+	+	+	+	+	+	+	+
No. of rotatable bonds ≤ 5 – 10	+	+	+	+	+	–	+	+	–	+

In the last step of our study the correlation between the nonspecific binding of the ^{99m}Tc radiopharmaceuticals to plasma proteins and quantum-chemical descriptors was estimated (Table 5). There is poor data regarding the affinity of ^{99m}Tc radiopharmaceuticals for protein molecules [53 – 55]. For example, the equilibrium dialysis carried out by Vanlić-Razumenić et al. showed the percentage of plasma proteins bound at 4 °C to 5 radiopharmaceuticals: Tc(III)-DMSA (82.7%), Tc-Exametazime (54.7%), Tc-MAG3 (52.7%), Tc-MDP (45.0%), and Tc-DTPA (5.7%) [20]. The above ^{99m}Tc complexes were selected for a correlation analysis. As seen in Table 5, the strongest positive correlation (i.e. the largest value of the Pearson's correlation coefficient, *Pearson's r* = -0.719) of nonspecific protein binding was revealed for the dipole moment (μ_g, a parameter obtained using *ab initio* quantum-chemical calculations) of the ^{99m}Tc radiopharmaceuticals, although this relationship was observed for slightly less than half of the studied complexes (*Adj.* R^2 = 0.355). It should be noted that high values of Pearson's correlation coefficients for the parameters *CLogP* and *Thickness* were also obtained, although semi-empirical calculations for the ^{99m}Tc complexes were less reliable than *ab initio* calculations [40]. Additionally, among the above three descriptors, μ_g and *Thickness* showed a strong cross-correlation (*Pearson's r* = 0.888), so it can be concluded that two quantum-chemical characteristics – μ_g and *CLogP*, determine the degree of the nonspecific binding of the ^{99m}Tc radiopharmaceuticals to plasma proteins (Table 5). Interestingly, the lipophilicity of a small organic molecule typically increases with a decrease in its dipole moment (overall polarity) [56].

Thus, a decrease in the dipole moment and an increase in lipophilicity induced higher nonspecific binding of the ^{99m}Tc radiopharmaceuticals to plasma proteins. This result is consistent with the previous data reported for Tc-Mebrofenin, Tc-DISIDA and their derivatives: the higher was the lipophilicity value, the better was binding to proteins [24 – 26]. Interestingly, despite the fact that our correlation analysis was carried out for hydrophilic ^{99m}Tc

radiopharmaceuticals (except Tc-Exametazime), the result was the same as that obtained previously for lipophilic radiopharmaceuticals (Tc-Mebrofenin, Tc-DISIDA) [24 – 26].

Table 5. Pearson's correlation coefficitnts (*Pearson's r*) and Adj. R^2 coefficients (*Adj. R^2*), showing the relationship between amount of protein binding (%) and quantum-chemical descriptors of the group of 5 complexes: Tc(III)-DMSA, Tc-Exametazime, Tc-MAG3, Tc-MDP and Tc-DTPA

	E_g	E_{H2O}	E_{solv}	E_{HOMO}	E_{LUMO}	η	μ_g	q_g	*CLogP*	*LogS*
Pearson's r	-0.197	-0.373	-0.311	0.223	0.326	0.090	-0.719	-0.330	0.611	0.086
Adj. R^2	-0.281	-0.148	-0.205	-0.265	-0.192	-0.322	0.355	-0.188	0.164	-0.324
	Mol. wt.	*Length*	*Width*	*Thickness*	*SASA*	*Volume*	*Heat of formation*	*No. of H-bond donors*	*No. of H-bond acceptors*	*No. of rotatable bonds*
Pearson's r	-0.321	0.181	-0.307	-0.851	-0.368	-0.430	0.359	0.187	-0.345	-0.629
Adj. R^2	-0.196	-0.290	-0.208	0.633	-0.153	-0.087	-0.161	-0.287	-0.175	0.195

CONCLUSIONS

To summarise, quantum-chemical geometry optimization, calculation of HOMO, LUMO and solvation energies, as well as energies of the $S_0 \rightarrow S_1$ electronic transition for ten commonly used ^{99m}Tc radiopharmaceuticals in the combined basis set (SBKJC on the Tc atom and 6-31G (d,p)/DFT – on other atoms) revealed the results consistent with the available experimental data. The estimated partial charge values on the Tc atom were unfaithful, although it was possible to draw trustworthy conclusions by comparing the obtained electron density distribution in the ^{99m}Tc complexes. Semi-empirical quantum-chemical calculations of the ^{99m}Tc radiopharmaceuticals by the PM6 method gave less reliable results than *ab initio* calculations.

Pertechnetate, Tc-MAG3, Tc(III)-DMSA, Tc-DTPA, Tc-Exametazime, Tc-ECD showed the best, and Tc-Sestamibi, Tc-Medronate, Tc-DISIDA, and Tc-Mebrofenin had worst compliance with Lipinski's "rule of five", and all the ^{99m}Tc coordinate complexes had a number of hydrogen bond acceptors higher than 5. Therefore, the search for new coordinating ligands would be valuable for the development of improved ^{99m}Tc radiopharmaceuticals.

Finally, the percentage of nonspecific binding of five ^{99m}Tc complexes (Tc-Exametazime, Tc-MAG3, Tc-MDP, Tc(III)-DMSA, Tc-DTPA) to blood plasma proteins increased with increasing lipophilicity and decreasing ground state dipole moment (Pearson's correlation coefficients were 0.611 and -0.719, respectively). The above correspondence between the quantum-chemical descriptors and the experimental data can be employed in designing new ^{99m}Tc radiopharmaceuticals for cancer theranostics, which would possess high nonspecific binding to plasma proteins.

Acknowledgements

This work was supported by the Ministry of Education and Science of Ukraine (the Young Scientist projects № 0125U000840 "Nanocomposite materials based on metal-organic frameworks for environmental remediation, ecological screening, and medical diagnostics" and № 0124U000968 "Development of economically affordable nanosystems for rapid identification and purification of water from heavy metal ions based on carbon nanoallotropes and amyloids from organic waste").

ORCID

Kateryna Vus, https://orcid.org/0000-0003-4738-4016; **Valeriya Trusova,** https://orcid.org/0000-0002-7087-071X
Valeriya Romashyna, https://orcid.org/0009-0004-4427-8861; **Uliana Malovytsia**, https://orcid.org/0000-0002-7677-0779
Olga Zhytniakivska, https://orcid.org/0000-0002-2068-5823; **Galyna Gorbenko,** https://orcid.org/0000-0002-0954-5053

REFERENCES

[1] M.U. Akbar, M.R. Ahmad, A. Shaheen, and S. Mushtaq, J. Radioanal. Nucl. Chem. **310**, 477 (2016). https://doi.org/10.1007/s10967-016-5019-7
[2] S. Upadhrasta, and R.C. Hendel, "SPECT Radiopharmaceuticals," in: *Handbook of Nuclear Cardiology: Cardiac SPECT and Cardiac PET*, edited by R.C. Hendel, and G.V. Heller (Springer Cham, 2024), pp. 39–47.
[3] M.R.A. Pillai, A. Dash, and F.R. Knapp, J. Nucl. Med. **54**, 313 (2013). https://doi.org/10.2967/jnumed.112.110338
[4] I. Amato, Chem. Eng. News **87**, 58 (2009). https://doi.org/10.1021/cen-v087n036.p058
[5] A. Signore, A. Annovazzi, R. Barone, E. Bonanno, C. D'Alessandria, M. Chianelli, S.J. Mather, *et al*., J. Nucl. Med. **45**, 1647-1652 (2004).

[6] S.M. Rathmann, Z. Ahmad, S. Slikboer, H.A. Bilton, D.P. Snider, and J.F. Valliant, Radiopharm. Chem. **1**, 311 (2019). https://doi.org/10.1007/978-3-319-98947-1_18
[7] A. Boschi, L. Uccelli, P. Martini, Appl. Sci. **9**, 2526 (2019). https://doi.org/10.3390/app9122526
[8] M.T. Hays, and F.A. Green, J. Nucl. Med. **14**, 149 (1973).
[9] R. J. Kowalsky, Technetium radiopharmaceutical chemistry. The University of New Mexico Health Sciences Center College of Pharmacy, Albuquerque, New Mexico.
[10] N. Ahmed, M. Zia, Chin. J. Acad. Radiol. **6**, 143–159 (2023). https://doi.org/10.1007/s42058-023-00128-7
[11] J. Chen, S. Tang, and P. Lü, J. Radioanal. Nucl. Chem. **334**, 4419 (2025). https://doi.org/10.1007/s10967-025-10237-5
[12] A. Khalaji, M. Rostampour, F. Riahi, D. Rafieezadeh, S.A.D. Tabatabaei, S. Fesharaki, and S.H. Tooyserkani, Int. J. Physiol. Pathophysiol. Pharmacol. **17**, 37 (2025). https://doi.org/10.62347/LQYR3145
[13] A. Boschi, L. Urso, L. Uccelli, P. Martini, and L. Filippi, EJNMMI Radiopharm. Chem. **9**, 36 (2024). https://doi.org/10.1186/s41181-024-00264-0
[14] B.J. Nelson, V. Krol, A. Bansal, J.D. Andersson, F. Wuest, and M.K. Pandey, Theranostics, **14**, 6446 (2024). https://doi.org/10.7150/thno.100339
[15] E. Gharepapagh, L. Namvar, and S. Rezaei, World J. Nucl. Med. **1**, 1 (2025).
[16] N. Urbano, M. Scimeca, V. Tancredi, E. Bonanno, and O. Schillaci, Semin. Cancer Biol. **84**, 302 (2022). https://doi.org/10.1016/j.semcancer.2020.01.007
[17] D. Hernández-Valdés, R. Alberto, and U. Jáuregui-Haza, RSC Adv. **6**, 107127 (2016). https://doi.org/10.1039/C6RA23142J
[18] T.F. De Andrade, H.F. Dos Santos, C. Fonseca Guerra, and D.F. Paschoal, J. Phys. Chem. A **126**, 5434 (2022). https://doi.org/10.1021/acs.jpca.2c01617
[19] S.T. Guo, J. Liu, W. Qian, W.H. Zhu, and C.Y. Zhang, Energ. Mater. Front. **2**, 292 (2021). https://doi.org/10.1016/j.enmf.2021.10.004
[20] N. Vanlić-Razumenić, J. Joksimović, B. Ristić, M. Tomić, S. Beatovć, and B. Ajdinović, Nucl. Med. Biol. **20**, 363 (1993). https://doi.org/10.1016/0969-8051(93)90060-8
[21] Curium Pharma, Nucl. Pharm. Kit (2015). https://pharmacyce.unm.edu/nuclear_program/neolibrary/libraryfiles/package_inserts/technescan%20mag3.pdf
[22] Y. Huh, J. Yang, O.U. Dim, Y. Cui, W. Tao, Q. Huang, and Y. Seo, Med. Phys. **48**, 2301 (2021). https://doi.org/10.1002/mp.14836
[23] J.G. McAfee, G. Gagne, H.L. Atkins, P.T. Kirchner, R.C. Reba, M.D. Blaufox, and E.M. Smith, J. Nucl. Med. **20**, 1273 (1979).
[24] M.K. Kim, J. Seidel, N. Le, I.S. Kim, T.M. Yoo, C. Barker, and C.H. Paik, Nucl. Med. Biol. **26**, 43 (1999). https://doi.org/10.1016/s0969-8051(98)00077-8
[25] S. Marie, I. Hernández-Lozano, O. Langer, N. Tournier, J. Nucl. Med. **62**, 1043 (2021). https://doi.org/10.2967/jnumed.120.261321
[26] A.D. Nunn, M. D. Loberg, R. A. Conley, J. Nucl. Med. **24**, 423 (1983).
[27] F. Morandi, N. Frank, J. Avenell, and G.B. Daniel, J. Vet. Intern. Med. **19**, 751 (2005). https://doi.org/10.1892/0891-6640(2005)19[751:qaohfb]2.0.co;2
[28] L. Maffioli, J. Steens, E. Pauwels, and E. Bombardieri, Tumori J. **82**, 12 (1996). https://doi.org/10.1177/030089169608200103
[29] V.V. Rao, J.L. Dahlheimer, M.E. Bardgett, A.Z. Snyder, R.A. Finch, A.C. Sartorelli, and D. Piwnica-Worms, Proc. Natl. Acad. Sci. U.S.A. **96**, 3900 (1999). https://doi.org/10.1073/pnas.96.7.3900
[30] W.S. Chen, K.E. Luker, J.L. Dahlheimer, C.M. Pica, G.D. Luker, D. Piwnica-Worms, Biochem. Pharmacol. **60**, 413 (2000). https://doi.org/10.1016/s0006-2952(00)00341-5
[31] L. Coover, Hosp. Phys. **35**, 16 (1999).
[32] R. Yaes, U.S. Food Drug Adm. **19**, 785 (2008). https://www.fda.gov/downloads/Drugs/.../DevelopmentResources/ucm072825.pdf
[33] *Int. At. Energy Agency Tech. Rep. Ser.* **466**, 1 (2008). Technical Reports Series No. 466. Technetium-99m radiopharmaceuticals: manufacture of kits.
[34] P. Csizmadia, J. Chem. Inf. Comput. Sci. (1999). https://doi.org/10.3390/ecsoc-3-01775
[35] S. James, K.P. Maresca, D.G. Allis, J.F. Valliant, W. Eckelman, J.W. Babich, and J. Zubieta, Bioconjug. Chem. **17**, 579 (2006). https://doi.org/10.1021/bc050297w
[36] O.C. Adekoya, G.J. Adekoya, E.R. Sadiku, Y. Hamam, and S.S. Ray, Pharmaceutics, **14**, 1972 (2022). https://doi.org/10.3390/pharmaceutics14091972
[37] S. Shahabi, S. Riahia, R. Kianib, S. Soleymanib, M.R. Ganjalib, and P. Norouzi, "A novel approach to modeling the selectivity coefficients of metallic cations using quantum mechanical calculations and chemometrics," Proc. Int. Conf. Chem. Chem. Eng. **2011**, 1 (2011).
[38] N.E. Binbay, Russ. J. Phys. Chem. A, **96**, 3161 (2022). https://doi.org/10.1134/S0036024423020188
[39] Periodic Table Database, https://periodictable.com/Properties/A/CovalentRadius.v.log.html
[40] Y. Minenkov, D.I. Sharapa, and L. Cavallo, J. Chem. Theory Comput. **14**, 3428 (2018). https://doi.org/10.1021/acs.jctc.8b00018
[41] B.M. Bode, and M.S. Gordon, J. Mol. Graph. Model. **16**, 133 (1998). https://doi.org/10.1016/S1093-3263(99)00002-9
[42] M.J. Hoque, A. Ahsan, and M.B. Hossain, Biomed. J. Sci. Tech. Res. **9**, 7360 (2018). https://doi.org/10.26717/BJSTR.2018.9.001852
[43] I.S. Chekman, G.O. Syrova, O.O. Kazakova, N.O. Gorchakova, I.F. Belenichev, M.I. Zagorodny, and O.O. Nagorna, Quantum chemistry: medical and pharmaceutical aspect, (2017). (in Ukrainian)
[44] Drugbank. https://go.drugbank.com/drugs/DB14082
[45] Drugbank. https://go.drugbank.com/drugs/DB09161
[46] Health Canada, Drug Prod. Database. https://pdf.hres.ca/dpd_pm/00050839.PDF
[47] L. Kabasakal, S. Atay, V.A. Vural, K. Özker, K. Sönmezoglu, M. Demir, and A.T. Işitman, J. Nucl. Med. **36**, 1398 (1995).
[48] L. Kabasakal, Eur. J. Nucl. Med. **27**, 351–357 (2000). https://doi.org/10.1007/s002590050045

[49] P. Liu, Z. Zhu, C. Zeng, and G. Nie, J. Biomed. Opt. **17**, 125002 (2012). https://doi.org/10.1117/1.JBO.17.12.125002
[50] M.K. Kim, J. Seidel, N. Le, I.S. Kim, T.M. Yoo, C. Barker, and C.H. Paik, Nucl. Med. Biol. **26**, 43 (1999). https://doi.org/10.1016/s0969-8051(98)00077-8
[51] TutorChase, Heat Form. Thermodyn. (2024). https://www.tutorchase.com/answers/a-level/chemistry/what-is-the-heat-of-formation-and-how-does-it-relate-to-thermodynamics
[52] S. Nhlapho, M.H.L. Nyathi, B.L. Ngwenya, T. Dube, A. Telukdarie, I. Munien, and U.A. Chude-Okonkwo, Sci. Pharm. **3**, 177 (2024). https://doi.org/10.58920/sciphar0304264
[53] G.B. Saha, *Fundamentals of nuclear pharmacy*, (Springer, New York. (2004).
[54] M. Rehling, Scand. J. Clin. Lab. Invest. **48**, 603 (1988). https://doi.org/10.1080/00365518809085779
[55] B. F. Lee, J. L. Yeh, N. T. Chiu, G. C. Liu, H. S. Yu, M. H. Wang, L. H. Shen, Kaohsiung J. Med. Sci. **24**, 1 (2008). https://doi.org/10.1016/S1607-551X(08)70066-4
[56] D. R. Silva, J. K. Daré, M. P. Freitas, Beilstein J. Org. Chem. **16**, 2469 (2020). https://doi.org/10.3762/bjoc.16.200

КВАНТОВО-ХІМІЧНІ РОЗРАХУНКИ РАДІОФАРМПРЕПАРАТІВ ТЕХНЕЦІЮ

К. Вус, В. Трусова, В. Ромашина, У. Маловиця, О. Житняківська, Г. Горбенко
Кафедра медичної фізики та біомедичних нанотехнологій, Харківський національний університет імені В.Н. Каразіна м. Свободи 4, Харків, 61022, Україна

Синтез радіофармпрепаратів є головним завданням ядерної медицини, причому Технецій-99m (^{99m}Tc) має ідеальні ядерні властивості для неінвазивної ядерної медичної діагностики методом однофотонної емісійної комп'ютерної томографії (SPECT) – дешевшим методом, ніж КТ, МРТ і ПЕТ, що підходить для країн, які розвиваються. Особливо актуальним у наш час є дизайн різноманітних ковалентно мічених радіофармпрепаратів ^{99m}Tc для діагностики і тераностики онкологічних захворювань. Однак для правильного підбору лігандів і розробки якісних візуалізуючих агентів на основі ^{99m}Tc, що не будуть порушувати функції біологічно активних молекул, науковці повинні добре розбиратися у координаційній хімії перехідних металів групи 7. У даній роботі методами *ab initio* (комбінований базис: SBKJC на атомі Tc та 6-31G (d,p)/DFT – на інших атомах, Gamess) та напівемпіричними (PM6, MOPAC) розраховано квантово-хімічні характеристики десяти радіофармпрепаратів ^{99m}Tc. Негативне (Tc-Exametazime, Tc-ECD) і позитивне (всі інші) значення параметра E_{LUMO} зумовлюють електрофільні та нуклеофільні властивості радіофармпрепаратів, відповідно. Аналізуючи значення абсолютної жорсткості комплексів виявлено, що досліджені радіофармпрепарати – це м’які реагенти, причому пертехнетат має найнижчу реактивну здатність, що узгоджується з літературними даними. Для більшості радіофармпрепаратів ^{99m}Tc дипольні моменти були подібними або до 10 разів вищими у порівнянні з дипольним моментом молекули води. Нарешті, виявлено сильну кореляцію між значеннями дипольних моментів основного стану, ліпофільністю п’яти радіофармпрепаратів (Tc-Exametazime, Tc-MAG3, Tc-MDP, Tc(III)-DMSA, Tc-DTPA) та відсотком їх неспецифічного зв'язування з білками плазми крові (коефіцієнти кореляції Пірсона складали -0.719 та 0.611, відповідно). Отриманні результати є корисними для дизайну нових тераностичних протиракових агентів на основі ^{99m}Tc, що мають високий ступінь зв'язування з білками плазми крові.

Ключові слова: *радіофармпрепарати ^{99m}Tc; квантово-хімічні розрахунки; неспецифічне зв'язування з білками; дипольний момент; ліпофільність*

East European Journal of Physics. 1. 520-524 (2026)
DOI:10.26565/2312-4334-2026-1-59 ISSN 2312-4334

INTERACTIONS OF PERTECHNETATE WITH PROTEINS: AN IN-SILICO STUDY

V. Trusova[1]*, P. Kuznietsov[2], I. Yakymenko[2], G. Gorbenko[1]
[1]Department of Medical Physics and Biomedical Nanotechnologies, V.N. Karazin Kharkiv National University
4 Svobody Sq., Kharkiv, 61022, Ukraine
[2]O.I. Akhiezer Department for Nuclear Physics and High Energy Physics, V.N. Karazin Kharkiv National University
4 Svobody Sq., Kharkiv, 61022, Ukraine
**Corresponding Author: valerija.trusova@karazin.ua*
Received December 29, 2025, revised February 7, 2026; accepted February 19, 2026

Technetium 99m is a radionuclide extensively used in clinical practice due to a range of its properties among which are short half-life, reduced radiation exposure and toxicity, short labeling time, high target to non-target ratio and low cost. In its highest oxidation state +VII, technetium exists in the form of pertechnetate ($[TcO_4]^-$) that serves as an effective imaging agent. One important determinant of pharmacokinetics and bioavailability of pertechnetate involves the possibility of its complexation with blood proteins. In the present work we performed in silico study of the pertechnentate complexes with three blood proteins, deoxyhemoglobin, albumin and transferrin. The molecular docking of $[TcO_4]^-$ to the examined proteins provided evidence for pertechnetate localization in the protein structural cavities containing positively charged amino acid residues, with the highest binding affinity being obverved for deoxyhemoglobin. At the same time, the molecular dynamics simulations indicated that, in contrast to deoxyhemoglobin, only the complexes of pertechnetate with plasma proteins albumin and transferrin remain stable and do not show significant variations in root mean square deviation of atomic positions, solvent accessible surface area, radius of gyration and secondary structure per residue. The results obtained may help in better understaning of pertechnetate pharmacokinetic behavior and enhancing its efficiency as an imaging agent.
Keywords: *Technetium 99m; Pertechnetate; Hemoglobin; Albumin; Transferrin; Molecular docking; Molecular dynamics*
PACS: 87.14.C++c, 87.16.Dg

Among a great variety radionuclides currently used in medical diagnostics one of the most widespread is technetium 99m (^{99m}Tc) [1]. This radionuclide is highly suitable for performing the single-photon emission computerized tomography (SPECT) due to a range of its favorable for nuclear medicine properties such as short half-life ~ 6 h, gamma photon energy 140 keV, reducing the radiation hazard, short labeling time, low cost, availability from ^{99}Mo/^{99m}Tc generator, high limit of accumulation by target organ and high target to non-target ratio, low toxicity, etc. [1-3]. Technetium is a transition metal in the group VII B with 8 oxidation states from – 1 to +VII, and in the highest oxidation state it commonly exists as pertechnetate, $^{99m}TcO_4^-$, which is the most stable form of Tc in aqueous solution [3]. This compound has been employed as an imaging agent in the scintigraphy of thyroid [4,5], salivary gland [6] and Meckel diverticulum [7]. Likewise, in radiochemical labeling $^{99m}TcO_4^-$ may appear as an undesirable impurity worsening the image resolution. Obviously, the biodistribution of pertechnetate is affected by the extent and nature of its interactions with biomolecules, particularly, with blood proteins. In our recent work we quantitatively examined the binding of $^{99m}TcO_4^-$ to structurally and functionally different proteins, human serum albumin, lysozyme and insulin using the precipitation-ultracentrifugation assay followed by radioactivity measurements [8]. It was demonstrated that the extent of pertechnetate association with blood plasma protein albumin is significantly higher than that of lysozyme and insulin taken for comparison. In a logical continuation of this research, the aim of the present study was to assess the stability of $^{99m}TcO_4^-$ complexes with three blood proteins, deoxyhemoglobin, albumin and transferrin, using the molecular docking and molecular dynamics techniques. Albumin is the predominant protein in human plasma, with a number of important functions among which are transport of a variety of substances, maintenance of osmotic pressure, regulation of immune response, etc. [9]. Hemoglobin is the main component of red blood cells responsible for transport of oxygen and carbon dioxide, modulation of erythrocyte metabolism, heat transduction, etc. [10]. Transferrin, a blood plasma glycoprotein, accounts for iron transport into cells through binding to specific transferrin receptors [11].

METHODS

The crystal structures of the functional proteins were taken from the Protein Data Bank (https://www.rcsb.org/) using the following PDB IDs:1AO6 (human serum albumin in its dimeric form), 2DN2 (human deoxyhemoglobin), 1D3K (human transferrin). To stabilize protein conformation in water, each examined protein structure was subjected to 2 ns molecular dynamics relaxation and then the relaxed structures were docked with pertechnetate using the HDOCK server (https://hdock.phys.hust.edu.cn/), which integrates a template-based modeling and free docking via a fast FFT-based algorithm [13]. The most energetically favorable docking complexes were visualized with the VMD software.

The MD simulations of the model systems pertechnetate – proteins were performed using the GROMACS software (version 2024.2) with the modified CHARMM36 force field. The parameterization of the CHARMM36 force field for the Tc metal center was made through introducing the metal−ligand bond lengths, bond angles and the force constants.

Cite as: V. Trusova, P. Kuznietsov, I. Yakymenko, G. Gorbenko, East Eur. J. Phys. 1, 520 (2026), https://doi.org/10.26565/2312-4334-2026-1-59

To add $[TcO_4]^-$ as a new residue to the force field, the modifications were made in the following files: aminoacids.rtp, atomtypes.atp, ffnonbonded.itp, ffbonded.itp, residuetype.dat. More specifically, in ffnonbonded.itp the Lennard-Jones parameters for Tc were taken as those for Ru (II) (ε = 1.748 kJ/mol, σ = 0.262 nm [14]), by analogy with the work of de Andrade and coauthors [12]. The parameters such as equilibrium distance b0, force constant kb, valence angle theta0, averaged force constant of valence-angle harmonic potential ktheta were taken from [15-17], and included in the file ffbonded.itp (sections bondtypes and angletypes). The mol2 file for $[TcO_4]^-$ was taken from supporting info [12] and converted to pdb format in UCSF Chimera. In the file aminoacids.rtp the following partial charges were introduced: Tc1 – 1.398377, O2 – -0.599668, O3 – -0.599521, O4 – -0.599668, O5 – -0.599521 calculated in [12] from ChelpG fitting. The best score docking complexes between the proteins and $[TcO_4]^-$ were placed in a rectangular water box containing neutralizing ions, with a minimum distance of 10 Å from the protein to the box edges. The calculations were conducted at a temperature of 310 K using the TIP3P water model, Nose-Hoover thermostat and Verlet barostat. The Particle Mesh Ewald method was used for correct treatment of the long-range electrostatic interactions. The minimization and equilibration of the systems were carried out during 50000 steps. The time interval for MD calculations was 10 ns. The MD trajectories were corrected using the gmx trjconv GROMACS command. The analysis of MD data was performed with the GROMACS commands gmx rms, gmx gyrate, gmx sasa and VMD plugin Timeline, to explore time evolution of root mean square deviation of atomic positions (RMSD), gyration radius, sovent accessible surface area SASA) and protein secondary structure per residue. The visualization of the snapshots of MD runs was performed in VMD.

RESULTS AND DISCUSSION

Presented in Fig. 1 are the top-scored docking positions for the complexes of pertechnetate with deoxyhemoglobin, albumin and transferrin. As can be seen, in all cases $[TcO_4]^-$ is located in the cavities in protein structures. A more detailed analysis of the docking results revealed that the binding affinity decreases in the row: deoxyhemoglobin > transferrin > albumin (Table 1).

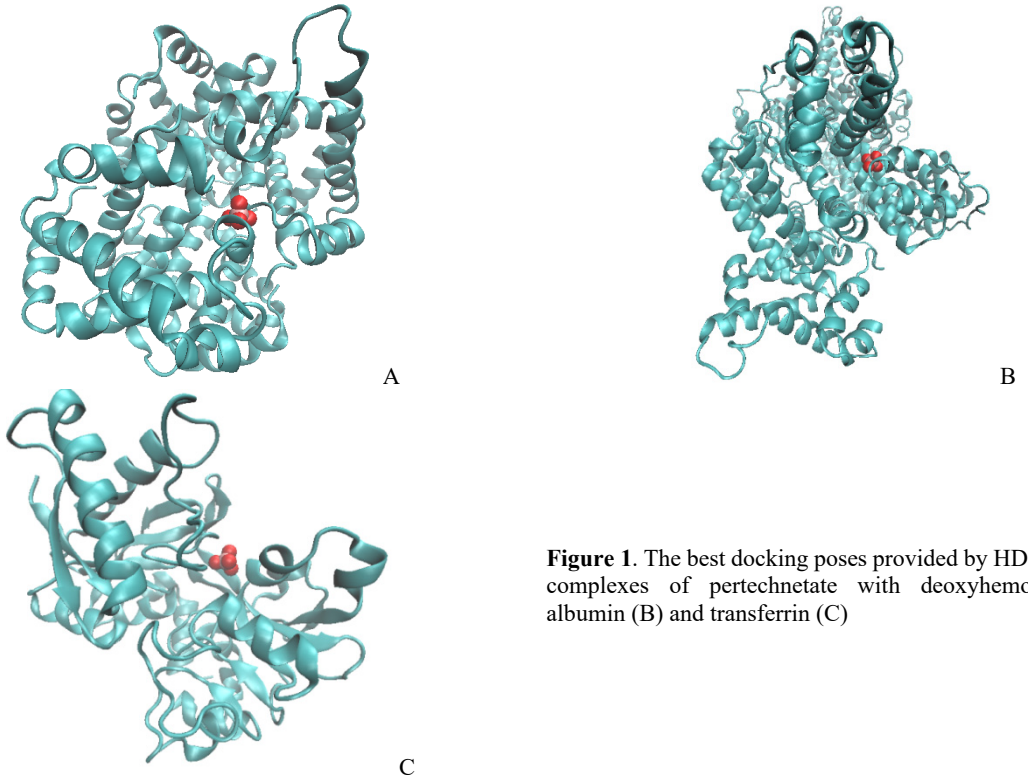

Figure 1. The best docking poses provided by HDOCK for .the complexes of pertechnetate with deoxyhemoglobin (A), albumin (B) and transferrin (C)

Notably, the sites accommodating $[TcO_4]^-$ contain positively charged amino acid residues (ARG_{40B} and ARG_{92C} for deoxyhemoglobin, ARG_{348A} , ARG_{484A} and ARG_{485A} for albumin, LYS_{296} for transferrin) suggesting that electrostatic interactions enhance the association of pertechnetate with proteins.

Table 1. Docking scores characterizing the binding affinities of pertechnetate for functional proteins and interface residues in the protein - $[TcO_4]^-$ complexes

Protein	Docking score	Interface residues
Deoxyhemoglobin	-68.30	TRP_{37B} THR_{38B} ARG_{40B} PHE_{41B} ASP_{99B} ASN_{102B} TYR_{42C} ARG_{92C} VAL_{93C} ASP_{94C}
Albumin	-57.77	VAL_{344A} ARG_{348A} GLU_{450A} ASP_{451A} LEU_{453A} SER_{454A} LEU_{457A} LEU_{481A} VAL_{482A} ASN_{483A} ARG_{484A} ARG_{485A} PRO_{486A}
Transferrin	-59.49	TYR_{85} TYR_{95} TYR_{96} GLN_{206} HSD_{207} SER_{208} GLU_{212} LYS_{296} SER_{298}

Next, to compare the stabilities of the examined complexes, we performed a series of 10 ns molecular dynamics simulations. Shown in Fig. 2 are the snapshots of MD simulations taken at the time points 0 ns and 10 ns.

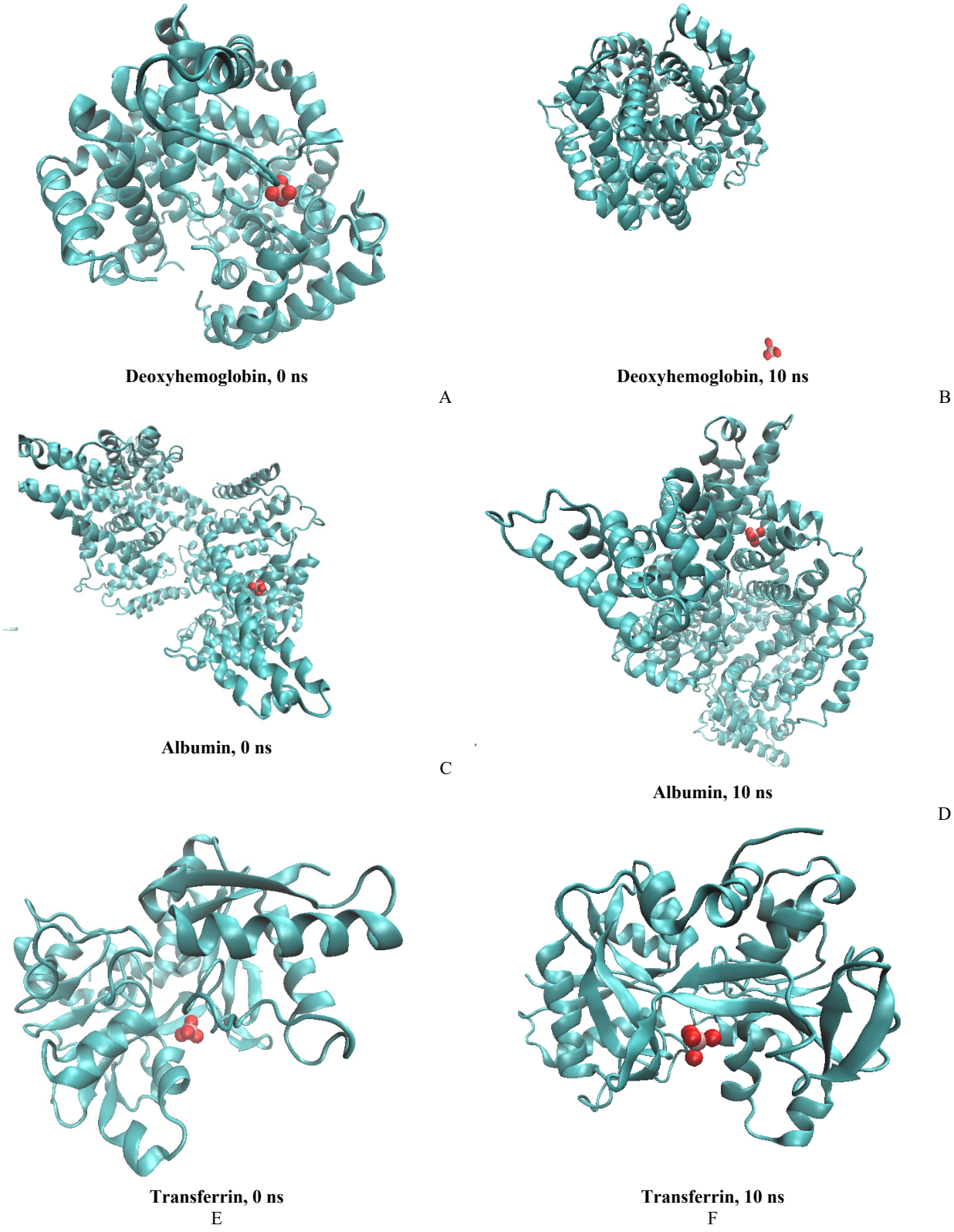

Deoxyhemoglobin, 0 ns A

Deoxyhemoglobin, 10 ns B

Albumin, 0 ns C

Albumin, 10 ns D

Transferrin, 0 ns E

Transferrin, 10 ns F

Figure 2. The snapshots of MD simutations of the complexes between pertechnetate and functional proteins

It appeared that within the time interval of MD simulation $[TcO_4]^-$ remains attached to albumin and transferrin, but dissociates from its complexes with deoxyhemoglobin, despite higher binding affinity to this protein compared to albumin and transferrin. The subsequent analysis of MD data obtained for albumin and transferrin revealed that the $[TcO_4]^-$ complexes with these proteins retain its stability during the simulation time, as judged from insignificant changes of the parameters such as RMSD, radius of gyration and total SASA (Fig. 3).

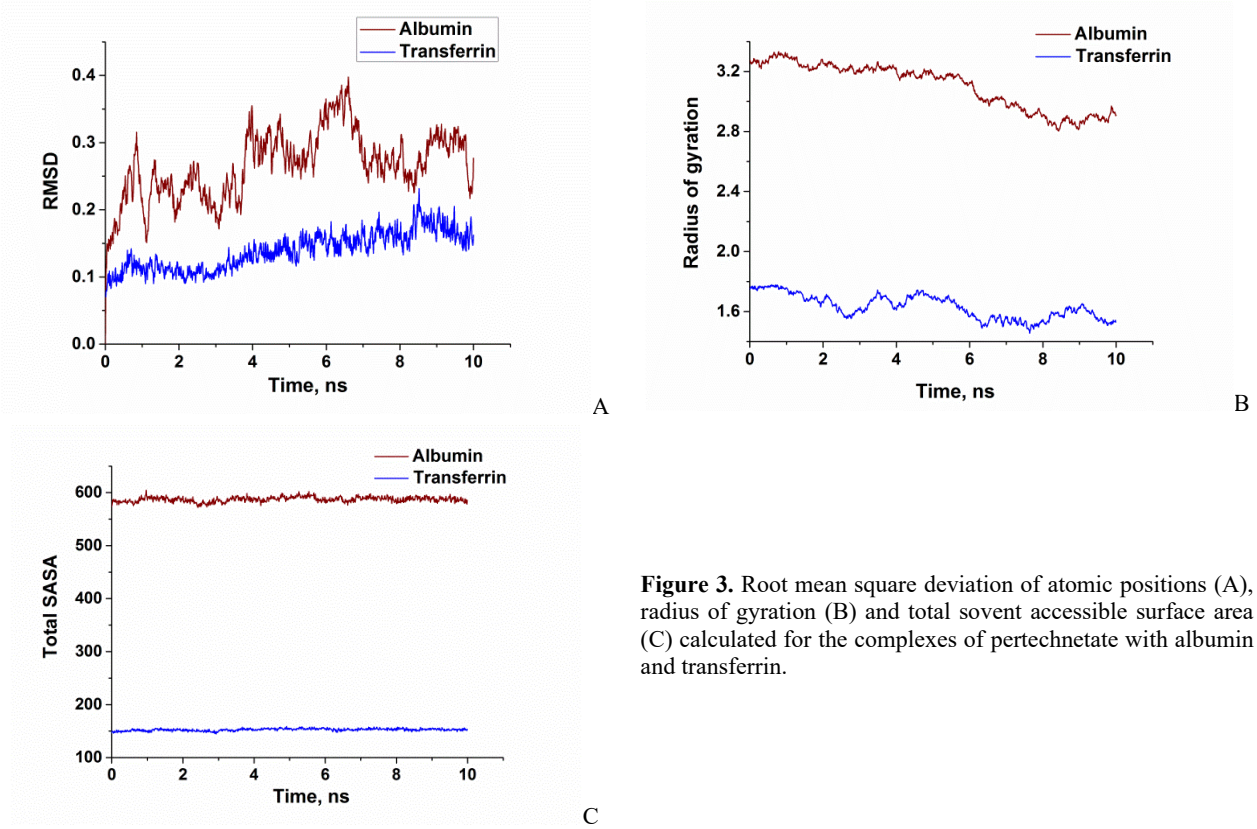

Figure 3. Root mean square deviation of atomic positions (A), radius of gyration (B) and total sovent accessible surface area (C) calculated for the complexes of pertechnetate with albumin and transferrin.

Accordingly, VMD Timeline analysis showed that the secondary structure of interfacial residues remain virtually unchanged during the simulation time in the complexes of pertechnetate with albumin and transferrin (Fig. 4).

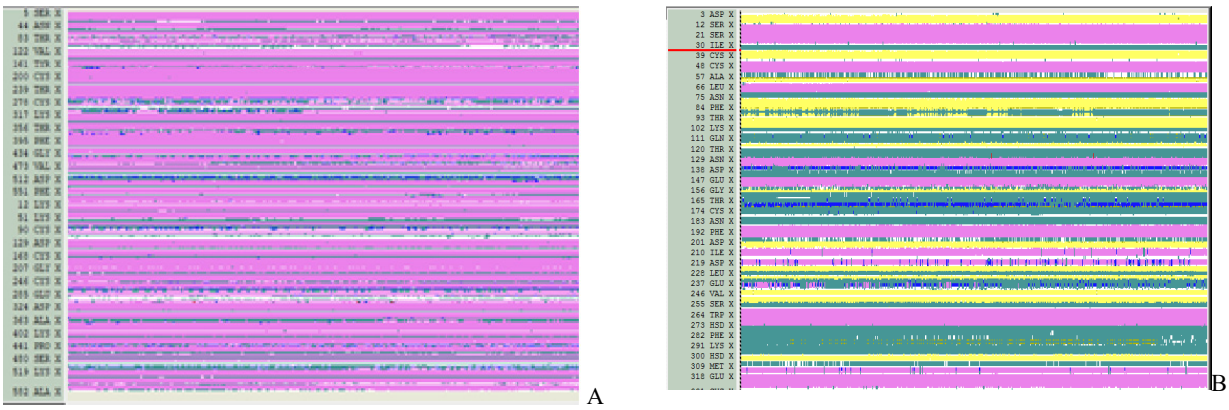

Figure 4. Time evolution of the protein secondary structure per residue provided by VMD Timeline plugin for albumin (A) and transferrin (B).

It should be mentioned that MD results presented here are in accordance with our recent experimental study showing that the binding capacity of albumin for pertechnetate is about two-fold higher than that of lysozyme and insulin [9]. Likewise, this work demonstrates the necessity of validating the docking data by subsequent MD simulation. According to our docking results, the strongest binding of $[TcO_4]^-$ was observed for deoxyhemoglobin, but the stability of this complex was not confirmed by MD calculations, in contrast to albumin and transferrin.

CONCLUSIONS

In summary, the present study was undertaken to gain further insights into the structural details of interactions between pertechnetate and three blood proteins, deoxyhemoglobin, albumin and transferrin using in silico approaches. The molecular docking data suggest that $[TcO_4]^-$displays binding preference for the cavities in protein structures, with the binding affinity being higher for deoxyhemoglobin compared to albumin and transferrin. The presence of positively charged amino acid residues in the binding sites points to the importance of ionic contacts for stabilization of the $[TcO_4]^-$ complexes with proteins. However, the molecular dynamics simulations evidenced that only the complexes of pertechnetate with plasma proteins, albumin and transferrin, are stable and do not dissociate within the MD calculation

time. The analysis of MD results in terms of the parameters such as RMSD, SASA, radius of gyration and secondary structure per residue provided the arguments in favor of structural stability of pertechnetate complexes with albumin and transferrin. These findings may have implications for the clinical use of pertechnetate and improvement of imaging procedures.

Acknowledgements

This work was supported by the Ministry of Education and Science of Ukraine (the project № Д3/174-2025).

ORCID

Valeriya Trusova, https://orcid.org/0000-0002-7087-071X; **Galyna Gorbenko,** https://orcid.org/0000-0002-0954-5053
Pylyp Kuznietsov, https://orcid.org/0000-0001-8477-1395; **Ivan Yakymenko,** https://orcid.org/0000-0001-8477-1395

REFERENCES

[1] E. Strub, D. Badea, J. Bruns, A. Frontera, N. Mayordomo, A. Sakhonenkova, M. R. Jungfer, M. Wickleder, C.Yong, and M. Zegke, Eur. J. Inorg. Chem. **28**, e202400780 (2025). https://doi.org/10.1002/ejic.202400780
[2] M. U. Akbar, M. R. Ahmad, A. Shaheen, and S. Mushtaq, J. Radioanal. Nucl. Chem. **310**, 477–493 (2016). https://doi.org/10.1007/s10967-016-5019-7
[3] N. Ahmed, and M. Zia, J. Acad. Radiol. **6**, 143–159 (2023). https://doi.org/10.1007/s42058-023-00128-7
[4] W. I. Li, T. K. Chan, K. K. Ng, and B. T. Kung, J. Clin. Imag. Sci. **15**, 3 (2025). https://doi.org/10.25259/JCIS
[5] L. Giovanella, G. Paone, T. Ruberto, L. Ceriani, and P. Trimboli, Endocrinol. Metab. **34**, 63–69 (2019). https://doi.org/10.3803/EnM.2019.34.1.63
[6] H. Zhu, W. Shen, Y. Zhu, Z. Liu, Q. Zhang, Z. Li, X. Hou, Y. Wang, Radiography **32**, 103217 (2026). https://doi.org/10.1016/j.radi.2025.103217
[7] P. Sahafi, M. H. Samadi; M. A. Kiani; A. Mohammadipour, and R. Sadeghi, Clin. Nucl. Med. **51**, 19-e20 (2026). https://doi.org/10.1097/RLU.0000000000005908
[8] V. Trusova, U. Malovytsia, P. Kuznietsov, I. Yakymenko, G. Yukhno, A. Krasnopyorova, N. Pidchenko, O. Tishchenko, and G. Gorbenko, Biophys. Chem**. 332**, 107592 (2026). https://doi.org/10.1016/j.bpc.2026.107592
[9] U. Kragh-Hansen, In: M. Otagiri, V. Chuang (eds) Albumin in Medicine. Springer, Singapore. (2016). https://doi.org/10.1007/978-981-10-2116-9_1
[10] B. Giardina, Mol. Aspects Med. **84**, 101040 (2022). https://doi.org/10.1016/j.mam.2021.101040
[11] K. Wang, A. Yuan, J. Yu, J. Wu, and Y. Hu, J. Pharm. Sci. **105**, 1269-1276 (2016). https://doi.org/10.1016/j.xphs.2015.12.007
[12] T. F. de Andrade, H. F. Dos Santos, C. F. Guerra, and D. F. Paschoal, J. Phys. Chem. A. **126,** 5434−5448 (2022). https://doi.org/10.1021/acs.jpca.2c01617
[13] Y. Yan, H. Tao, J. He, and S-Y. Huang, Nat. Protoc. **15**, 1829–1852 (2020). https://doi.org/10.1038/s41596-020-0312-x
[14] F. Šebesta, V. Sláma, J. Melcr, Z. Futera, and J. Burda, J. Chem. Theory Comput. **12,** 3681–3688 (2016). https://doi.org/10.1021/acs.jctc.6b00416
[15] R. D. Hancock, D. E. Reichert, and M. J. Welch, Inorg. Chem. **35**, 2165–2166 (1996). https://doi.org/10.1021/ic951422q
[16] L. He, S. Liu, L. Chen, X. Dai, J. Li, M. Zhang, F. Ma, C. Zhang, Z. Yang, R. Zhou, Z. Chaia, and S.Wang, Chem. Sci. **10**, 4293–4305. (2019). https://doi.org/10.1039/C9SC00172G
[17] D. E. Reichert, and M. J. Welch, Coord. Chem. Rev. **212**, 111–131 (2001). https://doi.org/10.1016/S0010-8545(00)00367-2

ВЗАЄМОДІЯ ПЕРТЕХНЕТАТУ З БІЛКАМИ: ДОСЛІДЖЕННЯ IN SILICO

В. Трусова[1], П. Кузнєцов[2], І. Якименко[2], Г. Горбенко[1]

[1]Кафедра медичної фізики та біомедичних нанотехнологій, Харківський національний університет імені В.Н. Каразіна м. Свободи 4, Харків, 61022, Україна

[2]Кафедра фізики ядра та високих енергій імені О.І. Ахієзера, Харківський національний університет імені В.Н. Каразіна м. Свободи 4, Харків, 61022, Україна

Технецій 99m – радіонуклід, який широко застосовується в клінічній практиці завдяки таким його властивостям, як короткий період напівжиття, допустимий рівень опромінення та низька токсичність, швидке мічення, високий ступінь накопичення в органі-мішені та низька вартість При найвищому ступені окислення +VII технецій існує у формі пертехнетату ($[TcO_4]^-$) який є ефективним візуалізуючим агентом. Одним із важливих детермінантів фармакокінетики та біодоступності пертехнетату є можливість його асоціації з білками крові. У даній роботі було проведене in silico дослідження комплексів пертехнетату з трьома білками крові – дезоксигемоглобіном, альбуміном та трансферином. Методом молекулярного докінгу між $[TcO_4]^-$ та досліджуваними білками були отримані докази локалізації пертехнетату в структурних порожнинах, що містять позитивно заряджені амінокислотні залишки, а найвища афінність була виявлена для дезоксигемоглобіну. В той же час, молекулярно-динамічні розрахунки показали, що, на відміну від дезоксигемоглобіну, тільки комплекси пертехнетату з білками плазми крові, альбуміном та трансферином, залишаються стабільними та не характеризується значущими варіаціями таких параметрів як середньоквадратичне відхилення атомних позицій, площа поверхні, доступна розчиннику, радіус інерції та вторинна структура амінокислотних залишків. Отримані результати можуть бути корисними для більш глибокого розуміння фармакокінетичної поведінки пертехнетату та підвищення його ефективності як візуалізуючого агента.

Ключові слова: *технецій 99m; пертехнетат; гемоглобін; альбумін; трансферин; молекулярний докінг; молекулярна динаміка*

EAST EUROPEAN JOURNAL OF PHYSICS. 1. 525-530 (2026)
DOI:10.26565/2312-4334-2026-1-60 ISSN 2312-4334

A MOLECULAR DOCKING STUDY OF AMYLOID-POLYSACCHARIDE COMPOSITES: I. INTERACTIONS WITH POLYPHENOLS

Valeriya Trusova*, Uliana Malovytsia, Olga Zhytniakivska, Galyna Gorbenko
Department of Medical Physics and Biomedical Nanotechnologies, V.N. Karazin Kharkiv National University
4 Svobody Sq., Kharkiv, 61022, Ukraine
**Corresponding Author email: valerija.trusova@karazin.ua*
Received January 2, 2026, revised February 13, 2026; accepted February 26, 2026

Filamentous protein aggregates, amyloid fibrils, currently attract considerable interest as a prospective nanomaterial for a variety of biomedical and industrial applications. Among their advantages are biocompatibility, high stability and mechanical strength, self-assembly capability, etc. The integration of other biopolymers such as polysaccharides into amyloid matrix enables creating novel nanomaterials with improved mechanical characteristics and higher loading capacity for biologically active compounds. In the present study we employed the molecular docking technique to ascertain the molecular details of the interactions between the lysozyme amyloid fibrils and a series of polyphenolic compounds including curcumin, gallic acid, salicylic acid, quercetin, resveratrol and sesamin, and to explore the effect of polysaccharide chitosan on such kind of interactions. It was shown that curcumin in enol form has the highest binding affinity for fibrillar lysozyme, while the lowest affinity was observed for salicylic acid. The binding sites for curcumin, gallic acid, quercetin, resveratrol and sesamin appear to occupy the groove on the wet fibril surface, while salicylic acid binds to the dry surface of the fibril. The interfacial amino acid residues in the fibril complexes with polyphenols and chitosan are identified. Chitosan was found to display the ability to interact with polyphenolic compounds within amyloid matrix, resulting in the enhancement of polyphenol binding. The data obtained provide a basis for further designing and experimental testing of the amyloid-chitosan nanocomposites loaded with polyphenols.
Keywords: *Lysozyme amyloid fibrils; Chitosan; Polyphenols; Binding sites; Binding affinity; Molecular docking*
PACS: 87.14.C++c, 87.16.Dg

The last decade has seen a paradigm shift in nanoscience with the growing accent on the use of proteins as building blocks for a variety of functional nanomaterials [1]. Particular attention in this context is paid to filamentous protein aggregates with a core cross-β sheet structure, amyloid fibrils that are featured by structural stability, unique mechanical properties, sequence-controlled surface functionalities, biocompatibility, self-healing ability, etc. [2]. Amyloid-based nanomaterials have been designed for a variety of biomedical and industrial applications [3]. To exemplify, amyloid fibrils with specific binding sites have been engineered for biosensing of disease biomarkers [5, 6] and environmental pollutants [7]. The drug delivery applications of fibrillized proteins showed high efficiency of encapsulation and controlled drug release [8]. Amyloid assemblies have been explored as biocompatible coatings for implants and medical devices [9] and scaffolds for tissue engineering and regeneration [10]. Functionalized amyloid fibrils appeared to be suitable for advanced energy storage due to their high conductivity and mechanical strength [11]. Likewise, optical properties of fibrillar aggregates doped with organic dyes or quantum dots enable their use for energy transfer and light harvesting [4]. A promising approach to the development of amyloid nanomaterials involves integration of protein fibrils with other biopolymers, particularly, polysaccharides [12]. Of these, the polymer of β-1,4-D-glucosamine, chitosan, attracts a lot of interest due to a wide spectrum of favorable properties among which are antimicrobial, immunomodulatory and antitumor activities, the abilities to enhance blood coagulation and promote wound healing [13]. In the recent work of Tian and coauthors the double network hydrogels have been prepared from the lysozyme amyloid fibrils and chitosan [14]. These composite hydrogels were found to have enhanced mechanical strength depending on chitosan concentration and high loading capacity for a polyphenolic compound, gallic acid. Another polyphenol, ferulic acid, was loaded into combined hydrogels from wheat gluten amyloid fibrils and chitosan [15]. It was demonstrated that such double networks can be used for more efficient delivery of ferulic acid with improvement of its bioavailability and bioaccessibility.

As the first step towards engineering the double hydrogels loaded by biologically active agents, the aim of the present study was to gain molecular docking insights into the interactions between the lysozyme amyloid fibrils, chitosan and a series of polyphenolic compounds including curcumin (enol and keto forms), gallic acid, salicylic acid, quercetin, resveratrol and sesamin. Lysozyme is an enzyme hydrolyzing the cell wall of Gram-positive bacteria and possessing anti-inflammatory, immunomodulatory and antiviral activities [16]. In the native state lysozyme is capable of hydrolyzing the cell wall of only Gram-positive bacteria, while in the fibrillar state it acts on both Gram-positive and Gram-negative bacteria, so that hydrogel matrix from lysozyme fibrils possesses additional functionality associated with its antibacterial activity [17]. Since lysozyme is an endogenous antibiotic, this functionality is especially important in the context of the problem of multidrug resistance. The biological activities of polyphenols are known to involve antimicrobial, anticancer, antioxidative, anti-inflammatory and anticoagulant effects [18, 19].

Cite as: V. Trusova, U. Malovytsia, O. Zhytniakivska, G. Gorbenko, East Eur. J. Phys. 1, 525 (2026), https://doi.org/10.26565/2312-4334-2026-1-60

METHODS

The structures of the examined polyphenolic compounds were drawn in MarvinSketch software, v.18.10, ChemAxon with subsequent geometry optimization in Avogadro 1.1.0 software using the Universal Force Field21. The structure of amyloid fibrils from hen egg white lysozyme deciphered by combining atomic force microscopy, cryo-electron microscopy and solid-state NMR was taken from the Protein Data Bank (PDB ID 8QV8) [20]. The structure of chitosan (CS) 12-mer was obtained from a database of polysaccharide 3D structures (http://polysac3db.cermav.cnrs.fr), protonated and optimized in Avogadro 1.1.0 software. The docking of polyphenols to amyloid fibrils was performed with the web-based server HDOCK that uses hybrid algorithm of template-based modeling and free docking [21]. The selected docking poses were visualized with the VMD software.

RESULTS AND DISCUSSION

Shown in Fig. 1 are the most energetically favorable complexes between the lysozyme amyloid fibrils and the examined polyphenolic compounds. As can be seen, most polyphenols bind to the wet surface of the fibril, and only salicylic acid associates with the dry surface.

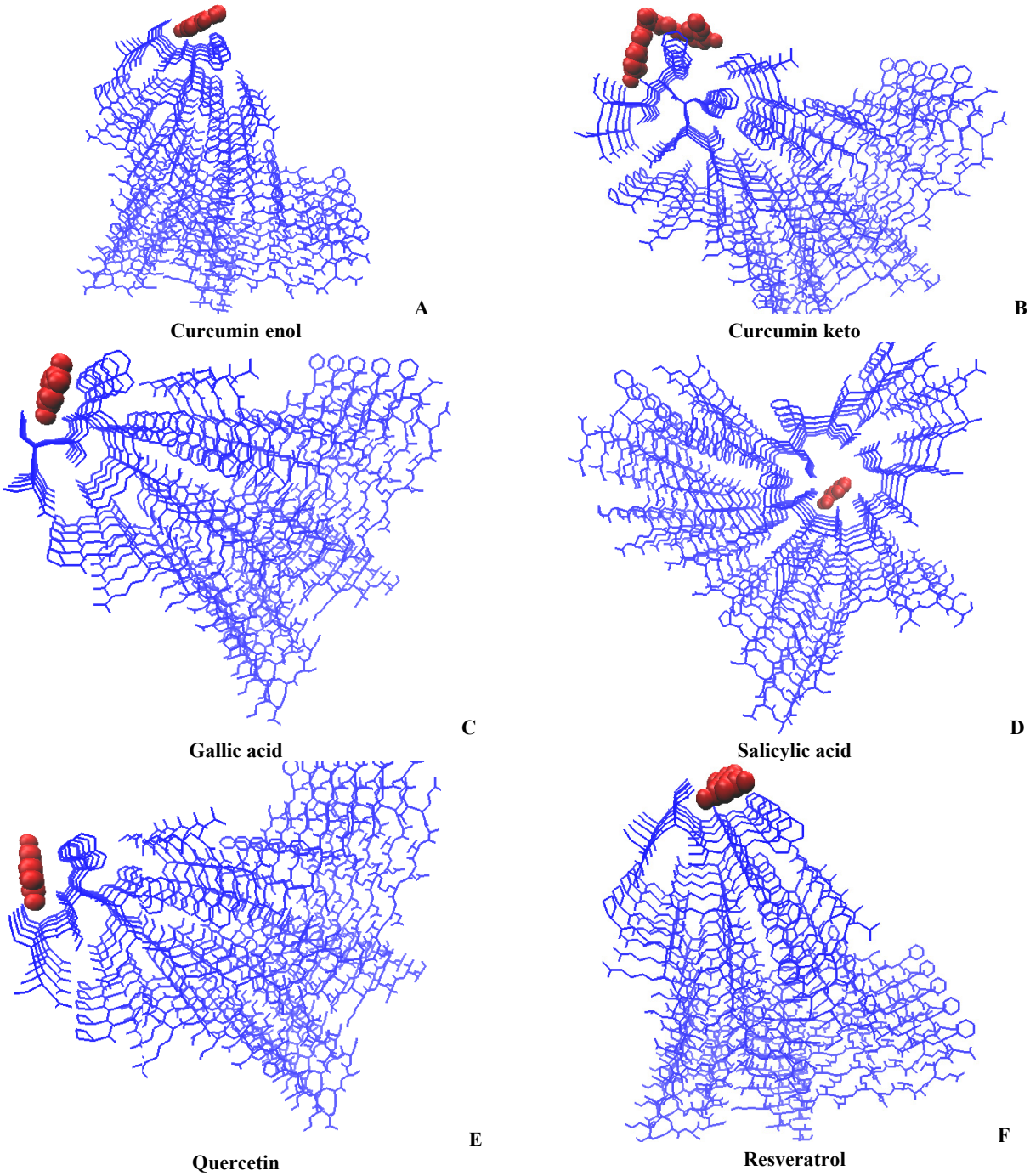

A **Curcumin enol**

B **Curcumin keto**

C **Gallic acid**

D **Salicylic acid**

E **Quercetin**

F **Resveratrol**

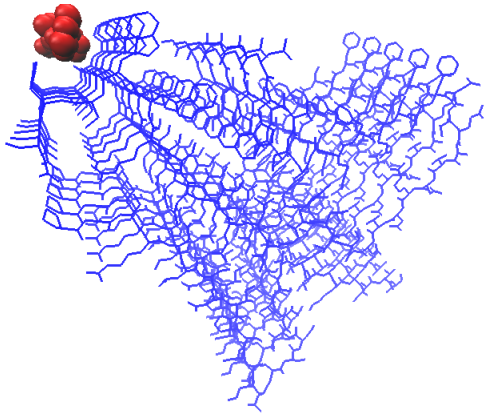

G

Sesamin

Figure 1. The best-score complexes of lysozyme fibrils with polyphenols.

The comparison of the best score values (Table 1) showed that curcumin (enol) forms the strongest complexes with the fibrils, with the binding affinities decreasing in the row: curcumin (enol) > quercetin ≥ sesamin > curcumin (keto) > resveratrol > gallic acid > salicylic acid.

Table 1. The best score values for the complexes of polyphenols with lysozyme amyloid fibrils and its composite with chitosan

Polyphenol	Lysozyme fibrils	Lysozyme fibrils + chitosan
		-316.62 (0.966)
Curcumin enol	-178.12 (0. 637)*	-178.27 (0.638)
Curcumin keto	-145.05 (0. 475)	-159.73 (0.549)
Gallic acid	-94.88 (0.249)	-115.91 (0.336)
Salicylic acid	-81.35 (0.202)	-95.93 (0.253)
Quercetin	-159.61 (0.548)	-169.16 (0.595)
Resveratrol	-120.92 (0.359)	-133.95 (0.420)
Sesamin	-157.11 (0.536)	-185.75 (0.671)

*Given in parentheses are the values of a confidence score for binding probability, with the values > 0.7 being considered as high confidence, 0.5-0.7 as moderate, and < 0.5 as low probability.

Notably, all polyphenols bound to the wet fibril surface reside in the groove with the interface residues such as tryptophan, cysteine and asparagine, while in the complexes of salicylic acid with the dry fibril surface the interface residues are represented by lysine, threonine, serine and aspartic acid (Table 2).

Table 2. The interface residues in the complexes of polyphenols with lysozyme amyloid fibrils and its composite with chitosan

Polyphenol	Lysozyme fibrils	Lysozyme fibrils + chitosan
		LYS_{33A} ARG_{45A} ASN_{46A} THR_{47A} SER_{50A} THR_{51A} ASP_{52A} LYS_{33C} GLU_{35C} ARG_{45C} ASN_{46C} THR_{47C} SER_{50C} THR_{51C} ASP_{52C} LYS_{33E} ARG_{45E} ASN_{46E} THR_{47E} SER_{50E} THR_{51E} ASP_{52E} LYS_{33G} ARG_{45G} THR_{47G} SER_{50G} THR_{51G} ASP_{52G} LYS_{33I} ARG_{45I} ASN_{46I} THR_{47I} SER_{50I} THR_{51I} ASP_{52I}
Curcumin enol	TRP_{63A} ASN_{65A} TRP_{63C} CYS_{64C} ASN_{65C} TRP_{63E} CYS_{64E} ASN_{65E} TRP_{63G} CYS_{64G} ASN_{65G} TRP_{63I}	TRP_{63A} ASN_{65A} TRP_{63C} CYS_{64C} ASN_{65C} TRP_{63E} CYS_{64E} ASN_{65E} TRP_{63G} CYS_{64G} ASN_{65G} TRP_{63I}
Curcumin keto	TRP_{63C} CYS_{64C} ASN_{65C} TRP_{63E} CYS_{64E} ASN_{65E} GLY_{26G} TRP_{63G} ASN_{65G}	LYS_{33I} GLU_{35I} ARG_{45I} SER_{50I} THR_{51I} ASP_{52I} TYR_{53I} ASN_{93I} CS_9 CS_{10} CS_{11}
Gallic acid	TRP_{63A} TRP_{63C} CYS_{64C} ASN_{65C} TRP_{63E} CYS_{64E} ASN_{65E} TRP_{63G} ASN_{65G}	LYS_{33E} GLU_{35E} ARG_{45E} ASP_{52E} LYS_{33G} GLU_{35G} ARG_{45G} ASP_{52G} LYS_{33I} GLU_{35I} ARG_{45I} ASP_{52I} CS_7 CS_8 CS_9
Salicylic acid	LYS_{33E} THR_{47E} SER_{50E} THR_{51E} ASP_{52E} LYS_{33G} THR_{47G} SER_{50G} THR_{51G} ASP_{52G} THR_{51I} ASP_{52I}	GLU_{35E} LYS_{33G} GLU_{35G} ARG_{45G} ASP_{52G} LYS_{33I} GLU_{35I} ARG_{45I} ASP_{52I} CS_8 CS_9 CS_{10}
Quercetin	TRP_{63C} CYS_{64C} ASN_{65C} TRP_{63E} CYS_{64E} ASN_{65E} TRP_{63G} CYS_{64G} ASN_{65G} TRP_{63I} ASN_{65I}	LYS_{33E} PHE_{34E} GLU_{5E} ARG_{45E} LYS_{33G} PHE_{34G} GLU_{35G} ARG_{45G} LYS_{33I} PHE_{34I} GLU_{35I} ARG_{45I} CS_7 CS_8 CS_9 CS_{10} CS_{11}
Resveratrol	TRP_{63C} CYS_{64C} ASN_{65C} TRP_{63E} CYS_{64E} ASN_{65E} TRP_{63G} CYS_{64G} ASN_{65G} TRP_{63I} ASN_{65I}	LYS_{33G} GLU_{35G} ARG_{45G} LYS_{33I} GLU_{35I} ARG_{45I} ASP_{52I} CS_8 CS_9 CS_{10} CS_{11}
Sesamin	ASN_{65A} TRP_{63C} CYS_{64C} ASN_{65C} TRP_{63E} CYS_{64E} ASN_{65E} TRP_{63G} CYS_{64G} ASN_{65G} TRP_{63I} CYS_{64I} ASN_{65I}	LYS_{33E} PHE_{34E} GLU_{35E} ARG_{45E} LYS_{33G} PHE_{34G} GLU_{35G} ARG_{45G} LYS_{33I} GLU_{35I} ARG_{45I} ASP_{52I} CS_7 CS_8 CS_9 CS_{10} CS_{11}

The best score and confidence score values observed for the chitosan complexes with fibrillar lysozyme suggest that this polysaccharide displays very high binding affinity for the lysozyme fibril (Table 1), accommodating within the grooves on the dry fibril surface (Fig. 2, A). The interface residues forming contacts with chitosan include amino acids with polar uncharged side chains (threonine, serine, asparagine, glutamine), positively charged (lysine, arginine), and negatively charged (aspartic acid) amino acid residues (Table 2).

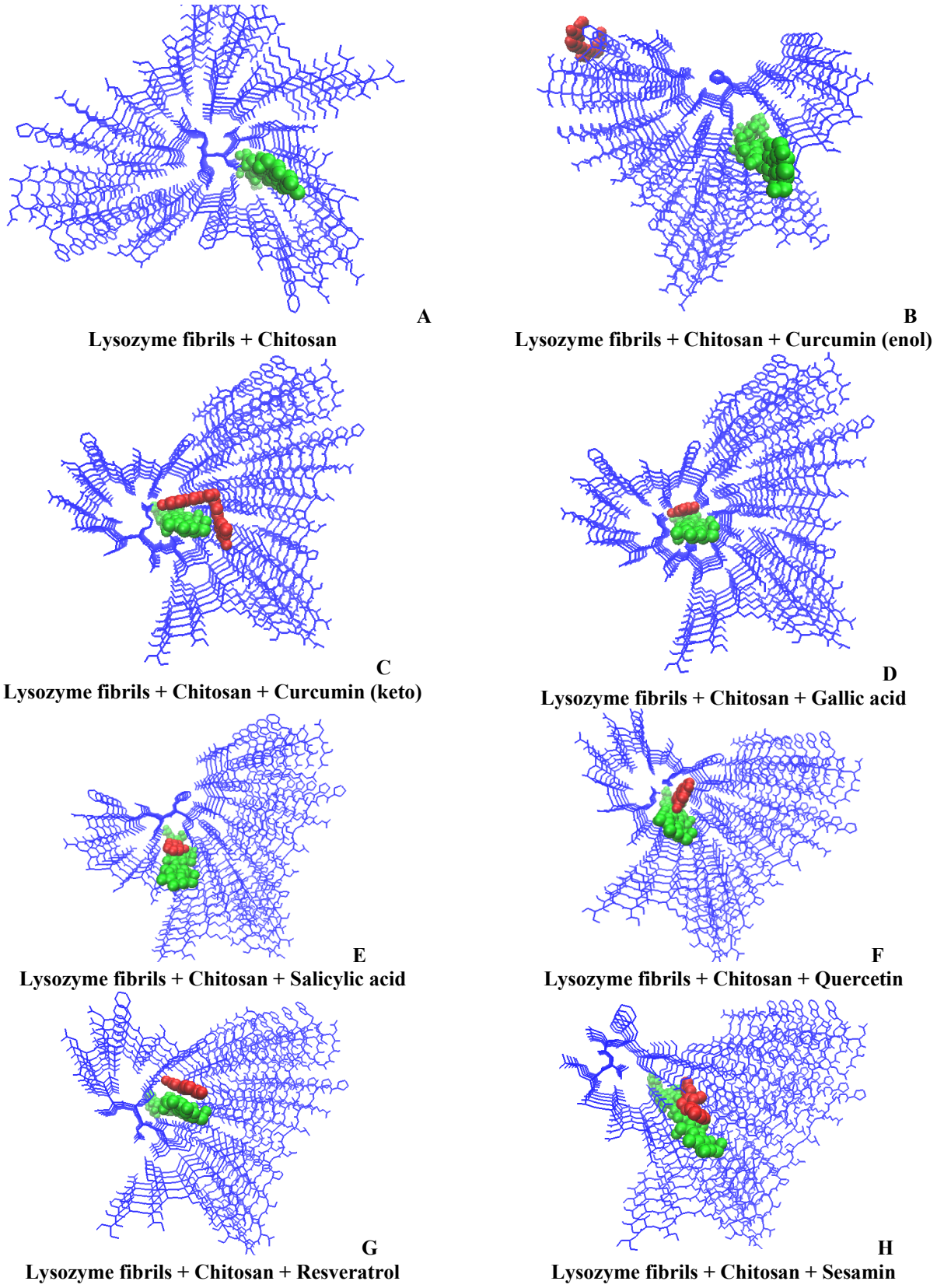

Figure 2. The best-score complexes of lysozyme fibrils with chitosan and polyphenols.

In the absence and presence of chitosan the binding site for curcumin enol remains the same, embracing TRP, CYS and ASN (Table 2). However, the other polyphenols exhibit unexpected behavior – they are localized within the same groove as chitosan and form contacts with both, fibril and polysaccharide (Fig. 2, C-H). Their binding motif involves LYS, GLU and ARG, complemented by PHE for quercetin and sesamin (Table 2). Accordingly, while for curcumin enol the binding affinity was not affected by chitosan, all other explored compounds showed marked increase in the binding affinity compared to the corresponding systems without the polysaccharide (Table 1). The strength of complexation between polyphenols and two-component binding matrix appeared to decrease in the order: sesamin > curcumin enol >quercetin > curcumin keto > resveratrol > gallic acid > salicylic acid. It should also be noted that the greatest enhancement of the binding affinity in the presence of chitosan was observed for gallic acid, salicylic acid and sesamin. These findings suggest that integration of lysozyme amyloid fibrils with chitosan may result in the increase of the extent of polyphenol loading and stimulate experimental efforts in this direction.

CONCLUSIONS

To summarize, the molecular docking of polyphenols representing different classes of these compounds to the fibrillar lysozyme and its complexes with chitosan revealed that: (i) the binding affinity of polyphenols to the lysozyme amyloid fibril decreases in the row: curcumin (enol) > quercetin ≥ sesamin > curcumin (keto) > resveratrol > gallic acid > salicylic acid; (ii) curcumin, gallic acid, quercetin, resveratrol and sesamin reside within the groove on the wet fibril surface with the repeating binding motif tryptophan, cysteine, asparagine; (iii) salicylic acid is localized on the dry fibril surface interacting with lysine, threonine, serine and aspartic acid; (iv) chitosan forms strong complexes with fibrillar lysozyme, and resides parallel to the fibril axis interacting with lysine, arginine, threonine, serine, asparagine, glutamine and aspartic acid; v) in the presence of chitosan the binding affinity of polyphenols markedly increases, with the magnitude of this effect being greatest for gallic acid, salicylic acid and sesamin; vi) in the double system fibrillar lysozyme + chitosan the examined polyphenolic compounds are capable of forming contacts with both amino acid residues and chitosan subunits. These findings can be regarded as a starting point for further development of the composite bionanomaterials for biomedical applications based on fibrillar lysozyme and chitosan.

Acknowledgements

This work was supported by the Ministry of Education and Science of Ukraine (the project "Design of novel biocompatible nanocomposites and improvement of ultrasound-based diagnostic methods for medical applications" No. 0126U001036).

ORCID

Valeriya Trusova, https://orcid.org/0000-0002-7087-071X; **Uliana Malovytsia,** https://orcid.org/0000-0002-7677-0779
Olga Zhytniakivska, https://orcid.org/0000-0002-2068-5823; **Galyna Gorbenko,** https://orcid.org/0000-0002-0954-5053

REFERENCES

[1] A.J. Capezza, and R. Mezzenga, Biomacromolecules, **25**, 4615 (2024). https://doi.org/10.1021/acs.biomac.4c00884
[2] Q. Xuan, J. Cai, Y. Gao, X. Qiao, T. Jin, M. Peydayesh, J. Zhou, *et al*., Adv. Mater. **37**, 2417774 (2025). https://doi.org/10.1002/adma.202417774
[3] B. Liu, H. Zhang, and X. Qin, Nanomaterials, **15**, 255 (2025). https://doi.org/10.3390/nano15040255
[4] L.B. Fallot, C. Natarajan, C.A. Anderson, E.A. Nagelli, F.J. Burpo, and R. Limbocker, ACS Appl. Mater. Interfaces **17**, 62839 (2025). https://doi.org/10.1021/acsami.5c11847
[5] L. Adler-Abramovich, and E. Gazit, Chem. Soc. Rev. **43**, 6881 (2014). https://doi.org/10.1039/C4CS00164H
[6] T.P.J. Knowles, and R. Mezzenga, Adv. Mater**. 28**, 6546 (2016). https://doi.org/10.1002/adma.201505961
[7] F. Zhang, Q. Zheng, Y. Tan, F. Wang, K.A.M. Salih, N. Zheng, M.F. Hamza, *et al*., Sep. Purif. Technol. **359**, 130617 (2025). https://doi.org/10.1016/j.seppur.2024.130617
[8] B. McVay, D. Wolfe, and A. Ramamoorthy, Langmuir **41**, 25849 (2025). https://doi.org/10.1021/acs.langmuir.5c03238
[9] K. Li, X. Zhang, L. Xu, K. Xu, X. Rao, S. Murugesan, V.A.R. Barão, *et al*., ACS Nano **19**, 39371 (2025). https://doi.org/10.1021/acsnano.5c14509
[10] M. Beregoi, S. Nistor, I.C. Ciobotaru, A. Nitescu, I. Zgura, M.C. Bunea, M. Enculescu, *et al*., Int. J. Biol. Macromol. **309**, 143160 (2025). https://doi.org/10.1016/j.ijbiomac.2025.143160
[11] X. Jiang, Y. Zhou, Y. Wang, J. Teng, K. Wang, J. Zhang, W. Li, *et al*., Adv. Funct. Mater. **35,** 2508900 (2025). https://doi.org/10.1002/adfm.202508900
[12] M. Usuelli, T. Germerdonk, Y. Cao, M. Peydayesh, M. Bagnani, S. Handschin, G. Nyström, and R. Mezzenga, Nanoscale, **13**, 12534 (2021). https://doi.org/10.1039/d1nr03133c
[13] S.G. Kou, L. Peters, and M. Mucalo, Carbohydr. Polym. **282**, 119132 (2022). https://doi.org/10.1016/j.carbpol.2022.119132
[14] Z. Tian, B. Ai, Y. Yang, X. Zheng, D. Xiao, L. Zheng, Z. Sheng, *et al*., Int. J. Biol. Macromol. **263**, 130011 (2024). https://doi.org/10.1016/j.ijbiomac.2024.130011
[15] F. Ren, R. Kang, T. Song, S. Lv, H. Zhang, and J. Wang, Int. J. Biol. Macromol. **277**, 134282 (2024). https://doi.org/10.1016/j.ijbiomac.2024.134282
[16] S.A. Ragland, and A.K. Criss, PLoS Pathog. **13**, e1006512 (2017). https://doi.org/10.1371/journal.ppat.1006512
[17] Z. WeiSihong, W. Xia, P. Shao, P. Sun, and N. Xiang. Biomacromolecules **22**, 890 (2021). https://doi.org/10.1021/acs.biomac.0c01599
[18] C. Weng, and G. Yen, Canc. Treat. Rev. **38**, 76 (2012). https://doi.org/10.1016/j.ctrv.2011.03.001
[19] T. Ozdal, E. Capanoglu, and F. Altay, Food Res. Int. **51**, 954 (2013). https://doi.org/10.1016/j.foodres.2013.02.009

[20] L. Frey, J. Zhou, G. Cereghetti, M.E. Weber, D. Rhyner, A. Pokharna, L. Wenchel, *et al*., Nat. Commun. **15**, 8448 (2024). https://doi.org/10.1038/s41467-024-52681-z
[21] Y. Yan, H. Tao, J. He, and S-Y. Huang, Nat. Protoc. **15**, 1829 (2020). https://doi.org/10.1038/s41596-020-0312-x

ДОСЛІДЖЕННЯ АМІЛОЇД – ПОЛІСАХАРИДНИХ КОМПОЗИТІВ МЕТОДОМ МОЛЕКУЛЯРНОГО ДОКІНГУ: І. ВЗАЄМОДІЯ З ПОЛІФЕНОЛАМИ

Валерія Трусова, Уляна Маловиця, Ольга Житняківська, Галина Горбенко
Кафедра медичної фізики та біомедичних нанотехнологій, Харківський національний університет імені В.Н. Каразіна м. Свободи 4, Харків, 61022, Україна

Філаментні білкові агрегати, амілоїдні фібрили, наразі викликають значний інтерес як перспективні наноматеріали для різноманітних біомедичних та промислових застосувань. Серед їхніх переваг такі властивості як біосумісність, висока стабільність та механічна стійкість, здатність до самоорганізації тощо. Інтеграція інших біополімерів, зокрема, полісахаридів в амілоїдний матрикс дозволяє створити нові наноматеріали з покращеними механічними характеристиками та вищою здатністю до навантаження біологічно активними речовинами. В даній роботі ми застосували метод молекулярного докінгу для з'ясування молекулярних деталей взаємодії між амілоїдними фібрилами лізоциму та серією поліфенольних сполук включаючи куркумін, галову кислоту, саліцилову кислоту, кверцетин, ресвератрол і сесамін, та дослідити вплив полісахариду хітозану на взаємодії такого типу. Було показано, що куркумін в єнольній формі має найвищу спорідненість до фібрилярного лізоциму, тоді як найнижча спорідненість була виявлена для саліцилової кислоти. Сайти зв'язування для куркуміну, галової кислоти, кверцетину, ресвератролу та сесаміну розташовуються в борозенці на зовнішній поверхні фібрили лізоциму, а саліцилова кислота зв'язується з внутрішньою поверхнею фібрили. Ідентифіковані амінокислотні залишки, що локалізуються на контактній ділянці в комплексах фібрил з поліфенолами та хітозаном. Встановлено, що хітозан здатний до взаємодії з поліфенольними сполуками всередині амілоїдного матриксу, що призводить до посилення зв'язування поліфенолів. Отримані дані створюють підґрунтя для подальшого дизайну та експериментального тестування амілоїд-хітозанових нанокомпозитів навантажених поліфенолами.

Ключові слова: *амілоїдні фібрили лізоциму; хітозан; поліфеноли; сайти зв'язування; спорідненість зв'язування; молекулярний докінг*

East European Journal of Physics. 1. 531–539 (2026)
DOI: 10.26565/2312-4334-2026-1-61 ISSN 2312-4334

IMPACT OF BARIUM DOPING ON THE STRUCTURAL AND OPTICAL PROPERTIES OF NiO THIN FILMS

Mohamed Begui[1*], **Mebrouk Ghougali**[1,2]
[1]*Faculty of Exact Sciences, Photonics Group, Renewable Energy Development Research Unit in Arid Zones (UDERZA), University of El Oued, El Oued, Algeria*
[2]*Faculty of Exact Sciences, LEVRES Laboratory, University of El Oued, 39000 El Oued, Algeria*
[*]*Corresponding Author e-mail: Begui-mohamed@univ-eloued.dz*
Received December 12, 2025; revised February 9, 2026; accepted February 25, 2026

This study investigates the influence of barium (Ba) doping on the structural and optical properties of nickel oxide (NiO) thin films synthesized via spray pyrolysis . NiO films with Ba concentrations of 0%, 2%, 4%, 6%, and 8% were analyzed using XRD, FT-IR, and UV–Vis spectroscopy. XRD results confirmed the formation of cubic NiO with a preferred (111) orientation. Increasing Ba content led to a reduction in peak intensities and the introduction of lattice strain, indicating the insertion of Ba^{2+} ions into the NiO lattice. Optical measurements showed high transparency of the films in the visible region, while the direct band gap decreased from 3.55 eV to 3.13 eV as the Ba concentration increased. These findings highlight the potential applicability of Ba-doped NiO in various optoelectronic devices.

Keywords: *Thin films; NiO; Spray pyrolysis; FT-IR; XRD*
PACS: 68.55.-a, 81.15.-z

1. INTRODUCTION

In recent years, thin films have attracted significant attention due to their wide-ranging applications in electronics, optoelectronics, and energy storage systems [1, 2, 3, 4]. Among the various materials employed in these technologies, transparent conducting oxides (TCOs) have shown remarkable promise, as they uniquely combine electrical conductivity with optical transparency an essential requirement for modern devices [3].

Nickel oxide (NiO) is a particularly attractive p-type TCO owing to its abundance, low cost, and favorable physical properties [1, 2]. It crystallizes in a face-centered cubic (NaCl-type) structure and possesses a relatively wide band gap, typically ranging from 3.25 to 4.00 eV. NiO exhibits high chemical stability, strong adhesion to substrates, and good transparency across the visible spectrum [4, 5]. These characteristics make it suitable for a variety of applications, including antiferromagnetic components [5], p-type transparent layers [6, 7], display technologies [8], photovoltaic devices [9], and gas sensors [10].

Numerous deposition techniques have been employed to produce NiO thin films, notably sol–gel processing [11], PECVD , PLD [12, 13], and magnetron sputtering [14, 15]. Among these, spray pyrolysis stands out as a cost-effective and versatile technique. It offers simplicity, compatibility with large-area deposition, and does not require high-vacuum equipment [16, 17]. Films fabricated by spray pyrolysis generally exhibit good uniformity and strong adhesion to glass substrates, making this approach attractive for large-scale industrial applications.

Doping is a widely used strategy for tailoring the structural, optical, and electrical characteristics of NiO thin films. Previous studies have shown that dopants such as Fe can significantly enhance performance by inducing lattice modifications or generating new energy levels [18]. In this context, barium (Ba) is an interesting dopant candidate due to its large ionic radius, which can influence the NiO lattice and potentially modulate its optoelectronic behavior.

The aim of the present study is to investigate the influence of barium doping on the structural and optical properties of NiO thin films prepared via spray pyrolysis. By varying the Ba concentration, we examine how this modification affects crystallinity, band gap energy, defect states, and optical constants. The results presented here are expected to contribute to the development of NiO-based materials for advanced optoelectronic applications.

2. METHODS AND MATERIALS

2.1. Thin Film Preparation

Nickel oxide (NiO) thin films were synthesized using the spray pyrolysis technique with varying concentrations of barium (Ba) as a dopant. The Ba doping levels examined were 0, 2, 4, 6, and 8 at.% relative to Ni.

The precursor solutions were prepared by dissolving nickel nitrate hexahydrate $Ni(NO_3)_2 \cdot 6H_2O$ and barium nitrate $Ba(NO_3)_2$, each at a concentration of 0.2 M, in distilled water. For the doped samples, the Ba nitrate solution was mixed with the nickel nitrate solution in volumetric ratios corresponding to the desired Ba atomic percentages (at.%). Since

Cite as: M. Begui, M. Ghougali, East Eur. J. Phys. 1, 531 (2025), https://doi.org/10.26565/2312-4334-2026-1-61

both precursor solutions were prepared at the same molar concentration (0.2 M), the Ba atomic percentage is directly determined from the volumetric mixing ratio and calculated as

$$Ba(at.\%) = \frac{V_{Ba}}{V_{Ba} + V_{Ni}} \times 100 \quad (1)$$

where V_{Ba} and V_{Ni} denote the volumes of Ba and Ni precursor solutions, respectively. The resulting solutions were continuously stirred and heated to 60°C to ensure complete homogenization.

Clean glass substrates were used for film deposition. The substrates were first cleaned with ethanol, followed by rinsing with deionized water to remove surface contaminants. Deposition was performed using a spray nozzle positioned 30 ± 1 cm above the substrate surface. Using a thermocouple and a digital temperature controller, the substrate temperature was maintained at 500 ± 10°C. The precursor solution was sprayed at a controlled flow rate of 2 mL/min.

During spray pyrolysis, thermal decomposition of the metal nitrates resulted in the formation of NiO films on the glass substrates according to the reaction [19]:

$$2\,\mathrm{Ni(NO_3)_2} + 6\,\mathrm{H_2O} \rightarrow 2\,\mathrm{NiO} + 4\,\mathrm{NO_2}\uparrow + \mathrm{O_2}\uparrow + 6\,\mathrm{H_2O}\uparrow .$$

2.2. Characterization Methods

The structural characteristics of the deposited films were investigated using X-ray diffraction (XRD) with a benchtop powder diffractometer (Proto Manufacturing AXRD) employing Cu Kα radiation (λ = 1.54184 Å) at 30 kV and 30 mA.

To study the optical properties, including transmittance and band gap energy, UV–Vis spectrophotometry was performed using a Shimadzu 3101 PC spectrometer covering a broad wavelength range from 200 to 1100 nm.

Fourier-transform infrared spectroscopy (FTIR) was carried out using a Shimadzu IR–Infinity 1 spectrometer in the range of 400–2000 cm^{-1} to analyze the vibrational modes and confirm the chemical bonding within the films.

The thickness t of the deposited thin films was determined using optical methods based on transmittance data, with the results summarized in Table 2.

3. RESULTS AND DISCUSSION

3.1. Structural Properties

3.1.1. X-Ray Measurement. The XRD patterns of both undoped and Ba-doped NiO thin films are presented in Figure 1. Prominent diffraction peaks appear at $2\theta \approx 37.3°$, 43.2°, and 62.8°, corresponding to the (111), (200), and (220) planes of cubic NiO respectively,These are in good agreement with the ICDD PDF Card No. 47-1049, confirming the formation of a face-centered cubic (Fm-3m) phase with a (111) preferred orientation. In the 4% Ba-doped sample, an additional weak diffraction peak appears at $2\theta \approx 59.14°$, which does not correspond to any characteristic reflection of cubic NiO. This peak is therefore attributed to the formation of a secondary Ba-containing phase, likely arising from excess Ba incorporation during film growth. With increasing Ba concentration, the intensity of the NiO diffraction peaks decreases, indicating increased lattice distortion and a reduction in long-range crystalline order [20]. A slight shift of the (111) peak position toward lower 2θ angles is observed with Ba incorporation, reflecting changes in the lattice parameters due to dopant-induced strain [21].

3.1.2. Crystallite Size and Structural Parameters. Using Bragg's law and the Scherrer formula [22], the lattice parameter and crystallite size were calculated and are summarized in Table 1. The variation of crystallite size (D) and lattice parameter (a) as a function of Ba concentration is illustrated in Figure 2. At low Ba content (2 at.%), the crystallite size increases, indicating an initial improvement in grain growth. A sharp reduction in crystallite size is observed at 4 at.% Ba doping, which is attributed to increased lattice distortion and the onset of a secondary Ba-containing phase. With further increase in Ba concentration (6 and 8 at.%), the crystallite size remains relatively reduced, reflecting enhanced defect formation and dopant-induced strain. The lattice parameter shows a non-monotonic variation with Ba content, confirming that Ba incorporation significantly affects the crystal structure of NiO thin films. These results demonstrate that excessive Ba doping degrades the structural quality of NiO films.

The non-monotonic evolution of crystallite size can be explained by the significant ionic radius mismatch between Ba^{2+} (135 pm) and Ni^{2+} (69 pm) ions. At low Ba concentration (2 at.%), partial substitution of Ni^{2+} by Ba^{2+} may introduce moderate lattice distortion that enhances atomic diffusion during film growth, promoting grain coalescence and increasing crystallite size [23]. With further increase in Ba content, the large ionic size of Ba^{2+} generates substantial lattice strain and defect formation within the NiO matrix. When the Ba concentration approaches approximately 4 at.%, the solubility limit of Ba in NiO is likely reached, leading to dopant segregation at grain boundaries and the appearance of a secondary Ba-containing phase [24]. This segregation restricts grain growth and results in crystallite size reduction. Therefore, the structural behavior reflects a competition between diffusion-assisted grain growth at low doping levels and strain-induced grain refinement at higher Ba concentrations.

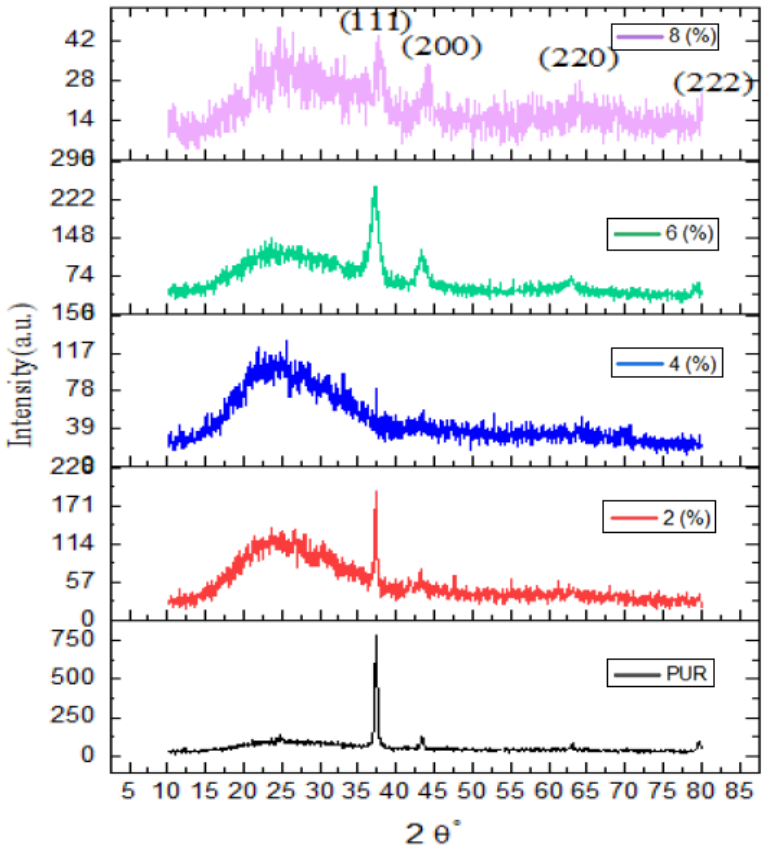

Figure 1. XRD patterns of Ba doped NiO thin films at different Ba concentrations.

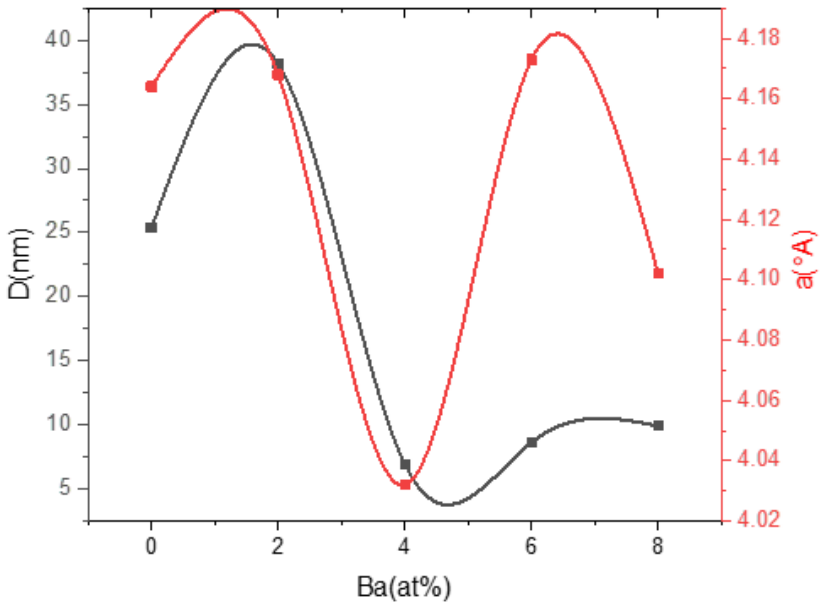

Figure 2. Variations of grain size, and lattice parameter as a function of Ba concentration.

Table 1. Structural parameters of undoped and Ba-doped NiO thin films, including diffraction angle (2θ), interplanar spacing (d_{hkl}), lattice constant (a), crystallite size (D), dislocation density (δ), and microstrain (ε).

Sample	2θ (deg)	d_{hkl} (Å)	(hkl)	a (Å)	FWHM (deg)	D (nm)	δ (10^{15} line/m^2)	Microstrain (ε)
NiO	37.249	–	(111)	–	–	–	–	–
(ICDD PDF	43.276	–	(200)	4.177	–	–	–	–
No. 47-1049)	62.879	–	(220)	–	–	–	–	–
	37.377	2.404	(111)					
Ba:NiO 0%	43.434	2.083	(200)	4.164	0.3306	25.36	1.54	0.00427
	63.113	1.473	(220)					
	37.339	2.407	(111)					
Ba:NiO 2%	43.335	2.088	(200)	4.168	0.2204	38.18	0.683	0.00285
	64.387	1.275	(220)					
Ba:NiO 4%	38.684	2.329	(111)	4.032	1.2210	6.91	20.9	0.0152
	59.142	–	Secondary phase	–	–	–	–	–
	37.317	2.409	(111)					
Ba:NiO 6 %	43.291	2.111	(200)	4.173	0.9742	8.65	13.4	0.0130
	62.817	0.042	(220)					
	38.027	2.368	(111)					
Ba:NiO 8%	44.057	2.055	(200)	4.102	0.8502	9.92	10.2	0.0110
	63.499	1.465	(220)					

3.2. FTIR Spectroscopy

Figure 3 displays the Fourier-transform infrared (FTIR) spectra obtained from both undoped and Ba-doped NiO thin films in the range of 400–2000 cm^{-1}. A prominent absorption band between 414–449 cm^{-1} corresponds to Ni–O stretching vibrations, confirming the presence of NiO. An additional band near 755–760 cm^{-1} is attributed to general metal–oxygen (M–O) bending vibrations [25].

These spectral features validate the formation of NiO and suggest that Ba doping does not fundamentally alter the Ni–O bonding environment, although minor shifts may indicate subtle structural perturbations.

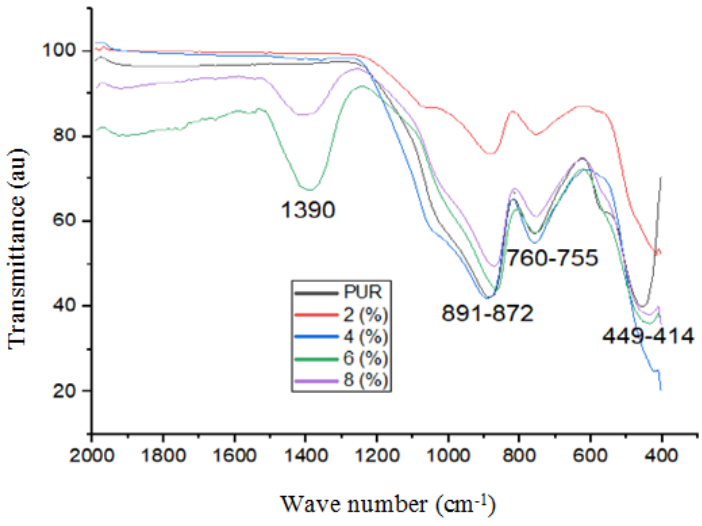

Figure 3. FTIR spectra of undoped and Ba-doped NiO thin films.

3.3. Optical Properties

3.3.1. Transmittance and Absorption. Figure 4 presents the transmittance spectra for all samples across the wavelength range of 300–900 nm. The undoped and lightly doped films (2% and 4%) exhibit transmittance values exceeding 60%, indicating high transparency. In contrast, films with higher Ba concentrations (6% and 8%) show reduced transparency, attributed to increased light absorption arising from dopant-induced defect states located near the conduction band edge.

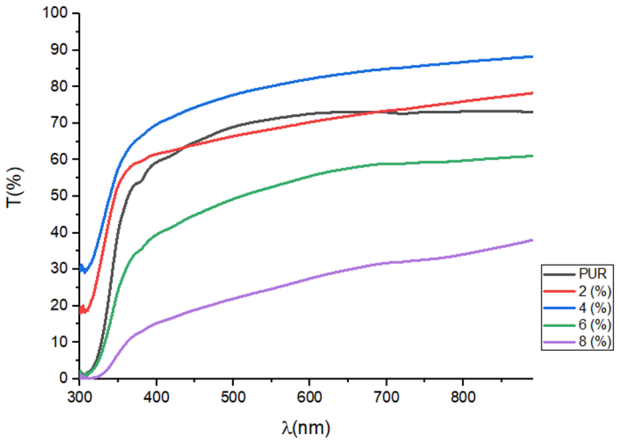

Figure 4. Transmittance spectra of NiO:Ba thin films.

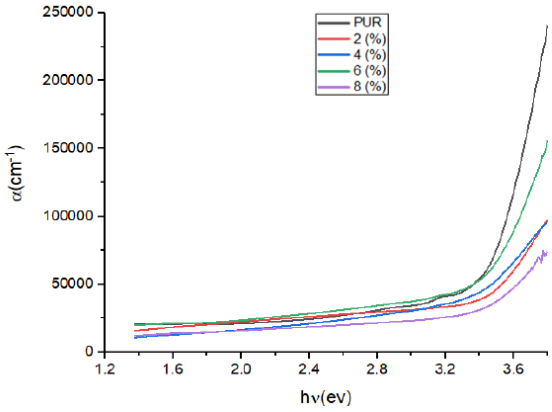

Figure 5. Absorption coefficient vs. photon energy for NiO:Ba films.

The absorption coefficient α was determined from the optical data of the thin films, taking into account both absorbance and film thickness. As illustrated in Figure 5, the absorption coefficient α increases progressively with rising Ba doping levels. This behavior indicates that the incorporation of barium enhances the films light absorption, which can be associated with modifications in the electronic band structure. The observed trend reflects the formation of additional energy levels or localized states within the material as Ba content increases, thereby facilitating greater photon absorption and effectively altering the optical response of the NiO thin films.

3.3.2. Energy of the Band Gap. The optical band gap E_g was estimated using the Tauc relation:

$$(\alpha h\nu)^n = A(h\nu - E_g), \tag{2}$$

where α is the absorption coefficient, $h\nu$ is the photon energy, A is a proportionality constant related to the transition probability, E_g is the optical band gap energy, and n depends on the nature of the electronic transition. For direct allowed transitions, $n = 2$ was used. Assuming a direct allowed transition for NiO, the band gap values were determined by extrapolating the linear region of the $h\nu$ plots to the energy axis, as shown in Figure 6. The band gap decreases from 3.55 eV (undoped) to 3.13 eV for the 8% Ba-doped film, indicating the formation of defect-related localized states and band tailing. This redshift in the absorption edge is a typical consequence of dopant-induced structural disorder.

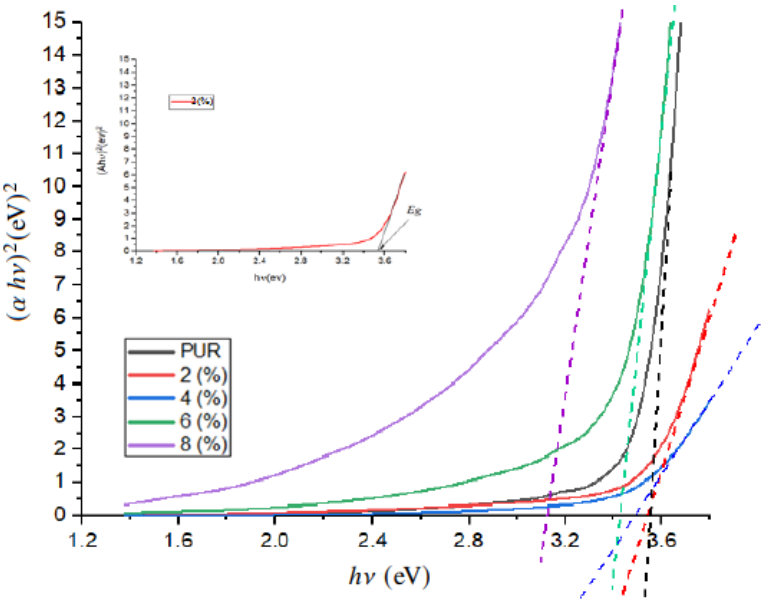

Figure 6. Tauc plots for band gap energy determination.

3.3.3. Urbach Energy (E_U). The Urbach energy E_U, which quantifies the extent of the tail of localized states in the band gap, was determined from the slope of the linear region in the $\ln(\alpha)$ versus photon energy $h\nu$ plot.

As shown in Figure 7 and Table 2, E_U increases with Ba doping (except at 6%), indicating that structural disorder and defect density become more pronounced at higher dopant concentrations. An inverse correlation is observed between E_g and E_U, consistent with typical behavior in disordered semiconductor systems.

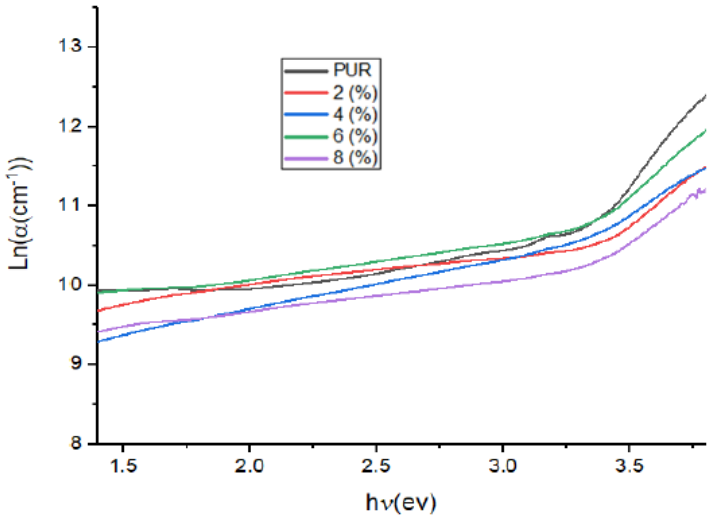

Figure 7. Urbach plots of NiO:Ba thin films.

Table 2. Values of thickness t, optical band gap energy E_g,and Urbach energy E_U of the undoped and Ba-doped NiO thin films

	$t(nm)$	$E_g(eV)$	$E_U(eV)$
Pure NiO:Ba	150.85	3.55	0.235
NiO:Ba(2%)	155.81	3.54	0.414
NiO:Ba(4%)	117.34	3.49	0.442
NiO:Ba(6%)	246.81	3.42	0.341
NiO:Ba(8%)	805.81	3.13	0.413

3.3.4. Extinction Coefficient and Refractive Index. The extinction coefficient k was determined from the absorption coefficient α and the wavelength λ as outlined in [26]. As shown in Figure 8, k increases with Ba doping, reflecting enhanced optical absorption.

Similarly, the refractive index n was calculated based on the reflectance R and the extinction coefficient, following the method described in [26]. Figure 9 shows that the refractive index n increases at lower photon energies and sharply decreases beyond approximately 3.4 eV, likely due to interband electronic transitions. The 8% Ba-doped sample exhibits anomalous behavior, which may be attributed to excessive defect formation.

3.3.5. Dielectric Function. The real (ε_r) and imaginary (ε_i) parts of the dielectric constant were calculated using the following relations [26]:

$$\varepsilon_r = n^2 - k^2 \tag{3}$$

$$\varepsilon_i = 2nk \tag{4}$$

Figure 10 and Figure 11 illustrate the variation of the real (ε_r) and imaginary (ε_i) parts of the dielectric constant as a function of photon energy ($h\nu$) for different Ba concentrations. For lower doping levels (2% and 4%), both components generally increase with photon energy and Ba content. However, at the highest doping concentration (8%), both ε_r and ε_i exhibit a significant decrease, particularly in the high-energy region above 2.5 eV. Throughout most of the measured range, the real part ε_r remains larger than the imaginary part ε_i, suggesting that light propagation is the dominant process compared to energy loss in these films. These results indicate that Ba doping effectively modifies the dielectric response, though the trend non-linearly depends on the Ba concentration.

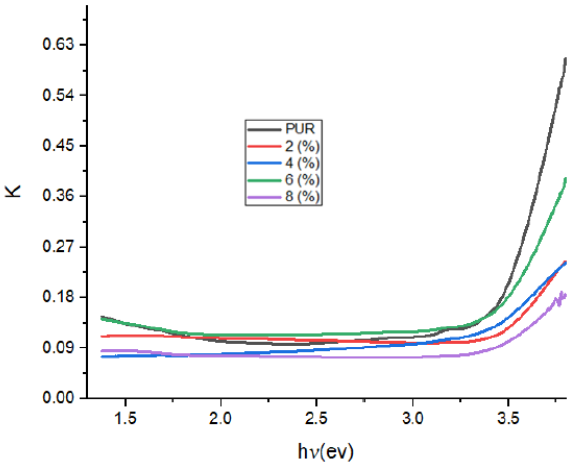

Figure 8. Effect of doping on extinction coefficient (k).

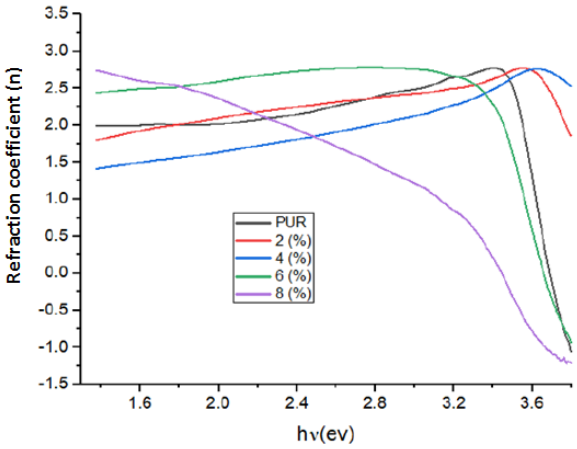

Figure 9. Effect of doping on refractive index (n).

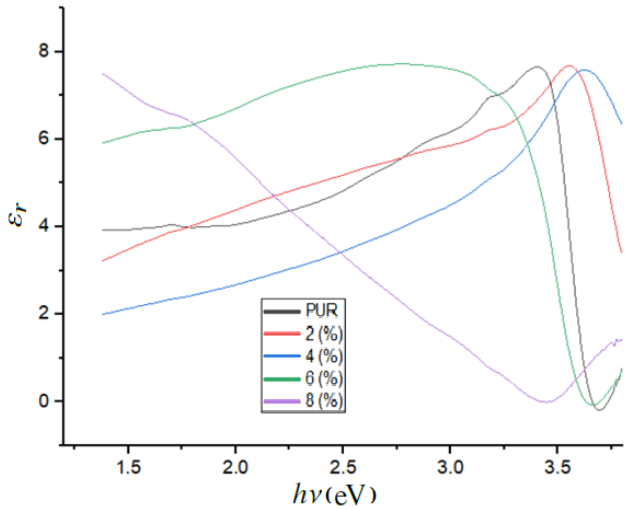

Figure 10. Real part of the dielectric constant vs. photon energy.

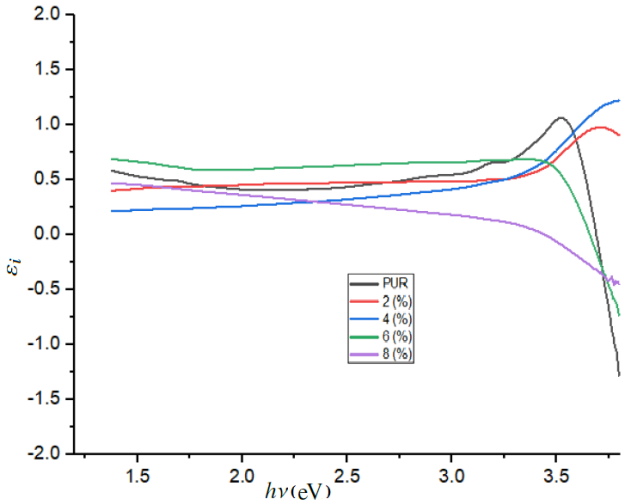

Figure 11. Imaginary part of the dielectric constant vs. photon energy.

4. CONCLUSIONS

NiO thin films, both undoped and Ba-doped, were successfully synthesized by the spray pyrolysis technique. X-ray diffraction analysis confirmed the formation of a single-phase cubic NiO structure with space group $Fm\bar{3}m$, characterized by dominant reflections along the (111), (200), and (220) planes. All films exhibited a preferred orientation along the (111) direction. The incorporation of Ba significantly influenced the structural properties of NiO, as evidenced by changes in peak intensities, lattice parameters, and crystallite size.

A detailed structural analysis revealed that low Ba doping slightly improves crystallinity, whereas higher Ba concentrations induce lattice distortion and structural disorder. The crystallite size shows a non-monotonic dependence on Ba content, increasing at low doping levels and decreasing markedly at higher concentrations due to enhanced strain and defect formation. In the 4% Ba-doped sample, the appearance of an additional weak diffraction peak was attributed to a secondary Ba-containing phase, indicating the solubility limit of Ba in the NiO lattice under the present deposition conditions. These results demonstrate that excessive Ba incorporation deteriorates the structural order of the films.

FTIR measurements confirmed the formation of Ni–O bonds in all samples, indicating successful oxide formation. Optical transmittance spectra in the 300–900 nm range revealed high transparency for all films, with a maximum transmittance of approximately 88% observed for the 4% Ba-doped sample. The optical band gap exhibited a gradual redshift with increasing Ba concentration, which is attributed to the introduction of defect-related localized states and increased structural disorder.

Furthermore, key optical constants, including the absorption coefficient, extinction coefficient, refractive index, and dielectric functions, were systematically evaluated and found to be strongly dependent on Ba doping. These variations further confirm the role of Ba incorporation in modifying the optical response of NiO thin films.

Overall, this study demonstrates that Ba doping provides an effective approach to systematically modulate the

structural and optical properties of NiO thin films. While moderate Ba incorporation can enhance certain optical characteristics, excessive doping leads to structural degradation. These findings highlight the potential of Ba-doped NiO thin films for optoelectronic applications such as transparent electrodes, photovoltaics, and gas sensors. Future work will focus on electrical and optoelectrical characterization to further assess their suitability for device applications.

ORCID

Mohamed Begui, https://orcid.org/0000-0001-8378-5058; **Mebrouk Ghougali**, https://orcid.org/0000-0003-0496-4555

REFERENCES

[1] M. Ghougali, O. Belahssen, and A. Chala, "Investigation of the Properties of NiO Thin Films Prepared by Spray Pyrolysis Technique," Journal of Nano- and Electronic Physics, **8**(4), 04059 (2016).

[2] O. Belahssen, M. Ghougali, and A. Chala, "Structural and Optical Properties of Nickel Oxide Thin Films Prepared by Spray Pyrolysis," Journal of Nano- and Electronic Physics, **10**(2), 02039 (2018). https://doi.org/10.21272/jnep.10(2).02039

[3] M. Ghougali, O. Belahssen, and A. Chala, "Effect of Substrate Temperature on the Properties of NiO Thin Films," Journal of Nano- and Electronic Physics, **9**(3), 03043 (2017). https://doi.org/10.21272/jnep.9(3).03043

[4] R. Sharma, A. D. Acharya, S. B. Shrivastava, T. Shripathi, and V. Ganesan, "Effect of thickness on structural, optical and electrical properties of NiO thin films," Optik, **125**(22), 6751–6756 (2014). https://doi.org/10.1016/j.ijleo.2014.07.104

[5] L. Cattin, B. Reguig, A. Khelil, M. Morsli, K. Benchouk, and J. Bernede, "Properties of NiO thin films deposited by chemical spray pyrolysis using different precursor solutions," Applied Surface Science, **254**(18), 5814–5821 (2008). https://doi.org/10.1016/j.apsusc.2008.03.071

[6] E. Fujii, A. Tomozawa, H. Torii, and R. Takayama, "Preferred orientations of NiO films prepared by plasma-enhanced metalorganic chemical vapor deposition," Japanese Journal of Applied Physics, **35**(3A), L328 (1996). https://doi.org/10.1143/JJAP.35.L328

[7] H. Sato, T. Minami, S. Takata, and T. Yamada, "Transparent conducting p-type NiO thin films prepared by magnetron sputtering," Thin Solid Films, **236**(1-2), 27–31 (1993). https://doi.org/10.1016/0040-6090(93)90636-4

[8] V. H. López-Lugo, M. García-Hipólito, A. Rodríguez-Gómez, and J. C. Alonso-Huitrón, "Fabrication of Li-Doped NiO Thin Films by Ultrasonic Spray Pyrolysis and Its Application in Light-Emitting Diodes," Nanomaterials, **13**(4), 197 (2023). https://doi.org/10.3390/nano13010197

[9] K. Yoshimura, T. Miki, and S. Tanemura, "Nickel Oxide Electrochromic Thin Films Prepared by Reactive DC Magnetron Sputtering," Japanese Journal of Applied Physics, **34**(5R), 2440 (1995). https://doi.org/10.1143/JJAP.34.2440

[10] H. L. Chen, Y. M. Lu, and W. S. Hwang, "Characterization of sputtered NiO thin films," Surface and Coatings Technology, **198**(1-3), 138–142 (2005). https://doi.org/10.1016/j.surfcoat.2004.10.032

[11] I. Hotovy, J. Huran, *et al*. "The influences of preparation parameters on NiO thin film properties for gas sensing application," Sensors and Actuators B: Chemical, **78** (1–3), 126–132 (2001). https://doi.org/10.1016/S0925-4005(01)00802-4

[12] US. Joshi, R. Takahashi, Y. Matsumoto, and H. Koinuma, "Structure of NiO and Li-doped NiO single crystalline thin layers with atomically flat surface," Thin Solid Films, **486**(1-2), 214-217 (2005). https://doi.org/10.1016/j.tsf.2004.11.219

[13] Y. Kakehi, S. Nakao, K. Satoh, and T. Kusaka, "Room-temperature epitaxial growth of NiO (1 1 1) thin films by pulsed laser deposition," Journal of Crystal Growth, **237-239**, 591-595 (2002). https://doi.org/10.1016/S0022-0248(01)01964-9

[14] H.-L. Chen, Y.-M. Lu, and W.-S. Hwang, "Thickness dependence of electrical and optical properties of sputtered NiO thin films," Thin Solid Films, **498**(1), 266–270 (2006). https://doi.org/10.1016/j.tsf.2005.07.124

[15] Zhi-Zhen Ye, *et al*. "Preparation and characterization of p-type ZnO films by DC reactive magnetron sputtering," Journal of Crystal Growth, **253**(1), 258–264, (2003). https://doi.org/10.1016/S0022-0248(03)01007-8

[16] B.A. Reguig, A. Khelil, L. Cattin, M. Morsli, and J.C. Bernède, "Properties of NiO thin films deposited by intermittent spray pyrolysis process," Applied Surface Science, **253**(9), 4330-4334, (2007). https://doi.org/10.1016/j.apsusc.2006.09.046

[17] T.H. Noh, W. Y. Jeung, I. K. Kang, S. H. Shin, and J. J. Lee, "Magnetic properties of Pr-Fe-B alloy powders prepared by mechanical grinding," Journal of Applied Physics, **70**(10), 6591–6593 (1991). https://doi.org/10.1063/1.349867

[18] D. Amaranatha Reddy, A. Divya, G. Murali, and R.P. Vijayalakshmi,"Synthesis and optical properties of Cr doped ZnS nanoparticles capped by 2-mercaptoethanol," Physica B, **406**(10), 1944–1949 (2011). https://doi.org/10.1016/j.physb.2011.02.062

[19] W. Brockner, C. Ehrhardt, and M. Gjikaj, "Thermal decomposition of nickel nitrate hexahydrate $Ni(NO_3)_2{\cdot}6H_2O$, in comparison to $Co(NO_3)_2{\cdot}6H_2O$ and $Ca(NO_3)_2{\cdot}4H_2O$," Thermochimica Acta, **456**(1), 64–68 (2007). https://doi.org/10.1016/j.tca.2007.01.031

[20] L. R.Singha, and R.K.L. Singh, "Effect of Dopant Concentration on Structural Properties of Chemical Bath Deposited Mn-Doped PbS Nanocrystalline Thin Films," Chalcogenide Letts, **17**(7), 375-384(2020)

[21] M. Ghougali, *et al*, "Investigation of the physical properties of nanostructured CO:NiO thin films," Chalcogenide Letters, **18**, 765–772 (2021). https://doi.org/10.15251/CL.2021.1812.765

[22] A. Patterson, "The Scherrer Formula for X-Ray Particle Size Determination," Physical Review, **56**(10), 978 (1939). https://doi.org/10.1103/PhysRev.56.978

[23] Kiprotich, Nancy, *et al*. "Effects of Tin Doping Concentration on the Structural and Optical Properties of Cadmium Oxide Nanoparticles," Advances in Materials, **14**(2), 55–64 (2025). https://doi.org/10.11648/j.am.20251402.13

[24] M. Kindelmann, *et al*., "Segregation-controlled densification and grain growth in rare earth-doped Y_2O_3", Journal of the American Ceramic Society, **104**(10), 4946–4959 (2021). https://doi.org/10.1111/jace.17907

[25] R. Barir, B. Benhaoua, S. Benhamida, *et al*., "Effect of Precursor Concentration on Structural Optical and Electrical Properties of NiO Thin Films Prepared by Spray Pyrolysis," Journal of Nanomaterials, **2017**, 5204639 (2017). https://doi.org/10.1155/2017/5204639

[26] M. E. Begum, M. Chowdhury, and M. B. Islam, "Structural, morphological and optical characterizations of spray pyrolyzed nickel oxide thin films," Results in Materials, **14** , 100265 (2022). https://doi.org/10.1016/j.rinma.2022.100265

ВПЛИВ ЛЕГУВАННЯ БАРІЄМ НА СТРУКТУРНІ ТА ОПТИЧНІ ВЛАСТИВОСТІ ТОНКИХ ПЛІВОК NiO

Мохамед Бегуі[1], **Мебрук Гудалі**[1,2]

[1]*Факультет точних наук, група фотоніки, дослідницький підрозділ розвитку відновлюваної енергетики в посушливих зонах (UDERZA), Університет Ель-Уед, Ель-Уед, Алжир*

[2]*Факультет точних наук, лабораторія LEVRES, Університет Ель-Уед, 39000 Ель-Уед, Алжир*

У цьому дослідженні досліджується вплив легування барієм (Ba) на структурні та оптичні властивості тонких плівок оксиду нікелю (NiO), синтезованих за допомогою розпилювального піролізу. Плівки NiO з концентрацією Ba 0%, 2%, 4%, 6% та 8% були проаналізовані за допомогою рентгенівської дифракції, ІЧ-спектроскопії з перетворенням Фур'є та УФ-видимої спектроскопії. Результати рентгенівської дифракції підтвердили утворення кубічного NiO з переважною (111) орієнтацією. Збільшення вмісту Ba призвело до зменшення інтенсивності піків та появи деформації решітки, що вказує на впровадження іонів Ba^{2+} у решітку NiO. Оптичні вимірювання показали високу прозорість плівок у видимій області, тоді як ширина забороненої зони зменшилася з $3,55\,eV$ до $3,13\,eV$ зі збільшенням концентрації Ba. Ці результати підкреслюють потенційну можливість застосування NiO легованого Ba в різних оптоелектронних пристроях.

Ключові слова: *тонкі плівки; NiO; розпилювальний піроліз; ІЧ-спектроскопія з перетворенням Фур'є; рентгенівська дифракція*

East European Journal of Physics. 1. 540-547 (2026)
DOI:10.26565/2312-4334-2026-1-62 ISSN 2312-4334

INFLUENCE OF NITROGEN PRESSURE ON THE ADHESION AND SCRATCH FAILURE MECHANISMS OF TiMoN/NbN MULTILAYER COATINGS DEPOSITED BY CATHODIC ARC PVD

O.V. Maksakova[1]*, V.M. Beresnev[1], S.V. Lytovchenko[1], M. Sahul[2], M. Čaplovičova[3], R.S. Galushkov[1]

[1]V.N. Karazin Kharkiv National University, 4, Svoboby Sq., 61000 Kharkiv, Ukraine
[2]Institute of Materials Science, Slovak University of Technology in Bratislava, 25, Jána Bottu Str., 917 24 Trnava, Slovakia
[3]Centre for Nanodiagnostics of Materials, Slovak University of Technology in Bratislava, Vazovova 5, 812 43 Bratislava, Slovakia
**Corresponding Author e-mail: o.maksakova@karazin.ua*
Received December 15, 2025; revised January 18, 2026; accepted February 2, 2026

Multilayer nitride coatings are widely used to improve the mechanical performance and durability of engineering components subjected to severe tribological loading. In the present work, the adhesion behaviour and failure mechanisms of nanolayered TiMoN/NbN multilayer coatings deposited by cathodic arc PVD were investigated as a function of nitrogen working pressure. Two coatings were synthesized at nitrogen pressures of 0.52 Pa and 0.13 Pa under otherwise identical deposition conditions. Microscopy analysis revealed that both coatings exhibit a well-defined nanolayered architecture consisting of alternating TiMoN and NbN layers with a modulation period of approximately 85 nm and a total thickness of about 9.5 μm. The decreasing of nitrogen pressure results in a higher density of macroparticles due to the longer mean free path of cathodic arc plasma species. Scratch adhesion tests performed under progressive loading conditions allowed identification of two characteristic failure events corresponding to buckling crack initiation and buckling spallation. The multilayer coating deposited at 0.13 Pa demonstrated slightly improved resistance to crack initiation (5.41 N) compared with the multilayer coating deposited at 0.52 Pa (4.72 N). However, both coatings exhibited similar values of the second critical load (12.4–12.5 N). The multilayer coating deposited at higher nitrogen pressure mainly undergoes adhesive failure with extensive substrate exposure. In contrast, the multilayer coating deposited at lower nitrogen pressure exhibits predominantly cohesive damage within the multilayer structure. The obtained results demonstrate that nitrogen pressure during cathodic arc deposition significantly affects the microstructure evolution and the mechanisms of adhesion failure in TiMoN/NbN multilayer coatings. The study provides insight into the optimization of deposition parameters for improving the mechanical reliability of multilayer nitride coatings.
Keywords: *PVD; Nitrides; Multilayer coatings; TiMoN; Microstructure; Composition; Adhesion*
PACS: 68.55.Jk, 68.65.Ac

1. INTRODUCTION

The adhesion strength of protective coatings is a crucial parameter that determines their actual performance. It is specifically the coating's ability to maintain a strong bond with the substrate under mechanical, thermal, and chemical stresses that influences the service life of a tool or component. For nitride PVD coatings (such as TiN, NbN, MoN, as well as CrN, ZrN, and others), adhesion is affected not only by the natural chemical affinity between the metal or nitride and the substrate but also by several factors: the energy of ion bombardment on the substrate, the level and type of residual stresses, the presence of transition layers (like Ti, TiN, Nb-enriched interlayers), and the hardness-to-elastic modulus ratio (H/E, H^3/E^2), which impacts resistance to crack initiation and propagation.

For example, for the MoN/TiN system it has been shown that a multilayer architecture with a Ti sublayer and a graded transition TiN layer allows the formation of a dense, fine-grained structure with high H/E and H^3/E^2 ratios, which directly correlates with increased adhesion strength in the Rockwell determine their actual performance: it is precisely the coating's abilitytest compared with monolayer TiN and MoN coatings [1]. For NbN coatings on austenitic steel AISI 316L it has been shown that reactive magnetron sputtering followed by controlled oxidation forms a multiphase NbN/Nb2O5 structure with increased microhardness and corrosion resistance; at the same time, cross-sectional polishing and indentation tests demonstrate preservation of the integrity of the “coating–steel” interface, that is, adhesion remains sufficient even after heat treatment [2]. Similarly, in the NbN/Ti system, it has been found that optimization of the N_2 flow rate during magnetron sputtering allows control of the stoichiometry and texture of NbN, which leads to increased conductivity and corrosion resistance of Ti bipolar plates without degradation of their mechanical integrity, that is, due to the formation of a dense, well-adhered interface [3].

The combination of these results shows that even for simple binary nitrides such as TiN, NbN, and MoN, achieving high adhesion is not a trivial task of interface engineering rather than merely the selection of the correct chemical system.

Against this background, interest is growing in alloyed and ternary nitrides based on Ti, Nb, and Mo, which combine high hardness and thermal stability with improved adaptation to substrate deformation. For TiNbN coatings deposited by cathodic arc evaporation on D2 tool steel, Gonzalez-Carmona et al. showed that varying the substrate temperature during deposition leads to the evolution of the FCC phase structure, changes in the lattice parameter, and changes in crystallite shape, which in turn significantly affect adhesion [4]. According to nanoindentation and scratch test data, the optimal

Cite as: O.V. Maksakova, V.M. Beresnev, S.V. Lytovchenko, M. Sahul, M. Čaplovičova, R.S. Galushkov, East Eur. J. Phys. 1, 540 (2026), https://doi.org/10.26565/2312-4334-2026-1-62

temperature range ensures not only maximum hardness, but also increased H/E and H^3/E^2 ratios, as well as higher critical failure loads Lc; at the same time, the damage mode changes from purely adhesive delamination to mixed cohesive–adhesive failure, which indicates strengthening of the interface.

For NbN layers used as adhesion interlayers or components of multilayer structures, it has been shown that their dense, fine-crystalline structure and ability to form oxide barrier phases (Nb_2O_5) additionally stabilize the "coating–metal" contact under corrosion and cyclic loading [2,5]. Another important example is the MoN/TiN multilayer, where the alternating layers based on Mo and Ti allow reduction of stress concentration at the interface, improvement of crack resistance, and provide somewhat higher adhesion compared with monolayer analogues; in this case, the Mo phase additionally contributes to lowering the friction coefficient due to the formation of lubricating MoO_3 oxides [1].

Particular attention in recent years has been devoted to TiMoN coatings, where molybdenum is introduced as an alloying element into the TiN matrix. In the work of Van Meter et al. on TiMoN films deposited by PEALD on different substrates, it was shown that wear resistance and adhesion behavior are closely related to interface engineering: control of the thickness and composition of the oxide layer at the "coating–substrate" interface makes it possible to significantly reduce the wear rate and avoid premature delamination [6]. In combination with the TiNbN results, this indicates that alloying TiN with Nb or Mo atoms and constructing multilayer systems based on Ti–Mo–Nb not only modifies the strengthening mechanism (solid-solution, dislocation, interfacial), but also allows deliberate control of adhesion through optimization of residual stresses, texture, and the gradient of properties from the substrate to the surface. That is why in further work it is logical to focus on Ti–Mo–NbN systems, where each of the elements has already demonstrated the ability to improve adhesion both in binary (TiN, NbN, MoN) and ternary (TiNbN, TiMoN) coatings, and their combination in multilayer architectures provides the potential for further enhancement of adhesion strength without loss of hardness and wear resistance.

Multilayer nitride coatings are considered as the next step compared with simple binary and ternary systems, since the periodic alternation of layers with different mechanical and chemical properties makes it possible to simultaneously increase hardness, crack resistance, and adhesion strength to the substrate due to stress redistribution and blocking of crack propagation at numerous interfaces [7,11]. In particular, for the nano-multilayer $(TiN/ZrN)_n$ deposited by PVD methods, it has been shown that a decrease in the bilayer thickness leads to significant grain refinement, an increase in microhardness, and the formation of wear tracks that are more resistant to wear and delamination; at the same time, in the work of Gonzalez-Carmona et al. it was emphasized that the multilayer architecture of TiN/ZrN provides higher resistance to local coating degradation compared with monolithic TiN and ZrN, which is directly related to the effective damping of stresses at the interlayer boundaries [7].

A similar approach has been implemented for WN-based multilayer systems WN/MeN (Me = Zr, Cr, Mo, Nb), where the introduction of a second nitride layer made it possible to form a nanocomposite structure with high hardness (more than 30 GPa), low specific wear, and stable performance under sliding friction; the authors showed that optimization of the thickness and sequence of WN/MeN layers makes it possible to maintain high load-bearing capacity and prevent premature spallation even under increased contact loads, which indicates the realization of so-called "architectural strengthening" also under adhesion-loaded conditions [8].

Particular attention is attracted by systems based on TiN and NbN, which are close in composition to our Ti–Mo–Nb-containing coatings: Sugumaran et al. demonstrated that a nanoscale TiN/NbN multilayer deposited using HIPIMS-UBM on a CoCrMo alloy forms an extremely dense structure free of intercolumnar pores with a hardness of ~28 GPa, a low coefficient of friction, and high critical loads in the scratch test, which the authors associate with the combination of intensive ion pre-treatment of the substrate and the superlattice structure of the coating [9]. Further analysis of TiN/NbN superlattices showed that under localized loading individual nanolayers can collectively rearrange without destruction of the integrity of the film; at the same time, focused ion beam cross-sections demonstrated very strong adhesion of the coating to the CoCrMo substrate, which the authors interpret as a consequence of the controlled formation of a graded transition layer and a high density of defects at the "substrate/first layer" interface [10].

Thus, modern studies of multilayer nitride systems – from $(TiN/ZrN)_n$ to WN/MeN and TiN/NbN – consistently indicate that the rational selection of pairs of transition metal nitrides (in particular based on Ti, Mo, Nb), control of the bilayer thickness, and the energy of the ion flux during deposition make it possible not only to increase hardness and wear resistance but also to ensure high adhesion characteristics that are critical for the long-term operation of protective coatings in contact-loaded components [7–11].

The evolution of multilayer nitride systems is not limited only to the combination of binary compounds; in recent years, considerable attention has been paid to architectures that combine binary and ternary nitrides, allowing even more flexible control of the mechanical and adhesive properties of coatings. For example, in multilayer systems of the type (TiZr)N/NbN, it has been established that the introduction of NbN layers into the structure of ternary TiZrN leads to the formation of a denser microstructure with increased crack resistance, and the critical loads Lc during scratch testing increase due to the optimal distribution of residual stresses between the layers [12]. Similarly, in TiSiN/CrN multilayers, it has been shown that the presence of Si in the upper layers forms amorphized barrier zones and reduces the probability of brittle cracking, while CrN provides a high load-bearing capacity of the interface; as a result, the system demonstrates increased adhesion strength and delayed initiation of delamination in the contact zone [13]. In addition, in works devoted to TiCrN/NbN and TiCrN/MoN multilayers, it has been established that the combination of hard and thermally stable TiCrN with more plastic NbN or oxide-forming MoN allows reduction of the concentration of local stresses and increases resistance to microcrack formation, which directly correlates with adhesion strength under conditions of increasing load [14].

A comprehensive analysis of the available literature data shows that although multilayer coatings combining binary and ternary nitrides demonstrate significant advantages over classical systems, the TiMoN/NbN combination remains practically unexplored, specifically in terms of adhesive properties. In the available sources, there are no systematic studies on the influence of technological parameters on the critical loads of delamination, failure mechanisms, and adhesive behavior of such multilayers. Therefore, the aim of this work is the experimental investigation of the adhesion characteristics of the multilayer TiMoN/NbN coating, focused on the influence of the working pressure during cathodic arc deposition (0.52 Pa and 0.13 Pa) on the formation of the interface and the failure patterns under localized mechanical loading.

2. EXPERIMENTAL DETAILS

2.1. Deposition

Multilayer TiMoN/NbN coatings were deposited by the cathodic arc evaporation method (CAE-PVD) using two cathodes: a Ti–Mo alloy with a ratio of 80:20 and high-purity niobium (Nb). The deposition was carried out in a vertical-type vacuum chamber equipped with a reactive gas flow control system and automatic switching of the arc between the cathodes. Before coating deposition, AISI 304 steel substrates underwent standard preparation: ultrasonic cleaning in an organic solvent, followed by Ar^+ ion etching at a high negative bias to remove oxide films and improve adhesion of the initial layer.

The coatings were formed as a multilayer structure by alternating evaporation of the Ti–Mo and Nb cathodes. The arc current was 110 A for the TiMo cathode and 90 A for the Nb cathode. High-purity nitrogen was used as the working reactive gas, and the pressure in the chamber during deposition was varied between two regimes: 0.52 Pa and 0.13 Pa, which made it possible to obtain two types of samples: 1-TiMoN/NbN and 2-TiMoN/NbN, respectively. The substrate bias voltage during deposition was –200 V, which ensured increased kinetic energy of ions and the formation of a dense structure of the nitride layers. The process duration was 90 min, resulting in a total coating thickness of 10–11 μm.

The number of formed layers was approximately 270, which corresponds to a superlattice regime with a period of several tens of nanometers. The process parameters and synthesis conditions of the investigated coatings are presented in Table 1 for convenience of comparison.

Table 1. Deposition parameters of the multilayer TiMoN/NbN coatings

Coating definition	Arc current Ti–Mo/Nb, A	Substrate bias, V	Nitrogen pressure, Pa	Deposition time, min	Thickness, μm
1-TiMoN/NbN	110/90	–200	0.52	90	9.5
2-TiMoN/NbN			0.13		

2.2. Characterization

The surface and cross-sectional microstructure at multiple magnifications, as well as the morphology of the surfaces after scratch testing, were characterized using a field-emission scanning electron microscope, FEI Nova NanoSEM 450. The acquired images were used to assess the surface morphology, the distribution of macroparticles, the growth characteristics, the multilayer architecture, and to determine the thickness and uniformity of the individual nanolayers.

Scratch adhesion tests were conducted using a Bruker UMT-2 tribometer under progressive loading. During the test, the normal load was gradually increased from 0.2 N to 46 N along a scratch length of approximately 5 mm over 50 s. This progressive loading mode allowed the identification of the critical loads corresponding to the onset of coating failure. The first critical load (Lc_1) was associated with the appearance of buckling cracks, while the second critical load (Lc_2) corresponded to buckling spallation, indicating local coating delamination.

After the scratch tests, the morphology of the scratch tracks was examined using a field-emission scanning electron microscope (Quanta 600 FEG) to analyze the failure mechanisms and damage evolution within the coating. To further investigate the compositional changes along the scratch tracks, energy-dispersive X-ray spectroscopy (Oxford Instruments high-performance SDD (Silicon Drift Detector)) analysis was performed at several characteristic locations.

3. EXPERIMENTAL RESULTS

3.1. Surface and cross-sectional structure

SEM analysis of the surface of multilayer TiMoN/NbN coatings presented in Figure 1 shows a morphology characteristic of coatings obtained by the cathodic arc deposition method. For both samples, the surface consists of a compact and continuous coating matrix, on which a significant number of spherical microparticles (macroparticles or droplets) are observed. Such particles are formed as a result of the emission of molten fragments of the cathode material during cathodic arc evaporation and are a typical feature of this deposition method.

The surface of the multilayer 1-TiMoN/NbN coating, deposited at a nitrogen pressure of 0.52 Pa, is characterized by a relatively smooth morphology with a moderate amount of the droplet phase. In the SEM image, spherical macroparticles of different sizes are observed, unevenly distributed over the coating surface. Most particles have a diameter in the range of approximately 1–5 μm, which is typical for cathodic arc coatings.

The surface of the multilayer 2-TiMoN/NbN coating, deposited at a lower nitrogen pressure of 0.13 Pa, demonstrates a significantly different morphology. The SEM image shows a much higher density of the droplet phase, and the macroparticles exhibit a wide size distribution, ranging from submicron to several micrometers. The coating surface appears more “saturated” with macroparticles, which are located closer to each other and form a more heterogeneous

surface topography. In addition to large particles, a considerable number of smaller particles are also observed, which may be the result of macroparticle fragmentation or secondary deposition of material.

The revealed difference in the morphology of the coatings is related to the influence of the working gas pressure on the transport and energy of plasma particles during cathodic arc deposition. At a lower nitrogen pressure (0.13 Pa), the mean free path of particles in the plasma increases, leading to more rectilinear transport of macroparticles from the cathode to the substrate. Under such conditions, macroparticles have a lower probability of collisions with gas molecules and, accordingly, are less decelerated in the plasma. This promotes their more efficient transfer to the substrate surface and, consequently, increases the amount of the droplet phase on the coating surface.

Conversely, at higher nitrogen pressure (0.52 Pa), the number of collisions between macroparticles and gas molecules increases. Such collisions may lead to partial deceleration or even deviation of macroparticle trajectories in the plasma, thereby reducing the probability of their deposition on the substrate surface. As a result, the coating surface becomes smoother and contains less of the droplet phase.

Such changes in morphology may significantly influence the service properties of the coating. Macroparticles may act as stress concentrators during mechanical loading and affect the tribological behavior of the coating. At the same time, the presence of the droplet phase may also influence the processes of crack initiation during scratch testing.

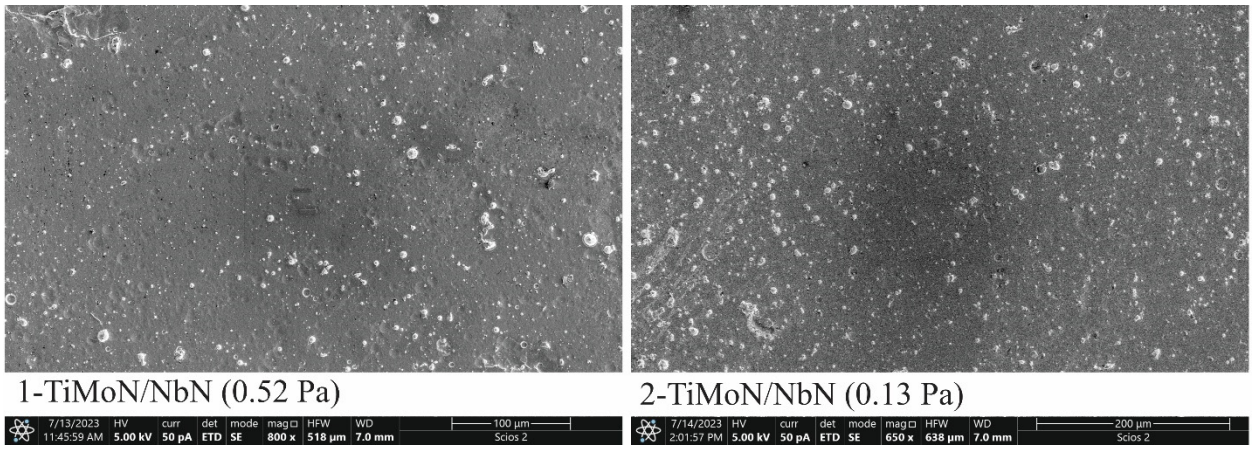

Figure 1. SEM images showing the surface morphology of the multilayer TiMoN/NbN coatings deposited at different nitrogen pressures

The cross-sectional SEM images presented in Figure 2 reveal that both investigated coatings exhibit a well-defined multilayer architecture characteristic of nanolayered nitride systems deposited by cathodic arc PVD. The coatings clearly consist of alternating light and dark layers corresponding to TiMoN and NbN constituents, respectively. Such contrast is typical due to differences in atomic number and electron scattering between the two phases. Apparently, the lighter layers correspond to the TiMoN phase, while the darker layers represent NbN. The multilayer sequence is continuous throughout the entire coating thickness, demonstrating a stable deposition process during cathodic arc evaporation. The interfaces between adjacent layers are well defined and nearly planar, indicating a relatively stable growth regime during deposition without significant interface roughening or intermixing. Moreover, both coatings exhibit a compact morphology with no visible pores, voids, or macroparticle inclusions in the cross-section, indicating a dense microstructure typical of energetic PVD deposition conditions. Measurements performed directly from the cross-sectional SEM images show that the overall coating thickness is approximately 9.5 µm for both coatings. Based on the periodic repetition of the alternating layers, the modulation period of the multilayer structure was estimated to be approximately 85 nm. This value corresponds to the combined thickness of one TiMoN layer and one NbN layer. Such nanoscale modulation is typical for multilayer nitride coatings designed to exploit superlattice-type strengthening effects.

The cross-section of the multilayer 1-TiMoN/NbN coating, deposited at a nitrogen pressure of 0.52 Pa, shows that the periodicity of the alternating layers is relatively uniform throughout the coating thickness. However, it is evident that the NbN layers are noticeably thicker than the TiMoN layers. This asymmetry in the thickness of the constituent layers apparently indicates that the effective deposition rate of NbN during the multilayer growth was higher than that of TiMoN. In cathodic arc deposition processes, the layer thickness in a multilayer coating is primarily determined by the deposition rate of each cathode material. Therefore, the thicker NbN layers observed in this coating most likely reflect either a higher plasma flux from the Nb cathode. Moreover, the interfaces between layers remain relatively smooth and continuous, which suggests that the growth process proceeded under stable plasma conditions. The multilayer architecture is preserved throughout the entire coating thickness, with no evidence of structural disruption, indicating high stability of the deposition process under a nitrogen pressure of 0.52 Pa.

The cross-section of the multilayer 2-TiMoN/NbN coating, deposited at a lower nitrogen pressure of 0.13 Pa, also exhibits a clearly defined multilayer architecture. The layer interfaces remain sharp and continuous, indicating that the reduction of nitrogen pressure did not disrupt the formation of the multilayer structure. However, in contrast to the coating deposited at 0.52 Pa, the relative thicknesses of the constituent layers appear more balanced in this sample. The NbN and TiMoN layers appear to be closer in thickness than the multilayer 1-TiMoN/NbN coating, although the NbN layers are still

slightly thicker. Apparently, the decrease in nitrogen pressure may influence the effective deposition kinetics of the different metal species in the plasma. Under lower nitrogen pressure conditions, the mean free path of plasma species increases, which can modify the arrival rate of metal ions at the growing surface. Such changes may affect the growth rates of the individual layers and, therefore, the relative thicknesses of the TiMoN and NbN layers within the multilayer sequence. Despite these differences, the multilayer architecture remains well preserved, and the coating retains a dense structure throughout the thickness. Evidently, the energetic conditions of cathodic arc deposition promote strong atomic mobility at the growing surface, allowing the formation of well-defined nanolayers even when the nitrogen pressure is reduced.

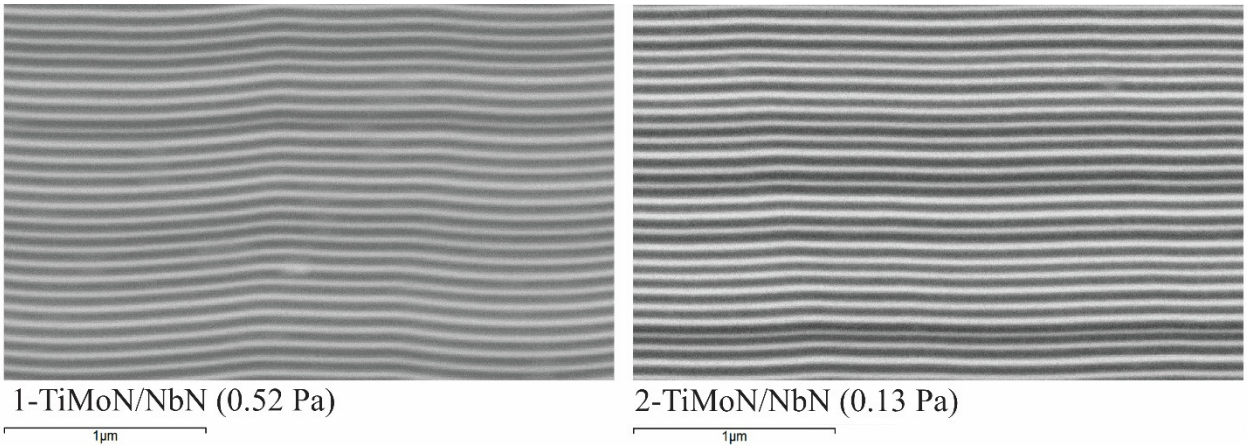

Figure 2. Cross-sectional SEM images of the multilayer TiMoN/NbN coatings deposited at different nitrogen pressures

This observation suggests that the nitrogen pressure influences the growth kinetics of the multilayer TiMoN/NbN system, possibly through changes in plasma density, ionization efficiency, and the effective deposition rates of the individual cathode materials. Such variations in layer thickness can affect the mechanical behaviour of multilayer coatings, as the modulation period and layer-thickness ratio are known to influence dislocation blocking and crack propagation mechanisms in nanolayered nitride coatings.

3.2. Scratch test damage morphology and compositional evolution

Scratch testing is one of the most informative methods for assessing the adhesion strength of hard coatings, as it allows investigation of the mechanisms of their failure under gradually increasing loads. The morphology of the scratch tracks obtained during progressive-load scratch testing provides important insights into the adhesion behaviour and failure mechanisms of the multilayer TiMoN/NbN coatings. SEM observations of the damaged surfaces, presented in Figure 3, reveal distinct deformation and fracture features associated with the critical loads Lc_1 (buckling cracks) and Lc_2 (buckling spallation) identified during the test. The coatings were tested under progressive loading conditions, which allowed gradual development of failure processes within the coating–substrate system.

The scratch track formed on the multilayer 1-TiMoN/NbN coating, deposited at a nitrogen pressure of 0.52 Pa, exhibits a relatively well-defined damage morphology. At the initial region of the track, the coating remains largely intact, while with increasing load, the first signs of coating instability become visible in the form of lateral cracks located near the edges of the groove. Apparently, the first critical failure event corresponds to buckling cracks occurring at $Lc_1 \approx 4.72$ N. These cracks appear primarily along the edges of the scratch track, where tensile stresses develop during coating bending as the substrate plastically deforms beneath the indenter. Evidently, the cracks propagate parallel to the sliding direction, which is characteristic of compressively stressed PVD coatings undergoing local buckling instability. With further increase of the load, larger damaged regions become visible. The central region of the track shows a relatively compact wear scar, while partial coating detachment is observed along the edges of the groove. This behaviour corresponds to the second critical load, $Lc_2 \approx 12.38$ N, associated with buckling spallation. In this stage, the previously formed buckled segments lose adhesion to the substrate and detach locally, forming flake-like fragments adjacent to the scratch groove. Moreover, the damage morphology indicates that the coating failure progresses gradually rather than catastrophically. The coating still remains partially attached to the substrate within the track, suggesting a relatively high adhesion strength of the multilayer structure.

The scratch track observed on the multilayer 2-TiMoN/NbN coating, deposited at a lower nitrogen pressure of 0.13 Pa, shows a somewhat different morphology. The groove appears slightly smoother and more continuous along the sliding direction, while the surrounding regions exhibit a more pronounced accumulation of plastically deformed coating material. Apparently, the first cracking event occurs at a slightly higher load, $Lc_1 \approx 5.41$ N, indicating somewhat improved resistance to the onset of buckling compared with the coating deposited at the higher nitrogen pressure. The cracks again originate at the edges of the scratch track, where tensile stresses develop due to substrate deformation. However, the damage pattern differs from that observed in the first coating. In this sample, the coating fragments tend to form periodic arcuate features along the groove edges. These structures resemble successive buckling segments that have partially detached and folded during sliding. Such morphology is typical for multilayer coatings undergoing progressive buckling-

induced delamination. The second critical event, $Lc_2 \approx 12.54$ N, corresponding to buckling spallation, occurs at a load very similar to that observed for the first coating. At this stage, segments of the coating detach from the substrate and accumulate near the edges of the scratch track.

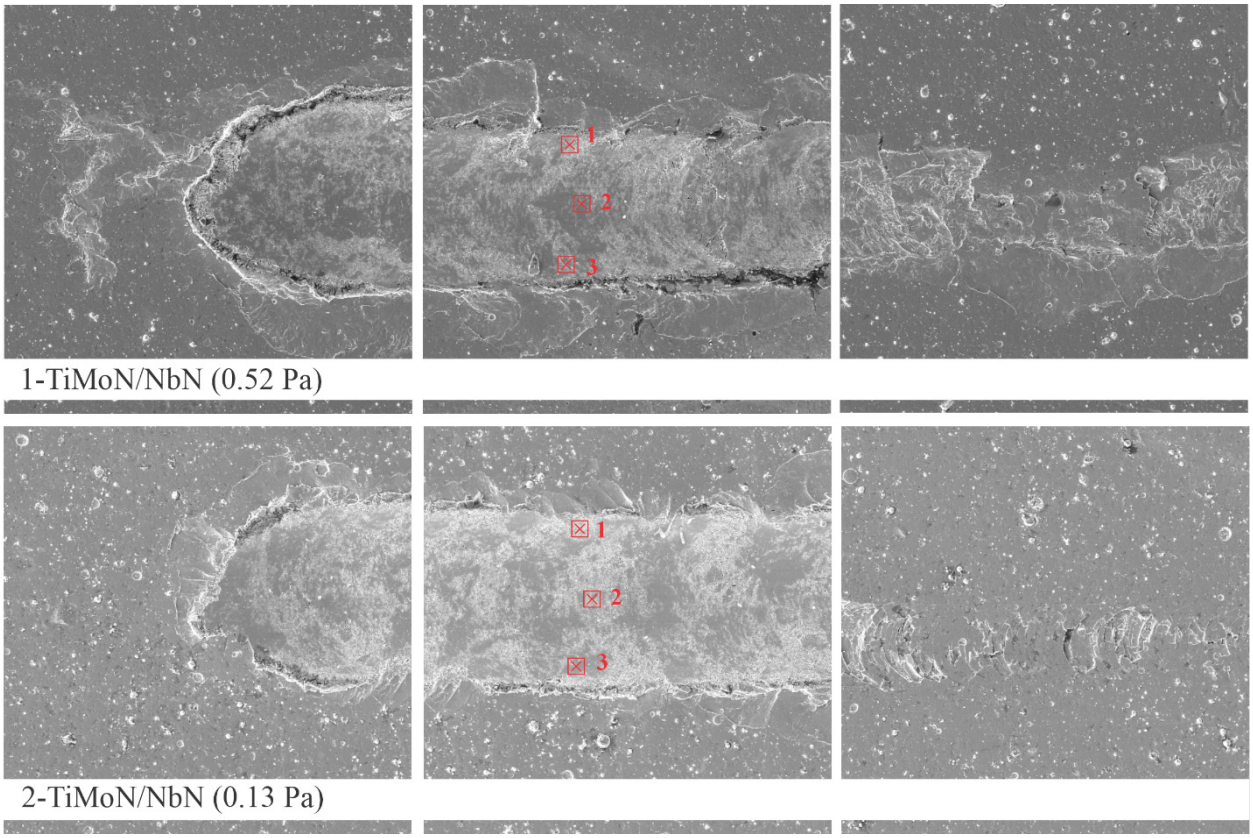

Figure 3. SEM images of the scratch tracks formed during progressive load scratch testing of the multilayer TiMoN/NbN coatings deposited at different nitrogen pressures. The locations of EDS analysis (Spectrum 1–3) are indicated

To evaluate the compositional changes within the scratch track, EDS measurements were carried out at three characteristic locations, namely at the upper edge of the groove (Spectrum 1), in the center of the groove (Spectrum 2), and at the lower edge of the groove (Spectrum 3), with the obtained elemental compositions presented in Table 2.

Table 2. Elemental composition of the scratch track regions obtained by EDS analysis for the multilayer TiMoN/NbN coatings deposited at different nitrogen pressures

Coating 1-TiMoN/NbN	Atomic %						
	O	Al	Ti	Cr	Fe	Nb	Mo
Spectrum 1	6.46	0.30	22.26	7.04	23.66	34.76	5.53
Spectrum 2	2.27	0.72	3.19	14.67	73.65	4.71	0.66
Spectrum 3	20.57	1.11	36.24	1.32	4.89	31.55	4.28
Mean	9.76	0.71	20.56	7.68	34.07	23.67	3.49
Coating 2-TiMoN/NbN	Atomic %						
	O	Al	Ti	Cr	Fe	Nb	Mo
Spectrum 1	16.58	0.50	45.81	0.68	1.56	23.10	11.78
Spectrum 2	19.04	0.84	44.82	0.79	3.27	26.53	4.71
Spectrum 3	12.14	0.56	39.99	2.78	11.63	28.53	4.36
Mean	15.55	0.67	34.17	4.22	19.84	20.73	4.79

The EDS results reveal significant compositional variations across the scratch track. At the upper edge of the track (Spectrum 1), the multilayer 1-TiMoN/NbN coating composition is dominated by Nb (34.76 at.%) together with Ti (22.26 at.%) and Fe (23.66 at.%). The presence of Fe clearly indicates that the substrate material is partially exposed or mixed with the coating debris during scratching. In the center of the groove (Spectrum 2), the composition is strongly dominated by Fe (73.65 at.%). This evidently indicates that the coating has been largely removed in this region, and the steel substrate is exposed. Only small amounts of Ti, Nb, and Mo remain, which likely originate from residual coating fragments or wear debris. At the lower edge of the track (Spectrum 3), the Nb and Ti contents increase again (31.55 and 36.24 at.% respectively), while the Fe concentration drops significantly. This observation suggests that coating fragments accumulate at the edges of the scratch track during the spallation process.

A somewhat different compositional trend is observed for the multilayer coating deposited at lower nitrogen pressure. At the upper edge of the groove (Spectrum 1), the Ti concentration is particularly high (≈ 45.81 at.%), accompanied by Nb (23.10 at.%) and Mo (11.78 at.%). The Fe content is very low (≈1.56 at.%), indicating that the coating remains largely intact in this region. In the center of the scratch track (Spectrum 2), Ti remains the dominant element (~44.82 at.%), while Nb and Mo are also present. Only a small amount of Fe (3.27 at.%) is detected, suggesting that the substrate exposure is significantly lower than in the coating deposited at 0.52 Pa. At the lower edge of the track (Spectrum 3), the Fe content increases to about 11.63 at.%, while Ti and Nb remain substantial. This indicates partial removal of the coating, accompanied by mixing of coating fragments with substrate material.

The comparison of the EDS results clearly indicates that the multilayer 1-TiMoN/NbN coating, deposited at a nitrogen pressure of 0.52 Pa, experiences more extensive exposure of the substrate within the center of the scratch track, as evidenced by the very high Fe concentration (≈73 at.%). In contrast, the multilayer 2-TiMoN/NbN coating, deposited at a lower nitrogen pressure of 0.13 Pa, retains a much higher fraction of the coating material within the track because the Fe concentration remains relatively low. Apparently, this suggests that the coating deposited at lower nitrogen pressure exhibits slightly improved resistance to complete coating removal during scratching.

The SEM observations combined with the EDS compositional analysis suggest that different failure modes dominate in the multilayer TiMoN/NbN coatings. In the 1-TiMoN/NbN coating, the very high Fe concentration detected at the center of the scratch track (≈73 at.% Fe) evidently indicates complete removal of the coating, exposing the steel substrate. Such damage morphology suggests that the failure is largely adhesive, occurring at the coating–substrate interface and resulting in local coating delamination.

In contrast, the multilayer 2-TiMoN/NbN coating exhibits a markedly lower Fe concentration within the scratch track, while Ti, Nb, and Mo remain the dominant elements. Apparently, this indicates that a significant portion of the coating remains inside the groove. The observed fragmentation and plastic deformation of the coating without full substrate exposure suggests that the failure mode is predominantly cohesive, occurring within the multilayer structure rather than at the coating–substrate interface.

4. DISCUSSIONS

The described results demonstrate that by varying the working gas pressure during CAE-PVD deposition, it is possible to deliberately control the adhesion behaviour of multilayer TiMoN/NbN coatings. The difference in the onset of buckling cracks between the two coatings may be related to the influence of nitrogen pressure on the microstructure formed during deposition. The pressure of the working gas during coating deposition can significantly affect the mechanisms of buckling-related failure. Lower nitrogen pressure generally leads to higher kinetic energy of the depositing species, since the mean free path of plasma particles increases and fewer collisions occur in the plasma.

Under such conditions, the arriving metal ions possess higher energy, which promotes enhanced ion bombardment of the growing surface and leads to the formation of a denser coating microstructure with improved adhesion to the substrate. As a consequence, the initiation of buckling cracks may occur at higher applied loads, while buckling spallation is observed only after significant accumulation of deformation within the coating–substrate system.

Apparently, the multilayer coating deposited at a lower nitrogen pressure of 0.13 Pa exhibits slightly improved resistance to crack initiation, as reflected by the higher Lc_1 value (5.41 N) than that of the multilayer coating deposited at a higher nitrogen pressure of 0.52 Pa (4.72 N). Conversely, when the nitrogen pressure is higher, the energy of depositing species may decrease due to more frequent collisions in the plasma, which can result in the formation of a comparatively less dense coating structure. Under such conditions, interfacial stresses may accumulate more rapidly, leading to the earlier onset of coating detachment during scratch loading.

However, the second critical load corresponding to buckling spallation remains very similar for both coatings ($Lc_2 \approx 12.4$–12.5 N), indicating that the ultimate adhesion strength of the coatings is comparable despite the differences in the initial crack initiation behaviour.

CONCLUSIONS

Multilayer TiMoN/NbN coatings with a nanolayered architecture were successfully deposited by cathodic arc PVD at nitrogen pressures of 0.52 Pa and 0.13 Pa. Both coatings exhibit a dense multilayer structure consisting of alternating TiMoN and NbN layers with a modulation period of approximately 85 nm and an overall thickness of about 9.5 μm.

Surface SEM observations revealed a typical cathodic arc morphology characterized by the presence of macroparticles. A decrease in nitrogen pressure leads to an increased density of macroparticles due to the longer mean free path of plasma species during deposition.

Scratch testing under progressive loading conditions identified two characteristic failure events corresponding to buckling crack initiation (Lc_1) and buckling spallation (Lc_2). The multilayer coating deposited at a lower nitrogen pressure of 0.13 Pa shows slightly higher resistance to crack initiation ($Lc_1 \approx 5.41$ N) compared with the multilayer coating deposited at 0.52 Pa ($Lc_1 \approx 4.72$ N).

SEM and EDS analyses of the scratch tracks revealed distinct failure modes in the investigated coatings. The coating deposited at 0.52 Pa exhibits predominantly adhesive failure associated with exposure of the steel substrate, whereas the coating deposited at 0.13 Pa demonstrates mainly cohesive failure within the multilayer structure.

The obtained results indicate that nitrogen pressure during cathodic arc deposition plays an important role in controlling the microstructure evolution and adhesion behaviour of TiMoN/NbN multilayer coatings.

Acknowledgments
This work was supported by the Ministry of Education and Science of Ukraine (MES) under the National Budget Program (Project 0124U001127).

ORCID
Olga Maksakova, https://orcid.org/0000-0002-0646-6704; **Vyacheslav Beresnev**, https://orcid.org/0000-0002-4623-3243
Serhiy Lytovchenko, https://orcid.org/0000-0002-3292-5468; **Martin Sahul,** https://orcid.org/0000-0001-9472-500X
Mária Čaplovičová, https://orcid.org/0000-0003-4767-8823; **Ruslan Galushkov**, https://orcid.org/0000-0002-9105-9774

REFERENCES

[1] J. Xu, *et al*., "Tribological Properties of MoN/TiN Multilayer Coatings Prepared via High-Power Impulse Magnetron Sputtering," Lubricants, **13**(8), 319 (2025). https://doi.org/10.3390/lubricants13080319
[2] T. Borowski, *et al*., "Influence of Magnetron Sputtering-Deposited Niobium Nitride Coating and Its Thermal Oxidation on the Properties of AISI 316L Steel in Terms of Its Medical Applications," Materials, **16**, 6890 (2023). https://doi.org/10.3390/ma16216890
[3] J. Chen, *et al*., "Excellent Anti-Corrosion and Conductivity of NbN Coated on Ti Bipolar Plate by Controlling N_2 Flow Rates," Journal of Alloys and Compounds, **976**, 173033 (2024). https://doi.org/10.1016/j.jallcom.2023.173033
[4] J.M. Gonzalez-Carmona, *et al*., "TiNbN Hard Coating Deposited at Varied Substrate Temperature by Cathodic Arc: Tribological Performance under Simulated Cutting Conditions," Materials, **16**, 4531 (2023). https://doi.org/10.3390/ma16134531
[5] T. Borowski, *et al*., "Properties of Oxidised NbN Coating Produced by Magnetron Sputtering on AISI 316L Steel in View of Its Biomedical Applications," SSRN preprint, (2023). https://doi.org/10.2139/ssrn.4391424
[6] J. Van Meter, *et al*., "Wear and Adhesion of PEALD Titanium Molybdenum Nitrides (TiMoN) Films," Wear, **570**, 205980 (2025). https://doi.org/10.1016/j.wear.2025.205980
[7] J.M. González-Carmona, *et al*., "Wear mechanisms identification using Kelvin probe force microscopy in TiN, ZrN, and TiN/ZrN hard ceramic multilayer coatings," Ceramics International, **46**(15), 24592–24604 (2020). https://doi.org/10.1016/j.ceramint.2020.06.248
[8] K. Smyrnova, *et al*., "Microstructure, Mechanical and Tribological Properties of Advanced Layered WN/MeN (Me = Zr, Cr, Mo, Nb) Nanocomposite Coatings," Nanomaterials, **12**(3), 395 (2022). https://doi.org/10.3390/nano12030395
[9] A.A. Sugumaran, *et al*., "TiN/NbN Nanoscale Multilayer Coatings Deposited by High Power Impulse Magnetron Sputtering to Protect Medical-Grade CoCrMo Alloys," Coatings, **11**(7), 867 (2021). https://doi.org/10.3390/coatings11070867
[10] P.E. Hovsepian, *et al*., "Microstructure and load-bearing capacity of TiN/NbN superlattice coatings deposited on medical-grade CoCrMo alloy by HIPIMS," Journal of the Mechanical Behavior of Biomedical Materials, **132**, 105267 (2022). https://doi.org/10.1016/j.jmbbm.2022.105267
[11] Y. Liu. *et al*., "Multilayer Coatings for Tribology: A Mini Review," Nanomaterials, **12**(9), 1388 (2022). https://doi.org/10.3390/nano12091388
[12] O. Maksakova, *et al*., "A Comparative Study of Microstructure and Properties of TiZrN/NbN and TiSiN/NbN Nanolaminate Coatings," in: *Nanocomposite and Nanocrystalline Materials and Coatings. Advanced Structured Materials*, edited by A.D. Pogrebnjak, Y. Bing, and M. Sahul, vol 214. (Springer, Singapore, 2024). https://doi.org/10.1007/978-981-97-2667-7_6
[13] S.-M. Yang, *et al*., "Microstructure Characterization of Multilayered TiSiN/CrN Thin Films," Journal of Nanoscience and Nanotechnology, **8**(5), 2688–2692 (2008). https://doi.org/10.1166/jnn.2008.592
[14] Y. Liu, *et. al*., "Multilayer Coatings for Tribology: A Mini Review," Nanomaterials, **12**, 1388 (2022). https://doi.org/10.3390/nano12091388

ВПЛИВ ТИСКУ АЗОТУ НА АДГЕЗІЮ ТА МЕХАНІЗМИ РУЙНУВАННЯ ПРИ СКРЕТЧ-ТЕСТУВАННІ БАГАТОШАРОВИХ ПОКРИТТІВ TiMoN/NbN, ОСАДЖЕНИХ МЕТОДОМ КАТОДНО-ДУГОВОГО PVD

О.В. Максакова[1], В.М. Береснєв[1], С.В. Литовченко[1], М. Сахул[2], М. Чапловичова[3], Р.С. Галушков[1]
[1]Харківський національний університет імені В.Н. Каразіна, майд. Свободи, 4, 61000 Харків, Україна
[2]Інститут матеріалознавства, Словацький технологічний університет у Братиславі, вул. Яна Ботту, 25, 917 24, Трнава, Словаччина
[3]Центр нанодіагностики матеріалів, Словацький технологічний університет у Братиславі, вул. Вазовова. 5, 812 43, Братислава, Словаччина

Багатошарові нітридні покриття широко використовуються для покращення механічних властивостей і довговічності інженерних компонентів, що працюють в умовах інтенсивного трибологічного навантаження. У цій роботі досліджено адгезійну поведінку та механізми руйнування наношарових багатошарових покриттів TiMoN/NbN, осаджених методом катодно-дугового PVD, залежно від робочого тиску азоту. Два покриття були синтезовані при тисках азоту 0,52 Па та 0,13 Па за інших однакових умов осадження. Мікроскопічний аналіз показав, що обидва покриття мають добре виражену наношарову архітектуру, що складається з чергування шарів TiMoN та NbN з періодом модуляції приблизно 85 нм і загальною товщиною близько 9,5 мкм. Зменшення тиску азоту призводить до більшої густини макрочасток через більшу довжину вільного пробігу плазмових частинок катодно-дугового розряду. Скретч-тести адгезії, виконані в умовах поступового збільшення навантаження, дозволили ідентифікувати дві характерні події руйнування, що відповідають зародженню тріщин та відшаруванню, що спричинені втрачанням стійкості. Багатошарове покриття, осаджене при 0,13 Па, продемонструвало дещо кращу стійкість до зародження тріщин (5,41 Н) порівняно з багатошаровим покриттям, осадженим при 0,52 Па (4,72 Н). Однак обидва покриття демонстрували подібні значення другого критичного навантаження (12,4–12,5 Н). Багатошарове покриття, осаджене при вищому тиску азоту, переважно зазнає адгезійного руйнування з інтенсивним оголенням підкладки, тоді як багатошарове покриття, осаджене при нижчому тиску азоту, демонструє переважно когезійні пошкодження всередині багатошарової структури. Отримані результати демонструють, що тиск азоту під час катодно-дугового осадження суттєво впливає на еволюцію мікроструктури та механізми адгезійного руйнування в багатошарових покриттях TiMoN/NbN. Дослідження надає уявлення щодо оптимізації параметрів осадження для покращення механічної надійності багатошарових нітридних покриттів.

Ключові слова: *вакуумно-дугова технологія; нітриди; багатошарові покриття; TiMoN; мікроструктура; склад; адгезія*

EAST EUROPEAN JOURNAL OF PHYSICS. 1. 548-557 (2026)
DOI:10.26565/2312-4334-2026-1-63 ISSN 2312-4334

COMPREHENSIVE ANALYSIS OF BIANCHI TYPE V MODEL IN $f(R, L_m)$ THEORY OF GRAVITY

P.R. Agrawal, H.G. Paralikar, A.P. Nile
Department of Mathematics, Brijlal Biyani Science College, Amravati, 444602, India
Corresponding Authors e-mail: prachi.gadodia@gmail.com, hparalikar05@gmail.com, ankushnile15@gmail.com
Received December 8, 2025; revised February 3, 2026; accepted February 27, 2026

In this article, a homogenous Bianchi Type V cosmological model has been investigated within the framework of $f(R,L_m)$ gravity. The solution of the field equations has been obtained by considering the special case $f(R,L_m)=R/2+L_m^n$, where n is free model parameter. The physical as well as the dynamical properties of the model have been analyzed, and graphical representations are provided to illustrate the properties of these parameters.
Keywords: *Biachi Type – V; Stability analysis; f(R, Lm) gravity, Perfect Fluid*
PACS: 04.50.Kd, 98.80.-k, 98.80.Jk

1. INTRODUCTION

Harko *et al.* (2010) introduced an advanced form of matter curvature coupling theory, known as $f(R,L_m)$ gravity, where f is a variable function that depends on the matter Lagrangian L_m and the Ricci scalar R. This theory represents a comprehensive extension of gravitational models in Riemannian space, where the trajectory of the test particle deviates from the standard geodesic path, resulting in an additional force that acts perpendicular to its four velocity vector. Functional expressions for $f(R)$ gravity incorporate logarithmic, exponential and power law models. An extension of this framework is known as $f(R,L_m)$ gravity which has recently emerged as $f(R,L_m)=f_1(R)+f_2(R)G(L_m)$, where f_1, f_2 and G are arbitrary functions of the Ricci scalar and the matter Lagrangian density respectively.

The Kasner-type static, cylindrically symmetric interior solutions were studied in the $f(R,L_m)$ theory of gravity by Harko *et al.* (2015), with explicit derivation of the thermodynamic parameters of the string. In the article, "Cosmology in $f(R,L_m)$ Gravity" Jaybhaye *et. al.* (2022a) analysed the model using the Pantheon ranges for the model and explored the variation in cosmological parameters based on the constraints set by these datasets. Additionally, the stability of the resulting model was also investigated.

Jaybhaye *et al.* (2022b) discussed about the constraints on energy conditions by employing cosmographic parameters like mean Hubble parameter, deceleration parameter, jerk parameter and snap parameter whereas Solanki *et al.* (2023) studied $f(R,L_m)$ gravity by considering non-linear models. They obtained the Wormhole solutions by assuming three different cases viz. linear barotropic, anisotropic and isotropic equation of state (EoS).

Singh *et al.* (2023) studied a constrained cosmological model in $f(R,L_m)$ gravity. Shukla *et al.* (2023) used equation of state parameter and Garg *et al.* (2023) used a linear equation of state parameter to study the expansion of the universe. Lobato *et al.* (2021) investigated Neutron stars with realistic equation of state, Patil *et al.* (2023) analyzed FLRW cosmology with Hybrid scale factor, Pawde *et al.* (2023) studied anisotropic behavior of universe with varying deceleration parameter and Jaybhaye *et al.* (2024) derived bouncing cosmological models in $f(R,L_m)$ gravity.

Avelino *et.al.* (2018) demonstrated that if the fluid is constituted by localized concentrations of energy with fixed rest mass and structure (solitons) then the average on-shell Lagrangian of a perfect fluid is given by $L_m=T$, where T is the trace of the energy-momentum tensor. The results give profound implications for theories of gravity where the matter Lagrangian appears explicitly in the equations of motion of the gravitational and matter fields, potentially leading to observable deviations from a nearly perfect cosmic microwave background black body spectrum. Sharif *et. al.* (2019) investigated the dynamics of perfect fluid spherical collapse in curvature-matter coupled $f(G,T)$ gravity.

To obtain the solution, Carvalho *et al.* (2021) used the Zel'dovich approximation and also explored the propagation of light in $f(R)$ cosmic string. Also, they compared the results with wakes formed by cosmic string solutions obtained in General Relativity and Scalar Tensor Theories of Gravity. da Silva *et al.* (2021) studied cosmic string in modified theories of gravitation. Also, several authors studied $f(R)$ theory of gravity in different content [Adhav *et al.* 2012; Hatkar *et al.* 2018; Agrawal and Nile 2024; Malik 2024]. Bishi *et al.* (2015) studied Bianchi type V

Cite as: P.R. Agrawal, H.G. Paralikar, A.P. Nile, East Eur. J. Phys. 1, 548 (2026), https://doi.org/10.26565/2312-4334-2026-1-63

string cosmological model with bulk viscosity in $f(R,T)$ Gravity by considering a special form and linearly varying parameter.

In line with the above discussion, we investigate, Bianchi type-V cosmological model in the context of $f(R,L_m)$ theory of gravity. The paper is structured as follows: Section 2, gives the basic theoretical approach of $f(R,L_m)$ gravity. Section 3 presents the metric and the solution of field equation for Bianchi type-V model. In section 4, the cosmological models of $f(R,L_m)$ gravity are derived whereas section 5 examines the stability of the derived models. The last section, provides discussions and concluding remarks.

2. $f(R,L_m)$ THEORY OF GRAVITY

The action for the $f(R,L_m)$ gravity given by Harko *et al.* (2010) is as

$$S=\int f(R,L_m)\sqrt{-g}d^4x\,, \tag{1}$$

where, $f(R,L_m)$ represents an arbitrary function of the Ricci scalar R and the matter Lagrangian term L_m.
The field equation can be acquired by varying action (1) for the metric tensor g_{uv},

$$f_R R_{\mu\nu}+(g^{\mu\nu}-\nabla_\mu\nabla_\nu)f_R-\frac{1}{2}(f-f_{L_m}L_m)g_{\mu\nu}=\frac{1}{2}f_{L_m}T_{\mu\nu}\,, \tag{2}$$

here $f_R\equiv\frac{\partial f}{\partial R}$, $f_{L_m}\equiv\frac{\partial f}{\partial L_m}$ and $T_{\mu\nu}$ represents the energy-momentum tensor for the perfect fluid, defined by

$$T_{\mu\nu}=\frac{-2}{\sqrt{-g}}\frac{\delta(\sqrt{-g}L_m)}{\delta g^{\mu\nu}}\,. \tag{3}$$

3. METRIC AND FIELD EQUATIONS IN $f(R,L_m)$ GRAVITY

The Bianchi type-V line element is given by

$$ds^2=dt^2-A^2dx^2-B^2e^{-2mx}dy^2-C^2e^{-2mx}dz^2\,, \tag{4}$$

here, A,B and C are functions of the cosmic time t.
The energy momentum tensor for perfect fluid is given by

$$T^\mu_\nu=(\rho+p)u_\mu u^\nu-pg^\mu_\nu\,, \tag{5}$$

where ρ is energy density, p is pressure and $u^\mu=(1,0,0,0)$ are components of four velocities of the cosmic time.
Since, we are studying the universe filled with the perfect fluid, which leads to (Chawla and Mishra 2013),

$$p=\gamma\rho\,, \tag{6}$$

where, the constant γ lies in $[0,1]$.
The dynamical parameters for the line element (4) are defined as follows.
The directional Hubble parameters are given by

$$H_x=\frac{\dot{a}_1}{a_1},\quad H_y=\frac{\dot{a}_2}{a_2},\quad H_z=\frac{\dot{a}_3}{a_3}\,. \tag{7}$$

The mean Hubble parameter H is given by

$$H=\frac{1}{3}\theta=\frac{1}{3}\frac{\dot{V}}{V}=\frac{1}{3}\left(H_x+H_y+H_z\right). \tag{8}$$

The deceleration parameter q is defined as

$$q=-1+\frac{d}{dt}\left(\frac{1}{H}\right). \tag{9}$$

The anisotropy parameter Δ of the expansion. shear scalar σ and the expansion parameter θ are respectively defined as,

$$\Delta = \frac{1}{3}\sum_{i=1}^{3}\left(\frac{H_i - H}{H}\right)^2 \tag{10}$$

$$\sigma^2 = \frac{1}{2}\left(\sum_{i=1}^{3} H_i^2 - \frac{1}{3}\theta^2\right) \tag{11}$$

$$\theta = 3H \tag{12}$$

4. COSMOLOGICAL MODEL OF $f(R, L_m)$:

Here, we consider the following form of $f(R, L_m)$ for our further investigation (Harko *et al.* 2014),

$$f(R, L_m) = \frac{R}{2} + L_m^n \tag{13}$$

where n is free model parameter.

For the particular $f(R, L_m)$ model given in equation (13), we take $L_m = \rho$ (Harko *et al.* 2014), the equation (2), (4) and (5) gives,

$$\frac{\ddot{B}}{B} + \frac{\ddot{C}}{C} + \frac{\dot{B}\dot{C}}{BC} - \frac{m^2}{A^2} = np\rho^{n-1} + (n-1)\rho^n - \Lambda \tag{14}$$

$$\frac{\ddot{A}}{A} + \frac{\ddot{C}}{C} + \frac{\dot{A}\dot{C}}{AC} - \frac{m^2}{A^2} = np\rho^{n-1} + (n-1)\rho^n - \Lambda \tag{15}$$

$$\frac{\ddot{A}}{A} + \frac{\ddot{B}}{B} + \frac{\dot{A}\dot{B}}{AB} - \frac{m^2}{A^2} = np\rho^{n-1} + (n-1)\rho^n - \Lambda \tag{16}$$

$$\frac{\dot{A}\dot{B}}{AB} + \frac{\dot{B}\dot{C}}{BC} + \frac{\dot{A}\dot{C}}{AC} - \frac{3m^2}{A^2} = -\rho^n - \Lambda \tag{17}$$

where the over dot represents the derivative with respect to cosmic time *t.*

Here, while studying, it is observed that the system of equations (14) - (17) contains four equations and six unknowns $A, B, C, p, \rho, \Lambda$. Hence, to solve them we need one more condition. Therefore, we consider relation between scale factor *A* and the spatial volume V as

$$A = V^{1/3} \tag{18}$$

Solving above field equations (14) to (17), using (18), we get

$$B = DV^{1/3} e^{\left[M\int \frac{dt}{V}\right]} \tag{19}$$

$$C = D^{-1}V^{1/3} e^{\left[-M\int \frac{dt}{V}\right]} \tag{20}$$

where D and M are constants of integration.

4.1 Model-I: Power Law

We consider power law given by as Sharif and Zubair (2012)

$$a = \alpha t^{\chi} \tag{21}$$

where, α and χ are the positive constant.

On using equations (21), the Hubble parameter, deceleration parameter, the spatial volume, the expansion parameter in terms of cosmic time *t* are obtained as

$$H = \frac{\chi}{t} \tag{22}$$

$$q = \frac{1}{\chi} - 1 \tag{23}$$

$$V = a^3 = (\alpha t^{\chi})^3 \tag{24}$$

$$\theta = 3H = \frac{3\chi}{t} \tag{25}$$

Using equations (14) to (21) the energy density obtained as

$$\rho = \frac{1}{n^{1/n}(\gamma+1)^{1/n}}\left[\frac{2\chi(\chi-1)-\chi^2}{t^2} + \frac{2M^2}{\alpha^6 t^{6\chi}} - \frac{M}{\alpha^2 t^{3\chi+1}} + \frac{\chi}{\alpha^3 t^{3\chi+1}} - \frac{2\chi}{t^{\chi-2}} + \frac{2m^2}{\alpha^2 t^{2\chi}}\right]^{1/n} \tag{26}$$

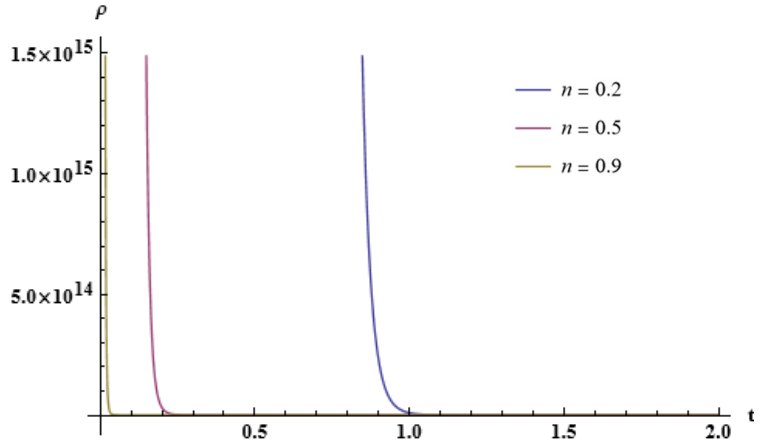

Figure 1. Energy density ρ verses cosmic time t is plotted by assuming $\chi = 1.1, M = 1, \alpha = 0.5, m = 1.5$

Using equations (6) and (26) the pressure is obtained as

$$p = \frac{\gamma}{n^{1/n}(\gamma+1)^{1/n}}\left[\frac{2\chi(\chi-1)-\chi^2}{t^2} + \frac{2M^2}{\alpha^6 t^{6\chi}} - \frac{M}{\alpha^2 t^{3\chi+1}} + \frac{\chi}{\alpha^3 t^{3\chi+1}} - \frac{2\chi}{t^{\chi-2}} + \frac{2m^2}{\alpha^2 t^{2\chi}}\right]^{1/n} \tag{27}$$

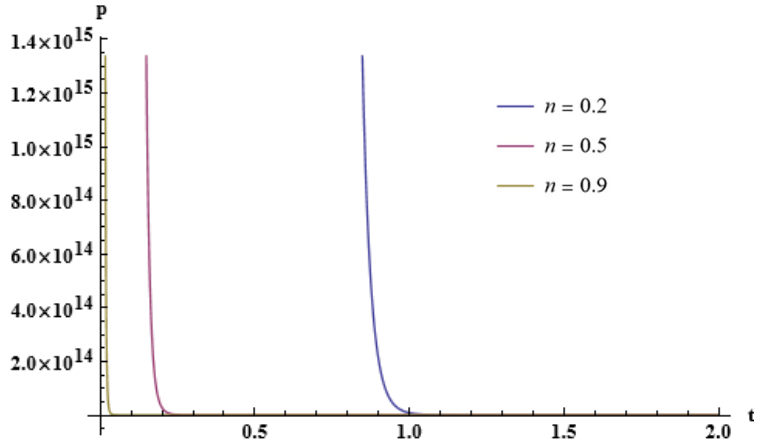

Figure 2. Pressure versus cosmic time t is plotted by assuming $\chi = 1.1, M = 1, \alpha = 0.5, m = 1.5$

Here, it is noted that the energy density depends on γ. Therefore, by selecting an appropriate numerical value for γ, three distinct types of universes can be identified as: the dust universe (γ = 0), the radiation-dominated universe (γ = 1/3), and the Zeldovich universe (γ = 1), as outlined below.

i) Dust Universe $(\gamma = 0)$:

For $\gamma = 0$, the model-I corresponds to the equation of state given in equation (6) which leads to $p = 0$. Hence the energy density for the dust universe is given by

$$\rho = \frac{1}{n^{1/n}}\left[\frac{2\chi(\chi-1)-\chi^2}{t^2} + \frac{2M^2}{\alpha^6 t^{6\chi}} - \frac{M}{\alpha^2 t^{3\chi+1}} + \frac{\chi}{\alpha^3 t^{3\chi+1}} - \frac{\alpha\chi}{t^{\chi-2}} + \frac{2m^2}{\alpha^2 t^{2\chi}}\right]^{1/n} \tag{28}$$

ii) Radiation-Dominated Universe ($\gamma = 1/3$)

For $\gamma = 1/3$, the model-I corresponds to the equation of state given in equation (6) which leads to $3p = \rho$. Hence the energy density for the Radiation Dominated Universe is given by

$$\rho = \frac{1}{\left(\frac{4}{3}n\right)^{1/n}}\left[\frac{2\chi(\chi-1)-\chi^2}{t^2}+\frac{2M^2}{\alpha^6 t^{6\chi}}-\frac{M}{\alpha^2 t^{3\chi+1}}+\frac{\chi}{\alpha^3 t^{3\chi+1}}-\frac{\alpha\chi}{t^{\chi-2}}+\frac{2m^2}{\alpha^2 t^{2\chi}}\right]^{1/n} \tag{29}$$

iii) Zeldovich Universe ($\gamma = 1$)

For $\gamma = 1$, the model-I corresponds to the equation of state given in equation (6) which leads to $p = \rho$. Hence the energy density for the Zeldovich universe is given by

$$\rho = \frac{1}{(2n)^{1/n}}\left[\frac{2\chi(\chi-1)-\chi^2}{t^2}+\frac{2M^2}{\alpha^6 t^{6\chi}}-\frac{M}{\alpha^2 t^{3\chi+1}}+\frac{\chi}{\alpha^3 t^{3\chi+1}}-\frac{2\chi}{t^{\chi-2}}+\frac{2m^2}{\alpha^2 t^{2\chi}}\right]^{1/n}, \tag{30}$$

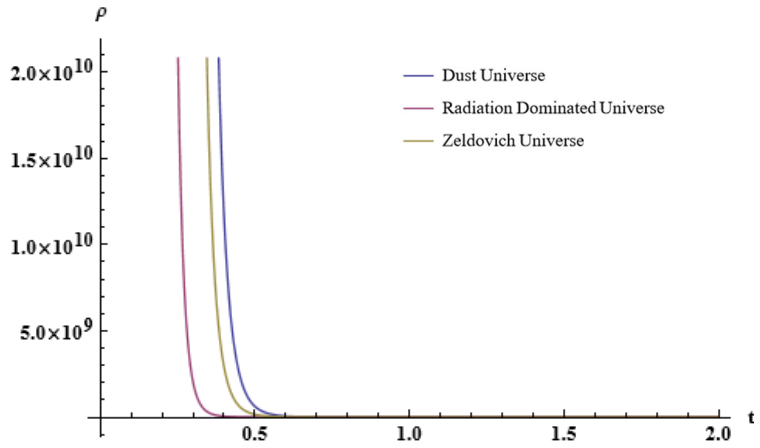

Figure 3. Energy density ρ for Dust Universe, Radiation Dominated Universe and Zeldovich Universe verses cosmic time t is plotted by assuming $\chi = 1.1, M = 1, \alpha = 0.5, n = 0.5, m = 1.5$

The Cosmological constant is obtained by using the equations (17) – (21) as

$$\Lambda = \frac{-3\gamma^2}{t^2}-\left(\left(n^{\frac{-1}{n}}(1+\gamma)^{\frac{-1}{n}}\right)\left[\frac{(-2+\chi)\chi}{t^2}+\frac{2\chi}{t^{\chi+2}}+\frac{2m^2t^{-2\chi}}{\alpha^2}+\frac{2M^2}{\alpha^6 t^{6\chi}}+\frac{\chi-\alpha M}{\alpha^3 t^{(1+3\chi)}}\right]^{\frac{1}{n}}\right)^n-\frac{4\gamma M}{\alpha t^{1+n}}+\frac{3m^2-M^2}{\alpha^2 t^{2\gamma}} \tag{31}$$

4.2. Model-II: Exponential Law

The exponential law is given by (reference)

$$a = e^{mt} \tag{32}$$

where m is the positive constant.

On using equations (8), (9), and equation (32), we obtained the Hubble parameter and the deceleration parameter in terms of cosmic time t as

$$H = m \tag{33}$$

$$q = -1,\ a = e^{mt} \tag{34}$$

The spatial volume, using equations (18) and (32) is obtained as

$$V = a^3 = e^{3mt} \tag{35}$$

By using equation (12), we obtain the expansion parameter as

$$\theta = 3m \tag{36}$$

On using equations (16) to (20) and equation (31), the energy density of the model is obtained as

$$\rho = \frac{1}{n^{1/n}(\gamma+1)^{1/n}}\left[\frac{18m^2M^2}{(-3m+1)^2e^{6mt}} + \frac{2m^2}{e^{2mt}}\right]^{1/n} \tag{37}$$

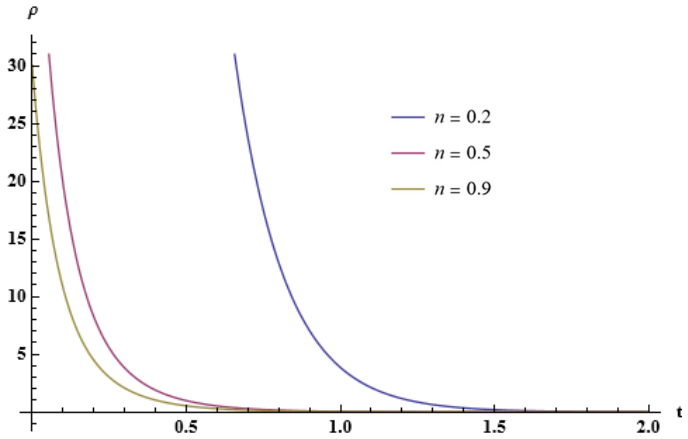

Figure 4. Energy density verses cosmic time t is plotted by assuming $\chi = 1.1, M = 1, \alpha = 0.5, m = 1.5$

On using the equations (6) & (37) the pressure of the model is obtained as

$$p = \frac{\gamma}{n^{1/n}(\gamma+1)^{1/n}}\left[\frac{18m^2M^2}{(-3m+1)^2e^{6mt}} + \frac{2m^2}{e^{2mt}}\right]^{1/n} \tag{38}$$

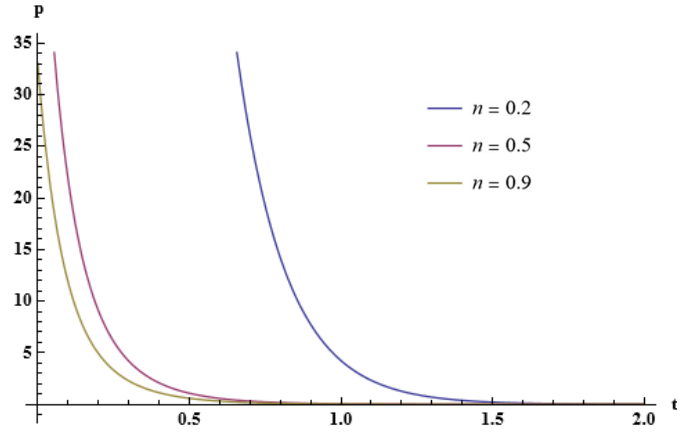

Figure 5. Pressure versus cosmic time t is plotted by assuming $\chi = 1.1, M = 1, \alpha = 0.5, m = 1.5$

In the case of Model-II, we also observe that the energy density depends on γ. Therefore, by selecting an appropriate numerical value for γ, three distinct types of universes can be identified as: the dust universe (γ = 0), the radiation-dominated universe (γ = 1/3), and the Zeldovich universe (γ = 1), $\gamma = 1/3$ as outlined below.

i) Dust Universe $(\gamma = 0)$:

For $\gamma = 0$, the model-II corresponds to the equation of state given in equation (6), which leads to $p = 0$. Hence, the energy density for the dust universe is given by

$$\rho = \frac{1}{n^{1/n}}\left[\frac{18m^2M^2}{(-3m+1)^2e^{6mt}} + \frac{2m^2}{e^{2mt}}\right]^{1/n}. \tag{39}$$

ii) Radiation-Dominated Universe $(\gamma = 1/3)$

For $(\gamma = 1/3)$, the model-II corresponds to the equation of state given in equation (6), which leads to $3p = \rho$. Hence, the energy density for the Radiation Dominated Universe is given by

$$\rho = \frac{1}{n^{1/n}(\frac{4}{3})^{1/n}}\left[\frac{18m^2M^2}{(-3m+1)^2 e^{6mt}} + \frac{2m^2}{e^{2mt}}\right]^{1/n}. \tag{40}$$

iii) Zeldovich Universe $(\gamma = 1)$

For $\gamma = 1$, the model-II corresponds to the equation of state given in equation (6), which leads to $p = \rho$. Hence, the energy density for the Zeldovich universe is given by

$$\rho = \frac{1}{n^{1/n}(2)^{1/n}}\left[\frac{18m^2M^2}{(-3m+1)^2 e^{6mt}} + \frac{2m^2}{e^{2mt}}\right]^{1/n}. \tag{41}$$

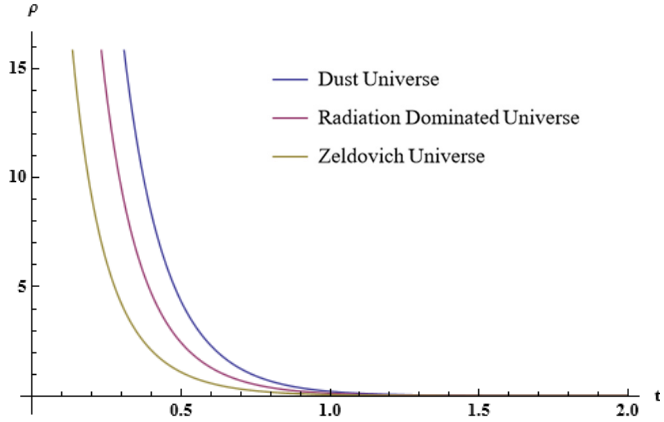

Figure 6. Energy density ρ for the Dust Universe, Radiation Dominated Universe, and Zeldovich Universe versus cosmic time t is plotted by assuming $\chi = 1.1, M = 1, \alpha = 0.5, n = 0.5, m = 1.5$

The Cosmological constant is obtained by using equations (17) – (20) and (32) as

$$\Lambda = \frac{1}{n(\gamma+1)}\left[\frac{18m^2M^2}{(-3m+1)^2 e^{6mt}} + \frac{2m^2}{e^{2mt}}\right] + \frac{3m^2(e^{2mt}-1)}{e^{2mt}} - \frac{9m^2M^2}{(-3m+1)^2 e^{6mt}} \tag{42}$$

Common Physical Parameter for Model-I and Model-II:

On using equation (10), the anisotropic parameter is given by

$$\Delta = \frac{1}{3}\sum_{i=1}^{3}\left(\frac{H_i}{H} - 1\right) = 0. \tag{43}$$

Using equation (11), the shear scalar is obtained as

$$\sigma^2 = \frac{3}{2}\Delta H = 0 \tag{44}$$

Graphical Representation of Physical and Kinematical Parameters

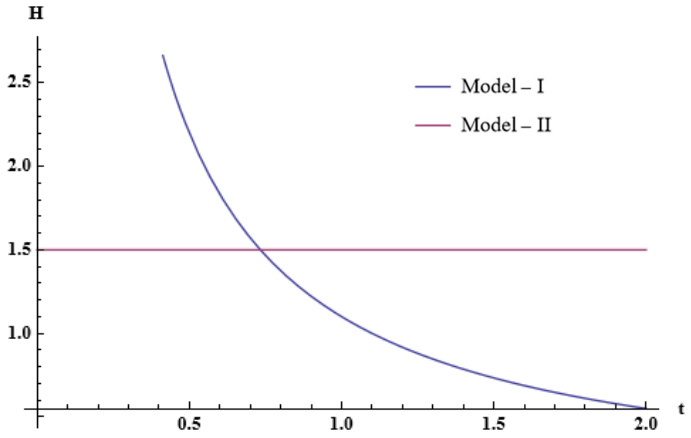

Figure 7. Hubble parameter verses cosmic time t is plotted by assuming $\chi = 1.1, \alpha = 0.5, m = 1.5$

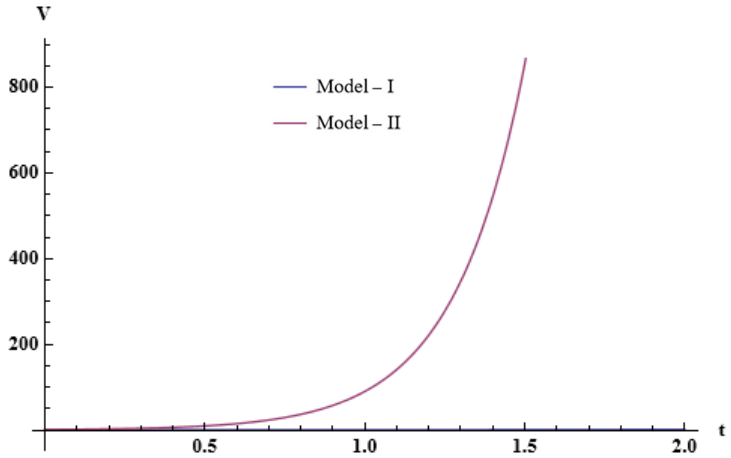

Figure 8. Spatial volume verses cosmic time t is plotted by assuming $\chi = 1.1, \alpha = 0.5, m = 1.5$

5. Stability of Models

To assess the stability of the models, the ratio of the sound speed $\frac{dp}{d\rho} = C_s^2$ is analyzed. According to Nimkar et al. (2023), the model is considered stable when this ratio satisfies $\frac{dp}{d\rho} > 0$, and unstable when $\frac{dp}{d\rho} < 0$. In the context of the present model, the sound speed ratio is derived as

$$\frac{dp}{d\rho} = \gamma, \tag{45}$$

Since, it is observed from equation (45) that $\frac{dp}{d\rho} = C_s^2$ remains positive for the selected values of the model parameters, indicating that the models are stable under the given conditions.

6. DISCUSSION AND RESULTS

In this work, we have studied the homogeneous Bianchi Type V cosmological model in the context of $f(R, L_m)$ gravity by considering two specific models as, Model-I is power law and Model-II is exponential law. The solutions of the modified field equations were obtained under the assumption of a functional form $f(R, L_m)$ as $f(R, L_m) = \frac{R}{2} + L_m^n$, where n is free model parameters and the findings are given as below.

In both the models,

- The Hubble parameter H decreases with cosmic time t, showing a accelerated expansion phase (Fig. 7).

- The deceleration parameter q remains constant, depending on the exponent.
- The spatial volume V increases exponentially with cosmic time t, confirming cosmic expansion (Fig. 8).
- Dust Universe ($\gamma = 0$): The energy density decreasing as $\rho \propto a^{-3n}$ (Fig.3 & Fig. 6).
- Radiation Dominated Universe $(\gamma = 1/3)$: Displays steeper decline in energy density.
- Zeldovich Universe $(\gamma = 1)$: Demonstrates even more rapid decay in energy density.
- Anisotropy Parameter (Δ) and Shear Scalar (σ^2) were calculated in equations (43), (44) and both were observed to decrease with time, which implies that the universe transits toward isotropy on late times.
- Expansion scalar and spatial volume both exhibits increasing trends, supporting an expanding universe.
- The square of the sound speed is found to be positive, which ensures that both cosmological models are dynamically stable for the selected values of parameters.
- In case of Model –I (Figs. 1 and 2), there is a sudden fall in both, the energy density ρ and pressure p and after some time they decrease gradually with respective cosmic time whereas, in Model-II (Figs. 4 and 5), the energy density ρ and pressure p both decrease monotonically over time, indicating that matter thins out as the universe expands.

CONCLUSIONS

In this study, we have examined the homogeneous Bianchi Type-V cosmological model within the framework of $f(R, L_m)$ gravity by formulating and analyzing two distinct scenarios. Model-I governed by a power-law expansion and Model-II governed by an exponential-law expansion. The exact solutions of the modified field equations are obtained under suitable assumptions on the functional form of the scale factor.

The analysis reveals that in both models, the Hubble parameter decreases with cosmic time while the deceleration parameter remains constant, corresponding to an accelerated expansion phase. The spatial volume exhibits exponential growth, confirming the overall expanding nature of the universe. For different models, the energy density was found to decay with time, with the sudden decline observed in the radiation $(\gamma = 1/3)$ and Zeldovich $(\gamma = 1)$ dominated epochs, while the dust case shows a slower decrease.

The anisotropy parameter and shear scalar both diminish as time progresses, demonstrating that the anisotropic Bianchi Type-V universe evolves towards isotropy at late times. Furthermore, the expansion scalar and spatial volume increase monotonically, further supporting the expansion scenario. The positivity of the squared sound speed guarantees that the models remain dynamically stable for the considered parameters.

A distinction between the two models lies in the behavior of energy density and pressure, while Model–I exhibits an initial sudden fall before approaching gradual decay, Model–II displays a monotonic decrease throughout the cosmic evolution. This comparative behavior highlights the role of the underlying law of expansion in shaping the dynamics of the evolving universe.

Compared with our, earlier FLRW study in $f(R, L_m)$ gravity, Katore *et. al.* (2025), which showed a constant deceleration parameter and sustained acceleration, the present Bianchi Type – V model extends the analysis to an anisotropic framework. While both models support late-time acceleration, the current work additionally demonstrates the evolution toward isotropy, thereby generalizing the earlier results within the same modified gravity.

Overall, the results suggest that the considered Bianchi Type-V cosmological model not only accommodate an accelerating universe but also successfully describes the dynamical evolution from anisotropy to isotropy at late times. Together with our previous FLRW analysis, the present study strengthens the viability of $f(R, L_m)$ gravity in explaining different cosmological phases within both isotropic and anisotropic frameworks, thereby reinforcing its relevance in modern cosmology.

ORCID

P.R. Agrawal, https://orcid.org/0000-0002-8040-937X; **H.G. Paralikar,** https://orcid.org/0009-0003-1301-5340
A.P. Nile, https://orcid.org/0009-0003-1504-9085

REFERENCES

[1] K.S. Adhav, "Bianchi Type-III Cosmic Strings Cosmological Model in *f*(*R*) Theory of Gravity," Bulgarian Journal of Physics, **39**(3), 197-206 (2012). https://www.bjp-bg.com/papers/bjp2012_3_197-206.pdf

[2] P.R. Agrawal, and A.P. Nile, "Accelerating Universe with Wet Dark Fluid in Modified Theory of Gravity," Astronomy and Computing, **48**, 100847 (2024). https://doi.org/10.1016/j.ascom.2024.100847

[3] P.P. Avelino, and R.P.L. Azevedo, "Perfect fluid Lagrangian and its cosmological implications in theories of gravity with nonminimally coupled matter fields," Physical Review D, **97**(6), 064018 (2018); Sharif, M., & Gul, M. Z. (2019). Dynamics of perfect fluid collapse in *f*(*G*, *T*) gravity. *International Journal of Modern Physics D*, *28*(03), 1950054.

[4] B.K. Bishi, and K.L. Mahanta, "Bianchi Type-V Bulk Viscous Cosmic String n Gravity with Time Varying Deceleration Parameter," Advances in High Energy Physics, **2015**, 91403 (2015). https://doi.org/10.1155/2015/491403
[5] G.C. Carvalho, M.E.X. Guimarães, P.O. Mesquita, and J.L. Neto, "Formation and Evolution of Wakes in the Spacetime Generated by a Cosmic String in $f(R)$ Theory of Gravity," preprint arXiv:2110.02353, (2021). https://doi.org/10.48550/arXiv.2110.02353
[6] C. Chawla, and R.K. Mishra, "Bianchi type-I viscous fluid cosmological models with variable deceleration parameter," Rom. J. Phys. **58**(1-2), 75-85 (2013).
[7] M.R. da Silva, "Cosmic Strings in Modified Theories of Gravity", Master's thesis, Universidade do Porto (Portugal), 2021.
[8] R. Garg, G.P. Singh, A.R. Lalke, and S. Ray, "Cosmological Model with Linear Equation of State Parameter in $f(R, L_m)$ Gravity," preprint arXiv:2310.17340, (2023). https://doi.org/10.48550/arXiv.2310.17340
[9] T. Harko, and F.S. Lobo, "$f(R, L_m)$ gravity," The European Physical Journal C, **70**(1-2), 373-379 (2010). https://dx.doi.org/10.1140%2Fepjc%2Fs10052-010-1467-3
[10] T. Harko, and M.J. Lake, "Cosmic Strings in $f(R, L_m)$ Gravity," The European Physical Journal C, **75**, 60-78 (2015). https://doi.org/10.1140/epjc/s10052-015-3287-y
[11] T. Harko, and F.S. Lobo, "$f(R, L_m)$ Gravity," The European Physical Journal C, **70**, 373-379 (2010). https://doi.org/10.1140/epjc/s10052-010-1467-3
[12] T. Harko, and F.S. Lobo, "Generalized Curvature-Matter Couplings in Modified Gravity," Galaxies, **2**(3), 410-465 (2014). https://doi.org/10.3390/galaxies2030410
[13] S.P. Hatkar, S.V. Gore, and S.D. Katore, "Kasner Type Magnetized String Cosmological Models in $f(R, T)$ Gravity," Serbian Astronomical Journal, (197), 1-11 (2018). https://doi.org/10.2298/SAJ1897001H
[14] L.V. Jaybhaye, R. Solanki, S. Mandal, and P.K. Sahoo, "Cosmology in $f(R, L_m)$ gravity," Physics Letters B, **831**, 137148 (2022a). https://doi.org/10.1016/j.physletb.2022. 137148
[15] L.V. Jaybhaye, S. Mandal, and P.K. Sahoo, "Constraints on Energy Conditions in $f(R, L_m)$ Gravity," International Journal of Geometric Methods in Modern Physics, **19**(04), 2250050 (2022b). https://doi.org/10.1142/S0219887822500505
[16] L.V. Jaybhaye, R. Solanki, and P.K. Sahoo, "Bouncing Cosmological Models in $f(R, L_m)$ Gravity," Physica Scripta, **99**(6), 065031 (2024). https://doi.org/10.1088/1402-4896/ad4838
[17] S.D. Katore, P.R. Agrawal, H.G. Paralikar, and A.P. Nile, "Dynamics of String Cosmological Model in $f(R, L_m)$ Theory of Gravity," East European Journal of Physics, (1), 70-78 (2025). https://doi.org/10.26565/2312-4334-2025-1-06
[18] R.V. Lobato, G.A. Carvalho, and C.A. Bertulani, "Neutron Stars in $f(R, L_m)$ Gravity with Realistic Equations of State: Joint-Constrains with GW170817, Massive Pulsars, and the PSR J0030+0451 mass-radius from NICER data," Eur. Phys. J. C, **81**, 1013 (2021). https://doi.org/10.1140/epjc/s10052-021-09785-3
[19] A. Malik, "A Study of Levia-Civita and Cosmic String Solutions in Modified $f(R)$ Gravity," preprint arXiv:2404.10793, (2024). https://doi.org/10.48550/arXiv.2404.10793
[20] A.S. Nimkar, and S.R. Hadole, "Stability of Cosmological Model in Self-Creation Theory of Gravitation," Journal of Scientific Research, **15**(1), (2023). http://dx.doi.org/10.3329/jsr.v15i1.59676
[21] V. Patil, J. Pawde, R. Mapari, and S. Waghmare, "FLRW Cosmology with Hybrid Scale Factor in $f(R, L_m)$ Gravity," East European Journal of Physics, (4), 8-17 (2023). https://doi.org/10.26565/2312-4334-2023-4-01
[22] J. Pawde, R. Mapari, V. Patil, and D. Pawar, "Anisotropic Behavior of Universe in $f(R, L_m)$ Gravity with Varying Deceleration Parameter," The European Physical Journal C, **84**(3), 320 (2024). https://doi.org/10.1140/epjc/s10052-024-12646-4
[23] O. Piattella, *Lecture notes in cosmology*, (Berlin, Springer, 2018).
[24] B.K. Shukla, R.K. Tiwari, D. Sofuoğlu, and A. Beesham, "FLRW Universe in $f(R, L_m)$ Gravity with Equation of State Parameter," East European Journal of Physics, (4), 376-389 (2023). https://doi.org/10.26565/2312-4334-2023-4-48
[25] R. Solanki, Z. Hassan, and P.K. Sahoo, "Wormhole Solutions in $f(R, L_m)$ Gravity," Chinese Journal of Physics, **85**, 74-88 (2023). https://doi.org/10.1016/j.cjph.2023.06.005

КОМПЛЕКСНИЙ АНАЛІЗ МОДЕЛІ БІАНКІ ТИПУ V В ТЕОРІЇ ГРАВІТАЦІЇ $f(R, L_m)$

П.Р. Агравал, Х.Г. Паралікар, А.П. Найл
Кафедра математики, Науковий коледж Бріджлал Біяні, Амраваті, 444602, Індія

У цій статті досліджено однорідну космологічну модель Б'янкі типу V в рамках $f(R, L_m)$ гравітації. Розв'язок рівнянь поля отримано шляхом розгляду окремого випадку $f(R, L_m) = R/2 + L_m^n$, де n вільний параметр моделі. Було проаналізовано фізичні та динамічні властивості моделі, а також наведено графічні зображення для ілюстрації властивостей цих параметрів.
Ключові слова: *тип Біанкі – V; аналіз стійкості; $f(R, L_m)$ гравітація; ідеальна рідина*